Slip Table Dynamic Behavior

by

Elizabeth Therese Smith

Submitted to the Department of Aeronautics and Astronautics
in partial fulfillment of the requirements for the degree of

Master of Science in Aeronautics and Astronautics

at the

MASSACHUSETTS INSTITUTE OF TECHNOLOGY

February 1995

Author ... .
Department of Aeronautics and Astronautics
September 2, 1994

Certified by .....
Professor Hugh L. McManus
Assistant Professor
Thesis Supervisor

Certified by .....
David M. Montoya
Section Leader, Los Alamos National Laboratory
Thesis Supervisor

Accepted by .. ..
Professor Harold Y. Wachman
Chairman, Departmental Graduate Committee

Slip Table Dynamic Behavior

by

Elizabeth Therese Smith

Submitted to the Department of Aeronautics and Astronautics
on September 2, 1994, in partial fulfillment of the
requirements for the degree of
Master of Science in Aeronautics and Astronautics

Abstract

A physical basis is set forth for selecting test specimen and control accelerometer locations for vibration tests conducted on a slip table. Experimental data is gathered from a shaker-slip table assembly at Los Alamos National Laboratory. Two models of the assembly are designed–one a linear Matlab model and the other an explicit time simulation code in Fortran. The system properties for both models are found using matrix methods of structural analysis. The linear model is used to find the free vibration frequencies and mode shapes of the system. The explicit time simulation model employs a Runge-Kutta algorithm with adaptive step size control for solving the equations of motion. In addition, it includes a drive signal update loop to more accurately model the experiment and to allow for system nonlinearities. The results attained analytically using the models are compared with those attained experimentally, and good correlation is found. To simulate test object placement, additional tests are run with various masses attached to the slip table. Again, analytical and experimental results are correlated. Finally, the analytical model is used to understand problems which can result from system nonlinearities; and to determine their effects on equipment performance.

Thesis Supervisor: Professor Hugh L. McManus
Title: Assistant Professor

Thesis Supervisor: David M. Montoya
Title: Section Leader, Los Alamos National Laboratory

Dedication

To my beloved grandparents,

be they with me in body or soul

Acknowledgments

First and foremost, I would like to thank my advisor, Professor Hugh McManus, for his advice, patience, kindness, and good humor.

I would also like to thank everyone in the Analysis and Testing Group at Los Alamos National Laboratory (WX-11) for making this thesis both possible and enjoyable. David Montoya, my advisor at Los Alamos National Lab, for his willingness to help and for being a wonderful friend. Norm Hunter for his advice, guidance, and endless hours of time and thought. Jim, Gerard, and Orlando for their help in running all of my tests and for their patience as I learned how to use the equipment. Paul Smith for envisioning this thesis and for his enthusiasm, constant support, and encouragement. John Ruminer for making my working at Los Alamos National Laboratory possible. Russ and Kay for putting up with me and my hair and for keeping me marginally sane! And everyone else at Los Alamos for making my stay so very enjoyable; they (Andrew, Jeff, Brian, and Don, to name a few) never stopped giving me a hard time.

Tariq for his encouragement and help in the proofreading of this thesis. John Corley, Arlene, and Charlie for their friendship and for providing musical interludes.

My family (Mom, Dad, Christina, Andrea, and Stephen) for their support not only during this thesis, but throughout my entire stay at MIT; and for that matter, for my entire life.

And finally to Iman, whose love and patience helped me to successfully complete this thesis and to enjoy these last few years at MIT so very much. He will be missed dearly.

Contents

List of Figures

List of Tables

List of Symbols

$a_i(t)$	Drive Signal in the Time Domain
a_0	Constant Fourier Coefficient
a_k	Constant Fourier Coefficient
$\boldsymbol{A}$	Arbitrary $n \times n$ Matrix
A_{123}	Area of Triangle 123
$\boldsymbol{b}$	Exact Strain Matrix
$\underline{\boldsymbol{b}}$	Approximate Strain Matrix
b_k	Constant Fourier Coefficient
B	Frequency Resolution Bandwidth
c	Damping
$c_1, \ldots, c_8$	Arbitrary Constants
$\boldsymbol{c}$	Damping Matrix
c_k	Complex Fourier Coefficient
C	Acoustic Velocity or Wave Speed
$C_i(\omega)$	Measured Control Spectrum of ith Control Update Loop
$C_i^E(\omega)$	Exponentially Averaged Control Spectrum of ith Update Loop
$D_i(\omega)$	Updated Drive Spectrum of ith Control Update Loop
$D_i^E(\omega)$	Exponentially Averaged Drive Spectrum of ith Update Loop
$\boldsymbol{e}$	Matrix of Total Elastic Strains
E	Young's Modulus of Elasticity
$E[x(t)]$	Expected or Mean Value of A Function $x(t)$
$E[x^2]$	Mean Square Value of $x(t)$
$f(t)$	Random Excitation Input

$\boldsymbol{F}(t)$	Force Matrix
F_0	Force Amplitude Constant
h	Step Size
$H(\omega)$	Frequency Response Function or Transfer Function
$H^a(\omega)$	Transfer Function Relating Two Accelerations
i	$\sqrt{-1}$
$\boldsymbol{I}$	Identity Matrix
k	Stiffness
$\boldsymbol{k}$	Stiffness Matrix
$\boldsymbol{k}_n$	Stiffnesses Due to Normal Stresses
$\boldsymbol{k}_s$	Stiffnesses Due to Shear Stresses
m	Mass
m	Mean Value of A Function
$\boldsymbol{m}$	Mass Matrix
N	Number of Samples or Averages
$p(x)$	Probability Density Function
P	Discount Averaging Parameter
$\boldsymbol{P}$	Vector of Forces
$R(\omega)$	Reference Spectrum
$R_{xx}(\tau)$	Auto-Correlation Function for $x(t)$
$R_{xy}(\tau)$	Cross-Correlation Function Between $x(t)$ and $y(t)$
$S_{xx}(\omega)$	Auto-Spectral Density Function For $x(t)$
$\tilde{S}_{xx}$	Weighted Spectral Density
$S_{xy}(\omega)$	Cross-Spectral Density Function Between $x(t)$ and $y(t)$
t	Thickness
t	Time
T	Period or Single Measurement Duration
T_t	Total Measurement Duration
u_x, u_y, u_z	Displacements in the x, y, and z Directions
$\boldsymbol{u}$	Vector of Displacements

v	Eigenvector
$W(\Omega)$	Spectral Window
$\boldsymbol{x}(t)$	Displacement Matrix
$\dot{\boldsymbol{x}}(t)$	$d\boldsymbol{x}/dt$ (Velocity Matrix)
$\ddot{\boldsymbol{x}}(t)$	$d^2\boldsymbol{x}/dt^2$ (Acceleration Matrix)
x_{ij}	$x_i - x_j$ (Matrix Structural Analysis Notation)
x_r	Discrete Time Series
$\ddot{x}_c(t)$	Acceleration at Control Accelerometer
$\ddot{x}_p(t)$	Acceleration at Arbitray Table Point, p
X_k	Discrete Fourier Transform of The Series x_r
$X(\omega)$	Fourier Transform of $x(t)$
$\boldsymbol{X}(\omega)$	Matrix of Complex Amplitude Constants
y_{ij}	$y_i - y_j$ (Matrix Structural Analysis Notation)
$\boldsymbol{Z}(\omega)$	Matrix of Impedance Functions
α	$1 - \nu$, A Constant
β	(Aspect Ratio) Ratio of A Rectangular Element's Dimensions
γ	$1 + \nu$, A Constant
$\delta\boldsymbol{U}$	Virtual Displacements
$\delta\boldsymbol{U}_i$	Virtual Strain Energy
$\delta\boldsymbol{W}$	Virtual Work
$\delta\boldsymbol{\epsilon}$	Virtual Strains
Δ	Sampling Interval
$\Delta\omega$	Frequency Spacing
$\boldsymbol{\epsilon}$	Matrix of Compatible Strains
ε_r	Normalized Random Error
ζ	Damping Factor
η	Non-Dimensional Coordinate
η^2_{xy}	Coherence Function
ϑ	Discount Averaging Parameter
κ	$1 - 3\nu$, A Constant

λ Eigenvalue

ν Poisson's Ratio

ξ Non-Dimensional Coordinate

ρ Density

σ Standard Deviation

σ^2 Variance

$\boldsymbol{\sigma}$ Stress Matrix, Stress Distribution

ω Frequency

ω_n Natural Frequency

τ Time Separation

Superscripts

db Driver Bar

fx Fixture

pj Pin Joint

sf Shaker-Fixture Interface

st Slip Table

Chapter 1

Introduction

1.1 Vibration Testing

Vibrations exist in all aspects of life, from the oscillations of our lungs as we breathe to the resonance in our voice box as we speak. In fact, the very atoms which constitute the universe vibrate incessantly. Some vibrations, however, are undesirable and can have harmful consequences. The severe vibrations found in many mission environments can damage both mechanical and electrical systems. Space payloads, weapon system components, and scientific instrumentation packages are among the many items whose function can be impaired by vibration. To understand and design systems capable of withstanding detrimental vibration conditions, potentially damaging vibration environments must be simulated. Structural response of test objects subjected to these simulated conditions is then measured and analyzed to determine failure modes and other undesirable behavior.

Vibration testing is a major tool used in the development of military and space hardware and commercial and consumer products to assure product reliability and safety. Testing provides a necessary supplement to the design and analysis of objects which will experience vibration environments. Free and forced vibrations of mechanical systems can be studied using analytical tools; however, as is the case with most mathematical models, the predicted behavior of the system is based on simplifying assumptions (particularly in the areas of material properties, damping, and nonlin-

earities). Models, therefore, while useful in forecasting the performance of a system during the design stages, are often inadequate, and it is advisable to test the final design in its prototype form before it is certified for safe operations. Information gained from such tests is important in defining the design limits of a test item, evaluating its physical characteristics and response to mechanical excitation (natural resonant frequencies, mode shapes, and damping parameters), and in predicting its operating limits. Simulating environmental vibration levels during product development assures that a design is suitable for its application, reduces design costs, lowers equipment failure rates, and increases personnel safety.

Vibration exciters are used to simulate mechanical vibrations and can generate waveforms which vary as functions of frequency, amplitude, and phase relation; such exciters fall into three categories. The first, mechanical in form, operates on the principal of either a rotating unbalance, a reciprocating follower motion, or an eccentric cam to generate an excitation force and a given displacement. The second, an electrohydraulic shaker, employs a fluid-pressure controlled piston-cylinder arrangement. The third, an electrodynamic exciter, is the most widely used type of vibration shaker and operates on the principal of a force generated by a changing current acting on a conductor in a magnetic field.

The experimental portion of this thesis was done at Los Alamos National Laboratory. The Environmental Testing Section of the Analysis and Testing Group there has two electrodynamic vibration exciters, each of which can be run in the vertical direction or rotated, attached to slip tables, and run in the horizontal direction.

1.2 Slip Tables

Slip Tables allow lateral displacements and come in a variety of forms. The two tables mentioned above, possessed by the Environmental Testing Section of the Analysis and Testing Group at Los Alamos National Laboratory, are manufactured by Kimball Industries. A magnesium slip plate rests upon a thin film of oil which is pumped over a precision ground granite surface. The thin oil film provides minimal shearing restraint

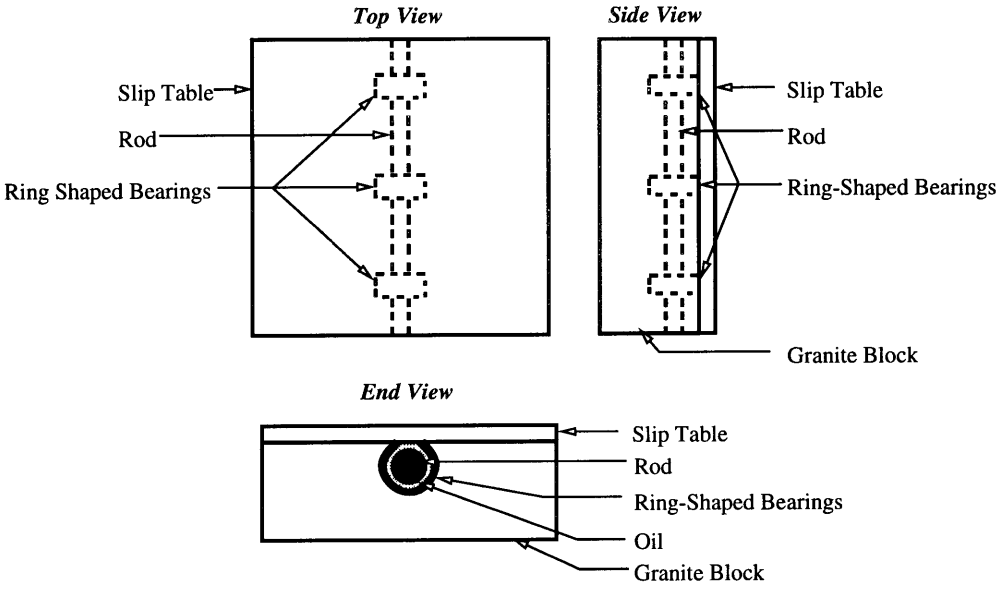

Figure 1-1: Hydrostatic Bearings

but immense stiffness normal to the surface, uniformly over the complete horizontal area. Lateral restraint is provided by hydrostatic bearings which are mounted to the under side of the slip plate (as shown in Figure 1-1). The bearings consist of three rings, mounted along the length of the slip plate, which ride on a rod situated in the granite block. They are referred to as hydrostatic because oil is pumped between the rings and the rod to facilitate movement [1]. This type of bearing line table (three bearings attached down the centerline) minimizes cross-axis acceleration.

There is a glass composite layer attached to the top of the slip plate to facilitate thermal testing. This glass composite layer provides insulation of the table from the environment imposed on the test object, thus preventing problems such as the oil cooling and becoming too viscous. The complete shaker-slip table assembly is supported by a concrete-filled reaction mass base which rests on an air isolation system. The shaker-slip table assembly is pictured in Figure 1-2.

The use of a slip table creates complications which are not present when using a vibration exciter alone. Because the center of gravity of a test article is separated vertically from that of the table, reaction moments are transmitted to the table. In

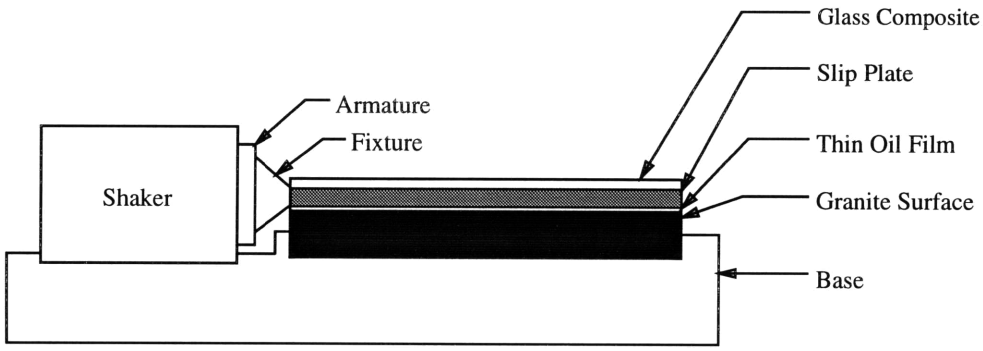

Figure 1-2: Shaker-Slip Table Assembly

addition, since shaker output is limited, large weights added to the shaker (such as the slip table itself and any attached test objects) reduce attainable vibration levels.

Slip table use is also constrained by the flexing and in-plane resonant modes of the slip plate. Ideally, a slip table would provide an infinitely stiff, massless connection between a shaker and a test item. For small slip tables, approximately one foot square, the assumption that the plate behaves as a rigid body is quite realistic, but as the size of the slip table increases and frequency increases, this assumption becomes increasingly erroneous. Many tables, including those at Los Alamos, are four feet square or larger, and are driven at frequencies up to 2000 Hz. The resonant responses in these slip tables can cause tremendous control problems. If a table anti-resonance is located at the control location, too much shaker input may be called for and the test will not run (the system will shut down before it reaches mechanical failure levels). In addition, anti-resonances or uncontrolled resonances in the table at the location of a test item cause inaccurate testing of the attached specimen.

Other complications resulting from the use of a slip table include the fact that the rigidity of the attachment between the shaker and the slip table, as well as the armature mass and stiffness, must be taken into consideration. Attachment to a slip table also requires that variables such as table deformation and friction and sticking between the table, base, and oil be accounted for.

These variables and potentially others may explain why, historically, there has been substantial difficulty in running tests using slip tables. Solutions to the problems

associated with slip table use include altering the table structure such that it does not resonate within the frequency limits specified by a given test plan. Due to time and monetary constraints, as well as to limits on shaker output, however, options such as increasing the table thickness, decreasing the table surface area, or increasing the table damping are not always available to overcome such problems. Instead, the complications resulting from the use of a slip table must be overcome using existing hardware–for example, by varying test object and control accelerometer placement to avoid anti-resonances and to control resonant behavior.

Currently, only empirical methods are available for determining where test objects and control accelerometers should be placed. An example is the fact that, from experience, test engineers know that optimal control of a test is attained only when the specimen is located as far out on the table as possible–at maximum distance from the shaker. But little previous work has been done to actually characterize slip tables and the control configurations related to their use. In fact, currently there is not a set of written guidelines to determine test specimen location, control accelerometer location or locations, and control strategy for vibration tests conducted on a slip table.

1.3 Objective

The objective of this thesis is to understand the physical basis underlying the current empirical methods for selecting test specimen and control accelerometer locations for vibration tests conducted on a slip table, and to set forth a basis for future improvements in testing techniques.

1.4 Approach

The approach taken by this thesis to meet the aforementioned objective involves five main components: research, experimentation, modeling, correlation, and application. The research portion entails a literature search of previous work done to characterize

and model shaker-slip table assemblies, as well as a collection of the empirical rules (folklore) for testing on slip tables. The experimental section involves instrumenting a shaker-slip table assembly with accelerometers and acquiring data; and the theoretical portion involves using both closed form and explicit computer solutions to model the behavior of the shaker-slip table assembly. The theoretical model also requires determining system properties using matrix structural analysis. The final two steps of the approach entail comparing and correlating the analytical and experimental results and then manipulating the theoretical model to predict the system's behavior under a variety of circumstances (different test object weights, various test object locations, joint non-linearities, etc.) These different aspects of the thesis are explained in detail in the chapters which follow.

Chapter Two describes how this thesis relates to prior work which has been done and introduces the basic technology which is necessary to understand this thesis.

Chapter Three is an explicit statement of the problem to be solved here.

Chapter Four outlines the experimental procedure and describes the specifics of the shaker-slip table assembly which was used.

Chapter Five specifies the theoretical model and includes a description of the variables involved in the physical system, an outline of the matrix structural analysis theory used to characterize the shaker-slip table assembly, and a description of the computer algorithms employed to solve the equations of motion and to update the drive signal.

Chapter Six presents and discusses the experimental and analytical results, compares and correlates the two, and looks at how sensitive the shaker-slip table assembly is to a variety of problems.

Finally, Chapter Seven offers conclusions on the physical behavior of the system and the performance of the theoretical models, and recommends how the models can be used as well as how they can be improved.

Chapter 2

Background

This background chapter is subdivided into two sections. The first describes the previous work done to characterize or model slip table dynamic behavior and explains its applicability to this study. The second presents a theoretical foundation for understanding the work conducted here.

2.1 Previous Work With Slip Tables

Limited work has been done to characterize or to model slip table dynamic behavior. An extensive literature search of the field provided one early model of the vibration characteristics of a slip table, some patents designed to improve slip table performance, and a few related papers discussing the properties of expander heads (which like slip tables, are attached to shakers for vibration testing, but which are used for vertical tests).

2.1.1 Vibration Characteristics of a Slip Table

In 1964, Malcolm Armstrong Cutchins did what he described as a "Preliminary Investigation of the Vibration Characteristics of a Slip Table" [2]. He attacked the complex problem of analyzing a shaker-slip table assembly using a very simple model–a bar of constant cross section, free at one end and along its length, and subjected to a sinu-

soidal force at the other end. He modeled objects to be tested using the shaker-table assembly as weights attached at various points along the bar. Cutchins' goals were to determine the fundamental frequencies of the shaker-slip table-test package assembly and to find the force transmissibility between the shaker input and the test package.

Using basic force-equilibrium equations with boundary conditions, Cutchins was able to analytically determine the fundamental frequencies of the structure, as well as the transmissibility of the system. To verify the analytical expressions he attained, Cutchins performed two different experiments using a mild steel bar, 1/2 inch in diameter and 24 inches long, and three blocks of varying weight (to simulate the test packages) with approximate dimensions of 2 in. $\times$ 2 in. $\times$ 1 in.

The first experiment, designed to determine the fundamental frequencies of the system, involved connecting the bar directly to a coupling mounted on the shaker and noting the drive frequency at which the displacement of the shaker-end of the bar became zero. Then, by adding a known weight to the coupling and again measuring the frequency at which the deflection of the shaker-end of the bar became zero, Cutchins was able to determine the fundamental frequencies of the structure using Dunkerley's method. The second experiment, used to determine the transmissibility of the input force to the test package, involved suspending the bar with wires from an overhead beam, and mounting a force gage on the bar at the location of the shaker input. The transmissibility was found by taking the ratio of the measured force at the shaker to the force acting on the concentrated weight. This latter force was calculated by multiplying the mass of the concentrated weight by its acceleration, which was measured using an accelerometer.

The fundamental frequencies which Cutchins attained experimentally were in good agreement with those he determined analytically, except when the position of the weight was moved close to the shaker. The transmissibilities which he determined analytically and experimentally were also in good agreement, with slight discrepancies resulting from difficulties choosing accelerometer locations as well as non-rigid body vibrations of the blocks representing the concentrated weights. Cutchins found the transmissibility curves to be continuous. In addition, he determined that much less

shaker input current is required to produce a large input force at or near the system's natural frequencies.

The model which Cutchins used to characterize the dynamic behavior of a slip table was very simple. Cutchins' model did not incorporate damping or allow for nonlinearities or asymmetries. Cutchins also did not consider closed-loop control of table behavior. While Cutchins' model is not itself very accurate or very complete, it does provide a good basis for further work.

2.1.2 Slip Table Damping

In 1991, Danny L. Gregory, Tommy G. Pridday, David O. Smallwood, and Tommy D. Woodall received a patent for their design of a "Composite Slip Table of Dissimilar Materials for Damping Longitudinal Modes" [3]. Their patent specifies a slip table consisting of three different layers of material: first, a metallic layer; second, a damping layer made of a visco-elastic material such as polyurethane; and third, a graphite-epoxy composite layer possessing a high acoustic velocity relative to that of the first layer. The layers are attached in any manner that permits a shear force to be transmitted between them. The slip table which their patent outlines possesses a higher natural frequency and stiffness than current slip tables, as well as increased damping of its longitudinal modes of vibration.

Prior to their patent, slip tables were only designed of either one material, such as steel, magnesium, or aluminum, or of a sandwich-style combination of one of these materials and a damping material (i.e. aluminum/damping material/aluminum). While the latter tables do provide some damping of table bending modes, neither design dampens the axial modes of vibration of the slip table. And, since in reality excitation is along the longitudinal axis and since the base and bearings act to prevent out-of-plane movement of the slip plate, it is these longitudinal modes which are of primary concern when using a slip table.

The idea behind making a table of three dissimilar materials is that the difference in acoustic velocities (which translates to the existence of different longitudinal modes) between the top and bottom layers will cause relative shear displacements between

them. These displacements will then be damped by the middle, viscoelastic layer. The frequency of the longitudinal vibrational modes of the table will be increased if the first and third layers of the table have a greater combined stiffness than do current slip tables. Gregory et al. specify that the top layer of their table be metallic in order to provide a hard outer surface for clamping and mounting test items. This makes the use of graphite-epoxy (with a modulus of elasticity (E) of about 3 to 3.5 times that of the aluminum first layer) ideal for the bottom layer. In addition, since the density (ρ) of the graphite-epoxy third layer is about half that of the aluminum first layer, the acoustic velocity ($C = \sqrt{E/\rho}$) or wave speed in the graphite epoxy layer is about 2.5 to 3 times that of the aluminum layer. The net results, then, are a decrease of approximately 20% in table mass, an increase of about 25% in table stiffness and natural frequencies, and about four times more damping in the table. According to Gregory et al., even greater weight reduction, as well as increased bending stiffness, would be possible if hollow box sections were used.

Finally, their patent outlines the previous patents awarded in the realm of slip tables. A description of some of these patents is included here to illustrate the breadth of work done to date in the field. U.S. Patent # 3,044,292 describes a slip table made of one inch thick aluminum alloy plate attached to I-beams. U.S. Patent # 3,369,393 describes a lightweight, welded plate to be used as a text fixture in vertical vibration tests. U.S. Patent # 4,164,151 describes a vibration generator attached to a hollowed table top, which is divided horizontally into four sections and filled with heavy balls. The heavy balls roll and bounce within their individual compartments to produce random shocks. U.S. Patent # 4,440,026 specifies a torsionally stiff flexure support for attachment of a slip table to a vibration exciter. This type of support permits motion along the axis of vibration, but prevents pivoting movement about the center axis of the slip plate. Finally, U.S. Patent # 4,489,612 describes a driver bar for connecting a shaker and a slip table and for coupling their motions. The driver bar attaches to the slip table by means of limbs which embrace opposite sides of the slip plate. The lightweight welded plate and the driver bar have been built and are in current use, though they are not employed for this study.

Gregory et al. propose a new slip table design which will increase the natural frequencies and damping of a slip table, thereby improving its performance. To the author's knowledge, however, none of these tables have been built due to the large monetary investment such an endeavor would require. Even so, this patent offers insight into the problems which exist in the current slip table hardware. Many of the same variables in slip table performance discussed by Gregory et al. are also addressed here. In this study, however, the variables are discussed and analyzed from the perspective of using existing hardware to overcome the problems they present, rather than from the perspective of redesigning slip table hardware to avoid them.

2.1.3 Expander Heads for Vibration Systems

There are a number of articles which attempt to model and characterize the dynamic behavior of expander heads for vibration systems. Expander heads are used for shaker tests run in the vertical direction. They are fixtures, generally welded magnesium plate structures, which can be attached to shakers to increase the surface area available for mounting test objects.

Louie J. Lipp wrote a series of articles ([4], [5], and [6]) outlining the equations necessary to calculate the natural frequencies and damping of square, constant thickness expander heads, as well as the equations required to calculate the fundamental frequencies of the inverted truncated pyramid expander head.

His motivation was to be able to design large vibration expander heads which allow the attachment of several test specimens for simultaneous testing. This way, test time and cost could be greatly reduced. The basic problem, then, was to design an expander head which would not resonate within the frequency limits specified by a given test plan. Resonances can cause components in the resonating area of the expander head to experience much higher vibrational loads than either the test plan requires or than those items attached to a non-resonating portion of the expander head receive. The problem is further complicated by the fact that the location of the resonating portion of the expander changes with frequency. The end result is potentially erroneous failure data.

Lipp concluded that while it may not be possible to design an expander head with a natural frequency higher than that required by the test plan, several methods can be applied to make the natural frequency as high as possible: making the expander head as round as possible; placing the test packages with the least weight per surface area of expander head covered at the edges of the expander head, and placing the heavier items toward the center of the expander head; manufacturing the expander head of a material with a high Young's modulus to density ratio; and making the expander head as thick as possible.

However, if it is impossible, due to shaker limitations, to design a monolithic expander head thick enough that the natural frequencies of the expander head exceed the highest frequency input by the shaker during a given test, then the expander head can be manufactured using more than one material in a sandwich structure. In this case, maximum benefit is attained if the plate with the highest stiffness is placed farthest from the neutral axis of bending. In addition, maximum damping is attained if the plate with the highest specific damping capacity is placed farthest from the neutral axis of bending.

If a constant thickness expander head cannot be designed with natural frequencies higher than those required by the test plan, a variable thickness expander head should be used. An inverted truncated pyramid expander head employs the idea of variable thickness by removing material from outer portions of the expander head, where it is dead mass, and placing it in the center where it adds strength. Such a design results in higher natural frequencies and significant weight reduction.

Ballinger, Brown, and Peterson address the same problem as Lipp, but from a slightly different perspective, in "Design Optimization of a Vibration Exciter Head Expander" [7]. They describe the application of structural optimization algorithms in designing the head expander for an electrodynamic shaker, with the constraint that bending modes of vibration of the expander head-shaker assembly occur at frequencies greater than the maximum frequencies required by test plans ($\sim$2100 Hz).

Like Lipp, Ballinger et al. acknowledge the fact that resonances in the expander head, which occur at frequencies lower than the maximum frequency called for by

a given test plan, can cause variations in vibration level between various points on the table. These resonant frequencies can be increased by making the head expander thicker, but head expanders having more dead weight than necessary reduce the attainable vibration levels of the table. Ballinger et al. proposed shape and size optimization to strike a balance between increased material and dead weight. They used the following criteria in their optimization: 2100 Hz must be the minimum frequency of bending modes, the table surface dimensions must stay the same, and the mounting bolt pattern for attachment to the shaker armature must remain constant. The items varied were the head expander material, the number and location of support ribs, the thickness of the head expander table and support ribs, and the shape and height of the support ribs.

Using the optimization module of the SDRC I-DEAS Engineering analysis package, they were able to optimize the head expander design to meet the 2100 Hz frequency requirement with a decrease in weight. In addition, they concluded that the shaker-head assembly, rather than just the expander head, must be optimized in order to achieve optimum dynamic performance for minimum weight.

The problems addressed by Lipp and Ballinger et al. are very similar to those addressed in this study, just applied to a different axis. Because they are dealing with the vertical axis, they face the excitation of bending modes within the expander head plate. In this study, the longitudinal modes of the slip plate are of concern. In both cases, however, the presence of resonant behavior in the plate, at frequencies below the maximum required by a given test plan, can cause serious problems ranging from erroneous data to loss of control. These articles propose table modifications to overcome the problems associated with low natural frequencies. This study, on the other hand, outlines a model to be used to understand the table behavior so that test object placement and control accelerometer location can be varied to overcome the problems arising from table resonances.

2.2 Theoretical Foundation

In this section, theoretical outlines of dynamics and vibration theory, numerical methods, finite element techniques, Fourier analysis, random vibration theory, and signal analysis techniques used in this work are presented.

2.2.1 Dynamics/Vibration Theory

Vibrating systems can be classified as either discrete or continuous. Discrete systems possess a finite number of degrees of freedom, while continuous systems have an infinite number of degrees of freedom. The number of degrees of freedom which a system possesses is defined as the minimum number of independent coordinates required to completely describe its motion. For example, an independent particle in space has three degrees of freedom; a finite rigid body has six degrees of freedom (three position components and three angles specifying its orientation); and a continuous elastic body possesses an infinite number of degrees of freedom. There is a one-to-one relationship between the number of degrees of freedom of a system and the number of natural frequencies and mode shapes it possesses. Using lumped masses, complex continuous systems can be reduced to systems with a finite number of degrees of freedom. The analysis of a two-degree-of-freedom system is explained here; but the techniques used can be extended to include systems containing any number of degrees of freedom.

A driven, viscously damped, two degree-of-freedom-system, as shown in Figure 2-1, has the following equations of motion:

$$\boldsymbol{m}\ddot{\boldsymbol{x}}(t) + \boldsymbol{c}\dot{\boldsymbol{x}}(t) + \boldsymbol{k}\boldsymbol{x}(t) = \boldsymbol{F}(t), \tag{2.1}$$

where $\boldsymbol{m}$, $\boldsymbol{c}$, $\boldsymbol{k}$, $\boldsymbol{x}(t)$, and $\boldsymbol{F}(t)$ are the mass, damping, stiffness, displacement, and force matrices, respectively, and are given by

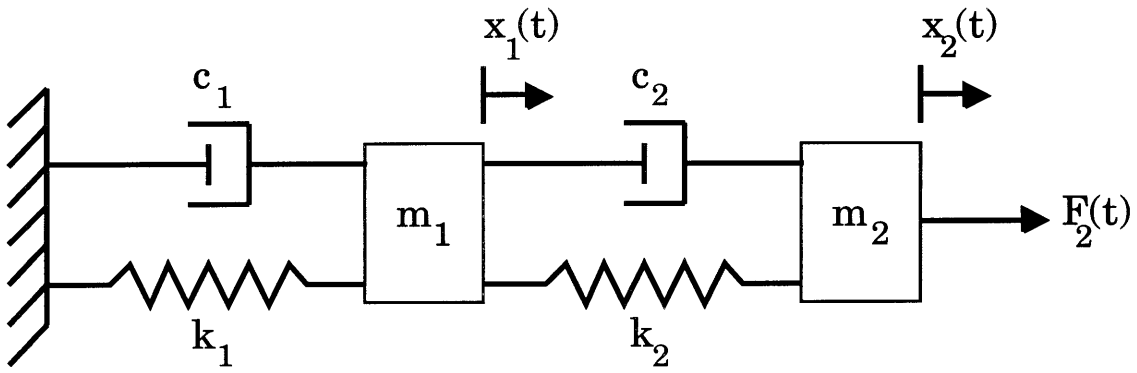

Figure 2-1: Driven Two-Degree-of-Freedom Oscillator

$$\boldsymbol{m} = \begin{bmatrix} m_1 & 0 \\ 0 & m_2 \end{bmatrix} \tag{2.2}$$

$$\boldsymbol{c} = \begin{bmatrix} c_1 + c_2 & -c_2 \\ -c_2 & c_2 \end{bmatrix} \tag{2.3}$$

$$\boldsymbol{k} = \begin{bmatrix} k_1 + k_2 & -k_2 \\ -k_2 & k_2 \end{bmatrix} \tag{2.4}$$

$$\boldsymbol{x}(t) = \begin{Bmatrix} x_1(t) \\ x_2(t) \end{Bmatrix} \tag{2.5}$$

$$\boldsymbol{F}(t) = \begin{Bmatrix} 0 \\ F_2(t) \end{Bmatrix}, \tag{2.6}$$

and $\ddot{\boldsymbol{x}} = d^2\boldsymbol{x}/dt^2$ and $\dot{\boldsymbol{x}} = d\boldsymbol{x}/dt$. If the excitation force is harmonic and of the form $F_2(t) = F_0 e^{i\omega t}$, where F_0 is an amplitude constant; the steady-state responses, $\boldsymbol{x}(t)$, can be assumed to be $x_1(t) = X_1 e^{i\omega t}$ and $x_2(t) = X_2 e^{i\omega t}$, where X_1 and X_2 are complex amplitude constants depending on the system parameters and the driving frequency, ω. Substituting these equations for the excitation force and the displacement into Equation 2.1 gives

$$-\omega^2 \boldsymbol{m}\boldsymbol{X} + i\omega \boldsymbol{c}\boldsymbol{X} + \boldsymbol{k}\boldsymbol{X} = \boldsymbol{F}, \tag{2.7}$$

where

$$\boldsymbol{X} = \left\{ \begin{array}{c} X_1(\omega) \\ X_2(\omega) \end{array} \right\} \tag{2.8}$$

and

$$\boldsymbol{F} = \left\{ \begin{array}{c} 0 \\ F_0 \end{array} \right\}. \tag{2.9}$$

Introducing the matrix of impedance functions, $\boldsymbol{Z}(\omega)$, which is defined as

$$\boldsymbol{Z}(\omega) = -\omega^2 \boldsymbol{m} + i\omega \boldsymbol{c} + \boldsymbol{k}, \tag{2.10}$$

Equation 2.7 can also be written as

$$\boldsymbol{Z}(\omega)\boldsymbol{X}(\omega) = \boldsymbol{F}. \tag{2.11}$$

Thus, the response magnitude, $\boldsymbol{X}(\omega)$, for any excitation frequency ω can be determined by multiplying both sides of the equation by the inverse of the impedance matrix

$$\boldsymbol{X}(\omega) = \boldsymbol{Z}^{-1}(\omega)\boldsymbol{F}, \tag{2.12}$$

to give

$$X_1(\omega) = \frac{Z_{22}(\omega)F_1 - Z_{12}(\omega)F_2}{Z_{11}(\omega)Z_{22}(\omega) - (Z_{12})^2(\omega)} \tag{2.13}$$

$$X_2(\omega) = \frac{-Z_{12}(\omega)F_1 + Z_{11}(\omega)F_2}{Z_{11}(\omega)Z_{22}(\omega) - (Z_{12})^2(\omega)}. \tag{2.14}$$

Note that in this case, $F_1 = 0$ and $F_2 = F_0$. Confining these equations to an undamped case ($\boldsymbol{c} = 0$) and allowing $m_1 = m_2 = m$ and $k_1 = k_2 = k$, for simplification purposes, gives

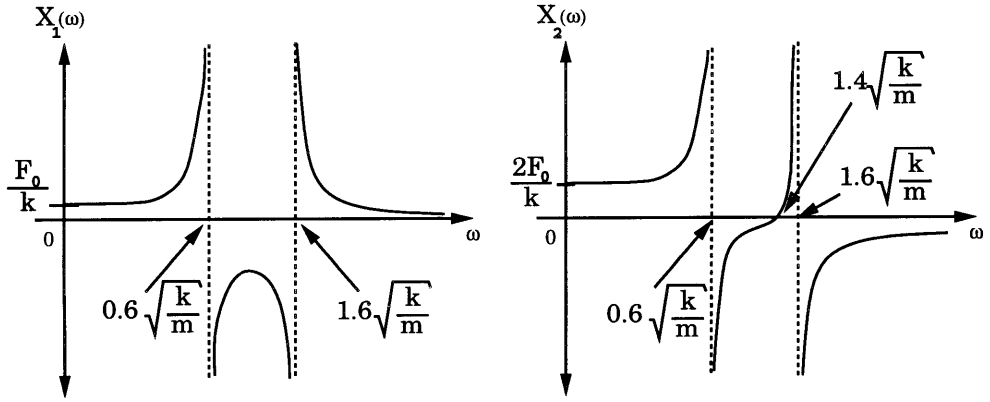

Figure 2-2: Undamped Motion of a Two-Degree-of-Freedom System

$$X_1(\omega) = \frac{kF_0}{(2k-\omega^2 m)(k-\omega^2 m)-k^2} \tag{2.15}$$

$$X_2(\omega) = \frac{(2k-\omega^2 m)F_0}{(2k-\omega^2 m)(k-\omega^2 m)-k^2}, \tag{2.16}$$

which are sketched in Figure 2-2. The points where the denominator in Equations 2.15 and 2.16 is equal to zero ($\omega_1 = 0.6\sqrt{k/m}$ and $\omega_2 = 1.6\sqrt{k/m}$) are commonly referred to as poles, resonances, or system natural frequencies; and the points where the numerators are equal to zero are called nodes, zeros, or anti-resonances. Figure 2-3 shows what these equations might look like with nominal damping, with the peaks no longer going to infinity. Increased damping results in decreased peak height.

Eigenvalues and Eigenvectors

Eigenvalues and eigenvectors provide another means for solving a system's equations of motion. The number λ is called an eigenvalue of an $n \times n$ matrix $\boldsymbol{A}$ if

$$|\boldsymbol{A} - \lambda \boldsymbol{I}| = 0, \tag{2.17}$$

where $\boldsymbol{I}$ is the identity matrix. The eigenvector associated with the eigenvalue λ is a nonzero vector, $\boldsymbol{v}$, such that $(\boldsymbol{A} - \lambda \boldsymbol{I})\,\boldsymbol{v} = 0$.

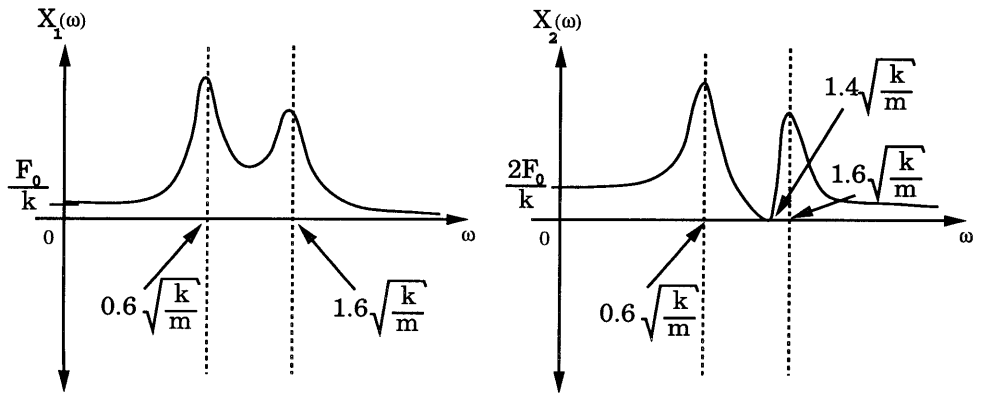

Figure 2-3: Damped Motion of a Two-Degree-of-Freedom System

Equation 2.17 corresponds to Equation 2.11 with $\boldsymbol{c}$ and $\boldsymbol{F} = 0$. Solving it is the same as setting the determinant of the impedance matrix equal to zero. Hence, the eigenvalues correspond to the resonant frequencies of the system ($\lambda = \omega^2$), and there are as many eigenvalues as there are degrees of freedom in the system. The eigenvectors corresponding to the eigenvalues are the modes shapes of oscillation of the system (i.e. the ratios of the complex amplitude constants, $\boldsymbol{X}(\boldsymbol{\omega})$, at each natural frequency).

A more in-depth explanation of dynamics and vibrations can be found in [8], [9], [10], [11], [12], and [13].

2.2.2 Runge-Kutta Method

Introduction

Many numerical techniques are available for solving ordinary differential equations which are too complex to solve exactly. Approximate solutions are based on power-series expansions, where the infinitesimal steps (dy's and dx's) of the ordinary differential equations are replaced by finite steps (Δy's and Δx's). Of the numerical methods used to solve ordinary differential equations, the Runge-Kutta is perhaps the easiest to use and the most common.

Fourth-Order Runge-Kutta

The Runge-Kutta method is based on the idea of advancing a solution, y from y_n to y_{n+1} using an approximate formula which coincides with the Taylor's series expansion of y at y_{n+1}. The Taylor series expansion of $y(x)$ at $x+h$, where h is the step size, is given by

$$y(x+h) = y(x) + \frac{dy}{dx}(h) + \frac{d^2y}{dx^2}\left(\frac{h^2}{2!}\right) + \frac{d^3y}{dx^3}\left(\frac{h^3}{3!}\right) + \frac{d^4y}{dx^4}\left(\frac{h^4}{4!}\right) + \cdots \tag{2.18}$$

In contrast to this equation, which requires higher-order derivatives, Runge-Kutta methods do not require derivatives beyond the first. Runge-Kutta routines are based on the Euler Method which advances a solution, y_n, from x_n to $x_{n+1} \equiv x_n + h$ as follows:

$$y_{n+1} = y_n + hf'(x_n, y_n). \tag{2.19}$$

Because the Euler method only uses derivative information from the beginning of the interval, however, it is not very accurate or very stable when used alone. In fact, Taylor's formula ($y_{n+1} - y_n - hf(x_n, y_n) = O(h^2)$) shows that the step's error is only one power of h smaller than the correction term, $hf'(x_n, y_n)$.

An improvement on the Euler method involves taking two Euler-style steps and is called the second-order Runge-Kutta method. This method involves stepping first to the midpoint of the interval, using the initial slope, k_1; and then using the slope at the midpoint, k_2, to compute the step across the entire interval, h,

$$k_1 = f'(x_n, y_n) \tag{2.20}$$

$$k_2 = f'(x_n + \frac{1}{2}h, y_n + \frac{1}{2}hk_1) \tag{2.21}$$

$$y_{n+1} = y_n + hk_2. \tag{2.22}$$

This method is called second order because it cancels out the first-order error term of the Euler method using symmetrization. The error term, now, is $O(h^3)$.

The fourth-order Runge-Kutta method works in a manner similar to the second-order one, but betters the technique by evaluating the derivative four times: once at the initial point, once at each of two trial midpoints, and once at a trial end point. The derivatives, k_1, k_2, k_3, and k_4, respectively, are

$$k_1 = f'(x_n, y_n) \tag{2.23}$$

$$k_2 = f'(x_n + \frac{1}{2}h, y_n + \frac{1}{2}hk_1) \tag{2.24}$$

$$k_3 = f'(x_n + \frac{1}{2}h, y_n + \frac{1}{2}hk_2) \tag{2.25}$$

$$k_4 = f'(x_n + h, y_n + hk_3), \tag{2.26}$$

which gives a final function value of

$$y_{n+1} = y_n + h(\frac{k_1}{6} + \frac{k_2}{3} + \frac{k_3}{3} + \frac{k_4}{6}). \tag{2.27}$$

The fourth-order Runge-Kutta method reduces the error term to $O(h^5)$, thereby improving accuracy while maintaining relative simplicity. For more information on Runge-Kutta algorithms, see [14], [15] and [16].

2.2.3 Matrix Methods of Structural Analysis

Introduction

Matrix structural analysis is based on the idea of modeling a continuous structure as an assembly of smaller, discrete elements. The elastic and inertial properties of these discrete structural elements can be determined, using assumed displacement or stress distributions, and then combined, according to elasticity theory (such that the equilibrium of forces at the joints and the compatibility of displacements between the elements are satisfied), to yield the static and dynamic properties of the complete continuous system. If the solutions of the various elements are selected properly, they

can be made to converge to the exact solution of the total structure as the element size is reduced. This method is ideal for the analysis of complex structures, and is what has been used to determine most of the spring constants for the theoretical model of the shaker-slip table assembly. The methods outlined in this section are presented in more detail in Przemieniecki Chapters 2, 3, and 5 ([17]).

Equations of Elasticity

The deformation of an elastic structure subjected to a system of loads can be completely described by displacements in the x, y, and z directions: u_x, u_y, u_z. The corresponding strains are the partial derivatives of these displacements (since for small deformations, the strain-displacement relations are linear),

$$\begin{aligned} e_{xx} &= \tfrac{\partial u_x}{\partial x} \\ e_{yy} &= \tfrac{\partial u_y}{\partial y} \\ e_{zz} &= \tfrac{\partial u_z}{\partial z} \\ e_{xy} = e_{yx} &= \tfrac{\partial u_y}{\partial x} + \tfrac{\partial u_x}{\partial y} \\ e_{yz} = e_{zy} &= \tfrac{\partial u_z}{\partial y} + \tfrac{\partial u_y}{\partial z} \\ e_{zx} = e_{xz} &= \tfrac{\partial u_x}{\partial z} + \tfrac{\partial u_z}{\partial x}. \end{aligned} \tag{2.28}$$

Neglecting thermal effects, these elastic strains can be related to the corresponding stresses using Hooke's law for linear isothermal elasticity,

$$\boldsymbol{\sigma} = E\boldsymbol{e}. \tag{2.29}$$

This gives

$$\begin{aligned} \sigma_{xx} &= \tfrac{E}{(1+\nu)(1-2\nu)}[(1-\nu)e_{xx} + \nu(e_{yy} + e_{zz})] \\ \sigma_{yy} &= \tfrac{E}{(1+\nu)(1-2\nu)}[(1-\nu)e_{yy} + \nu(e_{zz} + e_{xx})] \\ \sigma_{zz} &= \tfrac{E}{(1+\nu)(1-2\nu)}[(1-\nu)e_{zz} + \nu(e_{xx} + e_{yy})] \\ \sigma_{xy} &= \tfrac{E}{2(1+\nu)}e_{xy} \\ \sigma_{yz} &= \tfrac{E}{2(1+\nu)}e_{yz} \\ \sigma_{zx} &= \tfrac{E}{2(1+\nu)}e_{zx}, \end{aligned} \tag{2.30}$$

where ν is Poisson's ratio and E is Young's modulus. Using a plane-stress assumption ($\sigma_{zz} = \sigma_{zx} = \sigma_{zy} = 0$), this system of equations can be reduced to describe a two-dimensional problem. Equations 2.30 becomes

$$\boldsymbol{\sigma} = \boldsymbol{x}\boldsymbol{e}. \tag{2.31}$$

where

$$\boldsymbol{\sigma} = \{\sigma_{xx}\ \sigma_{yy}\ \sigma_{xy}\}^T, \tag{2.32}$$

$$\boldsymbol{x} = \frac{E}{(1-\nu^2)} \begin{bmatrix} 1 & \nu & 0 \\ \nu & 1 & 0 \\ 0 & 0 & \frac{1-\nu}{2} \end{bmatrix}, \tag{2.33}$$

and

$$\boldsymbol{e} = \{e_{xx}\ e_{yy}\ e_{xy}\}^T. \tag{2.34}$$

Unit Displacement Theorem

The unit displacement theorem is used to find the vector of forces, $\boldsymbol{P}$, required to maintain equilibrium in a structure subjected to a known stress distribution, $\boldsymbol{\sigma}$. If virtual displacements (infinitesimal changes in $\boldsymbol{U}$), $\delta\boldsymbol{U}$, are applied to a structure in the same directions and at the same points as the forces, virtual strains, $\delta\boldsymbol{\epsilon}$, will result. The virtual work ($\delta\boldsymbol{W} = \boldsymbol{P}\delta\boldsymbol{U}$) can then be equated to the virtual strain energy in the structure ($\delta\boldsymbol{U}_i = \int_v \boldsymbol{\sigma}^T \delta\boldsymbol{\epsilon}\, dV$) to give

$$\boldsymbol{P}\delta\boldsymbol{U} = \int_v \boldsymbol{\sigma}^T \delta\boldsymbol{\epsilon}\, dV. \tag{2.35}$$

In a linear elastic structure, the virtual strains, $\delta\boldsymbol{\epsilon}$ are proportional to the virtual displacements, $\delta\boldsymbol{U}$:

$$\delta\epsilon = \underline{\epsilon}\delta\boldsymbol{U} \tag{2.36}$$

where $\underline{\epsilon}$ represents the matrix of compatible strains due to unit displacements applied at the same locations and in the same directions as the forces. Combining Equations 2.35 and 2.36 and rearranging gives the unit-displacement theorem,

$$\boldsymbol{P} = \int_v \underline{\epsilon}^T \boldsymbol{\sigma}\, dV. \tag{2.37}$$

Determination of Element Stiffness

For a linear system, the total strains, $\boldsymbol{e}$, are equal to the product of the matrix of exact strains, $\boldsymbol{b}$, due to unit displacements, and the vector of displacements, $\boldsymbol{u}$:

$$\boldsymbol{e} = \boldsymbol{b}\boldsymbol{u}. \tag{2.38}$$

Combining Equations 2.31, 2.37, and 2.38 gives

$$\boldsymbol{P} = \boldsymbol{k}\boldsymbol{u} \tag{2.39}$$

where the element stiffness, $\boldsymbol{k}$, is

$$\boldsymbol{k} = \int_v \underline{\epsilon}^T \boldsymbol{x}\boldsymbol{b}\, dV. \tag{2.40}$$

The compatible strain distributions, $\underline{\epsilon}$, are determined quite easily; however, the exact strain distributions, $\boldsymbol{b}$, are usually much more difficult to find. One way of overcoming this problem is to approximate the matrix $\boldsymbol{b}$ by selecting it in such a way that it satisfies only the equations of compatibility. This approximate matrix, $\underline{\boldsymbol{b}}$, will then be equal to $\underline{\epsilon}$, and can be substituted into Equation 2.40 to give

$$\boldsymbol{k} \simeq \int_v \underline{\boldsymbol{b}}^T \boldsymbol{x}\underline{\boldsymbol{b}}\, dV. \tag{2.41}$$

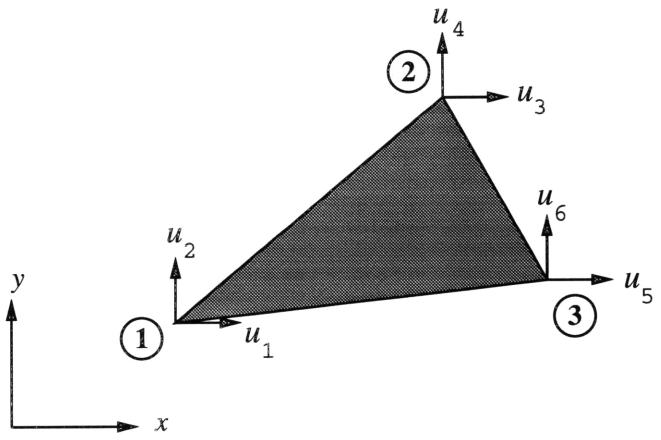

Figure 2-4: Triangular Plate Element [17]

Triangular Elements

The stiffness relationships for triangular plate elements are determined using assumed displacement variations. One such displacement variation is

$$u_x = c_1 x + c_2 y + c_3 \tag{2.42}$$

$$u_y = c_4 x + c_5 y + c_6. \tag{2.43}$$

The six arbitrary constants, $c_1, \ldots, c_6$, are determined using assumed displacements, in the x and y directions, at the three vertices of a triangle, as shown in Figure 2-4. Therefore, Equations 2.42 and 2.43 become

$$u_x = \frac{1}{2A_{123}} \left\{ \begin{array}{c} [y_{32}(x - x_2) - x_{32}(y - y_2)]u_1 + [-y_{31}(x - x_3) + x_{31}(y - y_3)]u_3 \\ +[y_{21}(x - x_1) - x_{21}(y - y_1)]u_5 \end{array} \right\} \tag{2.44}$$

and

$$u_y = \frac{1}{2A_{123}} \left\{ \begin{array}{c} [y_{32}(x - x_2) - x_{32}(y - y_2)]u_2 + [-y_{31}(x - x_3) + x_{31}(y - y_3)]u_4 \\ +[y_{21}(x - x_1) - x_{21}(y - y_1)]u_6 \end{array} \right\}, \tag{2.45}$$

where

$$A_{123} = \frac{1}{2}(x_{32}y_{21} - x_{21}y_{32}) = \text{Area of triangle 123} \tag{2.46}$$

and, using the notation of Przemieniecki [17],

$$x_{ij} = x_i - x_j \tag{2.47}$$

$$y_{ij} = y_i - y_j. \tag{2.48}$$

Differentiating Equations 2.44 and 2.45 gives the strains for the triangular element,

$$\boldsymbol{e} = \underline{\boldsymbol{b}}\boldsymbol{u}, \tag{2.49}$$

where

$$\boldsymbol{e} = \{e_{xx}\ e_{yy}\ e_{xy}\}^T \tag{2.50}$$

$$\underline{\boldsymbol{b}} = \frac{1}{2A_{123}} \begin{bmatrix} y_{32} & 0 & -y_{31} & 0 & y_{21} & 0 \\ 0 & -x_{32} & 0 & x_{31} & 0 & -x_{21} \\ -x_{32} & y_{32} & x_{31} & -y_{31} & -x_{21} & y_{21} \end{bmatrix} \tag{2.51}$$

$$\boldsymbol{u} = \{u_1\ u_2\ u_3\ u_4\ u_5\ u_6\}^T. \tag{2.52}$$

The stiffness matrix, $\boldsymbol{k}$, is found using Equations 2.33, 2.41 and 2.51. For convenience of presentation, $\boldsymbol{k}$ is written as the sum of the stiffnesses due to normal stresses, $\boldsymbol{k}_n$, and the stiffnesses due to shear stresses, $\boldsymbol{k}_s$,

$$\boldsymbol{k} = \boldsymbol{k}_n + \boldsymbol{k}_s, \tag{2.53}$$

where

$$\boldsymbol{k}_n = \frac{Et}{4A_{123}(1-\nu^2)} \times$$

$$\begin{bmatrix} y_{32}^2 & -\nu y_{32}x_{32} & -y_{32}y_{31} & \nu y_{32}x_{31} & y_{32}y_{21} & -\nu y_{32}x_{21} \\ -\nu y_{32}x_{32} & x_{32}^2 & \nu x_{32}y_{31} & -x_{32}x_{31} & -\nu x_{32}y_{21} & x_{32}x_{21} \\ -y_{32}y_{31} & \nu x_{32}y_{31} & y_{31}^2 & -\nu y_{31}x_{31} & -y_{31}y_{21} & \nu y_{31}x_{21} \\ \nu y_{32}x_{31} & -x_{32}x_{31} & -\nu y_{31}x_{31} & x_{31}^2 & \nu x_{31}y_{21} & -x_{31}x_{21} \\ y_{32}y_{21} & -\nu x_{32}y_{21} & -y_{31}y_{21} & \nu x_{31}y_{21} & y_{21}^2 & -\nu y_{21}x_{21} \\ -\nu y_{32}x_{21} & x_{32}x_{21} & \nu y_{31}x_{21} & -x_{31}x_{21} & -\nu y_{21}x_{21} & x_{21}^2 \end{bmatrix} \tag{2.54}$$

and

$$\boldsymbol{k}_s = \frac{Et}{8A_{123}(1+\nu)} \times \begin{bmatrix} x_{32}^2 & -x_{32}y_{32} & -x_{32}x_{31} & x_{32}y_{31} & x_{32}x_{21} & -x_{32}y_{21} \\ -x_{32}y_{32} & y_{32}^2 & y_{32}x_{31} & -y_{32}y_{31} & -y_{32}x_{21} & y_{32}y_{21} \\ -x_{32}x_{31} & y_{32}x_{31} & x_{31}^2 & -x_{31}y_{31} & -x_{31}x_{21} & x_{31}y_{21} \\ x_{32}y_{31} & -y_{32}y_{31} & -x_{31}y_{31} & y_{31}^2 & y_{31}x_{21} & -y_{31}y_{21} \\ x_{32}x_{21} & -y_{32}x_{21} & -x_{31}x_{21} & y_{31}x_{21} & x_{21}^2 & -x_{21}y_{21} \\ -x_{32}y_{21} & y_{32}y_{21} & x_{31}y_{21} & -y_{31}y_{21} & -x_{21}y_{21} & y_{21}^2 \end{bmatrix}. \tag{2.55}$$

Rectangular Elements

As with the triangular plate elements, the stiffness relationships for rectangular plate elements are determined using assumed displacement variations. A non-dimensional coordinate system which simplifies subsequent analyses is defined. The origin of the local coordinate system is the lower left-hand corner of the rectangle, and the non-dimensional coordinates are

$$\xi = \frac{x}{a} \tag{2.56}$$

$$\eta = \frac{y}{b}, \tag{2.57}$$

where a and b are the dimensions of the rectangle (as shown in Figure 2-5). A possible

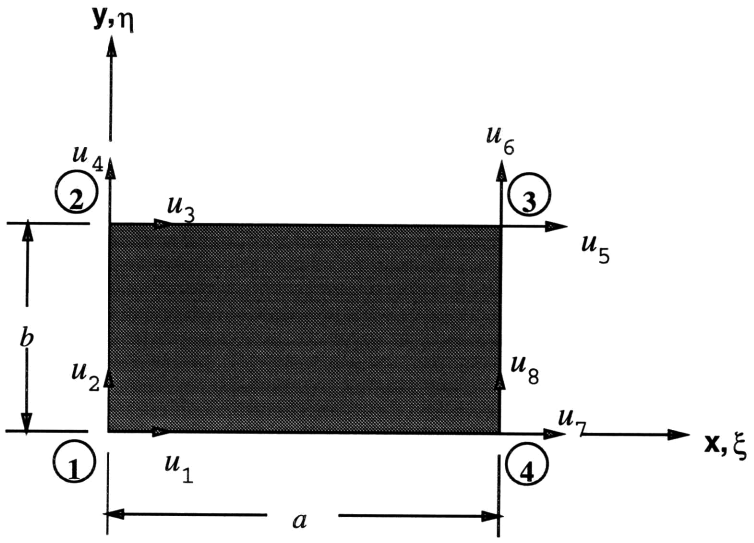

Figure 2-5: Rectangular Plate Element [17]

displacement variation for the rectangle is

$$u_x = c_1\xi + c_2\xi\eta + c_3\eta + c_4 \tag{2.58}$$

$$u_y = c_5\xi + c_6\xi\eta + c_7\eta + c_8. \tag{2.59}$$

The eight arbitrary coefficients, $c_1, \ldots, c_8$, are determined using the assumed displacements, in the x and y directions, at the four corners of the rectangle, as shown in Figure 2-5. With the arbitrary constants determined, Equations 2.58 and 2.59 are rewritten as

$$u_x = (1-\xi)(1-\eta)u_1 + (1-\xi)\eta u_3 + \xi\eta u_5 + \xi(1-\eta)u_7 \tag{2.60}$$

$$u_y = (1-\xi)(1-\eta)u_2 + (1-\xi)\eta u_4 + \xi\eta u_6 + \xi(1-\eta)u_8. \tag{2.61}$$

Differentiating Equations 2.60 and 2.61 gives the total strains for the rectangle

$$\boldsymbol{e} = \underline{\boldsymbol{b}}\boldsymbol{u}, \tag{2.62}$$

where

$$\boldsymbol{e} = \{e_{xx}\ e_{yy}\ e_{xy}\}^T \tag{2.63}$$

with

$$e_{xx} = \frac{\partial u_x}{\partial x} = \frac{1}{a}\frac{\partial u_x}{\partial \xi} \tag{2.64}$$

$$e_{yy} = \frac{\partial u_y}{\partial y} = \frac{1}{b}\frac{\partial u_y}{\partial \eta} \tag{2.65}$$

$$e_{xy} = \frac{\partial u_x}{\partial y} + \frac{\partial u_y}{\partial x} = \frac{1}{b}\frac{\partial u_x}{\partial \eta} + \frac{1}{a}\frac{\partial u_y}{\partial \xi}, \tag{2.66}$$

and

$$\underline{\boldsymbol{b}} = \begin{bmatrix} \frac{-(1-\eta)}{a} & 0 & \frac{-\eta}{a} & 0 & \frac{\eta}{a} & 0 & \frac{1-\eta}{a} & 0 \\ 0 & \frac{-(1-\xi)}{b} & 0 & \frac{1-\xi}{b} & 0 & \frac{\xi}{b} & 0 & \frac{-\xi}{b} \\ \frac{-(1-\xi)}{b} & \frac{-(1-\eta)}{a} & \frac{1-\xi}{b} & \frac{-\eta}{a} & \frac{\xi}{b} & \frac{\eta}{a} & \frac{-\xi}{b} & \frac{1-\eta}{a} \end{bmatrix} \tag{2.67}$$

$$\boldsymbol{u} = \{u_1\ u_2\ \cdots\ u_8\}^T. \tag{2.68}$$

The stiffness matrix, $\boldsymbol{k}$, is found using Equations 2.33, 2.41, and 2.67:

$$\boldsymbol{k} = \frac{Et}{12(1-\nu^2)} \times \begin{bmatrix} 4\beta+\frac{2\alpha}{\beta} & \frac{3}{2}\gamma & 2\beta-\frac{2\alpha}{\beta} & \frac{3}{2}\kappa & -2\beta-\frac{\alpha}{\beta} & -\frac{3}{2}\gamma & -4\beta+\frac{\alpha}{\beta} & -\frac{3}{2}\kappa \\ \frac{3}{2}\gamma & \frac{4}{\beta}+2\alpha\beta & -\frac{3}{2}\kappa & -\frac{4}{\beta}+\alpha\beta & -\frac{3}{2}\gamma & -\frac{2}{\beta}-\alpha\beta & \frac{3}{2}\kappa & \frac{2}{\beta}-2\alpha\beta \\ 2\beta-\frac{2\alpha}{\beta} & -\frac{3}{2}\kappa & 4\beta+\frac{2\alpha}{\beta} & -\frac{3}{2}\gamma & -4\beta+\frac{\alpha}{\beta} & \frac{3}{2}\kappa & -2\beta-\frac{\alpha}{\beta} & \frac{3}{2}\gamma \\ \frac{3}{2}\kappa & -\frac{4}{\beta}+\alpha\beta & -\frac{3}{2}\gamma & \frac{4}{\beta}+2\alpha\beta & -\frac{3}{2}\kappa & \frac{2}{\beta}-2\alpha\beta & \frac{3}{2}\gamma & -\frac{2}{\beta}-\alpha\beta \\ -2\beta-\frac{\alpha}{\beta} & -\frac{3}{2}\gamma & -4\beta+\frac{\alpha}{\beta} & -\frac{3}{2}\kappa & 4\beta+\frac{2\alpha}{\beta} & \frac{3}{2}\gamma & 2\beta-\frac{2\alpha}{\beta} & \frac{3}{2}\kappa \\ -\frac{3}{2}\gamma & -\frac{2}{\beta}-\alpha\beta & \frac{3}{2}\kappa & \frac{2}{\beta}-2\alpha\beta & \frac{3}{2}\gamma & \frac{4}{\beta}+2\alpha\beta & -\frac{3}{2}\kappa & -\frac{4}{\beta}+\alpha\beta \\ -4\beta+\frac{\alpha}{\beta} & \frac{3}{2}\kappa & -2\beta-\frac{\alpha}{\beta} & \frac{3}{2}\gamma & 2\beta-\frac{2\alpha}{\beta} & -\frac{3}{2}\kappa & 4\beta+\frac{2\alpha}{\beta} & -\frac{3}{2}\gamma \\ -\frac{3}{2}\kappa & \frac{2}{\beta}-2\alpha\beta & \frac{3}{2}\gamma & -\frac{2}{\beta}-\alpha\beta & \frac{3}{2}\kappa & -\frac{4}{\beta}+\alpha\beta & -\frac{3}{2}\gamma & \frac{4}{\beta}+2\alpha\beta \end{bmatrix} \tag{2.69}$$

where

$$\alpha = 1 - \nu \tag{2.70}$$

$$\gamma = 1 + \nu \tag{2.71}$$

$$\kappa = 1 - 3\nu, \tag{2.72}$$

and

$$\beta = \frac{b}{a}. \tag{2.73}$$

Assembling Elements

The method of matrix structural analysis is based on the idea of regarding a continuous structure as an assemblage of finite elements. For this assemblage of elements to accurately represent the structure, the boundary displacements of the discrete elements must match. Equations 2.44 and 2.45, for the triangular plate element, and Equations 2.60 and 2.61, for the rectangular plate element, show that along any edge, the assumed displacements vary linearly and depend only on the displacements of the two vertices which define that particular edge. Therefore, the compatibility of displacements along shared element boundaries is satisfied, and the properties of two elements can be combined using the principle of linear superposition, as illustrated in Figure 2-6. Figure 2-6 only illustrates the combination of mass properties; stiffness and damping properties are assembled in the same manner.

Notation is key in avoiding confusion when assembling elements. For this thesis, an underlined property (mass, stiffness, or damping) indicates a property of the actual shaker-slip table assembly. An underlined property combined with a superscript indicates a property of one component of the shaker-slip table assembly (i.e. $\underline{k}_{HG}^{fx}$ = stiffness of HG connection for the fixture (fx) alone–not attached to the shaker or the driver bar). A non-underlined property indicates a property of an arbitrary discrete element, used only for computational purposes. If there is a superscript, it designates which specific element the property is for (i.e. k_{42}^{A} = stiffness between 4

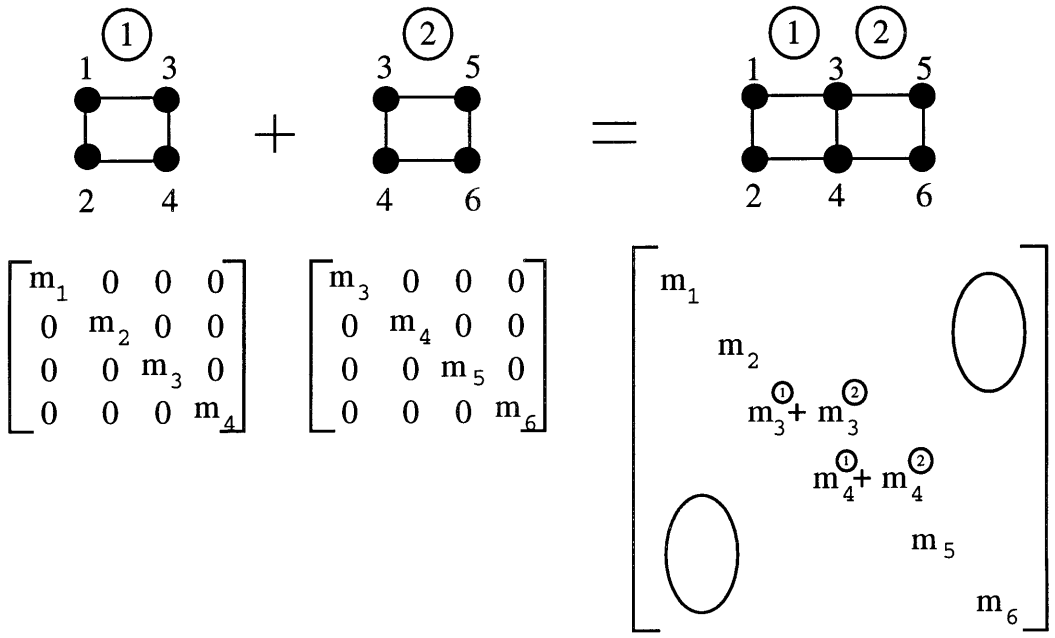

Figure 2-6: Assembly of Two Elements

and 2 for discrete element A).

2.2.4 Fourier Analysis

Fourier Series

Any periodic function can be represented as a sum of harmonic functions. If $x(t)$ is a periodic function of time, with period T, then $x(t)$ can be expressed as an infinite trigonometric series of the form

$$x(t) = a_0 + \sum_{k=1}^{\infty}(a_k \cos\frac{2\pi kt}{T} + b_k \sin\frac{2\pi kt}{T}), \tag{2.74}$$

where a_0, a_k, and b_k are constant Fourier coefficients given by

$$a_0 = \frac{1}{T}\int_{-T/2}^{T/2} x(t)\,dt \tag{2.75}$$

$$\underset{k\geq 1}{a_k} = \frac{2}{T}\int_{-T/2}^{T/2} x(t)\cos\frac{2\pi kt}{T}\,dt \tag{2.76}$$

$$\underset{k\geq 1}{b_k} = \frac{2}{T}\int_{-T/2}^{T/2} x(t)\sin\frac{2\pi kt}{T}\,dt. \tag{2.77}$$

Any periodic function, $x(t)$, with period T, can also be expressed in the form of a complex Fourier series (since $e^{i\theta} = \cos\theta + i\sin\theta$) as

$$x(t) = \sum_{k=-\infty}^{\infty} c_k e^{i(\frac{2\pi k}{T})t}, \tag{2.78}$$

where the complex Fourier coefficients, c_k, are given by

$$c_k = \frac{1}{T}\int_{-T/2}^{T/2} x(t)e^{-i(\frac{2\pi k}{T})t}\,dt. \tag{2.79}$$

When the period T becomes large, the frequency spacing between adjacent harmonics, $\Delta\omega$ ($\Delta\omega = 2\pi/T$), becomes small, and the Fourier coefficients become more tightly packed. In the limit when $T \to \infty$, $x(t)$ no longer represents a periodic phenomenon (i.e. the periodic function now has an infinite period and is therefore non-periodic) and can therefore no longer be broken down into its discrete frequency components. In this case, the Fourier series in Equations 2.74 and 2.78 become Fourier integrals and

the Fourier coefficients in Equations 2.75-2.77 and 2.79 become continuous functions of frequency called Fourier transforms.

The Fourier Integral

When the period, T, goes to infinity, the frequency spectrum becomes continuous and the frequency spacing becomes infinitesimal. Hence, Equation 2.79 can be rewritten as

$$\lim_{T\to\infty} Tc_k = \lim_{T\to\infty} \int_{-T/2}^{T/2} x(t)e^{-i\omega t}\,dt = \int_{-\infty}^{\infty} x(t)e^{-i\omega t}\,dt. \tag{2.80}$$

Defining $X(\omega)$ as

$$X(\omega) = \lim_{T\to\infty} Tc_k = \int_{-\infty}^{\infty} x(t)e^{-i\omega t}\,dt, \tag{2.81}$$

Equation 2.78 becomes

$$\begin{aligned} x(t) &= \lim_{T\to\infty} \sum_{k=-\infty}^{k=\infty} c_k e^{i\omega t} \frac{2\pi T}{2\pi T} \\ &= \sum_{k=-\infty}^{k=\infty} \lim_{T\to\infty} c_k T e^{i\omega t} \left(\frac{2\pi}{T}\right) \frac{1}{2\pi} \\ &= \frac{1}{2\pi} \int_{-\infty}^{\infty} X(\omega) e^{i\omega t}\,d\omega. \end{aligned} \tag{2.82}$$

$X(\omega)$ is a complex quantity known as the Fourier transform of $x(t)$. Equation 2.82 gives the frequency decomposition of the non-periodic function $x(t)$ in a continuous frequency domain, just as Equations 2.74 and 2.78 did for a periodic function in a discrete frequency domain. Equations 2.81 and 2.82 are known as the Fourier transform pair for a non-periodic function.

Discrete Fourier Transforms

Experimental measurements of processes are usually done digitally. A segment of data, $x(t)$, from a process being measured is sent to an analog-to-digital converter,

which samples it at a series of N equally spaced times (x_r for $r = 0, \ldots, (N-1)$). The integrals in the Fourier transform equations are thus approximated with summations.

Rewriting Equation 2.79 gives

$$X_{k_{k\geq 0}} = \frac{1}{T}\int_0^T x(t)e^{-i(\frac{2\pi k}{T})t}\,dt, \tag{2.83}$$

where the range of the integral has been changed (which makes no difference since $x(t)$ has period T) and the variable c_k has been denoted by X_k to be consistent with the Fourier transform definition. For a set of discrete values, the integral in Equation 2.83 is approximately replaced by the summation

$$X_k = \frac{1}{T}\sum_{r=0}^{N-1} x_r e^{-i(\frac{2\pi k}{T})(r\Delta)}\Delta. \tag{2.84}$$

Substituting $T = N\Delta$, where Δ is the time spacing between samples, into Equation 2.84 gives

$$X_k = \frac{1}{N}\sum_{r=0}^{N-1} x_r e^{-i(\frac{2\pi kr}{N})} \quad \text{for } k = 0, 1, 2, \ldots, (N-1). \tag{2.85}$$

Equation 2.85 does not provide enough information to allow the continuous time series $x(t)$ to be obtained, but it does allow all of the discrete values of the time series x_r to be regained exactly. Any typical value, x_r, of the series is given by the inverse formula

$$x_r = \sum_{k=0}^{N-1} X_k e^{i(\frac{2\pi kr}{N})} \quad \text{for } r = 0, 1, 2, \ldots, (N-1). \tag{2.86}$$

The discrete Fourier transform (or DFT for short) of the series x_r, $r = 0, 1, 2, \ldots, (N-1)$, then, is given by Equation 2.85, and the inverse discrete Fourier transform by Equation 2.86.

The Fast Fourier Transform

The fast Fourier transform (or FFT) is an algorithm for calculating discrete Fourier transforms (DFT's). Directly calculating the DFT, X_k, of N numbers, requires N^2

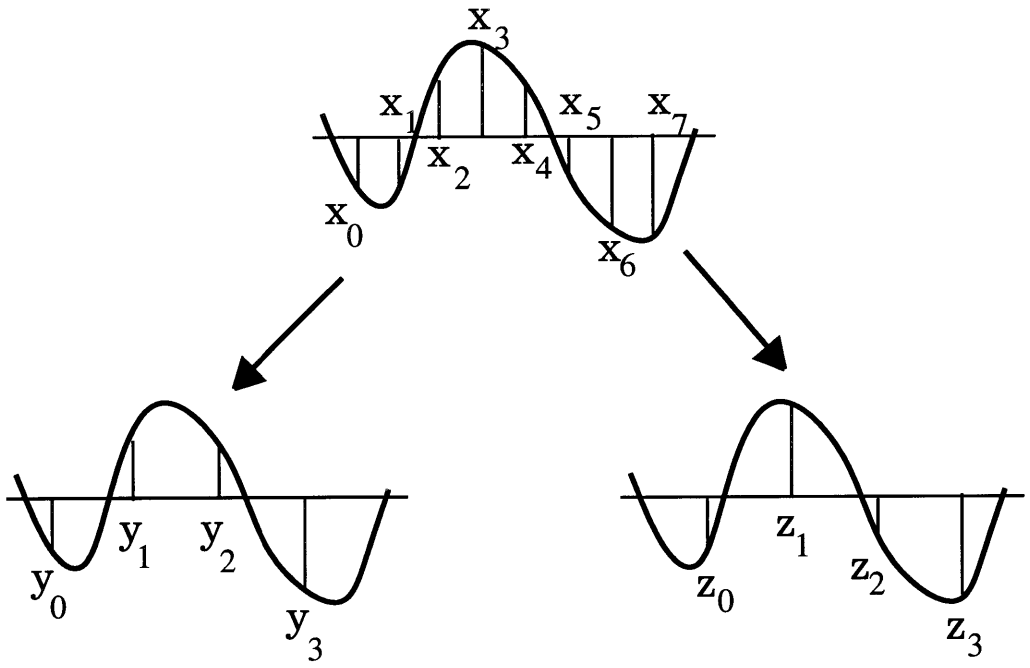

Figure 2-7: Partitioning a Sequence into Two Shorter Sequences

multiplications of the form $x_r e^{-i(\frac{2\pi kr}{N})}$. Using the FFT, however, reduces the required number of operations to $N \log_2 N$; thereby offering an enormous reduction in processing time. In addition, since fewer operations are required, round-off errors are reduced, and accuracy is accordingly increased.

The FFT algorithm works by partitioning a full sequence of numbers, x_r, into a number of shorter sequences. Instead of calculating the DFT of the original sequence, only the DFT's of the shorter sequences are determined. These individual DFTs are then combined to yield the full DFT of x_r.

A sequence, x_r, $r = 0, 1, 2, \ldots, (N-1)$, where N is an even number, can be partitioned into two shorter sequences y_r and z_r, one containing the even-numbered points from the original sequence, x_r, and one containing the odd-numbered points (as shown in Figure 2-7). y_r and z_r are given by

$$y_r = x_{2r} \quad r = 0, 1, 2, \ldots, (N/2-1) \tag{2.87}$$

$$z_r = x_{2r+1} \quad r = 0, 1, 2, \ldots, (N/2-1) \tag{2.88}$$

The DFT's of these two shorter sequences are Y_k and Z_k where,

$$Y_k = \frac{1}{N/2} \sum_{r=0}^{N/2-1} y_r e^{-i\frac{2\pi kr}{N/2}} \quad k = 0, 1, 2, \ldots, (N/2 - 1) \tag{2.89}$$

and

$$Z_k = \frac{1}{N/2} \sum_{r=0}^{N/2-1} z_r e^{-i\frac{2\pi kr}{N/2}} \quad k = 0, 1, 2, \ldots, (N/2 - 1). \tag{2.90}$$

The DFT of the original sequence, X_k (Equation 2.85), can be rearranged into two separate sums resembling those in Equations 2.89 and 2.90

$$X_k = \frac{1}{N} \left(\sum_{r=0}^{N/2-1} x_{2r} e^{-i\frac{2\pi(2r)k}{N}} + \sum_{r=0}^{N/2-1} x_{2r+1} e^{-i\frac{2\pi(2r+1)k}{N}} \right), \tag{2.91}$$

which can be combined with Equations 2.87-2.90 to give

$$X_k = \frac{1}{2}(Y_k + e^{-i(\frac{2\pi k}{N})} Z_k) \tag{2.92}$$

for $k = 0, 1, 2, \ldots, (N/2 - 1)$.

This equation is the key to the fast Fourier transform because it shows that the DFT of the original sequence can be obtained directly from the DFT's of the two half-sequences Y_k and Z_k. Plus, if the original number of samples, N, in the sequence x_r is a power of 2, then the half-sequences y_r and z_r may themselves be partitioned into half-sequences, and so on, until all that remains are individual terms.

Equation 2.92 only applies to X_k for $0 \leq k \leq N/2 - 1$, however, and X_k for k running the whole way from 0 to $(N - 1)$ are necessary. The second half of values can be found using the fact that Y_k and Z_k are periodic in k and repeat themselves with period N/2 such that

$$Y_{k-N/2} = Y_k \tag{2.93}$$

$$Z_{k-N/2} = Z_k. \tag{2.94}$$

This allows the complete DFT to be calculated as

$$X_k = \frac{1}{2}(Y_k + e^{-i(\frac{2\pi k}{N})}Z_k) \quad \text{for} \quad k = 0, 1, 2, \ldots, (N/2 - 1) \tag{2.95}$$

$$X_k = \frac{1}{2}(Y_{k-N/2} + e^{-i(\frac{2\pi k}{N})}Z_{k-N/2}) \quad \text{for} \quad k = N/2, (N/2 + 1), \ldots, (N - 1). \tag{2.96}$$

Permitting k to run only from 0 to $N/2$ and defining a new variable W as $W = e^{-i(\frac{2\pi}{N})}$ allows Equations 2.95 and 2.96 to be written in more conventional notation as

$$X_k = \frac{1}{2}(Y_k + W^k Z_k) \quad k = 0, 1, 2, \ldots, (N/2 - 1) \tag{2.97}$$

$$X_{k+N/2} = \frac{1}{2}(Y_k - W^k Z_k) \quad k = 0, 1, 2, \ldots, (N/2 - 1). \tag{2.98}$$

This is the traditional computational "butterfly" which occurs in most FFT computer programs. For additional information on Fourier series, Fourier transforms, DFTs, and FFTs, see [13], [15], [16], and [18].

2.2.5 Random Vibrations

Phenomena whose outcome at a future instant of time cannot be predicted are classified as nondeterministic and referred to as random. Random signals cannot be described by explicit mathematical relationships; instead, they must be described in terms of probability statements and statistical averages. The three most important statistics to understand here are probability functions, correlation functions, and spectral density functions.

Random processes are considered to be ergodic, or stationary, if all of the probability distributions associated with them are time-invariant. In other words, all the probability distributions taken along any single sample record are the same as along any other single sample record taken from the same random process. If all of the probability distributions are not invariant with time, a process is either weakly stationary or non-stationary, depending on the extent of the variance. The random phenomena

involved in this study, as well as most random physical phenomena which are of interest to engineers in general, are assumed to be stationary. This is because signals which are very long compared with the period of the lowest frequency component of interest, are considered to be approximately stationary. Therefore, only the random vibration theory necessary to describe stationary processes is presented.

Probability Functions

The expected or mean value of a function $x(t)$ is given by

$$E[x(t)] = \frac{1}{T}\int_0^T x(t)\,dt = \int_{-\infty}^{\infty} xp(x)\,dx, \tag{2.99}$$

where $p(x)$ is the probability density function associated with $x(t)$. The probability density function describes the probability, $p(x)\,dx$, that a random variable lies in the range x to $x + dx$. For a stationary random process, $E[x(t)] = E[x]$, since stationary processes are time-invariant. The mean-square value of $x(t)$, $E[x^2]$, is the average value of x^2 and is given by

$$E[x^2] = \frac{1}{T}\int_0^T x^2\,dt = \int_{-\infty}^{\infty} x^2 p(x)\,dx. \tag{2.100}$$

The time integrals in the above two equations are approximations based on the assumption that, for a sufficiently large time interval, T, all values within the range 0 to T are equally probable. Hence, $dt/T \sim p(x)\,dx$.

The root-mean-square value of the signal is the positive square root of $E[x^2]$. The standard deviation of $x(t)$, denoted by σ, and the variance, σ^2, are defined by

$$\sigma^2 = E[x^2] - (E[x])^2. \tag{2.101}$$

Correlation Functions

The auto-correlation function for a random signal, $x(t)$, is defined as the average value of the product $x(t)x(t+\tau)$. It describes the degree of dependence of the value of x at some time, t, on its value at some other time, $t + \tau$. For a stationary random

signal, the auto-correlation is independent of absolute time, and depends only on the time separation, τ. It is defined as

$$R_{xx}(\tau) = E[x(t)x(t+\tau)] = \frac{1}{T}\int_0^T x(t)x(t+\tau)\,dt. \tag{2.102}$$

The auto-correlation is an even function ($R_{xx}(\tau) = R_{xx}(-\tau)$) which does not contain any phase information, and whose maximum value is at $\tau = 0$ (when $\tau = 0$, $R_{xx} = E[x^2]$). The cross-correlation function between two different stationary random signals (e.g. the input, $x(t)$, and the output, $y(t)$) is defined as

$$R_{xy}(\tau) = E[x(t)y(t+\tau)] = \frac{1}{T}\int_0^T x(t)y(t+\tau)\,dt. \tag{2.103}$$

Unlike the auto-correlation function, it is not an even function, $R_{xy}(\tau) \neq R_{xy}(-\tau)$, rather $R_{xy}(\tau) = R_{yx}(-\tau)$.

Spectral Density Functions

The auto-correlation function provides information concerning the properties of a random variable in the time domain. The auto-spectral density function provides similar information in the frequency domain and is defined as the Fourier transform of the correlation function

$$S_{xx}(\omega) = \frac{1}{2\pi}\int_{-\infty}^{\infty} R_{xx}(\tau)e^{-i\omega\tau}\,d\tau. \tag{2.104}$$

$S_{xx}(\omega)$ is a real, even function of frequency and is known as the auto-spectral density of the random signal, $x(t)$. The cross-spectral density, $S_{xy}(\omega)$, is the Fourier transform of the cross-correlation function, and it is the complex quantity given by

$$S_{xy}(\omega) = \frac{1}{2\pi}\int_{-\infty}^{\infty} R_{xy}(\tau)e^{-i\omega\tau}\,d\tau. \tag{2.105}$$

The cross-spectral density provides a measure of the mutual power between two signals.

Digital Spectral Analysis

The experimental estimation of spectra from measured data does not follow the above mentioned formal mathematical route, however. With the development of the FFT in the late 1960's, spectra no longer had to be calculated from correlation functions but could be found directly from the time histories of the sampled data. It became quicker and more accurate to calculate spectral estimates directly from the original time series using the method described below.

The equation of motion for a driven, damped single-degree-of-freedom system is given by

$$m\ddot{x} + c\dot{x} + kx = f(t). \tag{2.106}$$

where $f(t)$ is a random excitation input. The solution to Equation 2.106 can be obtained using a frequency response approach. The complex frequency response, or transfer function, of a system is denoted by $H(\omega)$ and is defined as the ratio of a system's output to its input, and can be written as

$$x(t) = H(\omega)f(t). \tag{2.107}$$

Multiplying both sides of Equation 2.107 by $e^{-i\omega t}/(2\pi)$ and taking the integral with respect to time gives

$$\frac{1}{2\pi}\int_{-\infty}^{\infty} x(t)e^{-i\omega t}\,dt = H(\omega)\frac{1}{2\pi}\int_{-\infty}^{\infty} f(t)e^{-i\omega t}\,dt, \tag{2.108}$$

which can be rewritten using the definition of a Fourier transform as

$$X(\omega) = H(\omega)F(\omega), \tag{2.109}$$

or

$$H(\omega) = \frac{X(\omega)}{F(\omega)}. \tag{2.110}$$

The magnitude of $H(\omega)$, then, is

$$|H(\omega)|^2 = \frac{X^*(\omega)X(\omega)}{F^*(\omega)F(\omega)}. \tag{2.111}$$

where $*$ is used to indicate a complex conjugate.

It can be shown that ([18])

$$S_{xx}(\omega) = X^*(\omega)X(\omega) \tag{2.112}$$

$$S_{xy}(\omega) = X^*(\omega)Y(\omega) \tag{2.113}$$

are the equivalents of Equations 2.104 and 2.105. Hence, for the single-degree-of-freedom example,

$$|H(\omega)|^2 = \frac{S_{xx}(\omega)}{S_{ff}(\omega)}, \tag{2.114}$$

The transfer function between the input and the output is found by multiplying the numerator and the denominator of Equation 2.110 by $F^*(\omega)$

$$H(\omega) = \frac{F^*(\omega)X(\omega)}{F^*(\omega)F(\omega)} = \frac{S_{fx}(\omega)}{S_{ff}(\omega)}. \tag{2.115}$$

In this thesis, data is collected in the form of acceleration time histories, and closed-loop control is used to govern table behavior. Hence, all transfer functions relate the acceleration at a given shaker-table point, $\ddot{x}_p(t)$, to the input control acceleration, $\ddot{x}_c(t)$ (instead of to $f(t)$, as above):

$$\ddot{x}_p(t) = H^a(\omega)\ddot{x}_c(t), \tag{2.116}$$

where $H^a(\omega)$ is used to indicate that this is a transfer function relating two accelerations. By analogy to the case where $f(t)$ is the input, the Fourier transform of Equation 2.116 is

$$H^a(\omega) = \frac{\ddot{X}_p(\omega)}{\ddot{X}_c(\omega)}. \tag{2.117}$$

Multiplying the numerator and the denominator of Equation 2.117 by $\ddot{X}_c^*(\omega)$ gives

$$H^a(\omega) = \frac{\ddot{X}_c^*(\omega)\ddot{X}_p(\omega)}{\ddot{X}_c^*(\omega)\ddot{X}_c(\omega)}, \tag{2.118}$$

which, using Equations 2.112 and 2.113, can also be written as

$$H^a(\omega) = \frac{S_{\ddot{x}_c\ddot{x}_p}}{S_{\ddot{x}_c\ddot{x}_c}}. \tag{2.119}$$

This is the form of all transfer functions used in this thesis. To review, it is attained by taking the FFT of the input and output time signals, using Equations 2.112 and 2.113 to calculate the auto-spectral density of the output ($S_{\ddot{x}_c\ddot{x}_c}$) and the cross-spectral density between the input and the output ($S_{\ddot{x}_c\ddot{x}_p}$), then substituting the values into Equation 2.119 to calculate the transfer function, $H^a(\omega)$.

For more information on random vibration analysis, see [9], [12], and [13], and [18].

2.2.6 Signal Analysis Techniques

Because it is impossible to analyze an infinitely long data record, errors exist in signal analysis. These errors can be kept to a minimum, however, if care is taken in data acquisition and attention is paid to certain statistical sampling considerations.

Averaging

In signal anlaysis, there is a fundamental relationship between the frequency bandwidth and the analysis time:

$$BT \geq 1, \tag{2.120}$$

where B is the frequency resolution bandwidth and T is the duration of the measurement.

Averaging is often used to improve the quality of frequency response function

measurements. The averaging of several independent time records is critical when dealing with wideband random signals, because sufficient data must be obtained to ensure that statistical values are representative of an actual signal. If n time records of length T are sampled, the total duration of the signal to be analyzed is defined by $T_t = nT$. The resolution bandwidth is still determined by the individual record length, T:

$$B = \frac{1}{T}, \tag{2.121}$$

which can also be written as

$$B = \frac{1}{N\Delta}, \tag{2.122}$$

where N is the number of digitally sampled values for a record of length T, and Δ is the time between samples. However, the ratio of the standard deviation of a measurement, σ, to its mean value, m, is a function of the total amount of digitized data, T_t. This quantitiy, σ/m, is sometimes called the normalized random error, ε_r, and is given by

$$\varepsilon_r = \frac{\sigma}{m} \simeq \frac{1}{\sqrt{BT_t}} = \frac{1}{\sqrt{n}}\frac{1}{\sqrt{BT}}. \tag{2.123}$$

Random errors result because averaging operations involve a finite number of sample records. The normalized random error, ε_r, for a signal can always be made smaller by increasing the number of averages, n. Of course, there are diminishing returns, and after a certain point, increasing the number of averages has little effect on the quality of the data.

It is sometimes convenient to overlap data segments to allow additional averages. While this procedure does not reduce the random error, it does produce smoother spectra than would be obtained if each data sample were used only once.

Aliasing

Aliasing is a problem which can result from the discretization of a continuous time history. Problems arise if the sampling interval, Δ, is chosen incorrectly. Too small a sampling interval produces a large quantity of unnecessary data, while too large a sampling interval results in the distortion of spectral data.

If the sampling interval is too large (i.e. sampling rate is too slow), high frequency signals may be misinterpreted as low frequency signals. This concept is easily illustrated by considering a digitized sine wave. At least two samples per cycle are required to define the frequency of the sine wave. This implies that for a given sampling interval, Δ, the highest frequency which can be reliably defined is $1/(2\Delta)$. Higher frequency components will not be detected and will instead be confused with the lower frequency components. The higher frequency components will fold back onto the lower frequency components, appearing reflected or aliased.

Aliasing can be avoided by selecting a sampling interval, Δ, such that the signal is digitized at a rate which is at least twice the highest frequency present. Another way to avoid aliasing is to use a suitable low-pass filter to remove all frequency components higher than the sampling frequency ($1/(2\Delta)$) before beginning the analysis. This procedure of applying a low-pass filter prior to digitization is referred to as anti-aliasing; and the frequency $1/(2\Delta)$ Hz is called the Nyquist frequency. The Nyquist frequency is the maximum frequency that can be detected from data sampled at a time spacing of Δ (seconds).

Windowing

Time windowing is a technique that can be used to reduce noise and to filter data. Window functions are generally weighting functions which can be applied in either the time or frequency domains to force data equal to zero at the beginning and end of a record.

Windows are applied to functions using the principle of convolution. The weighted spectral density, $\tilde{S}_{xx}$, can be obtained from the true spectral density, S_{xx} as

$$\tilde{S}_{xx}(\omega) = \int_{-\infty}^{\infty} W(\Omega - \omega) S_{xx}(\Omega)\, d\Omega, \tag{2.124}$$

where $W(\Omega)$ is the spectral window, and it satisfies

$$\int_{-\infty}^{\infty} W(\Omega)\, d\Omega = 1. \tag{2.125}$$

In reality, all finite time records are windowed functions since their ends are truncated. However, when this truncation process is abrupt, problems result. The Fourier transform of a rectangular window is pictured in Figure 2-8. This spectral window has lobes to the side of its main peak, which are a major concern. Theses lobes can distort the spectrum of the signal which the window is applied to, and produce unwanted spectral components. This phenomenon is called leakage and is caused by the fact that the rectangular window function turns on and off so rapidly. The situation can be remedied by multiplying the input data by a window function that changes more gradually with respect to time. Triangular (tapered), exponential, Hanning (cosine tapering), and Hamming (modified Hanning) windows all satisfy this criterion of gradually decaying to zero and thus minimize leakage. Figure 2-8 shows some of these common filters and their frequency spectra. Of course, the ideal window would produce a rectangular spectral window, with a flat spectrum and no leakage, thus providing a true representation of all frequency components. However, since such a window is not available, the Hanning window is often used when processing continuous random vibration signals.

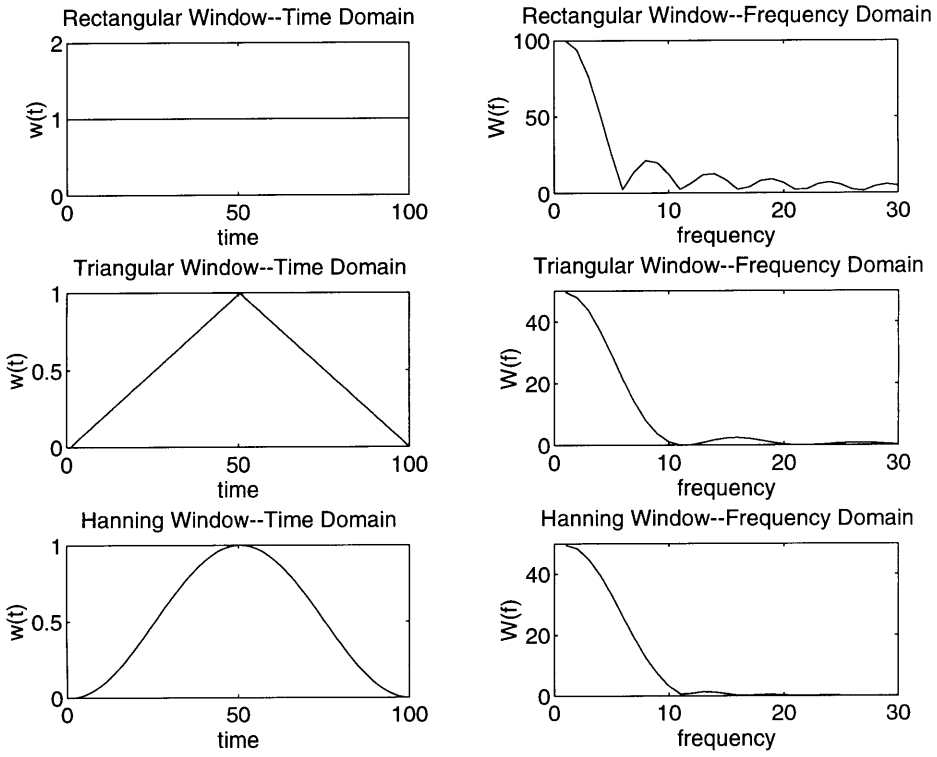

Figure 2-8: Some Typical Window Functions

Coherence

The coherence function, $\eta_{xy}^2(\omega)$, measures the degree of correlation between signals. It is defined as

$$\eta_{yx}^2(\omega) = \frac{S_{xy}(\omega)S_{yx}(\omega)}{S_{xx}(\omega)S_{yy}(\omega)}, \tag{2.126}$$

where x is the input and y is the output. The coherence function provides an estimate of the proportion of the output that is due to the input and is such that $0 \leq \eta_{xy}^2(\omega) \leq 1$. For an ideal single input, single output system, with no extraneous noise at the input or output stages, $\eta_{xy}^2(\omega) = 1$. Generally, though, $\eta_{xy}^2(\omega) < 1$. This can be due to non-linearities in the system relating $x(t)$ to $y(t)$, the presence of extraneous noise, or the fact that the output $y(t)$ is due to additional inputs besides $x(t)$. In each of these cases, the measured response cannot be completely attributed to the measured excitation, and a less-than-unity coherence results.

Low coherence can be an indicator of problems in the data acquisition setup. If coherence is low at modal peaks, leakage is probably affecting the measurements. Inadequate frequency resolution could also be a cause of low coherence at modes, with the analyzer frequency resolution not fine enough to adequately describe the rapidly changing functions encountered at resonance and anti-resonance. This problem of inadequate frequency resolution is called bias error. Low coherence at anti-resonances is generally acceptable, since there is no response to measure (thus a low signal to noise ratio). Low coherence often occurs at low frequencies, where there is difficulty in using a shaker to input power to a structure. Also, piezoelectric accelerometers tend to perform poorly at very low frequencies because their output is proportional to the shear rate in the crystals. Sometimes accelerometers with larger masses are required to provide better coherence at low frequencies.

For more information on signal analysis techniques, see [9], [12], and [13], and [18].

Chapter 3

Problem Statement

Resonant responses in the slip table can cause control problems resulting in the over or under-testing of attached test specimens. These problems (associated with table resonances and anti-resonances) must be overcome using existing hardware, by varying test object and control accelerometer placement. To select such placements correctly, an improved understanding of slip table dynamic behavior is required. In this work, such an understanding is gained by addressing two problems: experimental characteristics of an existing table, and the development of a numerical model of table behavior.

Experimental data characterizing the behavior of the shaker-slip table assembly is required. Dynamic response measurements are necessary at sufficient locations to completely characterize the behavior of the table and attached hardware. Of particular importance are responses in all axes over the full frequency range of interest as well as the effects of control accelerometer and test article placement.

An analytical model is necessary to determine the response of a specified shaker-slip table assembly, with and without test specimens attached. Given the geometry, material properties, control accelerometer and test mass placement, control algorithm, and reference control spectrum; the model must predict the overall system response, including its natural frequencies, mode shapes, and response spectra. The model will be implemented as a computer algorithm and its predictions correlated with the results of the experiments.

The verified computer algorithm will yield a basic understanding of the physics of the shaker-slip table assembly. In addition, the model will be used to understand the problems which result from system nonlinearities and to determine their effects on equipment performance. Finally, a basis for selecting control accelerometer and test object locations will be determined.

Chapter 4

Experimental Procedure

4.1 Overview

This chapter describes the acquisition of experimental data characterizing the behavior of the shaker-slip table assembly at Los Alamos National Laboratory. Included is a description of the equipment used, the test setups employed, and the procedure followed. The goal of these experiments was to acquire input and output time history data which could be used to gain an understanding of the physical behavior of the shaker-slip table system and to verify the accuracy of the theoretical models (Chapter 5) in predicting system behavior.

4.2 Equipment

Figure 4-1 shows the basic components of the vibration system used. The generator provides a user-specified signal which is amplified by a power amplifier and sent to the electrodynamic shaker. The shaker translates this electrical signal into mechanical motion and transmits that motion to the slip table. Motion of various points on the shaker and slip table are measured using accelerometers; and the accelerometer signals are passed through signal conditioning amplifiers and on to control and data acquisition signal analyzers. The data acquisition signal analyzer stores the data, and the control analyzer uses the control accelerometer signal to compute an updated

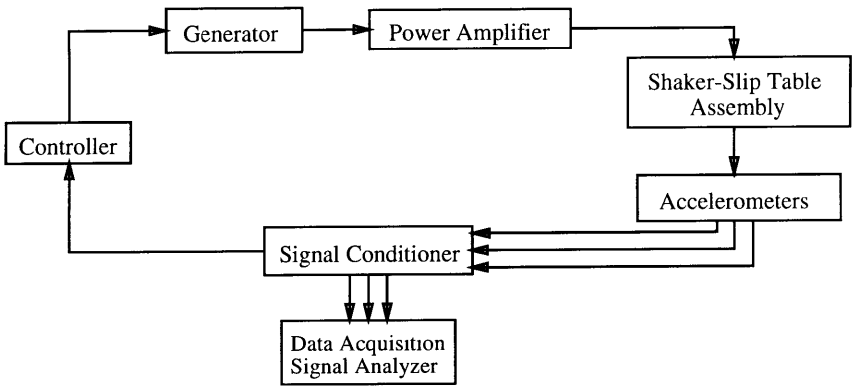

Figure 4-1: Basic Components of a Vibration Measurement System

drive signal to pass to the generator. Because the control accelerometer signal is used in modifying the drive signal, this process is called closed-loop. Vibration systems are also run open-loop; but closed-loop control is standard when operating the shaker-slip table assembly used here. Closed-loop control is used to protect equipment. With proper closed-loop control, a system should never reach mechanical failure levels, as it could in the open-loop case.

4.2.1 Shaker and Slip Table

The shaker used is an Unholtz-Dickie model T-1000. A schematic of this electrodynamic shaker is shown in Figure 4-2. The stationary coils of the electromagnet receive the time-varying input signal supplied by the generator and produce a time-varying magnetic field. A coil, attached to the moving portion of the shaker, is placed into this magnetic field. When current passes through this coil, a force is generated. This force is what drives the moving element of the shaker, and hence, the attached slip table.

To avoid shocks and other unintended loadings, the coil and the moving element of the shaker must have a linear motion. For this reason, they are suspended from a flexible support, as shown in Figure 4-2. This attachment to a flexible support causes the electrodynamic exciter to have two natural frequencies: one corresponding to the natural frequency of the flexible support (generally fairly low and heavily damped),

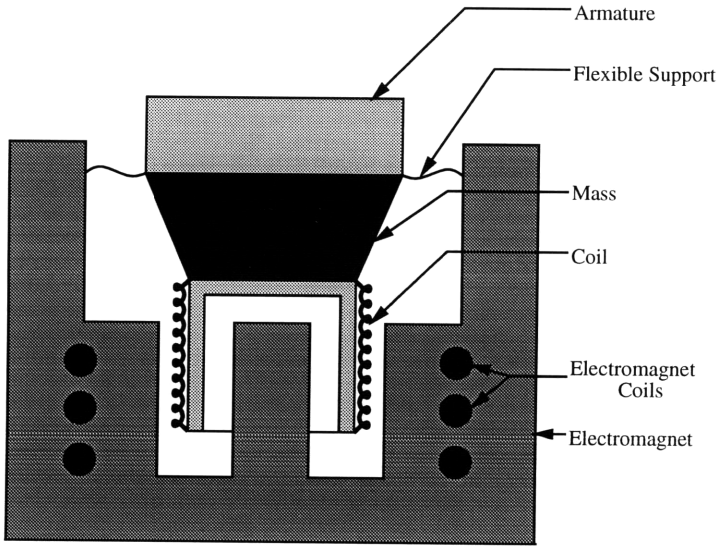

Figure 4-2: Schematic Diagram of Electrodynamic Shaker (not to scale)

and a second one corresponding to the natural frequency of the armature (generally rather high and less heavily damped). The operating range of the shaker falls between these two frequencies. The Unholtz-Dickie model T-1000 used here has the first mode at 300 Hz and the other at 2300 Hz. Since the mode at 300 Hz is heavily damped, it is of little concern. The mode at 2300 Hz, however, can cause control problems if excited.

The slip table, manufactured by Kimball Industries, consists of a concrete-filled reaction mass base supported by an air isolation system, along with the slip plate itself, which is made of magnesium (see Figure 1-2). The magnesium plate, with dimensions of $48'' \times 48'' \times 2''$, rests upon a thin oil film which is pumped over the precision ground granite surface. Hydrostatic bearings, mounted to the under side of the slip plate and within the granite block, constrain table motion to the axis of excitation. A glass composite layer, attached to the top of the slip plate, facilitates thermal testing. It is $5/8''$ thick. (For a more detailed explanation of the slip table design, see Chapter 1).

Shaker and slip table motions are coupled by means of a magnesium fixture, pin,

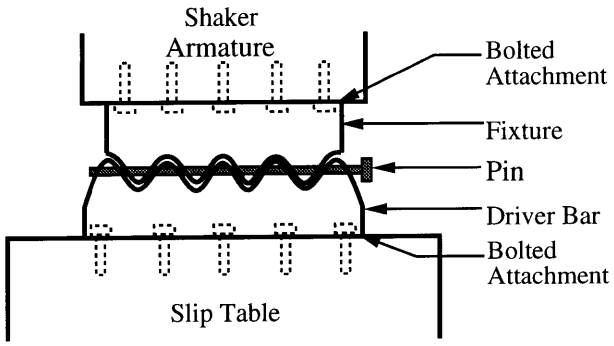

Figure 4-3: Shaker-Slip Table Interface

and driver bar. The fixture bolts to the armature of the shaker, and then attaches to the driver bar using interlocking fingers and a tight-fitting pin. The driver bar, in turn, bolts to the slip table. The bolted connections are very rigid, employing numerous bolts, each torqued to 65 ft-lbs. The complete shaker-table interface is illustrated in Figure 4-3, with a detailed sketch of the fixture, including some dimensions and bolt holes, given in Figure 4-4. A schematic (modified from [1]) of the fixture, driver bar, and pin (referred to as the SL Shaft) is shown in Figure 4-5. Note that in the actual system, the interlocking fingers are more rounded than they appear here and that the driver bar looks different.

Figure 4-6 is a schematic (taken from [1]) of the shaker-slip table assembly. The fixture (referred to as the SL driver bar), slip plate, oil system, and concrete seismic base are among the items labelled. Figure 4-7 shows the actual shaker-slip table assembly used for these tests. The metal frame, made of angle irons, surrounding the slip plate is a stand for a thermal shroud and is not relevant here.

The specific characteristics of the Unholtz-Dickie shaker and the Kimball slip table used are given in Tables 4.1 and 4.2. The moment constraints given in Table 4.2 are the maximum moments which a test object can exert on the slip table before table performance is compromised.

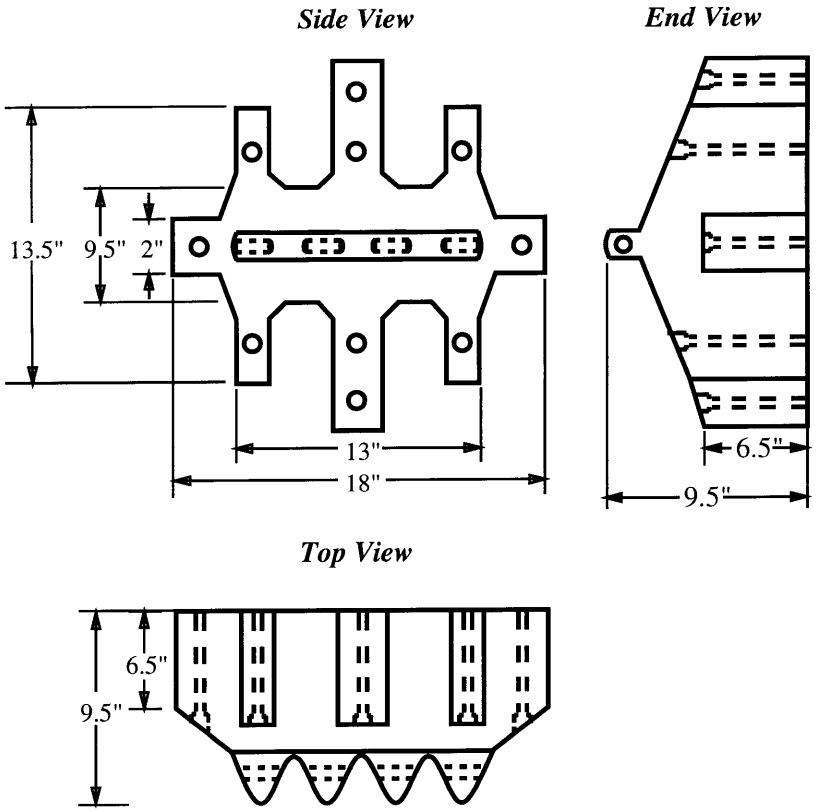

Figure 4-4: Fixture

Table 4.1: T1000 Unholtz-Dickie Shaker

Force with the TA130 (32KVA) Amplifier	
Sine	11,000 lbs peak
Random	8,000 lbs rms
Force with the TA360 (196KVA) Amplifier	
Sine	16,000 lbs peak
Random	15,500 lbs rms
Stroke	1.75 in. peak-to-peak
Armature natural frequency	2300 Hz
Armature weight	95 lbs
Armature diameter	17.25 in

Table 4.2: Slip Table Moment Constraints

Pitch	944 kilo-pound-inches
Roll	824 kilo-pound-inches
Yaw	600 kilo-pound-inches

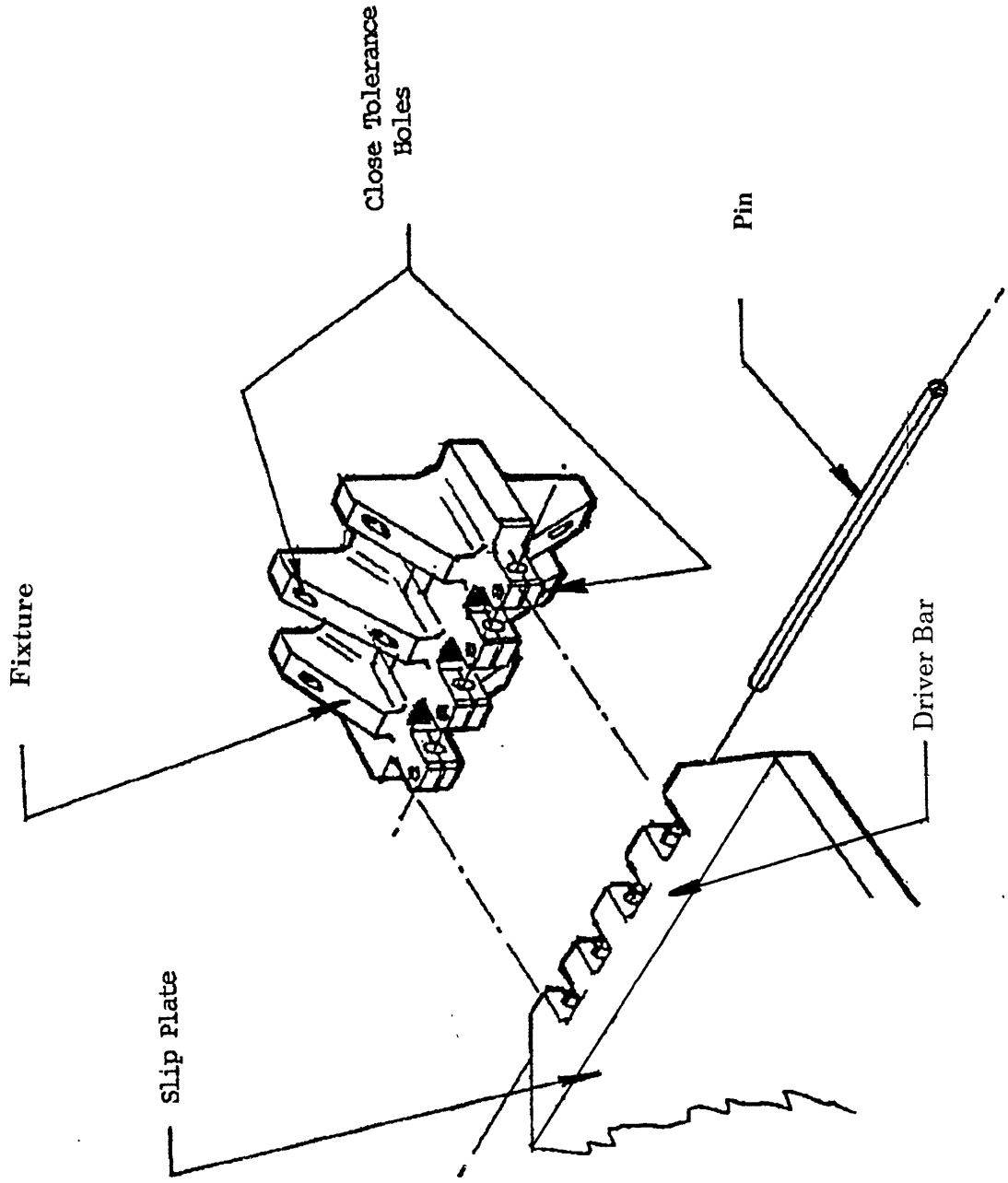

Figure 4-5: Fixture-Driver Bar Interface

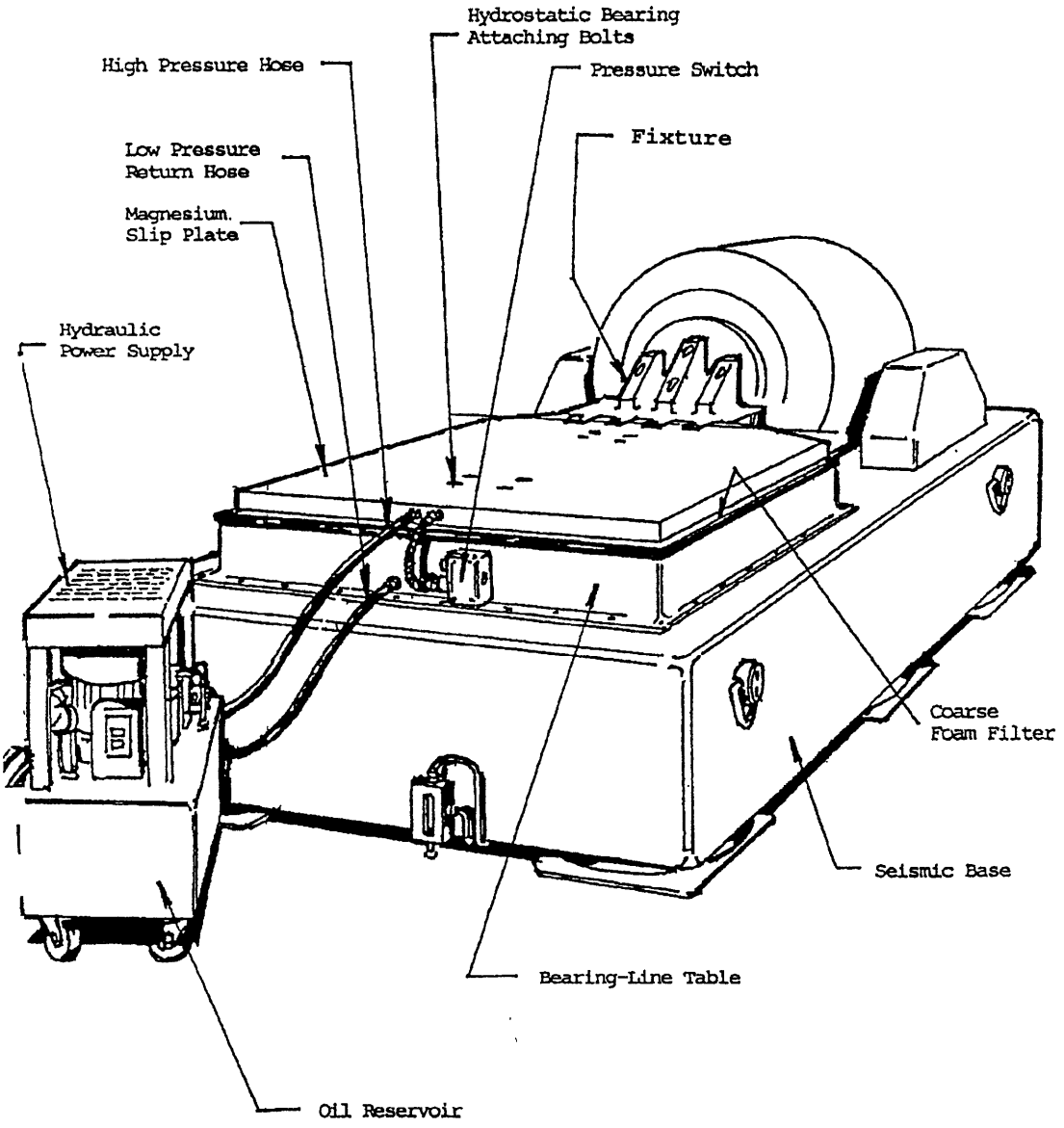

Figure 4-6: Shaker-Slip Table Assembly

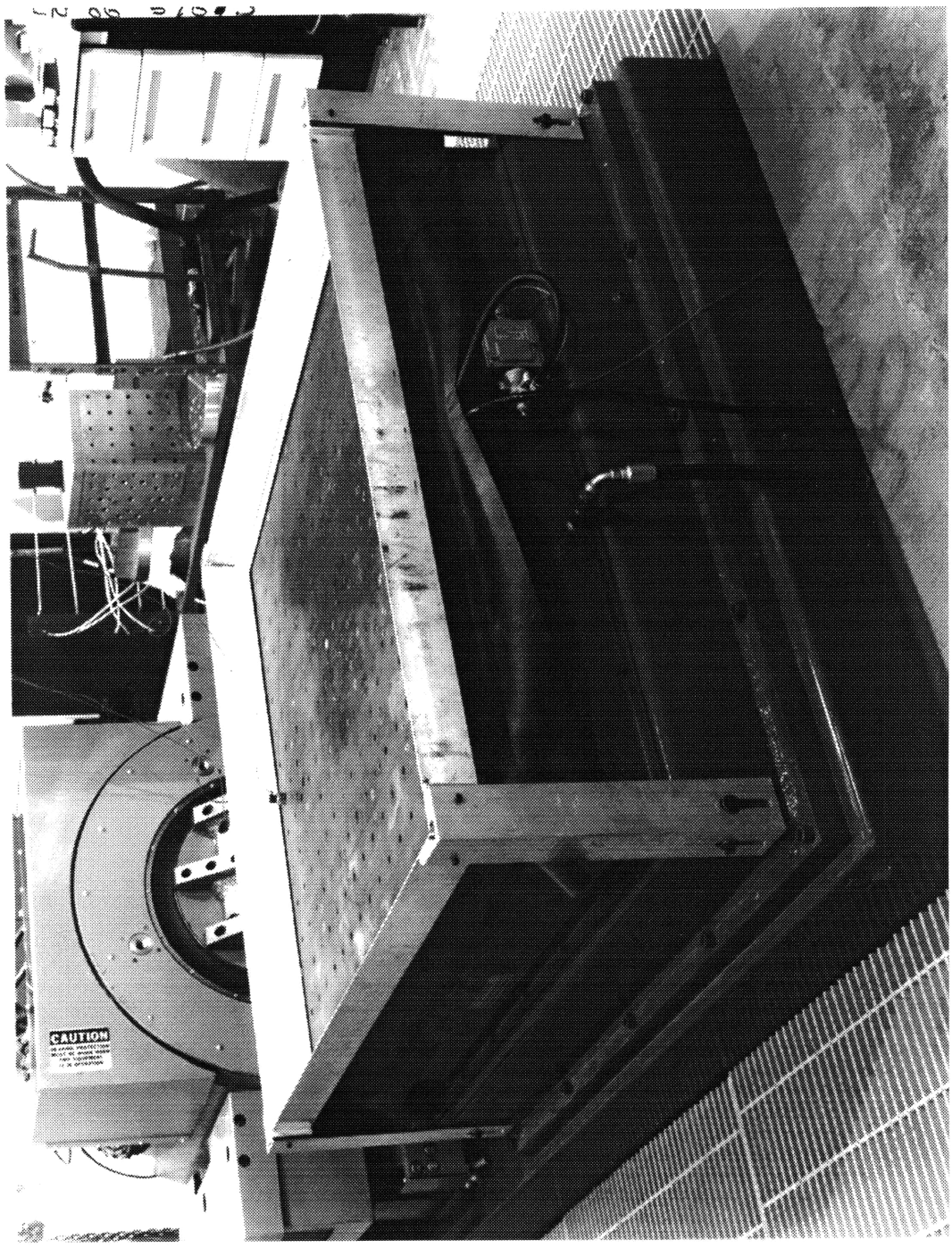

Figure 4-7: Shaker-Slip Table Assembly at Los Alamos National Laboratory

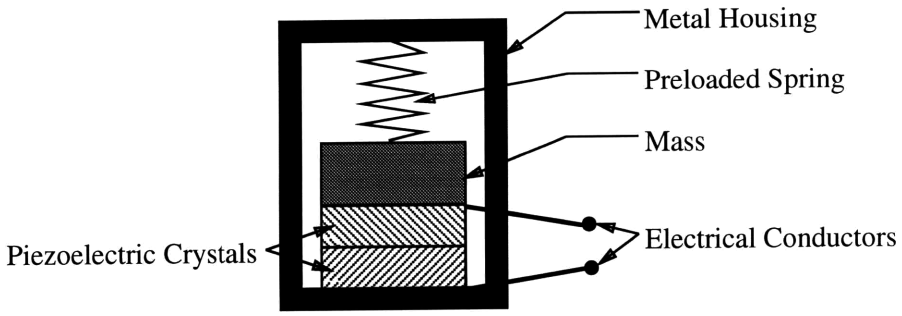

Figure 4-8: Piezoelectric Accelerometer

4.2.2 Instrumentation

General purpose piezoelectric accelerometers were used to measure the vibrations of the shaker-slip table assembly and to convert these vibrations into equivalent electrical signals to be collected by the signal analyzer. Accelerometers were chosen because they are the most commonly used vibration transducer. They have a wide frequency range, come in all shapes and sizes, and are in general very rugged. Among accelerometers, piezoelectric accelerometers, where the sensing element is a piezoelectric crystal, are the most common. The basic construction of the piezoelectric accelerometers used is outlined in Figure 4-8. It consists of a spring-mounted mass in contact with a piezoelectric element, with all components located in a metal housing. When the base of the accelerometer vibrates, the mass applies a dynamic load to the piezoelectric crystal. The piezoelectric crystal generates an electrical charge proportional to this load and hence proportional to the acceleration of the mass.

The specific characteristics of the accelerometers used are listed in Table 4.3. Both are piezoelectric, shear type accelerometers manufactured by Endevco. The 2221D accelerometers are standard piezoelectric accelerometers which put out a very small electrical charge. A signal conditioner converts this electrical charge to a voltage and amplifies it into a signal strong enough to be measured by the analyzer. The signal conditioner used was manufactured by PCB. The 2251A-10 accelerometers are integral electronic piezoelectric accelerometers, with built-in electronics which perform the charge-to-amplified voltage conversion within the accelerometer. For these, the signal conditioner simply supplies a 4mA current source to power the electronics package.

Table 4.3: Endevco Piezoelectric Accelerometers

Accelerometer Model	2221D	2251A-10
Frequency Range	20-8000 Hz	5-8000 Hz
Temperature Range	-65 – +350degF	-67 – +257degF
Natural Frequency	30,000 Hz	40,000 Hz
Sensitivity	$\sim$ 20 pC/g	$\sim$ 10 mV/g
Mounting Torque	10 in-lbs.	5 in-lbs

Different accelerometer types were used because only limited quantities of each were available.

4.2.3 Control and Data Acquisition Equipment

Genrad 2514 and Genrad 2515 signal analyzers were used to control, analyze, and store data. Such analyzers collect, filter, Fourier transform, and average raw transducer time histories. In addition, they provide visual displays of data in both the time and frequency domains, to facilitate quality control and analysis.

Input Signal

The control analyzer was used to designate the specific forcing function for driving the shaker-slip table assembly. Random excitation was chosen over harmonic or transient excitation because of the limitations associated with their use. Harmonic excitation, where a sinusoidal force is slowly swept through the frequency range of interest and the system response is measured at all frequencies, is rather time consuming. It is not frequently used, except in situations where only a few discrete frequencies dominate a system's behavior. In addition, it has the disadvantage that it only excites a single resonance at any given time; so interaction between resonances cannot be studied. Transient excitation, on the other hand, like random excitation, excites a structure over a wide range of frequencies and thus acts on all of the resonances at the same time. This simulates the real environment better. Transient excitation, however, unlike random excitation, is not repeatable and is thus not good for characterizing

nonlinearities.

Signal Analysis

Continuous random vibration signals input to the shaker-table assembly produce continuous random vibration responses. These responses are measured by the accelerometers and sent to the signal conditioner. The analog output voltage of the signal conditioner is sent to the analyzer where it is discretely sampled. The discretely sampled random time histories are analyzed in both the time and frequency domains. Time domain signals are observed, using an oscilloscope, to give an overall feel for the quality of the signals, showing their form, peak magnitude, r.m.s. signal levels, and any peculiarities. Frequency domain, or spectral, signals are examined to identify individual vibrational modes.

As mentioned in Section 2.2.5, spectral density functions are calculated using the Fourier transformation of the discrete time series representation of the time signal. This Fourier transformation is performed by the spectrum analyzers using the FFT algorithm described in Section 2.2.4. The resulting auto-spectral density functions provide a representation of the frequency content of the signals; but because they are real, they do not contain any phase information. Cross-spectral density functions (as defined in Section 2.2.5), on the other hand, provide a measure of the mutual power between two signals; and, because they are complex, they provide both magnitude and phase information. Frequency response functions ($H(\omega)$), or transfer functions (also defined in Section 2.2.5), describe the relationships between the system's inputs and outputs, and are also complex. A variety of frequency response functions are available to describe a system, including receptances (displacement to force ratios), dynamic stiffnesses (force to displacement ratios), mobilities (velocity to force ratios), impedances (force to velocity ratios), inertances (acceleration to force ratios), and apparent masses (force to acceleration ratios). Since all of the data gathered here is done using accelerometers, frequency response functions relating acceleration to acceleration are used (see Section 2.2.5). Frequency response data is analyzed using magnitude and phase angle plots.

Control Loop

The control analyzer uses the auto-spectral density of the control accelerometer signal to update the drive signal. Initially, the shaker drive signal is just the reference spectrum, $R(\omega)$, defined during setup of the control analyzer. The drive signal, however, is continually updated. Updating consists of modifying the drive spectrum until the control spectrum (spectrum at the chosen control accelerometer) is identical to the reference spectrum. Control strategy, loop stages, and update equations are described below [19].

The control accelerometer signal is sent to the control analyzer, where it is digitized and transformed into a power spectral density (PSD) function (see Sections 2.2.4 and 2.2.5 for an explanation of these processes). This discretization and transformation process is performed N times, where N is the number of frames averaged together for each drive signal update, and is specified in the control analyzer setup (see Section 2.2.6 for a discussion of averaging). The resulting averaged PSD is designated $C_i(\omega)$, where $i = 1, 2, 3, \ldots$ up to the total number of drive updates. This averaging of multiple frames per drive update loop improves the statistical accuracy of the control spectrum.

Weighted linear averaging is used in updating the drive signal. When applied repeatedly to a signal with a constant initial error, the averaging algorithm results in an exponential convergence to the correct signal. Hence, in this application, the averaging scheme is referred to as "exponential averaging", and all quanties calculated using it will be called "exponentially averaged". An exponentially averaged control spectrum, $C_i^E(\omega)$, is calculated by exponentially averaging the newly measured control spectrum, $C_i(\omega)$, with the previous exponentially averaged control spectrum, $C_{i-1}^E(\omega)$:

$$C_i^E(\omega) = \left(1 - \frac{1}{P}\right) C_{i-1}^E(\omega) + \frac{1}{P} C_i(\omega), \tag{4.1}$$

where $P = 2^\vartheta$, and ϑ is a control loop parameter chosen during setup of the control analyzer. Note that for the first loop, the previous exponentially averaged control spectrum is just the newly attained control spectrum, $C_1(\omega)$.

Once $C_i^E(\omega)$ has been calculated, the updated drive spectrum, $D_i(\omega)$, can be computed using the the exponentially averaged drive spectrum of the previous loop, $D_{i-1}^E(\omega)$, and the ratio of the reference control spectrum, $R(\omega)$, to the updated exponentially averaged control spectrum, $C_i^E(\omega)$:

$$D_i(\omega) = D_{i-1}^E(\omega) \left(\frac{R(\omega)}{C_i^E(\omega)} \right). \tag{4.2}$$

Note that for the first update, the exponentially averaged drive spectrum of the previous loop, $D_0^E(\omega)$ is just the reference spectrum, $R(\omega)$. For subsequent loops, however, the updated exponentially averaged drive spectrum, $D_i^E(\omega)$, must be computed. It is formed using the previous exponentially averaged drive spectrum, $D_{i-1}^E(\omega)$, and the updated drive spectrum, $D_i(\omega)$. The same discount averaging used to calculate the exponentially averaged control spectrum, $C_i^E(\omega)$, is used here:

$$D_i^E(\omega) = \left(1 - \frac{1}{P}\right) D_{i-1}^E(\omega) + \frac{1}{P} D_i(\omega). \tag{4.3}$$

This exponentially averaged drive spectrum, $D_i^E(\omega)$, will be used in computing the updated drive spectrum of the next loop.

The updated drive signal (calculated in Equation 4.2), $D_i(\omega)$, must be converted to a real drive signal in the time domain before it can be sent to the shaker. The drive signal, $D_i(\omega)$, is a PSD function that lacks phase. It is converted to a complex frequency function by adding phase information, using a random number generator. The complex drive spectrum is then converted to a real drive signal in the time domain, $a_i(t)$, via the inverse FFT algorithm (see Section 2.2.4). This step completes the drive update loop.

The updated drive signal, $a_i(t)$, is filtered, passed through a D/A converter, transmitted to the power amplifier and sent to the shaker. At the end of the next loop (approximately 3.4 seconds later), another updated drive spectrum is calculated. This process continues as long as the test is active.

4.3 Test Setup

The actual experimental procedure began with the instrumentation of the slip table and the shaker-table interface using piezoelectric accelerometers. Accelerometer locations were chosen to provide ample monitoring of table modes and any nonlinear behavior. Nine accelerometers, designated numbers 1 through 9, were placed on the table in a grid-like fashion as illustrated in Figure 4-9. The accelerometers were mounted normal to the surface with their sensitivity axis aligned with the desired measuring direction (the x-axis of Figure 4-9). The accelerometer arrangement facilitated measurement of at least the first three extensional modes of the table while allowing unsymmetric and uneven modal behavior to be monitored as well. Eight additional accelerometers, designated A through H, were placed across the interface between the shaker and the table. These interface accelerometers, also mounted normal to the surface and with their sensitivity axis aligned with the x-axis of Figure 4-9, were intended to monitor any deviant or nonlinear behavior across the various connecting joints. The interface accelerometers are shown in Figure 4-9, with a close-up of the fixture connecting the shaker to the slip table pictured in Figure 4-10.

The accelerometers were mounted to one-inch square accelerometer blocks using connecting threaded studs. The accelerometer blocks were in turn mounted to the shaker-slip table assembly using dental cement. Accelerometer attachment is illustrated in Figure 4-11. Accelerometer blocks were used since the accelerometers could not be directly mounted to the shaker or slip table surfaces via threaded studs because the receiving holes on the shaker and slip table surfaces were either the wrong size or not available at the desired locations.

The accelerometers were attached to the accelerometer blocks using the manufacturer-specified bolt torques listed in Table 4.3. The cables were taped down to avoid "cable whip", which can add noise to the data.

With the accelerometers in place, the Genrad control and data acquisition signal analyzers were prepared. Because tests are normally run on the slip table at frequencies between 10 and 2000 Hz, that was the frequency range chosen for these tests.

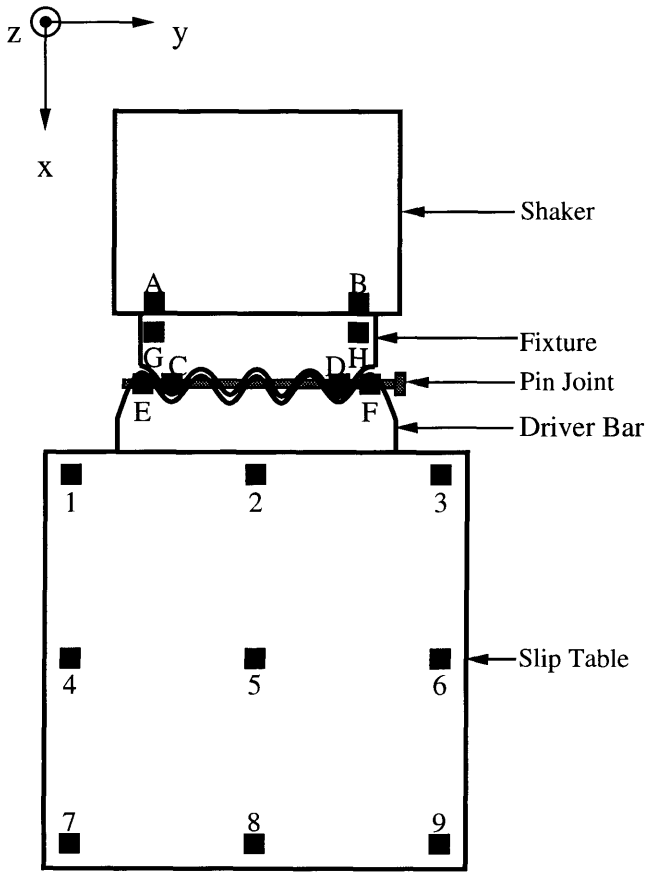

Figure 4-9: Accelerometer Locations

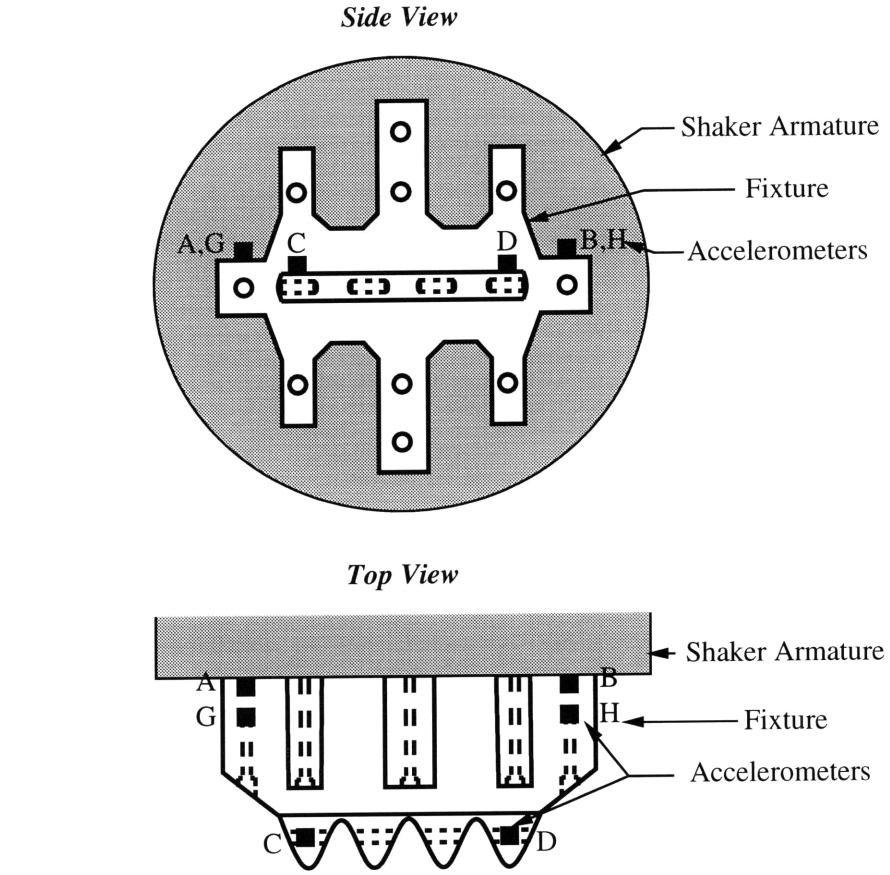

Figure 4-10: Interface Accelerometer Locations

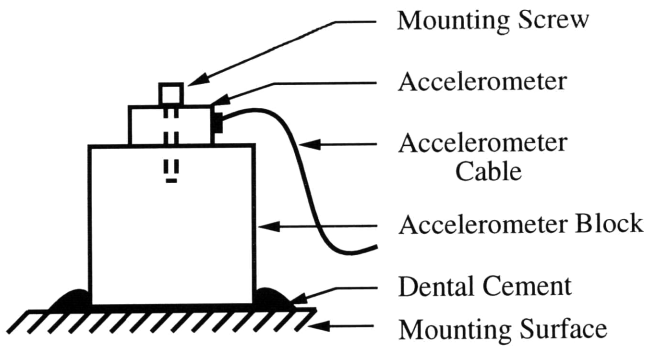

Figure 4-11: Accelerometer Mounting

This ensured measurement of the dynamic behavior of the shaker-slip table assembly under all standard operating conditions. Because of slight hardware differences in the analyzers, the actual ranges for the two were chosen as 10 to 2000 Hz for the controller, and 0 to 2560 Hz for the data acquisition signal analyzer.

Based upon the desired frequency range, the Genrad analyzers' software chose an appropriate anti-aliasing filter to constrain the frequency range. In addition, to avoid aliasing, they chose a sampling interval Δ ($\Delta \leq$ .0025sec) such that the Nyquist frequency $1/(2\Delta)$ Hz was at least twice the maximum frequency of interest. (See Section 2.2.6 for more information on sampling frequencies and aliasing).

Frequency resolution was specified by choosing the number of frequency lines (at each frequency line, a data point is stored) for the analyzers. Again, because of slight differences in the hardware, different numbers of frequency lines were chosen for the two Genrad analyzers (400 for the controller and 640 for the data acquisition signal analyzer). This choice of frequency lines dictated the maximum effective bandwidth of the calculation, B, to be $B = 2000/400 = 5$ Hz. (See Section 2.2.6 for more information on resolution). Using this effective bandwidth, and the sampling interval, Δ, the Genrad determined the number of points, N, to discretely sample from each record ($BT \geq 1$ and $N = T/\Delta$ from Section 2.2.6).

The required accuracy of the calculation, $1-(\sigma/m)$, was chosen to be 90%; so, using the formula $\sigma/m \simeq 1/(\sqrt{BT})$, it was determined that approximately 16 averages were necessary. Overlap averaging was used, as is standard for the Genrad analyzers. Averaging was conducted in the frequency domain on spectra which were convoluted with Hanning windows. For more information on averaging and windowing, see Section 2.2.6.

As mentioned in Section 4.2.3, a continuous random excitation signal was chosen to drive the shaker-slip table assembly. This signal was produced by the generator, amplified by the small power amplifier (TA130) and sent to the shaker. The exact form of the random excitation signal was determined by the control spectrum, chosen to be a flat spectrum with low amplitude (1.417 g's rms–see Section 2.2.5 for a description of rms signal levels). Such a spectrum was chosen over a non-uniform one because at

it excites all frequencies with equal magnitude at the control accelerometer location and is more straightforward to analyze. The accelerometer located farthest from the shaker, channel 8 in Figure 4-9, was chosen as the control accelerometer, in accordance with standard testing procedure at Los Alamos National Laboratory.

The complete lists of parameters entered into the Genrad 2514 controller and into the Genrad 2515 data acquistion signal analyzer are given in Tables 4.4 and 4.5, respectively. Note that these are the actual dialogs with the analyzers. All parameters have been included for completeness, but only those important for understanding the experimental setup have been explained here.

Verification that everthing was properly hooked up and that the accelerometer sensitivities were properly dialed into the signal conditioner and into the analyzers was done using an accelerometer simulator. It simulated an accelerometer output which was fed through the signal conditioner and into the analyzers. There, the signal was measured and checked for noise and proper output level.

4.4 Test Procedure

With everything correctly hooked up, the system was excited. The control analyzer was used to attain the desired excitation at the control accelerometer. The control spectrum is shown in Figure 4-12. The input level was gradually stepped from 1/12th the desired level to the full desired level of 1.417 g's rms. During this gradual level increase, the time domain signals of the accelerometers were examined to ensure that the expected responses were being attained, and that problems were not apparent. In addition, the gradual level increase allowed the control loop compensation to be implemented gradually.

Once the drive signal was brought up to full level, but before data was taken and stored, the time histories and the coherence function were examined. (For a detailed explanation of coherence, see Section 2.2.6). This was done to ensure that clipping of signal peaks was not occurring, to make sure that expected signal levels were being attained (another check that calibration and parameter entry into the signal analyzer

Table 4.4: Control Parameters

Bandwidth:		2000.0
Resolution:		400.0
Frequency Increment (Hz):		5.000
Equalization Parameters:		
	Frames/Loop:	4
	Discount Exponent:	3
	Fast Initial Equalization:	Y
Reference Spectrum Initial Slope:		0.0
	Alarm Limits (+dB, -dB):	3.000, -3.000
	Abort Limits (+dB, -dB):	6.000, -6.000
Reference Spectrum Frequency (Hz):		10.0
	Level (Gsqr/Hz):	0.001000
	Alarm Limits (+dB, -dB):	3.000, -3.000
	Abort Limits (+dB, -dB):	6.000, -6.000
Reference Spectrum Frequency (Hz):		2000.0
	Level (Gsqr/Hz):	0.001000
	Alarm Limits (+dB, -dB):	3.000, -3.000
	Abort Limits (+dB, -dB):	6.000, -6.000
Reference Spectrum Final Slope:		70.00
Grms:		1.417
Alarm/Abort Range:		
	Low Freq (Hz), High Freq (Hz):	10.00, 2000.0
	Lines to Trigger Alarm:	10
	Lines to Trigger Abort:	20
Alarm Level (Grms):		3.000
Abort Level (Grms):		4.000
Low Level (-dB):		-12.00
Auto Start? (Y/N):		N
Level Increment (dB):		3.000
Start-up Time (sec):		1.600
Shut-down Time (sec):		2.000
Test Time (hr, min, sec):		0,5,0
Level Scheduling? (Y/N):		N
16-Ch Selector? (Y/N):		N
Control Channels:		1
Extremal Control? (Y/N):		N
Auxiliary Channel:		0
Accel Sens (mV/g):		
	Ctl. Ch. 1:	100.0
Prestored Drive? (Y/N):		N
Drive Clipping? (Y/N):		N
Automatic Mode Only? (Y/N):		N
Spectra Storage? (Y/N):		N
Loop-Check Max Drive (Volts):		.1000
	Print Gain and Pause after Loop-Check? (Y/N):	Y
AC Coupling? (Y=AC/N=DC):		Y

Table 4.5: Data Acquisition Parameters

Channel Setup:		
	Ch. 1 0=Linear, 1=Log data channel:	0.
	Sensitivity (Linear EU/VOLT):	10.000
	Max Expected Engr. Unit (Linear):	20.
	Channel-1 Label:	Control
	Units:	G's
	...and so on for the other channels	
Auto-Ranging [Y/N]:		N
Data Processing Selections:		
	Auto/Cross Chan Mode [A/C, Ref=Ch1]:	C
	Disk Storage of Time Histories [Y/N]:	N
	Time/Freq Domain Averaging [T/F]:	F
	On-Line Averaging (0=Linear, 1=Expon., 2=APS Peak Hold, 3=Linear and Peak Hold of APS data):	0
	Window (0=None, 1=Unnormalized Hanning, 2=Norm Hann, 3=Flat top, 4=Blackman)	2
	Playback/Record speed ratio:	1.00
Analog Input:		
	Fmin (0=Baseband, > 0=Zoom):	0.00
	Fmax (Hz):	2560.00
	Number of Freq. Lines:	640
	Number of Averages:	16
	Coupling Code (0=AC, 1=DC, 2=Bias):	0
Trigger Setup:		
	Use Remote Control Interface? (Y/N)	N
	Trig Source (0=Off, +/- 1-N, 100=Ext):	0
Output Setup:		
	D/A Output (0=Off, 1=Ran, 2=Sine, 3=Chirp, 4=Chirp Down):	0
Misc. Information:		
	Beep at user responses (0=No, 1=Yes):	0
	Display every Nth data frame:	16

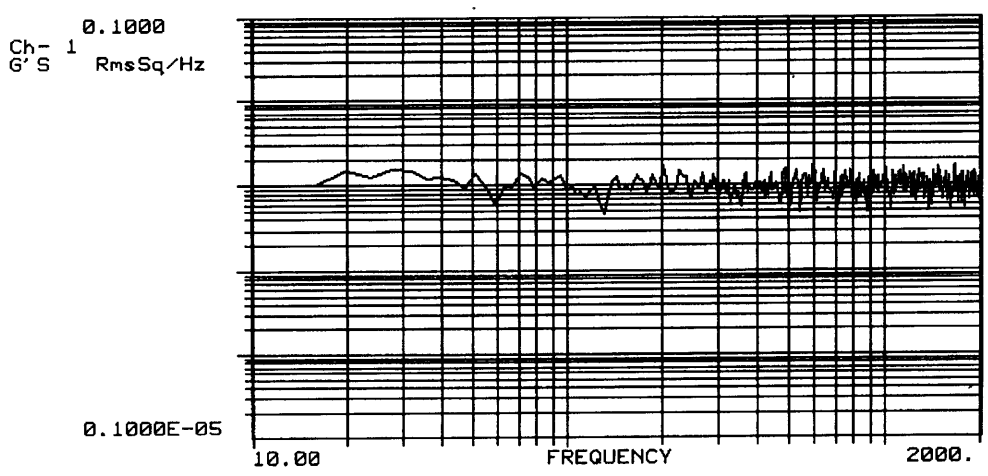

Figure 4-12: Control Spectrum

had been done properly), and to ensure that there was no unexpected behavior. In addition, monitoring the coherence ensured that valid data was being collected by the signal analyzer. In all cases, time history data looked good, and the peaks in the frequency response coincided with a good coherence, close to unity.

The magnitudes and the phases of the 17 accelerometers of Figure 4-9 were recorded. Specifically, their auto-spectral densities and transfer functions with respect to the control accelerometer were saved. This data is analyzed in the results chapter, Chapter 6. All transfer function data is included in Appendix C.

4.5 Additional Tests

Additional tests were run, using the same test setup and procedure described in Sections 4.3 and 4.4, to determine the effect of varying the location of the control accelerometer. Instead of using the outboard accelerometer (number 8 in Figure 4-9), accelerometers 5 and 2 were used, in turn, as the control accelerometers. This data, along with that of the other addtional tests to be described below, is analyzed in Chapter 6.

Other tests were run, again using the same test setup and procedure described in Sections 4.3 and 4.4, with the accelerometers set up to measure motion along the y

and z-axes. The purpose of these tests was to verify the assumption that movement in the y and z-axes was relatively insignificant compared to that in the x-direction. The transfer functions (with respect to the control channel) for these tests are included in Appendix C.

Finally, tests were run with simulated test objects attached. These tests were also run using the test setup and procedure of Sections 4.3 and 4.4, but they were run using the large power amplifier (of Table 4.1) instead of the smaller one. This was done because of hardware-related difficulties. This switching between amplifiers did not affect the data acquired, since both amplifiers are capable of the output levels required for the tests conducted here. Two different masses (weighing the amounts of typical test objects) and two different locations on the slip table were tested. The masses used were flat, octagon-shaped plates, approximately 15″ in diameter and weighing 56 lbs each. One and then two of these masses were attached at each of the two locations designated in Figure 4-13 (#1 and #2), resulting in four additional tests. The masses were mounted on the slip table using sixteen bolts torqued to 65 ft-lbs each. Accelerometer data was collected from the seventeen locations marked $1-9$ and $A-H$ in Figure 4-13, as well as from an accelerometer mounted atop the attached mass. This additional data was taken to verify the assumption that the mass was rigidly attached to the table.

In all cases, the signal analysis equipment reduced the test data to acceleration transfer functions with respect to the control accelerometer. Magnitude and phase, as functions of frequency, were calculated and stored. Because the frequency and magnitude of anti-resonances is of primary concern in this thesis, only magnitude results are discussed here (in Chapter 6). The transfer function magnitude plots are all included in Appendix C.

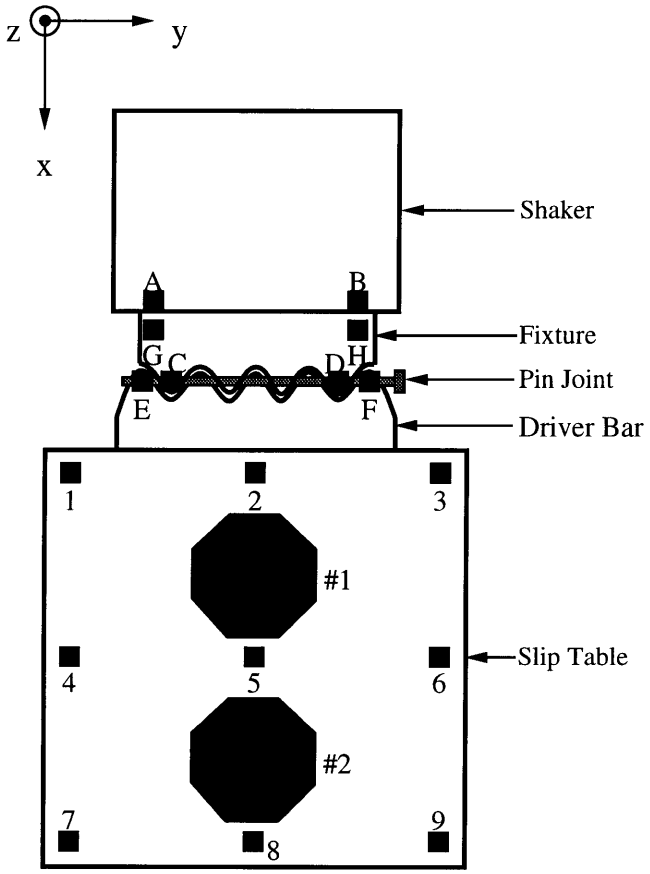

Figure 4-13: Mass Locations

Chapter 5

Theoretical Model

5.1 Philosophy and Overview

In this chapter, two mathematical models are developed to characterize the dynamic behavior of the shaker-slip table assembly. Both models use lumped masses to model the continuous shaker-slip table assembly as a discrete system. In addition, both models employ linear springs and dampers. Mass locations are chosen to coincide with the accelerometer locations of the experiments. This facilitates comparison and correlation of the experimental data with the results obtained using the theoretical models. Figure 5-1 shows the lumped mass locations (represented as heavy dots) as well as the linear springs (drawn as straight lines). All table masses are represented with a number (1-9), and all interface masses are represented by a letter (A-H). Only neighboring masses are attached via a spring. System mass and stiffness properties are determined using the matrix methods of structural analysis described in Section 2.2.3. Damping is determined using the experimental data.

The two models differ in the technique they use for solving the equations of motion. The first employs Matlab to find a closed form solution to the equations of motion. It calculates the eigenvalues and eigenvectors of the system, thus determining system natural frequencies and associated mode shapes. The second uses time steps to provide an iterative solution. An explicit time solution is attained using Runge-Kutta algorithms in a Fortran routine.

The models, based upon basic principles, are intended to provide a quantitative understanding of the physical system. In addition, because the explicit time simulation model is simple, it is readily manipulated to determine to what extent system malfunctions affect the validity of tests run using the shaker-table assembly. Since closed form solutions can only be obtained for linear systems, the explicit time simulation model is key for characterizing system malfunctions. While under ideal operating conditions, the shaker-table assembly may perform linearly, system malfunctions in the oil, bearings, and joint can lead to nonlinear behavior. The completed explicit time simulation model is also used to determine the effect of varying test object placement.

5.2 Determination of System Properties

5.2.1 Mass

The shaker-slip table assembly is reduced to a system with a finite number of degrees of freedom, using lumped masses. The mass locations (illustrated in Figure 5-1) are chosen to coincide with the locations of the accelerometers, with two additional masses used in the shaker-fixture and fixture-fixture interfaces for modelling purposes. The approximate masses of the separate components of the shaker-slip table assembly ([20] and measurements made by the test engineers at Los Alamos National Laboratory) are given in Table 5.1. The lumped masses are determined from these component masses using matrix structural analysis theory. Reference [11] describes the general procedure for dividing up a continuous system into discrete masses. Each of the four square table elements (as shown in Figure 5-2) weighs one fourth of the table mass or 44.3 kg; each of the three triangles in the driver bar weighs 1.7 kg; each of the four triangles in the fixture weighs 5.2 kg; and each of the four triangles in the shaker weighs 10.8 kg. Since each table square has four corners, each corner node is 11.1 kg. Similarly, for the other components, each driver bar node is 0.6 kg, each fixture node is 1.7 kg, and each shaker node is 3.6 kg. Assembling the indvidual masses for each

Table 5.1: Shaker-Slip Table Component Masses

Slip Table	177.2 kg
Driver Bar	5.2 kg
Fixture	20.9 kg
Shaker Armature	43.2 kg

Table 5.2: Lumped Masses

$\underline{m}_1$	=	11.7 kg	$\underline{m}_A$	=	7.2 kg
$\underline{m}_2$	=	24.0 kg	$\underline{m}_B$	=	7.2 kg
$\underline{m}_3$	=	11.7 kg	$\underline{m}_C$	=	3.4 kg
$\underline{m}_4$	=	22.2 kg	$\underline{m}_D$	=	3.4 kg
$\underline{m}_5$	=	44.4 kg	$\underline{m}_E$	=	1.2 kg
$\underline{m}_6$	=	22.2 kg	$\underline{m}_F$	=	1.2 kg
$\underline{m}_7$	=	11.1 kg	$\underline{m}_G$	=	10.6 kg
$\underline{m}_8$	=	22.2 kg	$\underline{m}_H$	=	10.6 kg
$\underline{m}_9$	=	11.1 kg	$\underline{m}_K$	=	14.4 kg
			$\underline{m}_L$	=	6.8 kg

node according to the methods outlined in Section 2.2.3 gives the masses listed in Table 5.2 at each node of the shaker-slip table structure. The masses are underlined to differentiate these shaker-slip table system masses from other masses to be used later.

5.2.2 Stiffness

The stiffnesses for the shaker-slip table assembly are determined using the method of matrix structural analysis outlined in Section 2.2.3. This method gives the stiffness properties for the rectangular and triangular elements of Figure 5-2. It assumes that any given element is made of a solid piece of material. This is the case with the slip table (solid plate), and can be assumed for the bolted interfaces. The bolted interfaces are assumed to be sufficiently rigid because of the large number of bolts used and the high torques placed on them. Due to the lack of rigidity of the connection at the pin-joint, however, the spring constants there have to be determined another way.

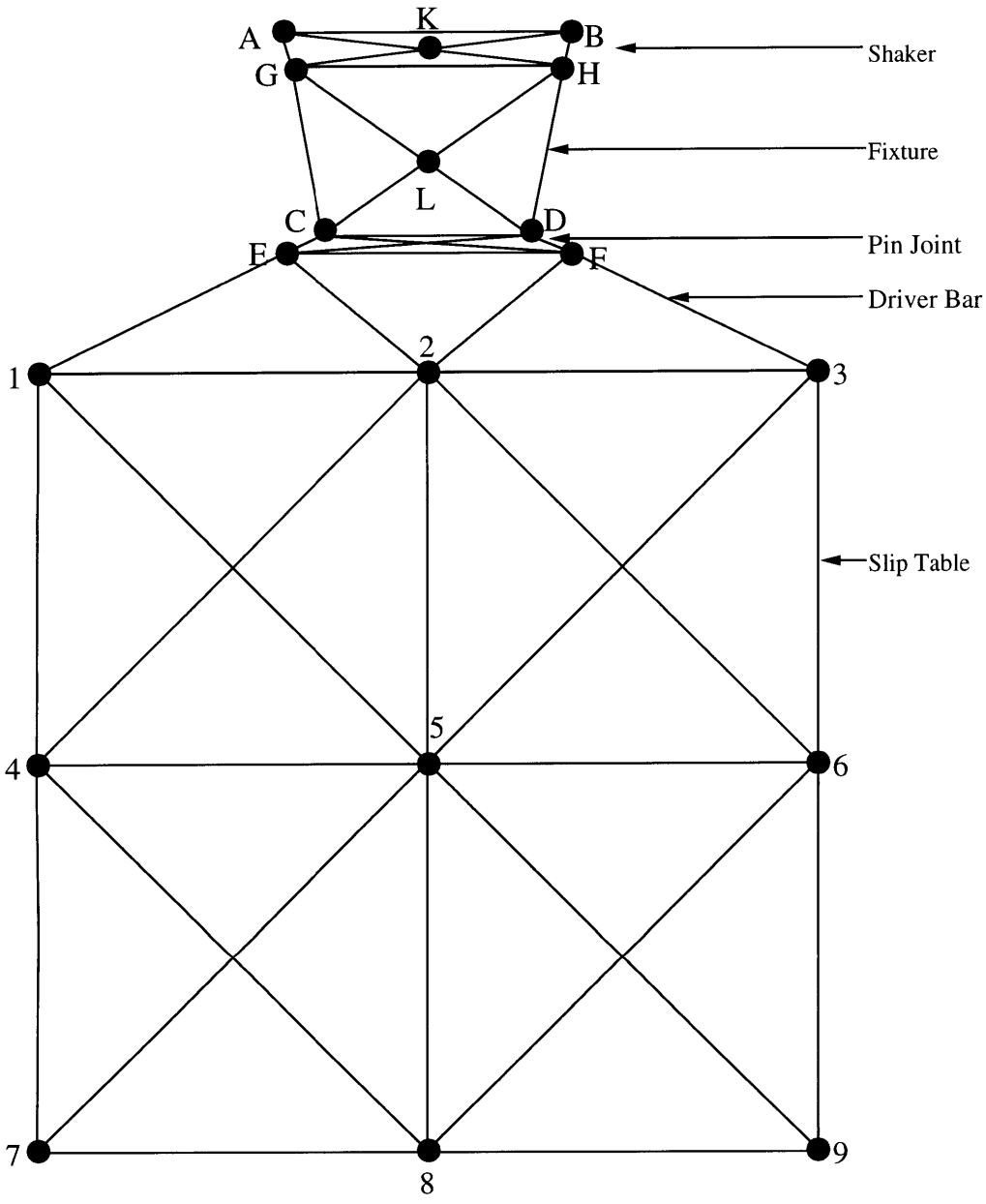

Figure 5-1: Analytical Model of the Shaker-Slip Table Assembly

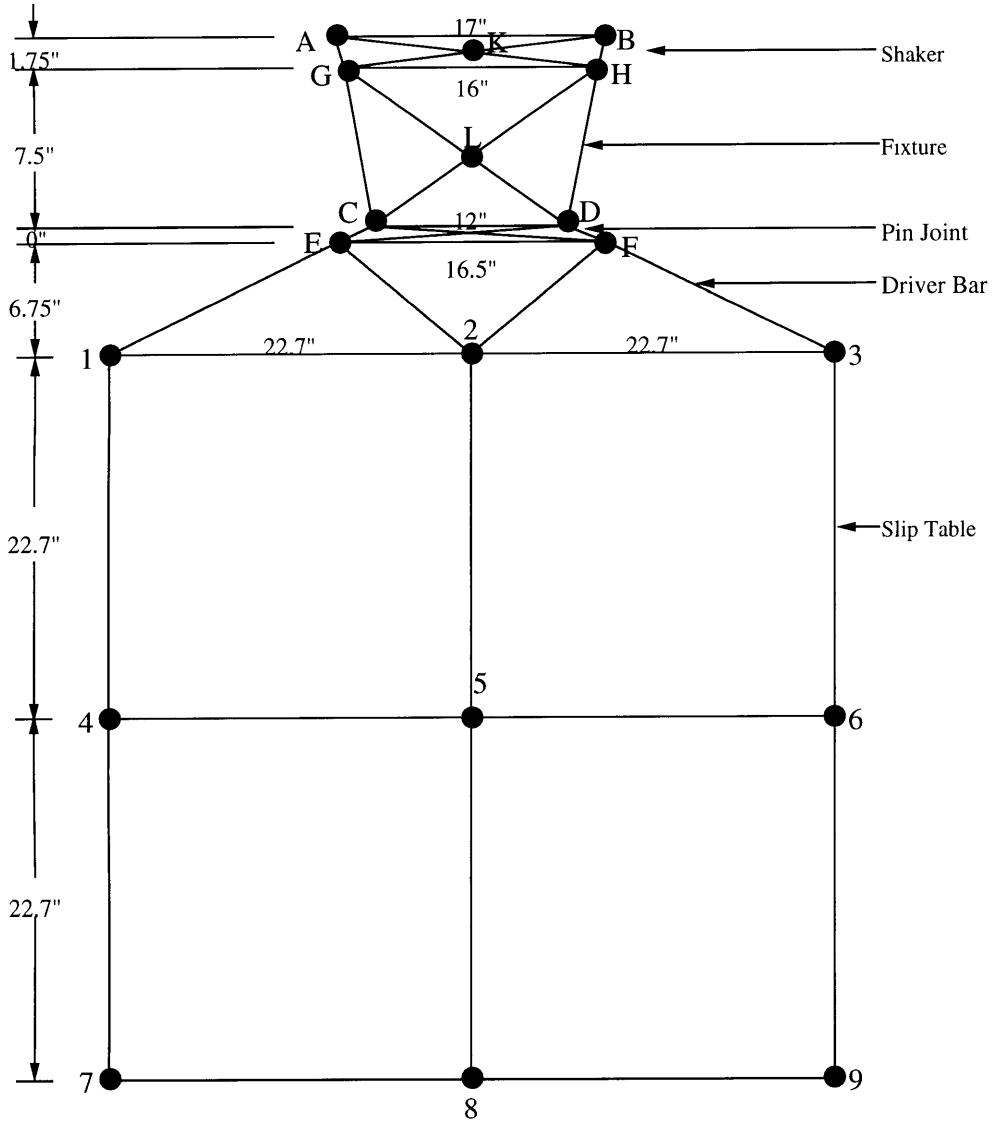

Figure 5-2: Discrete Elements of the Shaker-Slip Table Assembly

The experimental data and a single-degree-of-freedom mass-spring system are used to calculate the spring constants in this interface.

Slip Table

The slip table is divided into four rectangular plate elements as shown in Figure 5-2. Rectangular plate elements were chosen over triangular ones because of their analytical simplicity when using the matrix structural analysis theory of Section 2.2.3.

The stiffnesses of the table springs are found using the stiffness matrix, $\boldsymbol{k}$, defined in Equation 2.69, and the constants, α, γ, κ, and β defined in Equations 2.70, 2.71, 2.72, and 2.73. Since this model of the shaker-slip table assembly is restricted to the x-axis, the only spring constants of interest are those along the x-axis. The two-dimensional matrix of Equation 2.69 is reduced to one dimension by setting y-axis displacements equal to zero. Hence, for a rectangular element as shown in Figure 2-5, the stiffnesses are:

$$k_{82} = \frac{Et}{12(1-\nu^2)} \times \left(\frac{2}{\beta} - 2\alpha\beta\right) \tag{5.1}$$

$$k_{84} = \frac{Et}{12(1-\nu^2)} \times \left(-\frac{2}{\beta} - \alpha\beta\right) \tag{5.2}$$

$$k_{86} = \frac{Et}{12(1-\nu^2)} \times \left(-\frac{4}{\beta} + \alpha\beta\right). \tag{5.3}$$

The subscripts used here indicate the corner displacements (of the rectangular element pictured in Figure 2-5) between which the stiffnesses are determined.

The constant term which precedes all of the above quantities, $\frac{Et}{12(1-\nu^2)}$, is computed. The magnesium slip table has a Young's modulus (E) of 6.5 Msi, and a Poisson's ratio (ν) of 0.35. The attached glass composite layer (G-10 material) has a Young's modulus of 2.5 Msi and a Poisson's ratio of 0.27. The glass composite layer and the slip plate are modelled as one entity for simplicity. Therefore, the effective constant is the sum of the individual constants of the two materials:

$$\left(\frac{Et}{12(1-\nu^2)}\right)^{\text{eff}} = \frac{E_1 t_1}{12(1-\nu_1^2)} + \frac{E_2 t_2}{12(1-\nu_2^2)}. \tag{5.4}$$

This gives

$$\left(\frac{Et}{12(1-\nu^2)}\right)^{\text{eff}} = 1.3750 \times 10^6 \text{ lbs/in.} \tag{5.5}$$

Using Equations 5.1- 5.3 and noting that $\alpha = 0.65$ and $\beta = 1$, the spring constants for a square slip table element are determined:

$$\begin{aligned} k_{82} &= -1.6974 \times 10^8 \text{N/m} \\ k_{84} &= 6.4261 \times 10^8 \text{N/m} \\ k_{86} &= 8.1234 \times 10^8 \text{N/m}. \end{aligned}$$

Translating these spring constants into the notation of the shaker-slip table assembly (see Figure 5-3) and assembling the four elements according to the method specified in Section 2.2.3 gives the stiffnesses shown in Table 5.3. Note the notation used (It was explained in Section 2.2.3, but is repeated here to avoid confustion): the k's are underlined to differentiate the k's of the actual shaker-slip table system from the stiffnesses of the arbitrary discrete elements used for computational purposes. The superscripts (st) indicate that these are the stiffnesses of the slip table. They are for a free-standing table and are not yet been combined with the stiffnesses of the driver bar.

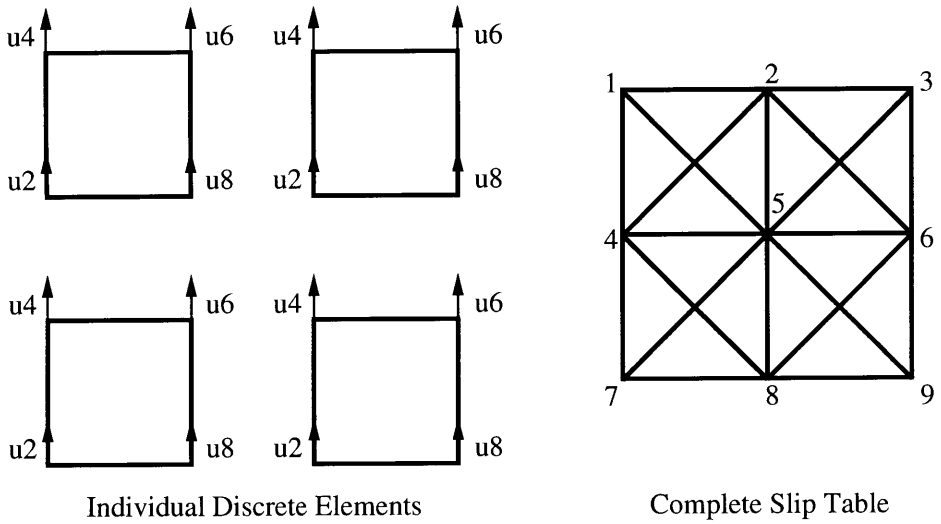

Figure 5-3: Slip Table

Table 5.3: Table Stiffnesses

Slip Table Stiffness	Equivalent Discrete Element Stiffness	Stiffness Value
$\underline{k}^{st}_{21}, \underline{k}^{st}_{32}, \underline{k}^{st}_{87}, \underline{k}^{st}_{98}$	k_{82}	-1.6974×10^8N/m
$\underline{k}^{st}_{54}, \underline{k}^{st}_{65}$	$2 \times k_{82}$	-3.3948×10^8N/m
$\underline{k}^{st}_{42}, \underline{k}^{st}_{51}, \underline{k}^{st}_{53}, \underline{k}^{st}_{62}, \underline{k}^{st}_{75}, \underline{k}^{st}_{84}, \underline{k}^{st}_{86}, \underline{k}^{st}_{95}$	k_{84}	6.4261×10^8N/m
$\underline{k}^{st}_{41}, \underline{k}^{st}_{63}, \underline{k}^{st}_{74}, \underline{k}^{st}_{96}$	k_{86}	8.1234×10^8N/m
$\underline{k}^{st}_{52}, \underline{k}^{st}_{85}$	$2 \times k_{86}$	1.6247×10^9N/m

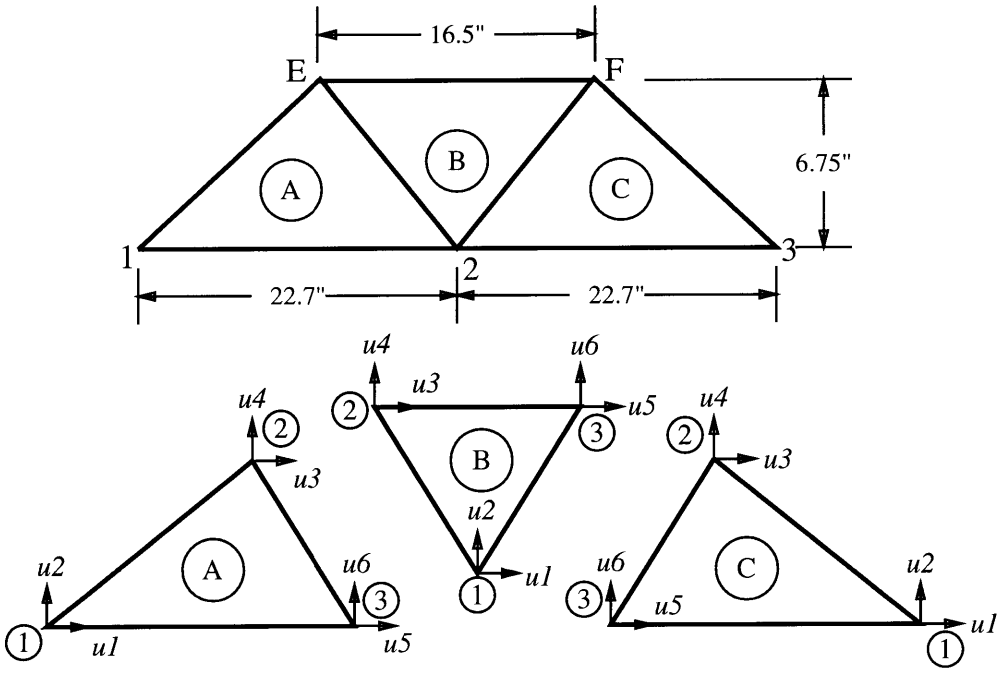

Figure 5-4: Driver Bar-Slip Table Interface

Driver Bar The elements of the driver bar are illustrated in Figure 5-4. The stiffness properties for the three triangles are analyzed separately. The stiffnesses of the driver bar springs are found using the sum of the normal and shear stiffness matrices ($\boldsymbol{k}_n$ and $\boldsymbol{k}_s$, respectively), defined in Equations 2.54 and 2.55. For a triangular element, as shown in Figure 2-4, whose motion is restricted to one dimension, the equations follow:

$$k_{42} = \frac{Et}{4A_{123}(1-\nu^2)} \times (-x_{32}x_{31}) + \frac{Et}{8A_{123}(1+\nu)} \times (-y_{32}y_{31}) \quad (5.6)$$

$$k_{62} = \frac{Et}{4A_{123}(1-\nu^2)} \times (x_{32}x_{21}) + \frac{Et}{8A_{123}(1+\nu)} \times (y_{32}y_{21}) \quad (5.7)$$

$$k_{64} = \frac{Et}{4A_{123}(1-\nu^2)} \times (-x_{31}x_{21}) + \frac{Et}{8A_{123}(1+\nu)} \times (-y_{31}y_{21}). \quad (5.8)$$

The values of the constant terms, $\frac{Et}{4A_{123}(1-\nu^2)}$ and $\frac{Et}{8A_{123}(1+\nu)}$, are calculated. Since the driver bar is made of magnesium, the Young's modulus and Poisson's ratio are 6.5 Msi and 0.35, respectively. Calculating the values of the constants for triangle A,

Table 5.4: Driver Bar Discrete Element Stiffnesses

Triangle A			Triangle B			Triangle C		
k_{42}^A	=	1.5878×10^9N/m	k_{42}^B	=	1.5877×10^9N/m	k_{42}^C	=	2.7811×10^9N/m
k_{62}^A	=	-8.8521×10^8N/m	k_{62}^B	=	1.5877×10^9N/m	k_{62}^C	=	-8.8521×10^8N/m
k_{64}^A	=	2.7811×10^9N/m	k_{64}^B	=	-6.2115×10^8N/m	k_{64}^C	=	1.5878×10^9N/m

Table 5.5: Driver Bar Stiffnesses

Driver Bar Stiffness	Equivalent Discrete Element Stiffness	Stiffness Value
$\underline{k}_{1E}^{db}, \underline{k}_{3F}^{db}$	k_{42}^A, k_{42}^C	1.5878×10^9N/m
$\underline{k}_{21}^{db}, \underline{k}_{32}^{db}$	k_{62}^A, k_{62}^C	-8.8521×10^8N/m
$\underline{k}_{2E}^{db}, \underline{k}_{2F}^{db}$	$k_{64}^A + k_{42}^B, k_{62}^B + k_{64}^C$	4.3688×10^9N/m
$\underline{k}_{FE}^{db}$	k_{64}^B	-6.2115×10^8N/m

whose area is $A_{123} = 76.61\,\text{in}^2$, gives

$$\begin{aligned} \frac{Et}{4A_{123}(1-\nu^2)} &= 4.8345 \times 10^4 \text{lbs/in}^3 \\ \frac{Et}{8A_{123}(1+\nu)} &= 1.5712 \times 10^4 \text{lbs/in}^3, \end{aligned}$$

since the driver bar is 2 in. thick. Using Equations 5.6 - 5.8, the spring constants for triangle A, as shown in Figure 5-4, are determined and are given in Table 5.4. The stiffnesses for triangle B and triangle C are computed in a similar manner and are also given in Table 5.4.

Translating these spring constants into the notation of the shaker-slip table assembly (see Figure 5-4) and assembling the three individual triangles according to the method specified in Section 2.2.3 gives the stiffnesses shown in Table 5.5. The superscripts (db) indicate that these are the stiffnesses of the driver bar. As with the slip table, these values are for the driver bar when nothing is attached to it.

Fixture The fixture is illustrated in Figure 5-5. It is divided into four triangles, A, B, C, and D, whose stiffness properties are determined using the methods outlined

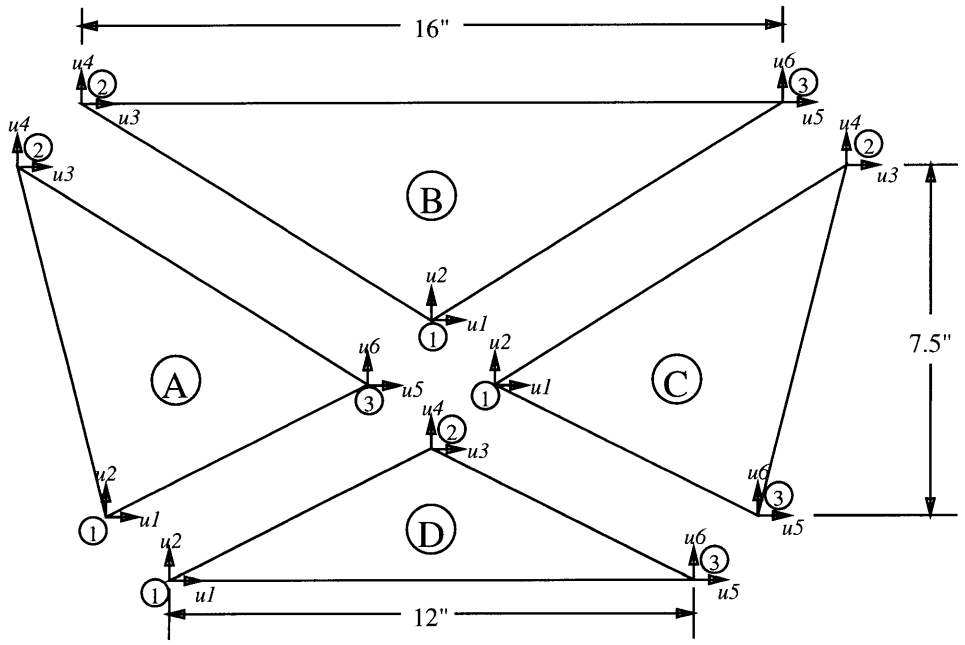

Figure 5-5: Fixture

for the driver bar. The fixture, made of magnesium, has a Young's modulus of 6.5 Msi and a Poisson's ratio of 0.35. The average thickness for the fixture is approximately 4.8 in. This gives the spring constants listed in Table 5.6, for Triangles A, B, C, and D.

Assembling the spring constants according to the methods outlined in Section 2.2.3 and changing notation to that of the shaker-slip table assembly provides the stiffnesses for the fixture as listed in Table 5.7. The fx superscripts indicate that these are the

Table 5.6: Fixture Discrete Element Stiffnesses

Triangle A			Triangle B		
k_{42}^A	=	2.6513×10^9N/m	k_{42}^B	=	5.8246×10^9N/m
k_{62}^A	=	1.6130×10^9N/m	k_{62}^B	=	5.8246×10^9N/m
k_{64}^A	=	-2.5580×10^8N/m	k_{64}^B	=	-2.6389×10^9N/m
Triangle C			Triangle D		
k_{42}^C	=	-2.5580×10^8N/m	k_{42}^D	=	5.8702×10^9N/m
k_{62}^C	=	1.6130×10^9N/m	k_{62}^D	=	-2.6638×10^9N/m
k_{64}^C	=	2.6513×10^9N/m	k_{64}^D	=	5.8702×10^9N/m

Table 5.7: Fixture Stiffnesses

Fixture Stiffness	Equivalent Discrete Element Stiffness	Stiffness Value
$\underline{k}^{fx}_{CG}, \underline{k}^{fx}_{DH}$	k^A_{42}, k^C_{64}	2.6513×10^9N/m
$\underline{k}^{fx}_{CL}, \underline{k}^{fx}_{DL}$	$k^A_{62} + k^D_{42}, k^C_{62} + k^D_{64}$	7.4832×10^9N/m
$\underline{k}^{fx}_{LG}, \underline{k}^{fx}_{LH}$	$k^A_{64} + k^B_{42}, k^B_{62} + k^C_{42}$	5.5688×10^9N/m
$\underline{k}^{fx}_{DC}$	k^D_{62}	-2.6638×10^8N/m
$\underline{k}^{fx}_{HG}$	k^B_{64}	-2.6389×10^8N/m

Table 5.8: Shaker-Fixture: Discrete Element Stiffnesses

Triangle A			Triangle B		
k^A_{42}	=	2.2399×10^{10}N/m	k^B_{42}	=	4.5028×10^{10}N/m
k^A_{62}	=	1.5744×10^9N/m	k^B_{62}	=	4.5028×10^{10}N/m
k^A_{64}	=	-1.1626×10^9N/m	k^B_{64}	=	-2.2432×10^{10}N/m
Triangle C			Triangle D		
k^C_{42}	=	-1.1626×10^9N/m	k^D_{42}	=	4.4872×10^{10}N/m
k^C_{62}	=	1.5744×10^9N/m	k^D_{62}	=	-2.2353×10^{10}N/m
k^C_{64}	=	2.2399×10^{10}N/m	k^D_{64}	=	4.4872×10^{10}N/m

fixture stiffnesses. As with the driver bar and the slip table, these values are for the fixture alone. They do not represent the fixture stiffnesses when the fixture is attached to the other components of the shaker-slip table assembly.

Shaker-Fixture The shaker-fixture interface is also divided into four triangles, A, B, C, and D, whose stiffness properties are determined using matrix structural analysis (same figure as Figure 5-5 except top width = 17″, bottom width = 16″, height = 1.75″). Both the shaker armature and the fixture are made of magnesium; hence the Young's modulus is 6.5 Msi, and Poisson's ratio is 0.35. The average thickness of material at the point of connection of the two pieces (and separating the accelerometers) is approximately 7.34 in. Thus, the stiffnesses for the four triangles are found and are given in Table 5.8.

Assembling the spring constants gives the stiffnesses for the shaker-fixture interface, as listed in Table 5.9. The sf superscripts indicate that these are the shaker-

Table 5.9: Shaker-Fixture Stiffnesses

Shaker-Fixture Stiffness	Equivalent Discrete Element Stiffness	Stiffness Value
$\underline{k}^{sf}_{GA}, \underline{k}^{sf}_{HB}$	k^A_{42}, k^C_{64}	2.2399×10^{10}N/m
$\underline{k}^{sf}_{GK}, \underline{k}^{sf}_{HK}$	$k^A_{62} + k^D_{42}, k^C_{62} + k^D_{64}$	4.6446×10^{10}N/m
$\underline{k}^{sf}_{KA}, \underline{k}^{sf}_{KB}$	$k^A_{64} + k^B_{42}, k^B_{62} + k^C_{42}$	4.3865×10^{10}N/m
$\underline{k}^{sf}_{HG}$	k^D_{62}	-2.2353×10^{10}N/m
$\underline{k}^{sf}_{BA}$	k^B_{64}	-2.2432×10^{10}N/m

fixture stiffnesses. As before, these values are for the shaker-fixture interface alone, and do not represent its stiffnesses when attached to the fixture.

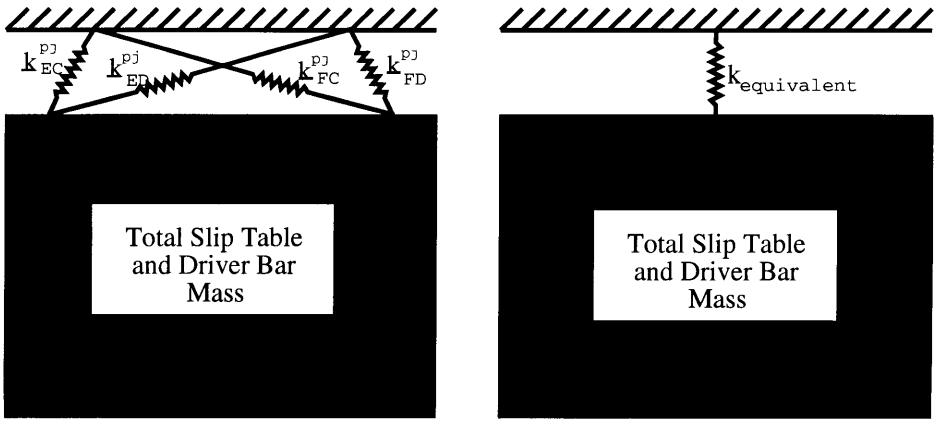

Figure 5-6: Single-Degree-of-Freedom Model of Fixture-Driver Bar Interface

Pin Joint The fixture and the driver bar portion of the slip table are connected via a pin joint. Because such an interface is not very rigid, it cannot be modelled using the aforementioned matrix structural analysis methods. The stiffnesses of the springs in this interface are instead calculated using the experimental data. A single-degree-of-freedom system, illustrated in Figure 5-6, is used to approximate the fixture-driver bar interface. (Using such a system model assumes that the total response of the system is dominated by the contribution of the mode whose natural frequency is closest at any given time, and requires that the structure not be too heavily or too lightly damped). Using the equation for the natural frequency of a single-degree-of freedom system [13]:

$$\omega_n = \sqrt{k/m}, \tag{5.9}$$

the stiffnesses of the interface are determined. The frequency used is that of the notch in the transfer function relating the vibrations at points C and D to the control point, 8. (Note: Because of symmetry in the shaker-table system, the transfer functions relating C to 8 and D to 8 are the same). The notch frequency (~380 Hz or 2405 rad/sec) is that at which the masses at C and D are still, while the masses outboard of them vibrate. Therefore, the total mass used in Equation 5.9 is the sum of the table mass (177 kg) and the driver bar mass (5.24 kg). Thus,

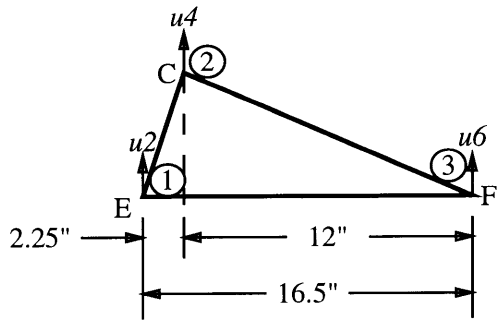

Figure 5-7: Triangular Element in Fixture-Driver Bar Interface

$$k = \omega^2 m = 1.0541 \times 10^9 \text{N/m}.$$

This value represents the total stiffness of the joint, spread among the four springs: $\underline{k}_{EC}^{pj}$, $\underline{k}_{ED}^{pj}$, $\underline{k}_{FC}^{pj}$, and $\underline{k}_{FC}^{pj}$ as shown in Figure 5-6 (where the superscript pj indicates that these are the stiffnesses of the pin joint). By symmetry, $\underline{k}_{EC}^{pj} = \underline{k}_{FD}^{pj}$ and $\underline{k}_{ED}^{pj} = \underline{k}_{FC}^{pj}$. In addition, using the matrix structural analysis theory of Section 2.2.3, it is evident that $\underline{k}_{EC}^{pj}$ and $\underline{k}_{FD}^{pj}$ must be greater than $\underline{k}_{ED}^{pj}$ and $\underline{k}_{FC}^{pj}$. The ratio of their stiffnesses is determined using a basic triangular element, as illustrated in Figure 5-7. For this element, the ratio of $\underline{k}_{EC}^{pj}$ to $\underline{k}_{FC}^{pj}$ is attained:

$$\frac{\underline{k}_{EC}^{pj}}{\underline{k}_{FC}^{pj}} \simeq \frac{k_{42}}{k_{64}}. \tag{5.10}$$

Combining Equations 2.53, 2.54, and 2.55, noting that $y_{ij} \simeq 0$, and canceling constant terms gives

$$\frac{k_{42}}{k_{64}} \simeq \frac{-x_{32}x_{31}}{-x_{31}x_{21}} = \frac{-14.25 \times 16.5}{-16.5 \times 2.25} = 6.3\,. \tag{5.11}$$

Therefore, the total stiffness is:

$$k \;=\; \underline{k}_{EC}^{pj} + \underline{k}_{FC}^{pj} + \underline{k}_{ED}^{pj} + \underline{k}_{FC}^{pj}$$

$$
\begin{aligned}
&= 2\underline{k}_{EC}^{pj} + 2(1/6.33)(\underline{k}_{EC}^{pj}) \\
&= 1.0541 \times 10^9 \text{N/m},
\end{aligned}
$$

and

$$
\begin{aligned}
\underline{k}_{EC}^{pj} &= \underline{k}_{FD}^{pj} = 4.5514 \times 10^8 \text{N/m} \\
\underline{k}_{FC}^{pj} &= \underline{k}_{ED}^{pj} = 7.1903 \times 10^7 \text{N/m}.
\end{aligned}
$$

Because the actual system is not a single-degree-of-freedom mass-spring system, these numbers do not work too well. Hence, they are refined using an iterative technique. The analytically generated transfer functions found using the theoretical model are compared with those attained experimentally (see results in Chapter 6 for x-axis tests with no mass attached). The stiffnesses are then changed according to the ratio of the square of the desired node frequency to that attained using the model,

$$
\frac{(\omega_{model})^2}{(\omega_{experiment})^2} = \frac{k_{model}}{k_{experiment}}, \tag{5.12}
$$

where the frequencies, ω_{model} and $\omega_{experiment}$, are the frequencies of the first notch in the transfer functions relating C and D to 8. The same ratio is used to change both stiffnesses. This process results in the following spring constants for the interface:

$$
\begin{aligned}
\underline{k}_{EC}^{pj} &= \underline{k}_{FD}^{pj} = 9.4610 \times 10^8 \text{N/m} \\
\underline{k}_{FC}^{pj} &= \underline{k}_{ED}^{pj} = 1.4946 \times 10^8 \text{N/m}.
\end{aligned}
$$

Assembling

Assembling the spring constants for the entire shaker-slip table assembly gives the complete stiffness properties for the model. These are given in Table 5.10. Again, the superscripts indicate which components the stiffnesses came from: st = slip table,

Table 5.10: Stiffnesses for The Shaker-Slip Table Assembly

Shaker-Slip Table Stiffnesses	Equivalent Stiffness	Stiffness Value
$\underline{k}_{41}, \underline{k}_{63}, \underline{k}_{74}, \underline{k}_{96}$	$\underline{k}^{st}_{41}, \underline{k}^{st}_{63}, \underline{k}^{st}_{74}, \underline{k}^{st}_{96}$	8.1234×10^8N/m
$\underline{k}_{52}, \underline{k}_{85}$	$\underline{k}^{st}_{52}, \underline{k}^{st}_{85}$	1.6247×10^9N/m
$\underline{k}_{42}, \underline{k}_{51}, \underline{k}_{53}, \underline{k}_{62}, \underline{k}_{75}, \underline{k}_{84}, \underline{k}_{86}, \underline{k}_{95}$	$\underline{k}^{st}_{42}, \underline{k}^{st}_{51}, \underline{k}^{st}_{53}, \underline{k}^{st}_{62}, \underline{k}^{st}_{75}, \underline{k}^{st}_{84}, \underline{k}^{st}_{86}, \underline{k}^{st}_{95}$	6.4261×10^8N/m
$\underline{k}_{21}, \underline{k}_{32}$	$\underline{k}^{st}_{21} + \underline{k}^{db}_{21}, \underline{k}^{st}_{32} + \underline{k}^{db}_{32}$	-1.0550×10^9N/m
$\underline{k}_{54}, \underline{k}_{65}$	$\underline{k}^{st}_{54}, \underline{k}^{st}_{65}$	-3.3948×10^8N/m
$\underline{k}_{87}, \underline{k}_{98}$	$\underline{k}^{st}_{87}, \underline{k}^{st}_{98}$	-1.6974×10^8N/m
$\underline{k}_{BA}$	$\underline{k}^{sf}_{BA}$	-2.2432×10^{10}N/m
$\underline{k}_{GA}, \underline{k}_{HB}$	$\underline{k}^{sf}_{GA}, \underline{k}^{sf}_{HB}$	2.2399×10^{10}N/m
$\underline{k}_{KA}, \underline{k}_{KB}$	$\underline{k}^{sf}_{KA}, \underline{k}^{sf}_{KB}$	4.3865×10^{10}N/m
$\underline{k}_{GK}, \underline{k}_{HK}$	$\underline{k}^{sf}_{GK}, \underline{k}^{sf}_{HK}$	4.6446×10^{10}N/m
$\underline{k}_{HG}$	$\underline{k}^{sf}_{HG} + \underline{k}^{fx}_{HG}$	-2.4992×10^{10}N/m
$\underline{k}_{CG}, \underline{k}_{DH}$	$\underline{k}^{fx}_{CD}, \underline{k}^{fx}_{DH}$	2.6513×10^9N/m
$\underline{k}_{LG}, \underline{k}_{LH}$	$\underline{k}^{fx}_{LG}, \underline{k}^{fx}_{LH}$	5.5688×10^9N/m
$\underline{k}_{CL}, \underline{k}_{DL}$	$\underline{k}^{fx}_{CL}, \underline{k}^{fx}_{DL}$	7.4832×10^9N/m
$\underline{k}_{DC}$	$\underline{k}^{fx}_{DC}$	-2.6638×10^9N/m
$\underline{k}_{EC}, \underline{k}_{FD}$	$\underline{k}^{pj}_{EC}, \underline{k}^{pj}_{FD}$	9.4610×10^8N/m
$\underline{k}_{ED}, \underline{k}_{FC}$	$\underline{k}^{pj}_{ED}, \underline{k}^{pj}_{FC}$	1.4946×10^8N/m
$\underline{k}_{FE}$	$\underline{k}^{db}_{FE}$	-6.2115×10^8N/m
$\underline{k}_{1E}, \underline{k}_{3F}$	$\underline{k}^{db}_{1E}, \underline{k}^{db}_{3F}$	1.5878×10^9N/m
$\underline{k}_{2E}, \underline{k}_{2F}$	$\underline{k}^{db}_{2E}, \underline{k}^{db}_{2F}$	4.3688×10^9N/m

db = driver bar, pj = pin-joint, fx = fixture, and sf = shaker-fixture.

5.2.3 Damping

The damping coefficients, $\boldsymbol{c}$, of the shaker-slip table assembly are determined in a similar manner to that used in the determination of the spring constants for the pin joint interface. To first order, a single-degree-of-freedom system can be used to approximate the damping coefficients. The equation for the damping coefficient of a single-degree-of freedom system is [13]

$$c = 2\zeta m\omega_n. \tag{5.13}$$

The damping factors, ζ, are estimated using the half power bandwidth of the frequency responses. The half power bandwidth is the frequency bandwidth, $\Delta\omega$, of the mode at $1/\sqrt{2}$ of its peak amplitude [13]. For lightly damped systems, the half power

bandwidth calculation for a force excited system is given by:

$$\frac{\Delta\omega}{\omega_n} \simeq 2\zeta. \tag{5.14}$$

Using this equation and the experimentally attained data (data presented in Chapter 6 for x-axis tests with no mass attached), the damping factors are approximated for the shaker-slip table system. The frequencies used are those of the first node in the experimentally attained transfer functions relating the motion of a given point to that at the control accelerometer. Frequencies and half power bandwidths are graphically extracted from the data. The average damping factor for all channels is estimated to be $\zeta = .01$ for the first notch. This value is used for all of the damping coefficient calculations. Note that the modal damping of the first node is used to describe the damping of all of the modes.

Using Equation 5.13, the damping coefficients are determined for the shaker-slip table assembly. Between each set of adjacent points, the frequency, ω_n, is taken from the experimentally attained transfer function between the two points (as with the pin-joint spring constant determinations), and the mass is taken to be the total mass outboard of the connection (again, as with the pin-joint example). In cases where more than one connection contributes to the same resonant frequency (as was the case at the pin joint), the contributions of each connection to the damping are taken to be proportional to the contribution of each to the stiffness. The experimental data used is that of the x-axis tests with no attached test objects and control at accelerometer 8. The resulting damping coefficients are given in Table 5.11. These coefficients are underlined for consistency in designating the properties of the shaker-slip table assembly.

5.3 Linear Matlab Model

Using the system properties determined in Section 5.2, a closed form solution to the equations of motion of the shaker-slip table assembly is found. Such a solution provides a supplement and check for the data attained using the explicit time simulation

model. The eigenvalues and corresponding eigenvectors of the system are found using Matlab, thus providing the resonant frequencies and mode shapes of the shaker-slip table assembly. The equations of motion are solved in the undamped, unforced case since the natural frequencies and mode shapes are not dependent upon damping or forcing function. In this case,

$$\boldsymbol{m}\ddot{\boldsymbol{x}} + \boldsymbol{k}\boldsymbol{x} = 0. \tag{5.15}$$

The mass matrix is the diagonal matrix consisting of all of the lumped masses and its components are given in Table 5.12. The subscripts of the masses in the first column indicate the location within the matrix (row-column). All m_{i-j} for $i \neq j$ are zero and are not listed in the table. As a reminder, the underlined terms are the actual system masses determined in Section 5.2. The stiffness matrix is found by writing out the equations of motion, and its members are listed in Tables 5.13 and 5.14. Table 5.13 contains the diaganol terms of the matrix, and Table 5.14 contains the off-diaganol terms. All stiffnesses not listed in the tables are equal to zero.

The eigenvalues and eigenvectors of the system are found from the matrix $\boldsymbol{m}^{-1}\boldsymbol{k}$, using the Matlab module *eig.m*. One important difference between this Matlab model and the actual shaker-slip table system is that the Matlab model is not constrained at the shaker. This lack of constraint is chosen since the exact boundary condition at the

Table 5.11: Damping Coefficients for the Shaker-Slip Table Assembly

$\underline{c}_{41}, \underline{c}_{63}, \underline{c}_{74}, \underline{c}_{96}$	=	2409kg/s	$\underline{c}_{HG}$	=	317kg/s
$\underline{c}_{52}, \underline{c}_{85}$	=	1673kg/s	$\underline{c}_{CG}, \underline{c}_{DH}$	=	7926kg/s
$\underline{c}_{42}, \underline{c}_{62}, \underline{c}_{84}, \underline{c}_{86}$	=	1339kg/s	$\underline{c}_{LG}, \underline{c}_{LH}$	=	1110kg/s
$\underline{c}_{21}, \underline{c}_{32}, \underline{c}_{87}, \underline{c}_{98}$	=	229kg/s	$\underline{c}_{CL}, \underline{c}_{DL}$	=	1110kg/s
$\underline{c}_{54}, \underline{c}_{65}$	=	335kg/s	$\underline{c}_{DC}$	=	317kg/s
$\underline{c}_{51}, \underline{c}_{53}, \underline{c}_{75}, \underline{c}_{95}$	=	1927kg/s	$\underline{c}_{EC}, \underline{c}_{FD}$	=	5457kg/s
$\underline{c}_{BA}$	=	325kg/s	$\underline{c}_{ED}, \underline{c}_{FC}$	=	873kg/s
$\underline{c}_{GA}, \underline{c}_{HB}$	=	10840kg/s	$\underline{c}_{FE}$	=	764kg/s
$\underline{c}_{KA}, \underline{c}_{KB}$	=	325kg/s	$\underline{c}_{1E}, \underline{c}_{3F}$	=	2442kg/s
$\underline{c}_{GK}, \underline{c}_{HK}$	=	325kg/s	$\underline{c}_{2E}, \underline{c}_{2F}$	=	4284kg/s

Table 5.12: Masses for the Matlab Model

m_{1-1}	=	$\underline{m}_1$	= 11.7 kg	m_{11-11}	=	$\underline{m}_B$	= 7.2 kg
m_{2-2}	=	$\underline{m}_2$	= 24.0 kg	m_{12-12}	=	$\underline{m}_G$	= 10.6 kg
m_{3-3}	=	$\underline{m}_3$	= 11.7 kg	m_{13-13}	=	$\underline{m}_H$	= 10.6 kg
m_{4-4}	=	$\underline{m}_4$	= 22.2 kg	m_{14-14}	=	$\underline{m}_C$	= 3.4 kg
m_{5-5}	=	$\underline{m}_5$	= 44.4 kg	m_{15-15}	=	$\underline{m}_D$	= 3.4 kg
m_{6-6}	=	$\underline{m}_6$	= 22.2 kg	m_{16-16}	=	$\underline{m}_E$	= 1.2 kg
m_{7-7}	=	$\underline{m}_7$	= 11.1 kg	m_{17-17}	=	$\underline{m}_F$	= 1.2 kg
m_{8-8}	=	$\underline{m}_8$	= 22.2 kg	m_{18-18}	=	$\underline{m}_K$	= 14.4 kg
m_{9-9}	=	$\underline{m}_9$	= 11.1 kg	m_{19-19}	=	$\underline{m}_L$	= 6.8 kg
m_{10-10}	=	$\underline{m}_A$	= 7.2 kg				

shaker is difficult to define. Since the Matlab model is primarily meant to generate the mode shapes of the system, this difference in boundary conditions should not have a great effect. Some modes which can not physically occur in the physical system will be generated, but these are disregarded.

5.4 Explicit Time Simulation Model

5.4.1 Overview

A fourth-order Runge-Kutta algorithm, with adaptive step size control, is used to solve the equations of motion of the shaker-slip table assembly. Equal excitation is provided to nodes A and B (the shaker) by a random white noise drive signal which is updated over time to achieve the desired control spectrum. This implementation of a control loop (same as that found in the control anlayzer of the experiment) allows nonlinear system problems to be simulated. The model is coded in Fortran and run on a DECstation 5000 (The complete Fortran code can be found in Appendix A). It consists of a driver routine and nine subroutines: *odeint*, *rkqc*, *rk4*, *derivs*, *input*, *interpolate*, *fft*, *spectrum*, and *filter*. These routines are taken in part from [15].

The driver routine acts as a user interface, starting and stopping all processes. The subroutine *odeint* is a secondary driver routine, responsible for calling the Runge-Kutta algorithms, implementing the control loop, and storing all data; *rkqc* is respon-

Table 5.13: Stiffnesses for the Matlab Model–Diaganol Matrix Terms

k_{1-1}	=	$\underline{k}_{1E} + \underline{k}_{21} + \underline{k}_{51} + \underline{k}_{41}$	=	1.9877×10^9 N/m
k_{2-2}	=	$\underline{k}_{21} + \underline{k}_{42} + \underline{k}_{52} + \underline{k}_{62} + \underline{k}_{32} + \underline{k}_{2F} + \underline{k}_{2E}$	=	9.5375×10^9 N/m
k_{3-3}	=	$\underline{k}_{3F} + \underline{k}_{32} + \underline{k}_{53} + \underline{k}_{63}$	=	1.9877×10^9 N/m
k_{4-4}	=	$\underline{k}_{41} + \underline{k}_{42} + \underline{k}_{54} + \underline{k}_{84} + \underline{k}_{74}$	=	2.5704×10^9 N/m
k_{5-5}	=	$\underline{k}_{51} + \underline{k}_{52} + \underline{k}_{53} + \underline{k}_{65} + \underline{k}_{95} + \underline{k}_{85} + \underline{k}_{75} + \underline{k}_{54}$	=	5.1409×10^9 N/m
k_{6-6}	=	$\underline{k}_{63} + \underline{k}_{96} + \underline{k}_{86} + \underline{k}_{65} + \underline{k}_{62}$	=	2.5704×10^9 N/m
k_{7-7}	=	$\underline{k}_{74} + \underline{k}_{75} + \underline{k}_{87}$	=	1.2852×10^9 N/m
k_{8-8}	=	$\underline{k}_{87} + \underline{k}_{84} + \underline{k}_{85} + \underline{k}_{86} + \underline{k}_{98}$	=	2.5704×10^9 N/m
k_{9-9}	=	$\underline{k}_{96} + \underline{k}_{95} + \underline{k}_{98}$	=	1.2852×10^9 N/m
k_{10-10}	=	$\underline{k}_{BA} + \underline{k}_{KA} + \underline{k}_{GA}$	=	4.3652×10^{10} N/m
k_{11-11}	=	$\underline{k}_{BA} + \underline{k}_{KB} + \underline{k}_{HB}$	=	4.3652×10^{10} N/m
k_{12-12}	=	$\underline{k}_{GA} + \underline{k}_{GK} + \underline{k}_{HG} + \underline{k}_{LG} + \underline{k}_{CG}$	=	5.2073×10^{10} N/m
k_{13-13}	=	$\underline{k}_{HB} + \underline{k}_{HK} + \underline{k}_{HG} + \underline{k}_{LH} + \underline{k}_{DH}$	=	5.2073×10^{10} N/m
k_{14-14}	=	$\underline{k}_{CG} + \underline{k}_{CL} + \underline{k}_{DC} + \underline{k}_{FC} + \underline{k}_{EC}$	=	8.5663×10^9 N/m
k_{15-15}	=	$\underline{k}_{DH} + \underline{k}_{DL} + \underline{k}_{DC} + \underline{k}_{ED} + \underline{k}_{FD}$	=	8.5663×10^9 N/m
k_{16-16}	=	$\underline{k}_{1E} + \underline{k}_{2E} + \underline{k}_{FE} + \underline{k}_{DE} + \underline{k}_{EC}$	=	6.4310×10^9 N/m
k_{17-17}	=	$\underline{k}_{2F} + \underline{k}_{3F} + \underline{k}_{FE} + \underline{k}_{FC} + \underline{k}_{FD}$	=	6.4310×10^9 N/m
k_{18-18}	=	$\underline{k}_{KA} + \underline{k}_{GK} + \underline{k}_{HK} + \underline{k}_{KB}$	=	1.8026×10^{11} N/m
k_{19-19}	=	$\underline{k}_{LG} + \underline{k}_{LH} + \underline{k}_{DL} + \underline{k}_{CL}$	=	2.6104×10^{10} N/m

sible for maintaining a suitable step size for the Runge-Kutta routine; *rk4* implements the basic Runge-Kutta formulas described in Section 2.2.2; *derivs* houses all of the system parameters and the equations of motion; *input* interpolates the drive signal for any given time value; *interpolate* interpolates the output time signals to evenly spaced intervals; *fft* uses the fast Fourier transform algorithm of Section 2.2.4 to transform data signals between the time and frequency domains; *spectrum* calculates the auto-spectral density of the signals involved in the drive update using the method outlined in Section 2.2.5; and *filter* applies a butterworth filter to the updated drive signal before it is input into the shaker-slip table system.

5.4.2 Solution of Differential Equations

The equations of motion for the system,

$$\boldsymbol{m}\ddot{\boldsymbol{x}} + \boldsymbol{c}\dot{\boldsymbol{x}} + \boldsymbol{k}\boldsymbol{x} = \boldsymbol{F}, \tag{5.16}$$

Table 5.14: Stiffnesses for the Matlab Model–Off-Diaganol Matrix Terms

$k_{1-2} = k_{2-1}$	=	$-\underline{k}_{21}$	=	1.0550×10^9 N/m
$k_{2-3} = k_{3-2}$	=	$-\underline{k}_{32}$	=	1.0550×10^9 N/m
$k_{4-5} = k_{5-4}$	=	$-\underline{k}_{54}$	=	3.3948×10^8 N/m
$k_{5-6} = k_{6-5}$	=	$-\underline{k}_{65}$	=	3.3948×10^8 N/m
$k_{7-8} = k_{8-7}$	=	$-\underline{k}_{87}$	=	1.6974×10^8 N/m
$k_{8-9} = k_{9-8}$	=	$-\underline{k}_{98}$	=	1.6974×10^8 N/m
$k_{10-11} = k_{11-10}$	=	$-\underline{k}_{BA}$	=	2.2432×10^{10} N/m
$k_{12-13} = k_{13-12}$	=	$-\underline{k}_{HG}$	=	2.4992×10^{10} N/m
$k_{14-15} = k_{15-14}$	=	$-\underline{k}_{DC}$	=	2.6638×10^9 N/m
$k_{16-17} = k_{17-16}$	=	$-\underline{k}_{FE}$	=	6.2115×10^8 N/m
$k_{1-4} = k_{4-1}$	=	$-\underline{k}_{41}$	=	-8.1234×10^8 N/m
$k_{2-5} = k_{5-2}$	=	$-\underline{k}_{52}$	=	-1.6247×10^9 N/m
$k_{3-6} = k_{6-3}$	=	$-\underline{k}_{63}$	=	-8.1234×10^8 N/m
$k_{4-7} = k_{7-4}$	=	$-\underline{k}_{74}$	=	-8.1234×10^8 N/m
$k_{5-8} = k_{8-5}$	=	$-\underline{k}_{85}$	=	-1.6247×10^9 N/m
$k_{6-9} = k_{9-6}$	=	$-\underline{k}_{96}$	=	-8.1234×10^8 N/m
$k_{1-16} = k_{16-1}$	=	$-\underline{k}_{1E}$	=	-1.5878×10^9 N/m
$k_{2-16} = k_{16-2}$	=	$-\underline{k}_{2E}$	=	-4.3688×10^9 N/m
$k_{2-17} = k_{17-2}$	=	$-\underline{k}_{2F}$	=	-4.3688×10^9 N/m
$k_{3-17} = k_{17-3}$	=	$-\underline{k}_{3F}$	=	-1.5878×10^9 N/m
$k_{14-16} = k_{16-14}$	=	$-\underline{k}_{EC}$	=	-9.4610×10^8 N/m
$k_{15-17} = k_{17-15}$	=	$-\underline{k}_{FD}$	=	-9.4610×10^8 N/m
$k_{12-14} = k_{14-12}$	=	$-\underline{k}_{CG}$	=	-2.6513×10^9 N/m
$k_{13-15} = k_{15-13}$	=	$-\underline{k}_{DH}$	=	-2.6513×10^9 N/m
$k_{10-12} = k_{12-10}$	=	$-\underline{k}_{GA}$	=	-2.2399×10^{10} N/m
$k_{11-13} = k_{13-11}$	=	$-\underline{k}_{HB}$	=	-2.2399×10^{10} N/m
$k_{2-4} = k_{4-2}$	=	$-\underline{k}_{42}$	=	-6.4261×10^8 N/m
$k_{1-5} = k_{5-1}$	=	$-\underline{k}_{51}$	=	-6.4261×10^8 N/m
$k_{3-5} = k_{5-3}$	=	$-\underline{k}_{53}$	=	-6.4261×10^8 N/m
$k_{2-6} = k_{6-2}$	=	$-\underline{k}_{62}$	=	-6.4261×10^8 N/m
$k_{5-7} = k_{7-5}$	=	$-\underline{k}_{75}$	=	-6.4261×10^8 N/m
$k_{4-8} = k_{8-4}$	=	$-\underline{k}_{84}$	=	-6.4261×10^8 N/m
$k_{6-8} = k_{8-6}$	=	$-\underline{k}_{86}$	=	-6.4261×10^8 N/m
$k_{5-9} = k_{9-5}$	=	$-\underline{k}_{95}$	=	-6.4261×10^8 N/m
$k_{15-16} = k_{16-15}$	=	$-\underline{k}_{ED}$	=	-1.4946×10^8 N/m
$k_{14-17} = k_{17-14}$	=	$-\underline{k}_{FC}$	=	-1.4946×10^8 N/m
$k_{14-19} = k_{19-14}$	=	$-\underline{k}_{CL}$	=	-7.4832×10^9 N/m
$k_{15-19} = k_{19-15}$	=	$-\underline{k}_{DL}$	=	-7.4832×10^9 N/m
$k_{12-19} = k_{19-12}$	=	$-\underline{k}_{LG}$	=	-5.5688×10^9 N/m
$k_{13-19} = k_{19-13}$	=	$-\underline{k}_{LH}$	=	-5.5688×10^9 N/m
$k_{12-18} = k_{18-12}$	=	$-\underline{k}_{GK}$	=	-4.6446×10^{10} N/m
$k_{13-18} = k_{18-13}$	=	$-\underline{k}_{HK}$	=	-4.6446×10^{10} N/m
$k_{10-18} = k_{18-10}$	=	$-\underline{k}_{KA}$	=	-4.3685×10^{10} N/m
$k_{11-18} = k_{18-11}$	=	$-\underline{k}_{KB}$	=	-4.3685×10^{10} N/m

are reduced to first order differential equations, with one variable being the derivative of another. First, rearranging Equation 5.16, gives

$$\ddot{\boldsymbol{x}} = \boldsymbol{m}^{-1}\left[\boldsymbol{F} - \boldsymbol{c}\dot{\boldsymbol{x}} - \boldsymbol{k}\boldsymbol{x}\right] = f(\dot{\boldsymbol{x}}, \boldsymbol{x}, t), \tag{5.17}$$

where $f(\dot{\boldsymbol{x}}, \boldsymbol{x}, t)$ is some function of $\dot{\boldsymbol{x}}$, $\boldsymbol{x}$, and t. Defining

$$\boldsymbol{x}_1 = \boldsymbol{x} \tag{5.18}$$

$$\boldsymbol{x}_2 = \dot{\boldsymbol{x}} \tag{5.19}$$

$$\tag{5.20}$$

allows Equation 5.17 to be rewritten in terms of two first order differential equations:

$$\dot{\boldsymbol{x}}_1 = \boldsymbol{x}_2 \tag{5.21}$$

$$\dot{\boldsymbol{x}}_2 = f(\boldsymbol{x}_1, \boldsymbol{x}_2, t). \tag{5.22}$$

The equations of motion for the shaker-slip table assembly, written in this form, are housed in *derivs* and are solved using *rk4*, *rkqc*, and *odeint*. *rk4* implements the basic formulas of the Runge-Kutta method, each time advancing the solution over an interval h. *rkqc* calls *rk4* and determines whether or not its results are compatible with a predetermined accuracy criterion. *rkqc* uses the largest step size possible, thereby resulting in computational efficiency. *odeint* starts and stops the integration and stores results.

5.4.3 Drive Signal Update

The control loop described in Section 4.2.3 is implemented in the explicit time simulation model, using the subroutines *odeint*, *spectrum*, *fft*, and *filter*. A Matlab routine (given in Appendix B) provides the initial butterworth filtered, random, drive signal

(the reference spectrum of Section 4.2.3). The reference and control accelerometer (channel 8) signals are converted to spectra, for comparison in the frequency domain, using *spectrum* and *fft*. Calculation of the new drive signal is performed by *odeint*, using the update algorithm of Section 4.2.3. Random phase is added to the real PSD function using a random number generator, and the complex function is converted back to a real time signal via the inverse FFT algorithm *fft*. Finally, the new time domain drive signal is butterworth filtered, using *filter*, and sent to *input* where it is interpolated and sent to *derivs* for input into nodes A and B.

An important difference between the actual experimental process and that produced here is in the update time. Whereas there is a 3.4 second lag between the collection of the control accelerometer data and the update of the drive signal in the experimental procedure, the process is modelled as instantaneous in the simulation. Since measurements in both cases are not taken until the drive signal has stabilized, however, this discrepancy is not important. With the actual shaker-slip table assembly, drive level is gradually increased to allow the control loop compensation to be implemented gradually. Once the system is at full level and the control and drive signals have stabilized, experimental data is taken. In the case of the explicit time simulation model, control loop update is performed instantaneously, but even so, data is not taken until the control signal has stabilized (which typically takes a few update loops).

5.4.4 Signal Analysis Considerations

Care is taken (as in the experimental procedure) to avoid errors arising from improper signal analysis techniques. Aliasing is overcome by enforcing a known frequency limit using a butterworth filter and by sampling the signal at a rate considerably over the Nyquist frequency. As with the experimental analysis, Hanning windows are used to prevent leakage in the spectral domain.

5.4.5 Interpolation

Linear interpolation routines (*input* and *interpolate*) are used with the input and the output of the explicit time simulation model, as well as within it. The input and output to the system are discrete data sets with a constant time spacing. The explicit time simulation model, however, because of its adaptive step size routine, does not always use or produce data at a constant interval. Hence, linear interpolation routines are implemented to go between what the adaptive step size Runge-Kutta algorithm requires and what is required outside of it (i.e. in the control update loop or in the program output) for analysis purposes.

5.4.6 Additional Tests

Four mass tests are run, using the two different masses and two different test object locations of the experimental procedure. In the experiments, masses are bolted to the table, thereby locally stiffening the table while also contributing mass. Hence, attachment of a test object is modelled as a mass attached in parallel between the nodes, rather than only as additional mass at each of the closest nodes. The type of attachment used is illustrated in Figure 5-8. Figure 5-8 is labelled for the case of the mass attached between 5 and 8. The values for the stiffnesses $\underline{k}_{m5}$ and $\underline{k}_{m8}$ cannot be determined with precision, as the exact stiffness of the bolted attachment between the mass and the table is unknown. As a first approximation, because the attached mass is the same material and the same thickness as the table, the stiffnesses $\underline{k}_{m5}$ and $\underline{k}_{m8}$ are taken to be equal to $\underline{k}_{85}$. This choice is validated by comparison with experimental results (See Section 6.5.3).

Two models are designed to test the effect of changing the stiffness of the fixture-driver bar interface (the pin joint). These models indicate the extent to which table behavior varies with the quality of the interface attachment. The stiffnesses of the pin joint are altered by 20%. In one model, $\underline{k}_{ec}$, $\underline{k}_{fd}$, $\underline{k}_{ed}$, $\underline{k}_{fc}$ are reduced to 80% of their full values. In the other model, they are increased to 120% of their full values.

Finally, a model is designed to determine the effect of nonlinear motion at the

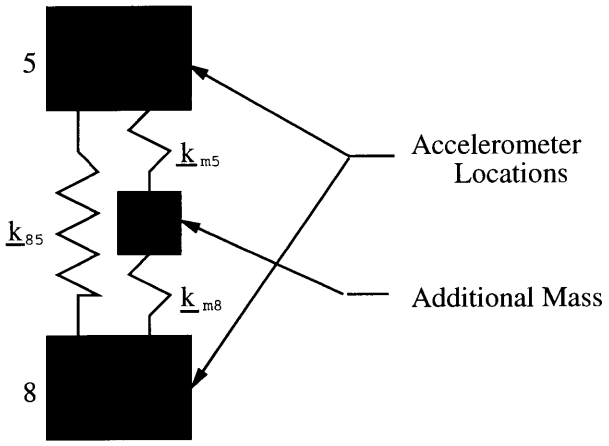

Figure 5-8: Mass Attachment in Theoretical Model

pin-joint. The load deflection curve shown in Figure 5-9 is used as a worst case description of the motion of the pin joint (assuming that the pin is loose in its housing) [21]. It includes a slipping motion with a low stiffness–one tenth the stiffness used in the previous calculations, followed by assumed pin contact with a stiffness equal to the one used previously. The curve is assumed to be reversible. Using the explicit time simulation model, without any modifications or test objects attached, the total deflection predicted at the pin joint is 2.454×10^{-8}m. Arbitrarily assuming that the slipping motion takes place for half of this deflection, and that the banging motion takes place for the other half, yields the deflection values shown in Figure 5-9. The results of these tests, and of all of the other model runs are presented in Chapter 6.

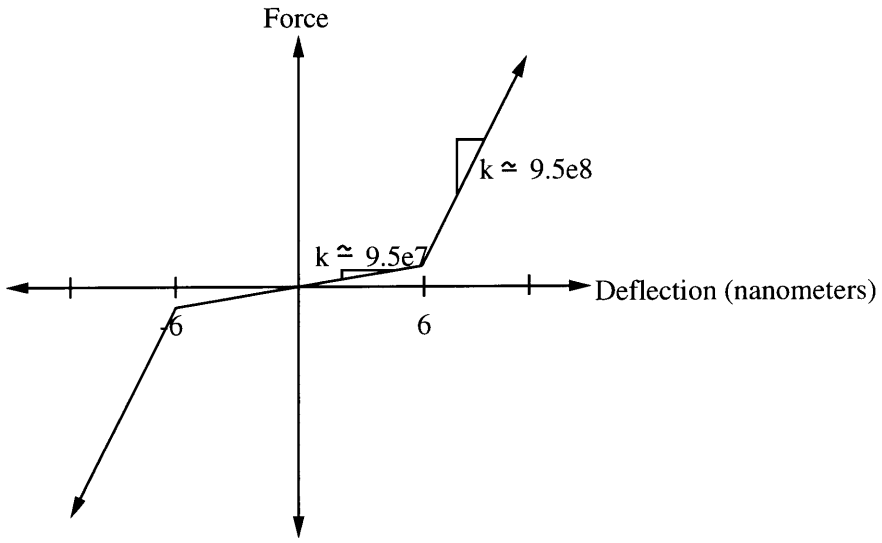

Figure 5-9: Pin-Joint Force Deflection Curve

Chapter 6

Results and Discussion

6.1 Introduction

In this chapter, experimentally attained and theoretically generated results characterizing the dynamic behavior of the slip table under various operating conditions are presented, compared and correlated. In addition, shaker-table behavior under operating conditions for which no experimental data was attained is predicted using the theoretical model.

6.2 Shaker-Slip Table Dynamic Behavior

6.2.1 Experimental Data

Some of the features of a typical experimentally attained transfer function are examined. Figure 6-1 shows the transfer function (attained for x-axis tests with no mass attached) relating the acceleration at accelerometer number 2 (see Figure 6-2 for a schematic showing accelerometer locations) to the motion of the control accelerometer (accelerometer number 8). Note that all results are presented in terms of acceleration transfer functions between a given accelerometer and the control accelerometer. A copy of all transfer functions can be found in Appendix C. The abscissa of the plots is frequency in Hz, and the ordinate shows the magnitude of the transfer function. A

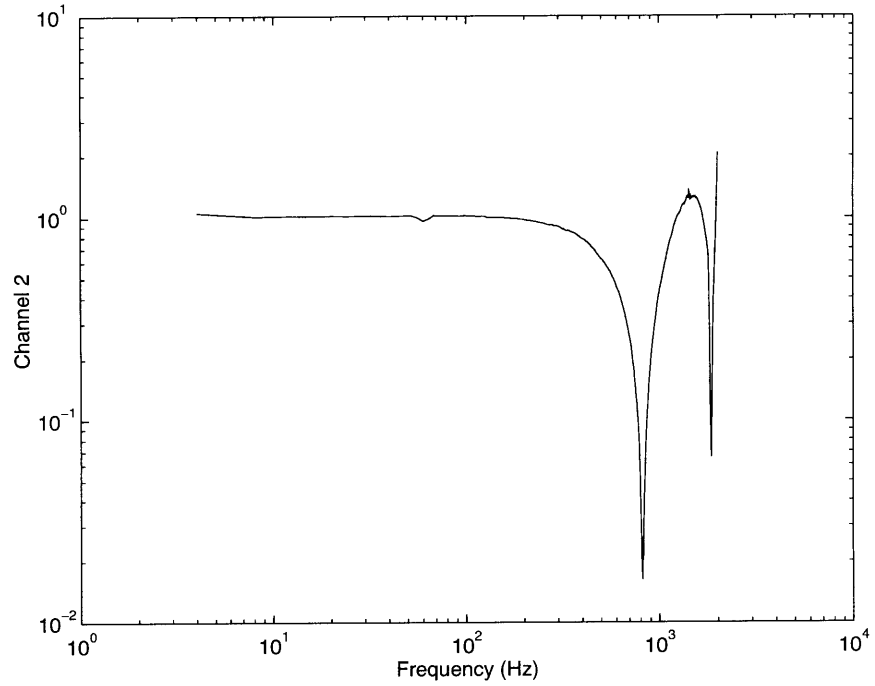

Figure 6-1: Transfer Function Relating Acceleration at 2 to that at 8

log scale is used for both axes, but the origin and scaling of the plots vary in order to emphasize different transfer function features.

Figure 6-1 shows the transfer function between 2 and 8. Note that the acceleration of 8 is controlled using the control spectrum of Figure 4-12, and is therefore white noise with a constant amplitude. The response at 2, however, is not white noise, but is more complex.

The transfer function data, as illustrated in Figure 6-1 for channel 2, is smooth, which incicates that good (rather noise free) data was acquired. Channel 2 shows no excited resonances of significant amplitude, due to the closed-loop control at channel 8. This means that no table modes causing a larger response at 2 than that experienced at 8 were excited in the frequency range tested. There is one minor exception near 1600 Hz, where the response at 2 is slightly larger than at the control accelerometer. In addition, there are two notches in the transfer function realting 2 to 8, which indicate two points at which the response at 2 is significantly less than that at 8.

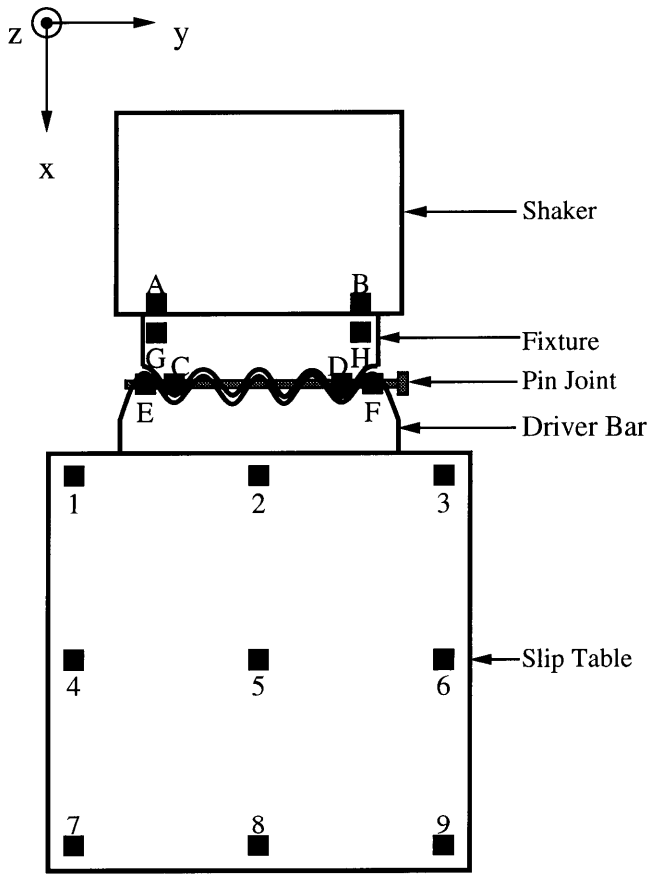

Figure 6-2: Analytical Model of the Shaker-Slip Table Assembly

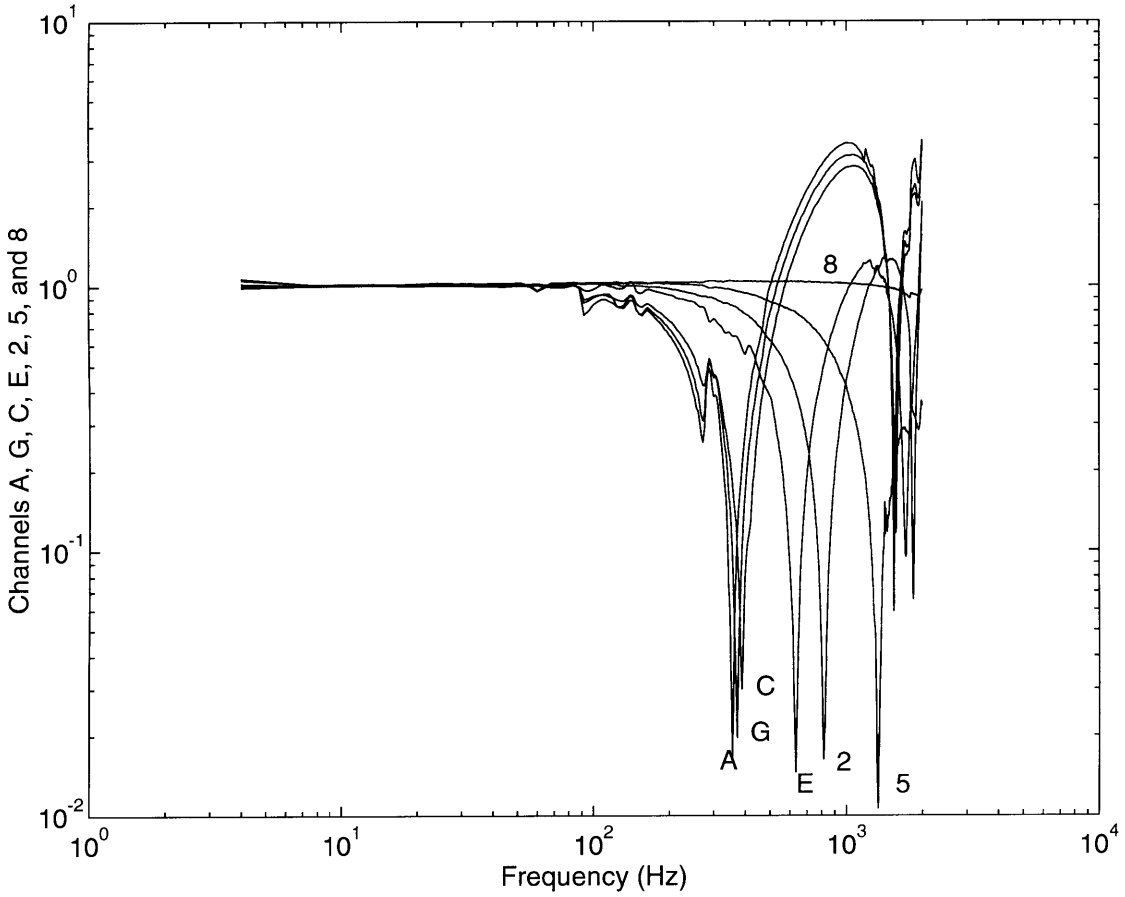

Figure 6-3: Node Frequency

6.2.2 Variation in Response with Location

Historically, optimal control in tests using slip tables has been attained only when test specimens and control accelerometers are located as far out on the table as possible–at a maximum distance from the shaker. The experimental data provides an understanding of why this occurs. Figure 6-3 shows the transfer functions for Channels A, G, C, E, 2, 5, and 8 with respect to the control channel, 8. These channels run along the length of the shaker-slip table assembly, with A located on the shaker armature and 8 located at the outboard (farthest from the shaker) edge of the slip table, as shown in Figure 6-2. The frequency of the first notch in the transfer functions increases when moving from accelerometer A to accelerometer 8.

Two important aspects of the data are that closed-loop control prevents resonant

peaks in the transfer function data and that elastic modes exist in the slip table and shaker-table interface. Accelerometer A, which is attached to the armature, shows the drive signal required to maintain a flat spectrum at channel 8. The first large notch in the transfer function for channel A is at the frequency of the first resonant mode of the shaker-slip table assembly. This notch at A restrains the resonant response at 8, which would otherwise be quite large. At a slightly higher frequency, the same notch appears in channels C and G. The frequency is almost the same, however, due to the rigid attachment between channels A, C, and G.

The first notch frequency at E, on the other hand, is quite different from that at A. E is located on the opposite side of the pin joint and participates in the first resonance of the table on the joint. The notch in channel E's transfer function indicates another resonant mode, in which channel E does not participate (i.e. there is a node at E). Note that there is a large amount of drive signal input at this frequency (i.e. no notch in channels A,C, and G) but that E remains still.

Transfer functions for channels 2 and 5 indicate similar behavior to that at E. The only difference is that the frequency of the modes where 2 and 5, respectively, remain stationary (are nodes) is higher.

6.2.3 Modal Behavior

Examining the complete transfer functions provides further insight into the modal behavior of the shaker-slip table assembly. The responses discussed above are part of a set of longitudinal modes. At ~370 Hz, the shaker (channel A) and fixture (channels G and C) remain stationary while everything outboard (the shaker and driver bar) oscillates. As the frequency increases, other modes are encountered. Near 720 Hz, the driver bar sits still while everything on either side vibrates (the shaker, fixture, and slip table); while around 820 Hz, the inboard point on the slip table (2) remains stationary while the rest of the table and the interface vibrates. Finally, near 1350 Hz, the center of the slip table is still, and all other masses vibrate.

Motion of the shaker-slip table assembly is fairly symmetric, as seen in Figure 6-4 and 6-5. Motion of the table center, however, differs from that of the table sides.

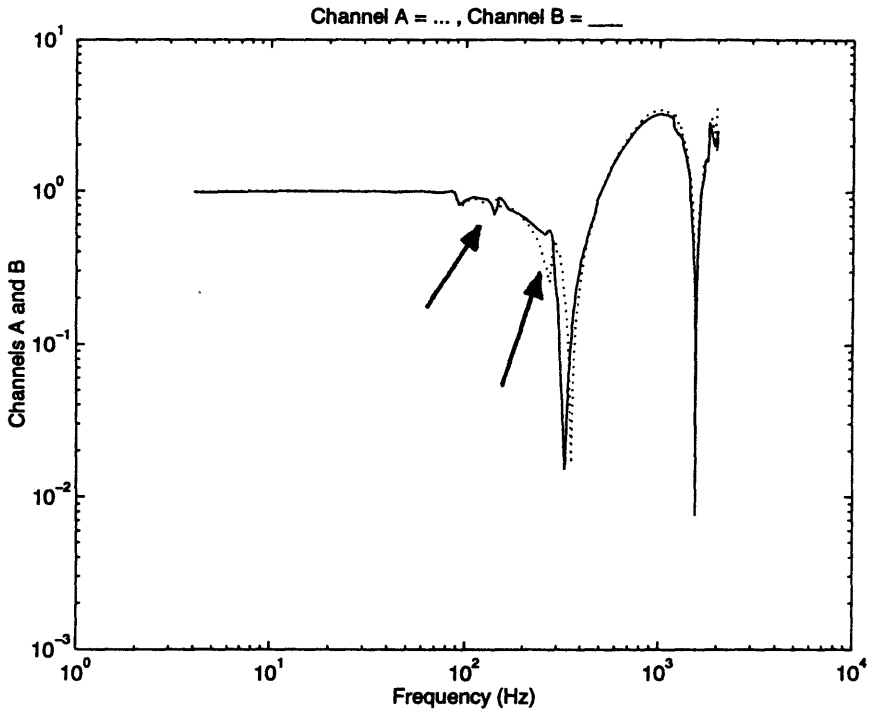

Figure 6-4: Side-to-Side Discrepancies in Shaker-Table Interface

These lateral variations are illustrated in Figures C-1 and C-2 (see Appendix C), where the side accelerometers (1, 3, 4, and 6) do not show the first notch present in the center channels (2 and 5). Near 1700 Hz, there is a second, reversed mode, where the side accelerometer channels show a notch not found in the center channels.

There is a rocking motion of the system (where the notches and peaks are reversed on the left and right sides of the shaker-slip table assembly) near 140 Hz and another near 275 Hz. These left-right discrepancies are present in the shaker armature and extend to the edge of the table. They are illustrated in Figures 6-4 and 6-5, for channels A and B and channels 7 and 9, respectively. The center nodes of the table do not participate in the rocking mode as is illustrated in Figure 6-3, where the motions at 2, 5, and 8 do not show any evidence of the rocking mode.

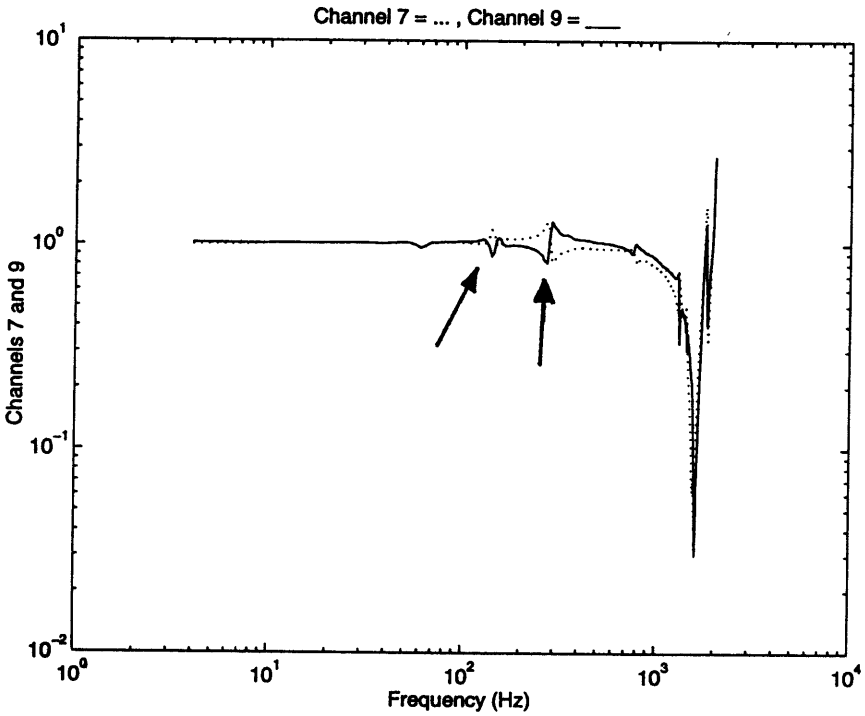

Figure 6-5: Side-to-Side Discrepancies in Slip Table

6.2.4 Pitch and Yaw

Experiments were run to measure motion along the y and z-axes. These tests were performed to verify the assumption that movements in the y and z-axes were negligible compared to those in the x-direction. This assumption was made in order to simplify the construction of the explicit time simulation model. Figures 6-6, 6-7, and 6-8 show the accelerations along the x, y, and z-axes for Channels 2, 8, and A, respectively. All transfer functions are taken with respect to the x-axis control accelerometer at 8 for consistency. The y and z-axis contributions are insignificant in all channels below $\sim$80 Hz. Above 80 Hz, the base-line levels of y and z-axis responses are about one and a half orders of magnitude smaller than those of the x-axis. There are, however, resonant peaks in the y and z-axes with peak magnitudes reaching 80% of x-axis vibration levels. Also, at noches in the x-axis transfer functions, the y and z-axis responses dominate the motion. Interesting to note is that large y and z-axis responses coincide with the frequencies of the x-axis rocking modes, as is illustrated in Figure 6-8. This is indicative of a problem with current test techniques where it is assumed that y and z-axis motions of the shaker-slip table assembly are negligible. In fact, it is clear that they are not. The implication of large y and z-axis responses will be further discussed in Section 6.4.3.

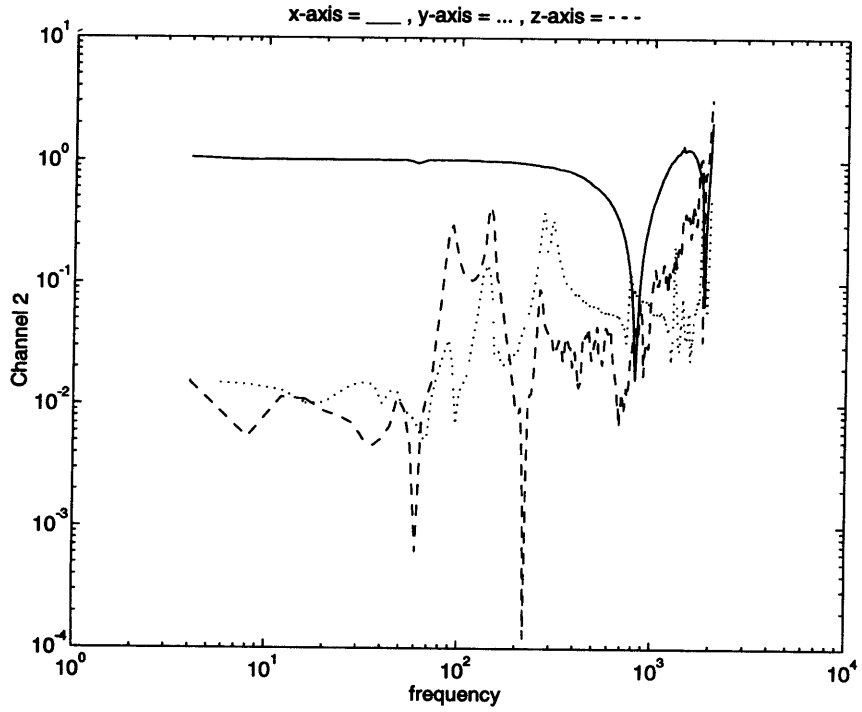

Figure 6-6: Channel 2 Vibrations in the X, Y, and Z-Axes

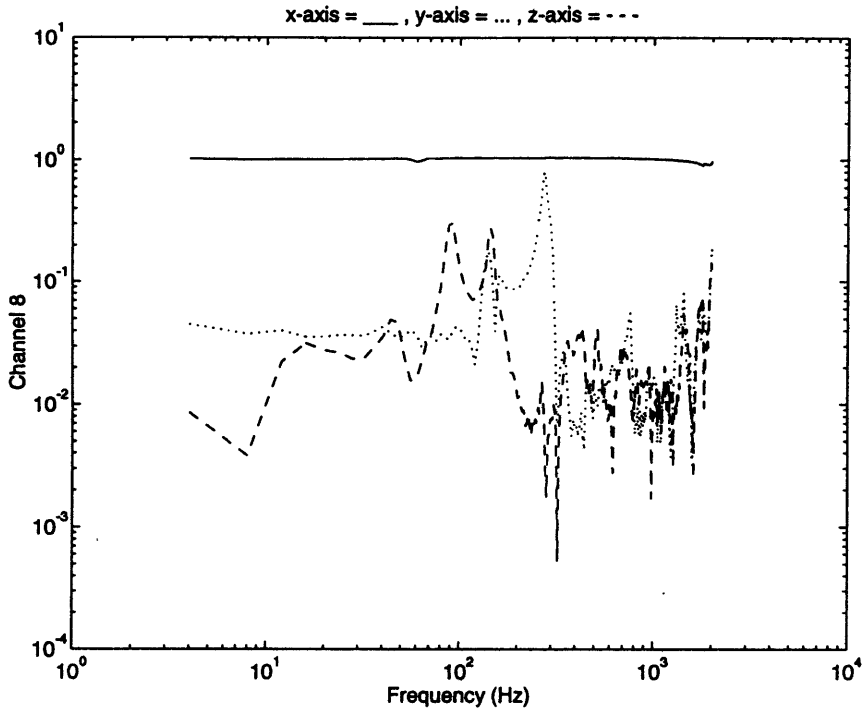

Figure 6-7: Channel 8 Vibrations in the X, Y, and Z-Axes

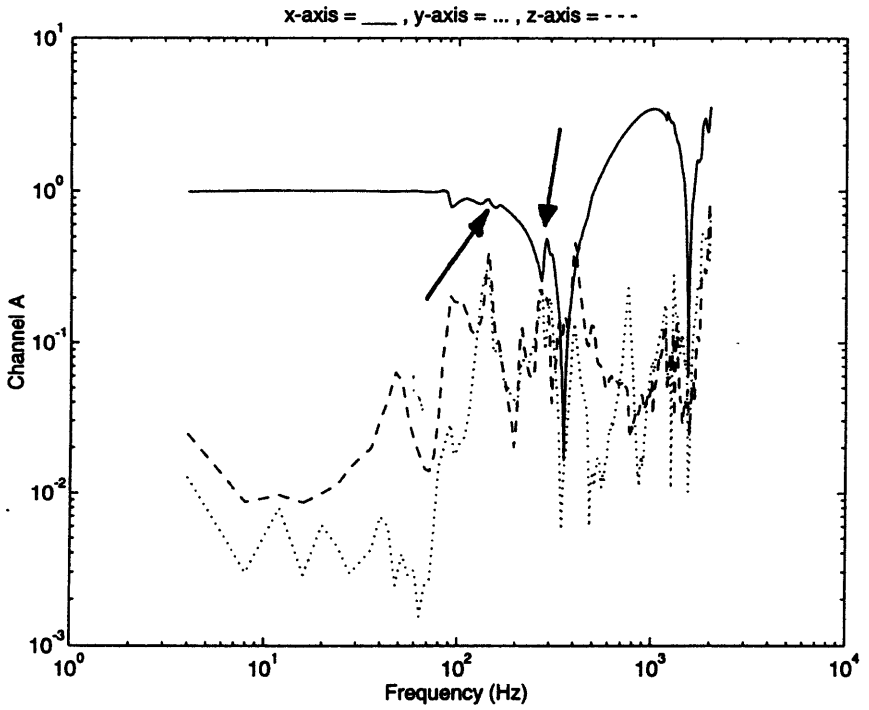

Figure 6-8: Channel A Vibrations in the X, Y, and Z-Axes

6.3 Linear Closed Form Model

Matlab was used to solve the linear equations of motion of the shaker-slip table assembly. Eigenvalues (square of the natural frequencies) and eigenvectors (mode shapes) were determined. The resulting natural frequencies in the range of interest (5-2000 Hz) and mode shapes associated with these frequencies are sketched in Figure 6-9. Note that while the relative motions of the nodes ($A - H$ and 1-9) are drawn to scale, the motions are not scaled properly to the drawn size of the shaker-slip table assembly.

Shown are the free modes of the shaker-slip table assembly, with the shaker armature unconstrained. These are the discrete modes of a relatively coarse model (few lumped masses), not of the continuous real system. Nevertheless, the mode shapes serve to illustrate and to clarify the experimental results.

The first mode, corresponding to $\omega_1 = 835$ Hz, indicates a node near 2, with a response everywhere else. This mode corresponds to that seen in the experiments at approximately 820 Hz, where there is a notch in the transfer function for channel 2. The second mode, at $\omega_2 = 1089$ Hz, is a system shearing mode. This motion is not seen in the experimental data. Instead, the experimental data indicates some rocking modes at low frequencies. The rocking modes, which result in similar x-axis behavior to that seen in Figure 6-9 at ω_2, are due to y and z-axis motions rather than table shearing. However, the Matlab model does not consider y and z-axis motion; hence these modes do not appear here.

The third and fourth modes, corresponding to ω_3 and ω_4 respectively, show smaller magnitude responses at the table edges than in the center. These modes approximately correspond to the experimental data, where the outside table channels have a notch which is not observed in the center channels. The data indicates that 5 has a higher magnitude of motion than 8 in this mode as well, with the transfer function for 5 having a larger response than 8 in frequencies near the frequency of the mode. The fifth and sixth modes, corresponding to ω_5 and ω_6 respectively, are not real for this system because of the asymmetric shaker movement they require. Finally, the

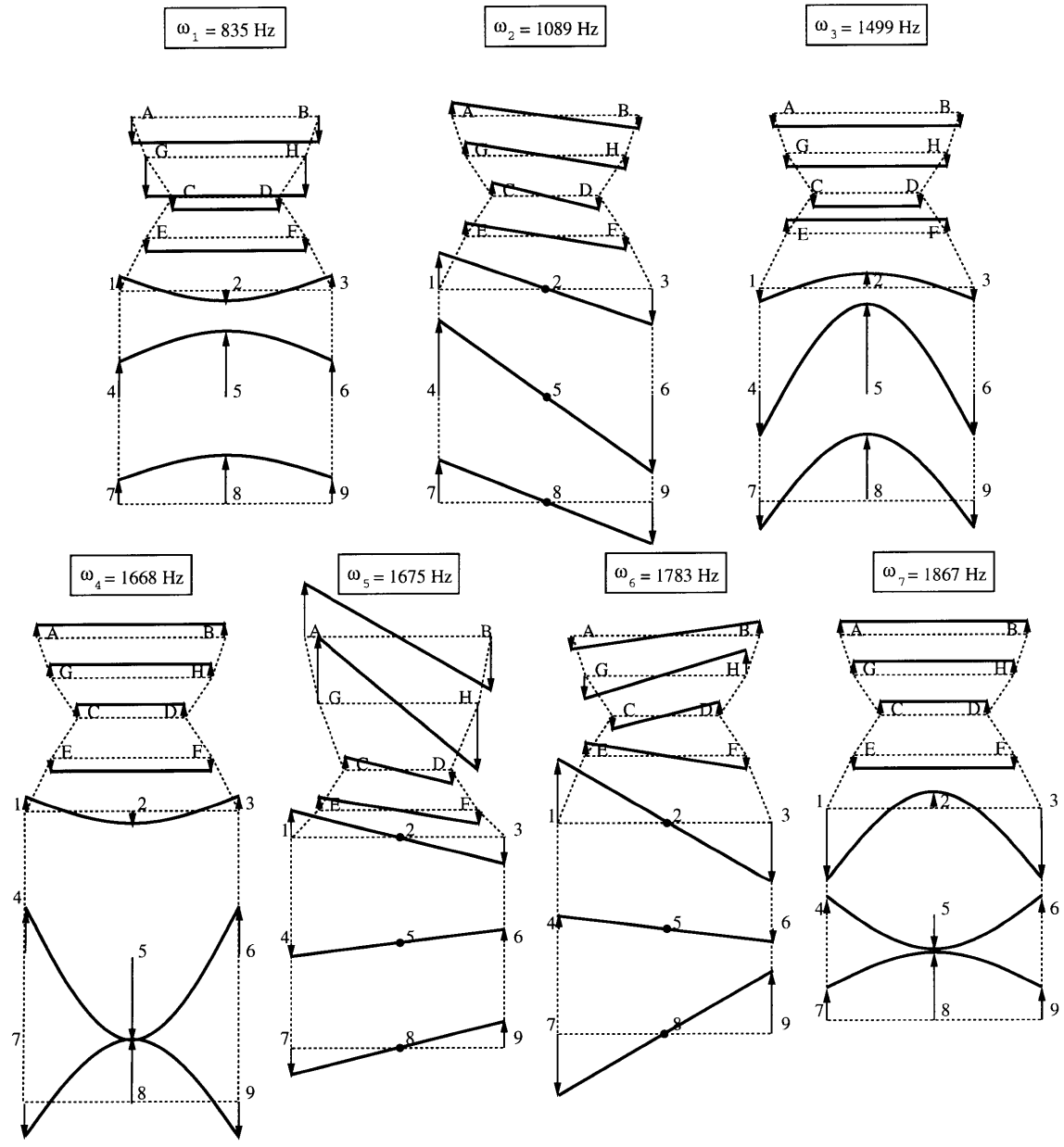

Figure 6-9: Mode Shapes for Shaker-Slip Table Assembly

resonance associated with ω_7 is a higher order version of the mode seen at ω_1. In addition, $\omega_7 = 1867$ Hz corresponds to the frequency of the second mode of the system seen in Figure 6-10 (also seen in Figure 6-3 as the second notch in channel A). The correlations noted here at frequencies above 1500 Hz are approximate. It is hard to single out specific modes from the data because the modal density is very high at high frequencies, both in the model and in the experimental data.

6.4 Explicit Time Simulation Model

6.4.1 Drive Signal Update

Drive signal update was performed in the explicit time simulation model. Figure 6-10 illustrates drive update. The dashed line represents the reference spectrum–the spectrum that was desired at the control location. Note that this is not a transfer function, as all of the other plots have been, but is instead a spectrum as defined in Section 2.2.5. Hence it is not taken with respect to 8, and has units of g^2/Hz. The solid line represents the spectrum of the initial signal at the control accelerometer, before update occurred. The dotted line represents the calculated drive spectrum required to achieve the reference spectrum at the control location. Figure 6-11 shows the inital motion at the control location and the final controlled motion. The controlled motion matches the reference spectrum; hence, drive signal update was accurately performed.

Note that the original response (generated by the reference drive spectrum) has resonances near 400 and 1800 Hz. As discussed with the experimental data, closed-loop control flattens the response at the control accelerometer by notching the input excitation signal. This phenomenon occurs here as well, showing that the model both captures the basic physics of shaker-slip table motion and models the control system accurately.

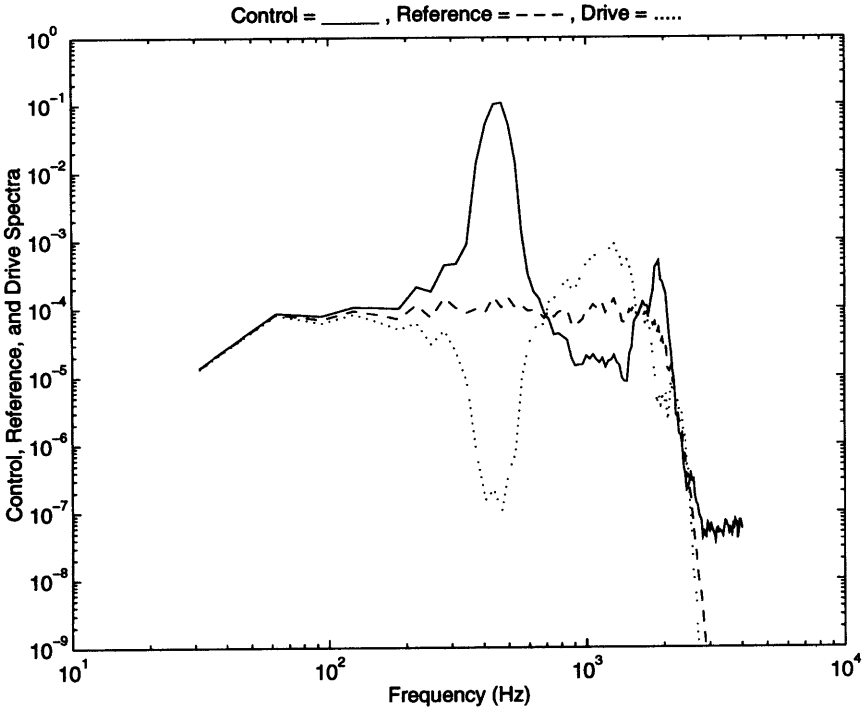

Figure 6-10: Drive Signal Update

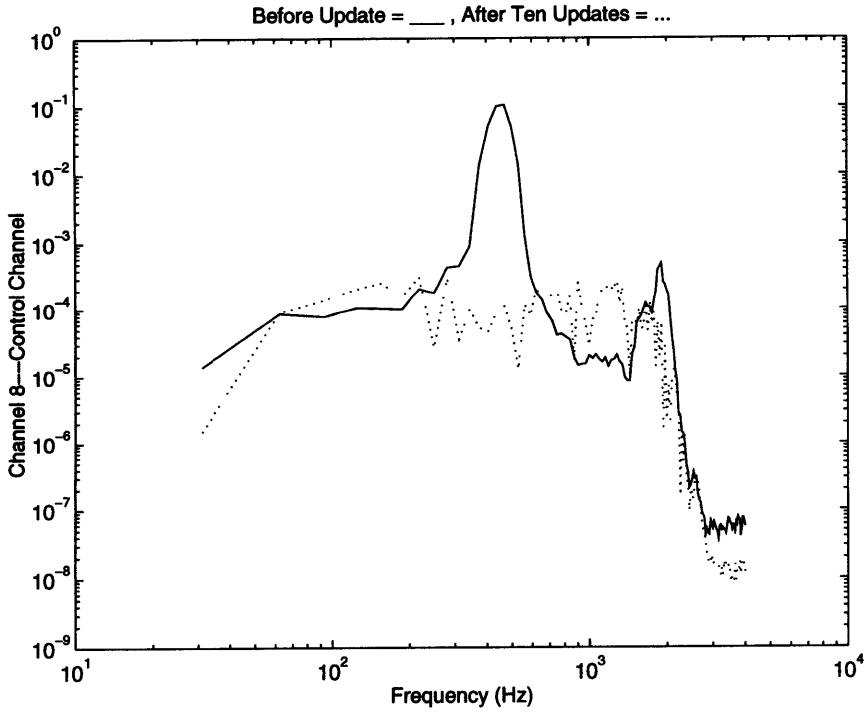

Figure 6-11: Control Channel Update

6.4.2 Notch Frequencies

Analytical models are often more helpful in predicting behavioral tendencies than in perfectly matching data. Hence, the analytically generated transfer functions for channels A, G, C, E, 2, 5, and 8 are plotted (Figure 6-12) and examined to determine if the trends noted in Section 6.2.2 for the experimental data are present. As in Section 6.2.2, the frequency of the first notch in the transfer functions increases when moving from accelerometer A to accelerometer 8. In addition, both the experimental and analytical results show that the largest changes in frequency occur when moving from C to E and from 2 to 5. Finally, no resonances are apparent. Hence, the explicit time simulation model does emulate the tendencies of the actual shaker-slip table assembly, at least with respect to anti-resonant frequencies (which are of primary importance in the determination of control accelerometer and test object location).

6.4.3 Correlation of Experimentally Attained and Analytically Generated Transfer Functions

The transfer functions attained using the explicit time simulation code correlated well with those attained experimentally. Some curves over-layed perfectly, as is shown in Figure 6-13 for channel 2. All other curves were close, as is illustrated in Figures 6-14 and 6-15 for channels 3 and A, respectively. Further correlation results appear in Section 6.5.3 and in Appendix D. The analytical model closely approximated the first notch frequencies. The discrepancies between the experimental and the predicted results can be attributed to slight inaccuracies in the analytical determination of system mass and stiffness properties. The assumption that all interfaces, except for the fixture-driver bar, can be approximated as solid pieces led to high estimates of interface stiffnesses and inaccurate mass distribution. The model was less accurate in predicting the magnitudes of the responses. This discrepancy can be attributed to the crude approximations used to determine the damping.

As stated above, the analytical model accurately predicted the response for frequencies in the vicinity of the first anti-resonances in the table, thereby successfully

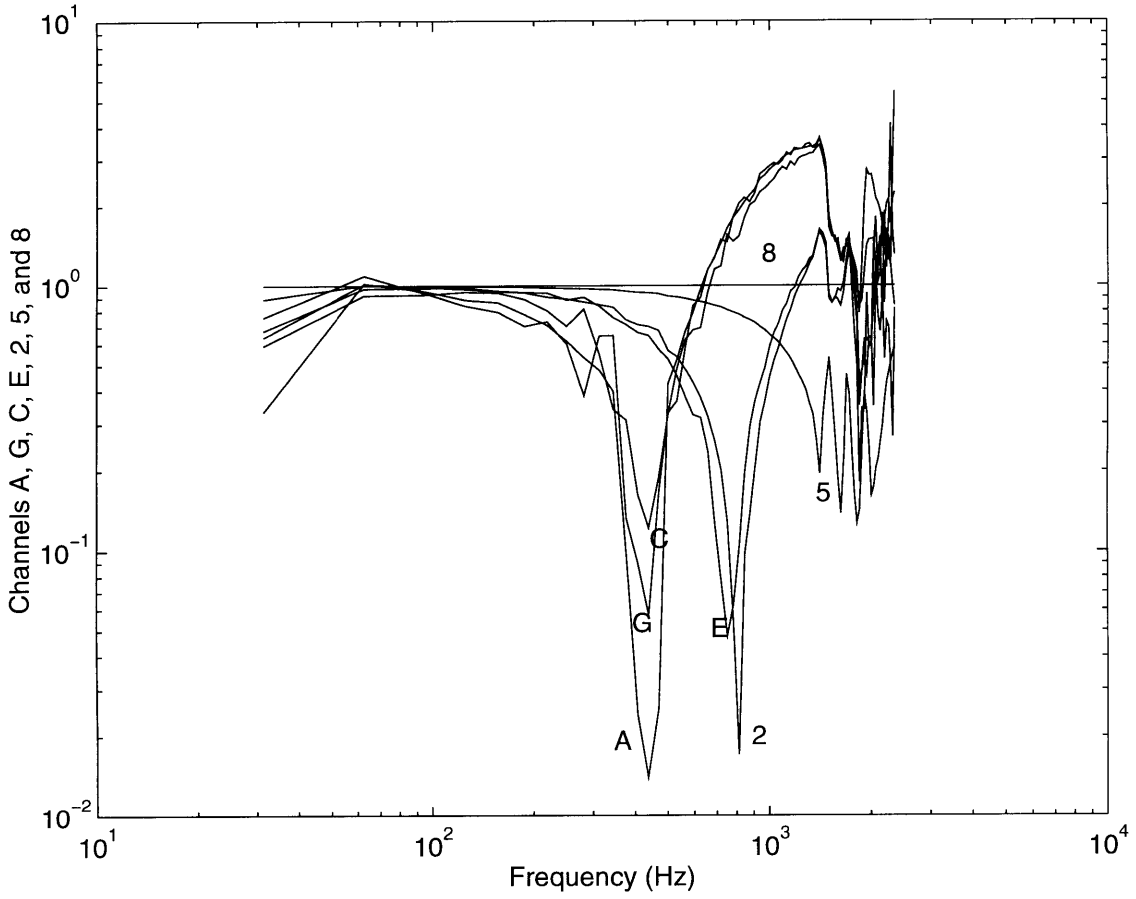

Figure 6-12: Analytically Generated Results–Node Frequency

predicting the first mode shape (a node at 2 with a response everywhere else). The related mode, with the table edges remaining stationary and the table center moving, was also predicted. At higher frequencies, however, the model predictions got quite noisy. Higher frequencies also led to noisy responses in the experimental data and in the linear Matlab model, due to increased modal density at high frequencies. The main concern of this thesis, hoewever, is that the model accurately characterized the behavior of the first modes.

Finally, the rocking mode described in Section 6.2.3 for the experimental data is not seen in the theoretical results, due to the lack of y and z contributions. At the frequency of the x-axis rocking mode, there are significant y and z-axis motions. The y and z-axis vibrations couple with the x axis motion, affecting the overall response. Since the theoretical model is constrained to the x-axis, it misses this behavior.

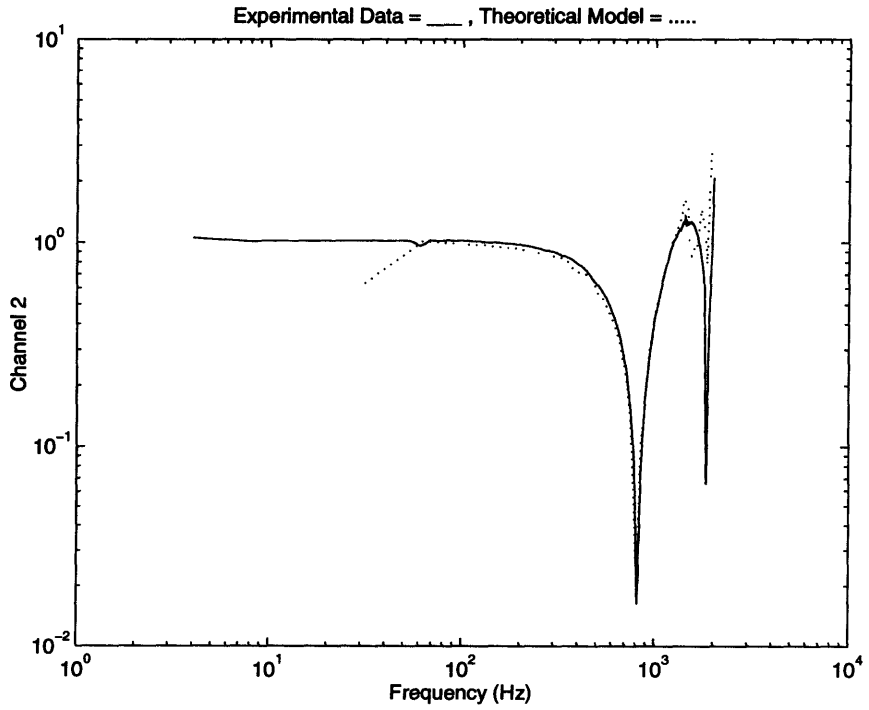

Figure 6-13: Comparison of Theoretically and Experimentally Attained Transfer Functions for Channel 2

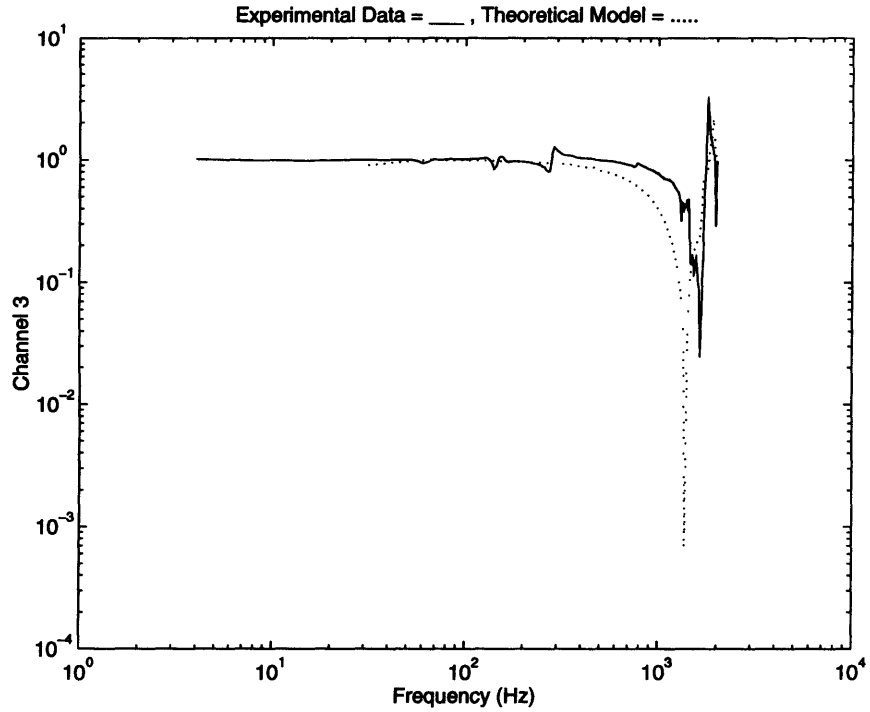

Figure 6-14: Comparison of Theoretically and Experimentally Attained Transfer Functions for Channel 3

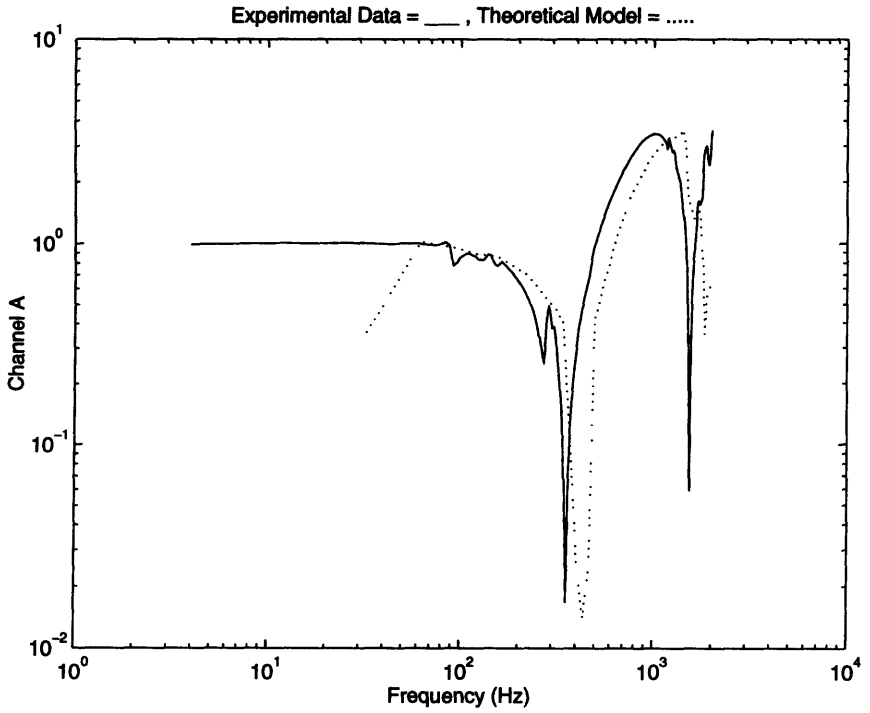

Figure 6-15: Comparison of Theoretically and Experimentally Attained Transfer Functions for Channel A

6.5 Variations in Test Configuration

6.5.1 Effect of Varying Control Location

The experiments addressing the effects of varying the location of the control accelerometer confirmed that control becomes more difficult as the accelerometer is moved inboard (toward the shaker) along the table. When the control accelerometer was at 8, the experiment ran smoothly. When it was moved to 5, the test again ran smoothly, but the drive signal took longer to equalize. Finally, when the control accelerometer was placed at 2, too much energy was required, alarm limits were exceeded, and the system shut down before it reached full level. The results of these tests are presented in Appendix C.

There are four figures in the Appendix for each of the three control locations (Figures C-75-C-86, Appendix C). The first is the spectrum at the control accelerometer and has units of g^2/Hz. The second, third, and fourth are the transfer functions relating the accelerations of the inboard (channel 2), center (channel 5), and outboard (channel 8) channels, respectively, to the acceleration of the control channel.

The first four plots are for outboard control and give the results previously discussed. The second set of plots are for center control (control at 5) and indicate that the system is severely overdriven to compensate for the anti-resonance at 5. The result is that channels 2 and 8 experience very large inputs at this frequency. The final set of four plots are for inboard control (control at 2) and show the same type of compensation for anti-resonances as seen with center table control. Note that the control spectrum in this case is at a lower level than that for outboard and center table control. This is because over-driving was so severe that the system shut down before full input levels were reached.

The discussion presented in Section 6.2.2 shows that locations closer to the drive input have an elastic anti-resonance in the frequency range of interest. If the control accelerometer location coincides with the location of an anti-resonance within the specified test frequency range, problems result. To counterbalance an anti-resonance in the control signal, the control analyzer increases the drive signal amplitude. At the

anti-resonant frequency, however, the rest of the table is substantially more excited than the control location in an attempt to reach the desired vibration levels at the control location. Hence, the shaker will put large amounts of power into the table until its alarm levels are reached causing it to shut down. Because the first notches in channels 8 and 5 occur at relatively high frequencies and are more heavily damped (smaller magnitude) than the first notch in channel 2, these tests were successful. The notch near 800 Hz in channel 2, however caused the system to shut down.

6.5.2 Effect of Attaching Test Objects–Experimental Data

Experiments were run in order to simulate the attachment of test objects. Two different masses at two locations on the slip table were tested (as illustrated in Figure 4-13). Measurements were taken to ensure that the masses were rigidly attached to the table (data presented in Appendix C). All plots have the abcissa scaled differently than previous plots in order to facilitate viewing the discrepancies in the notch frequencies.

A key feature of the data is the appearance of a peak in the transfer functions. This is illustrated in Figure 6-16 for Channel 1 with a mass attached between 2 and 5. The phenomenon occurs in all channels, with masses attached between both 2 and 5 and between 5 and 8. An explanation is that the attachment of a mass induces an anti-resonance at the control location. Closed-loop control compensates for this and keeps the spectrum at the control accelerometer (8) flat (see Figure C-40). The result is that the rest of the system is overdriven.

In addition, there is a decrease in the frequency of the first notch in the transfer functions of all channels inboard of the mass location. This is illustrated in Figures 6-17 and 6-18 for channels 2 and A with a mass attached between 5 and 8. The decrease in frequency of the second notch is more severe and varies among channels. It is especially problematic for side table channels, as is illustrated in Figure 6-19 for channel 1 with a mass attached between 5 and 8. Here, the notch may be indicative of a new mode shape as opposed to a simple reduction in frequency of the old one. The behavior is unclear because of the complicated motion at high frequencies and the introduction of the driven peak in the same frequency range.

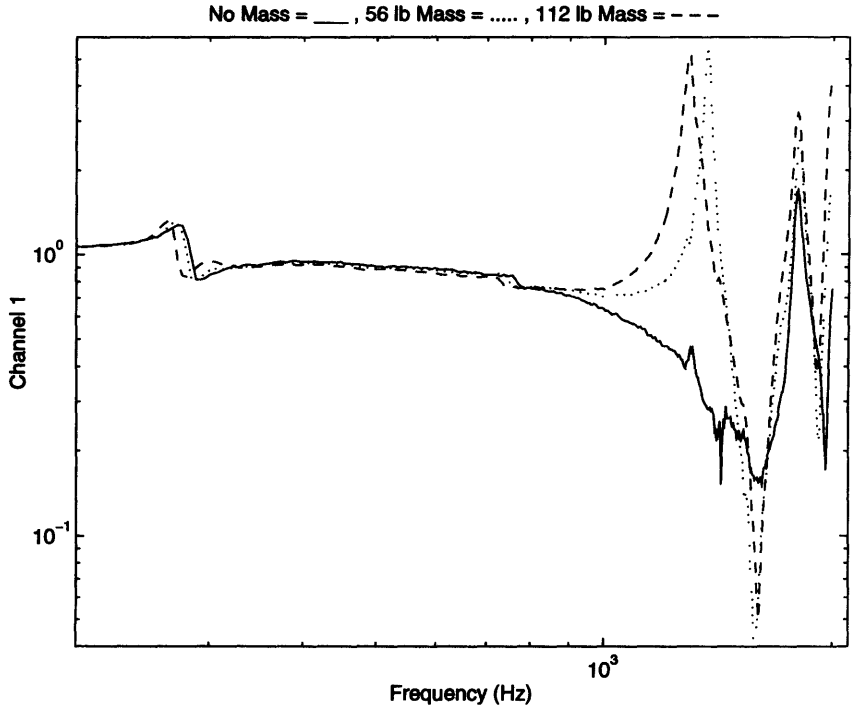

Figure 6-16: Effect at 1 of Adding a Mass Between 2 and 5

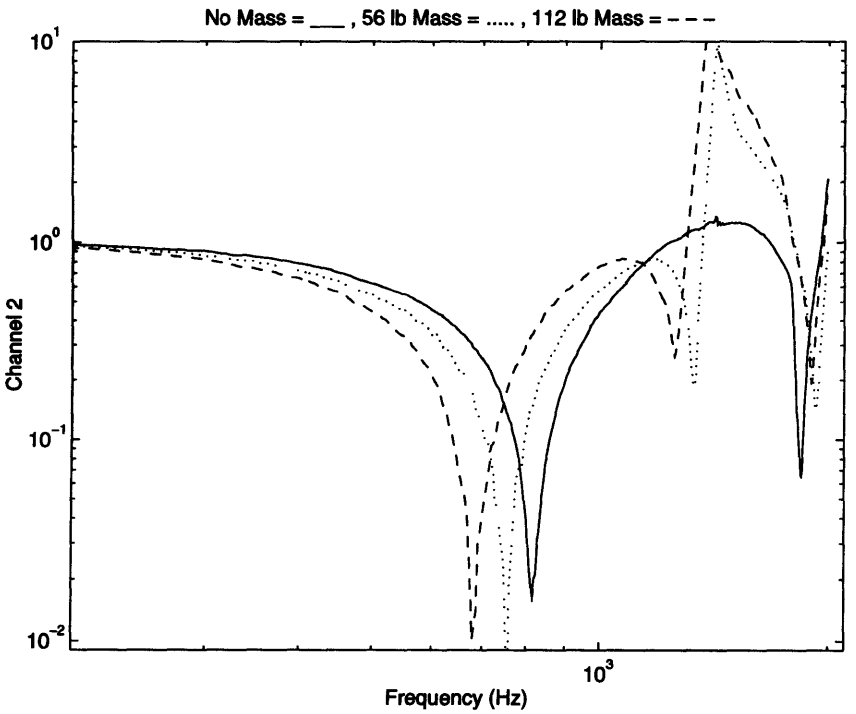

Figure 6-17: Effect at 2 of Adding a Mass Between 5 and 8

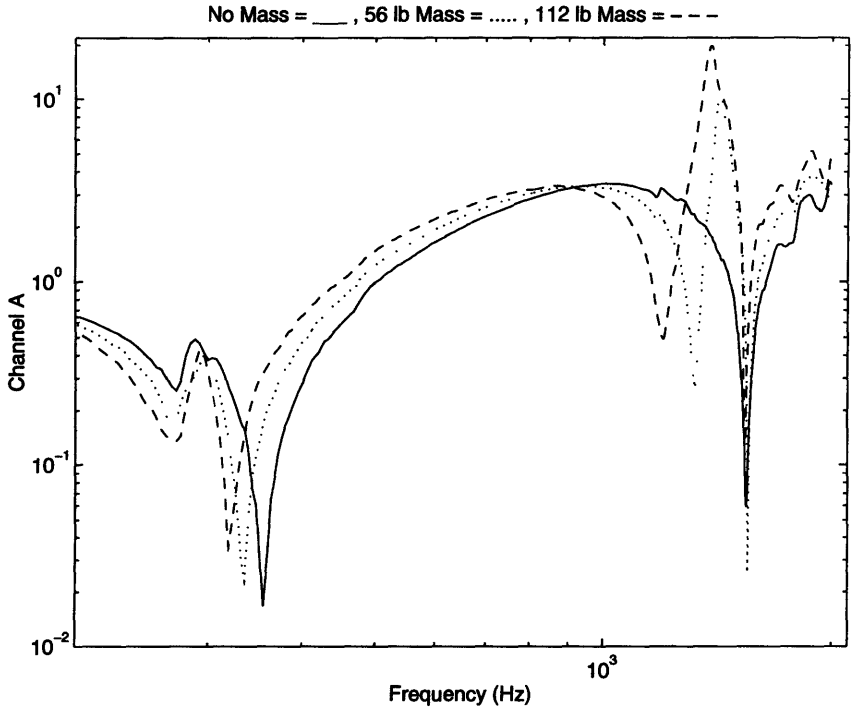

Figure 6-18: Effect at A of Adding a Mass Between 5 and 8

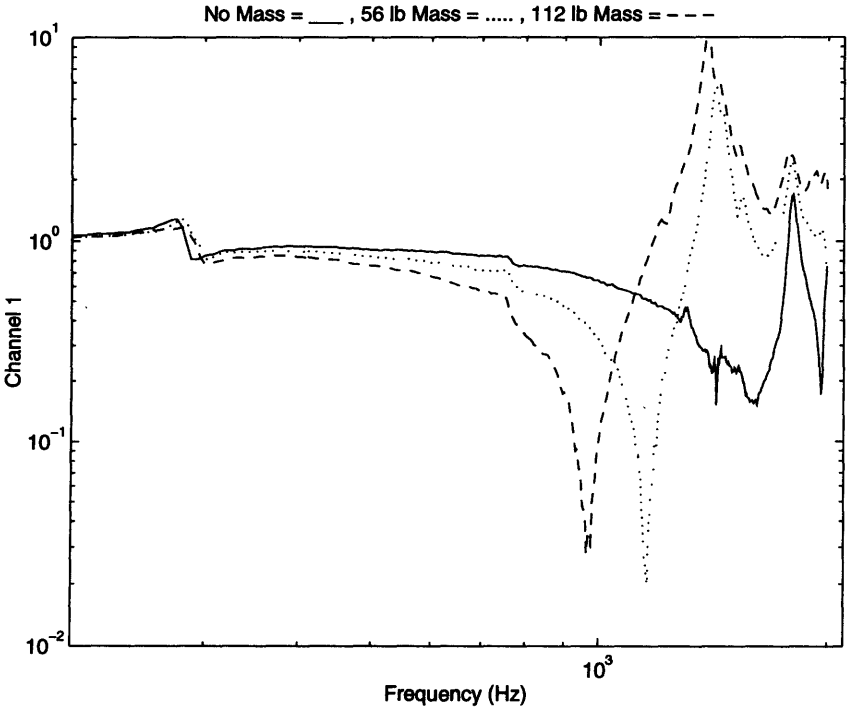

Figure 6-19: Effect at 1 of Adding a Mass Between 5 and 8

The experimental data also indicates that the attachment of a larger mass results in a greater reduction in notch frequency than attachment of a smaller one. This point is illustrated in Figure 6-17 for channel 2 with 56 lb and 112 lb masses attached between 5 and 8. The result makes sense considering the equation for the natural frequency of a single-degree-of-freedom system: $\omega^2 = k/m$.

Measurements were taken to ensure that the masses were rigidly attached to the table. The response measured at the accelerometer mounted on the mass fell between the responses of the two surrounding slip plate accelerometers. Figures C-22, C-23, and C-25 (see Appendix C) illustrate the point for a 56 lb mass attached between 2 and 5. Hence, the attachment of the masses was rigid.

Finally, attaching a mass between the outboard accelerometers (5 and 8) resulted in a higher frequency first anti-resonance and a smaller amplitude resonance in the transfer function of the attached mass, than did attaching a mass between 2 and 5. This is shown in Figures C-62 and C-70 (see Appendix C) for a 112 lb mass attached between accelerometers 2 and 5 and between 5 and 8, respectively.

6.5.3 Theoretical Results and Correlation

The results attained analytically using the explicit time simulation code with attached test masses correlate well with the experimental data. The analytical results contain the key features of the experimental data, including the over-excitation of the system due to the anti-resonance at 8, which is induced by the attachment of a mass. The correlation is indicated in Figure 6-20 for channel 4 with a 56 lb mass attached between 5 and 8. The theoretical model also predicts the reduction in notch frequency in the transfer function of all channels inboard of the mass attachment point. This is illustrated in Figures 6-21 and 6-22 for channels A and 4, with 56 and 112 lb masses attached between 5 and 8. Finally, the analytical model is able to predict that high frequency responses are altered by the attachment of a mass, as illustrated in Figures 6-23 and 6-24 for channels 1 and 2, respectively, with a 56 lb mass attached between 5 and 8, but its results do not correlate perfectly with those attained experimentally. Additional correlations of analytical results and experimental data can be

found in Appendix D.

Some discrepancies exist between the experimental data and the analytically predicted results. The notch frequencies do not match perfectly, as illustrated in Figures 6-23 and 6-25 for channel 1 with a 56 lb mass attached between 5 and 8 and channel 4 with a 56 lb mass attached between 2 and 5, respectively. These discrepancies between the actual and the modelled data can be attributed to crudeness in the determination of mass and stiffness system properties. In addition, correlation between the theoretical and experimental results is not very good at high frequencies; however, as mentioned previously, this is not relevant in this thesis, where the frequencies of the first notch are of primary concern. Finally, the analytically generated tranfer functions for side table channels differ more from the experimental transfer functions than do those of the center table channels. This is illustrated in Figures 6-23 and 6-24 for channels 1 and 2 with a 56 lb mass attached between 5 and 8 and is due to inaccuracy in the method used to model mass attachment. The theoretical model assumes that the attached mass only affects the two closest, center accelerometers (i.e. 5 and 8 for attachments between 5 and 8); but the mass also affects the neighboring side-table accelerometers (4, 6, 7, and 9), as well.

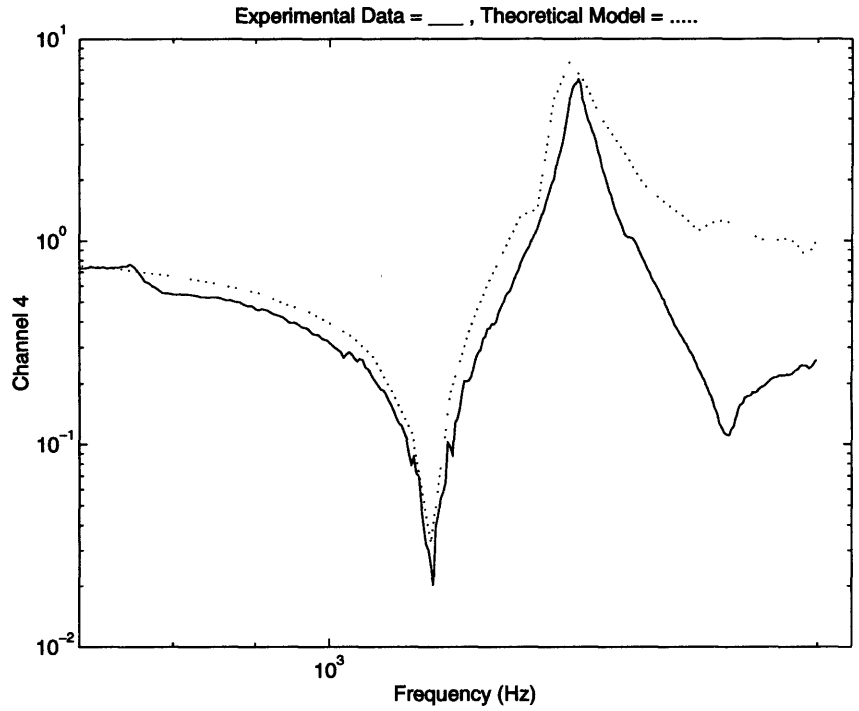

Figure 6-20: 56lb Mass Between 5 and 8: Comparison of Theoretically and Experimentally Attained Transfer Functions for Channel 4

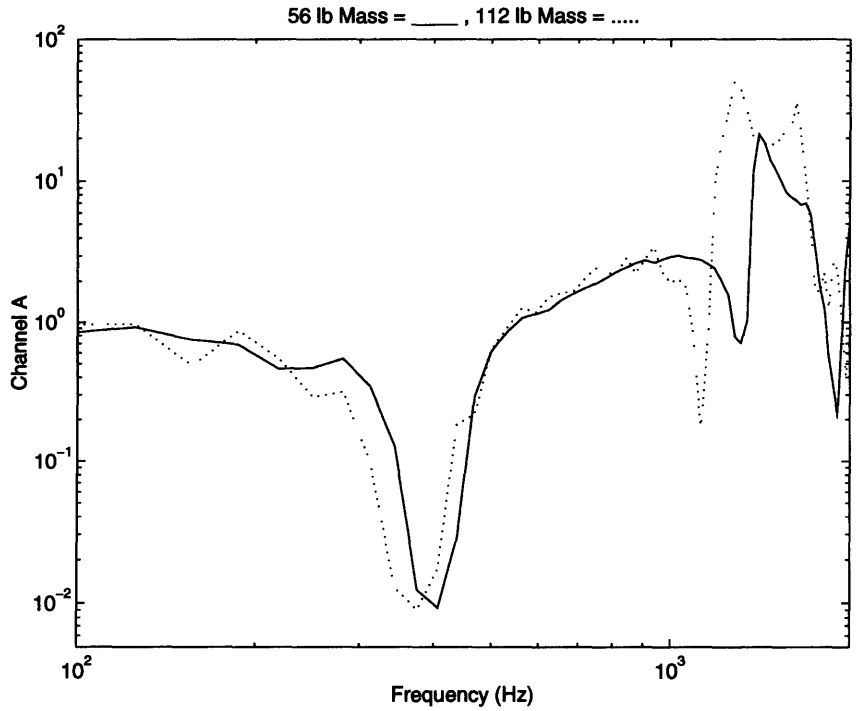

Figure 6-21: Analytically Predicted Effect at A of Adding a Mass Between 5 and 8

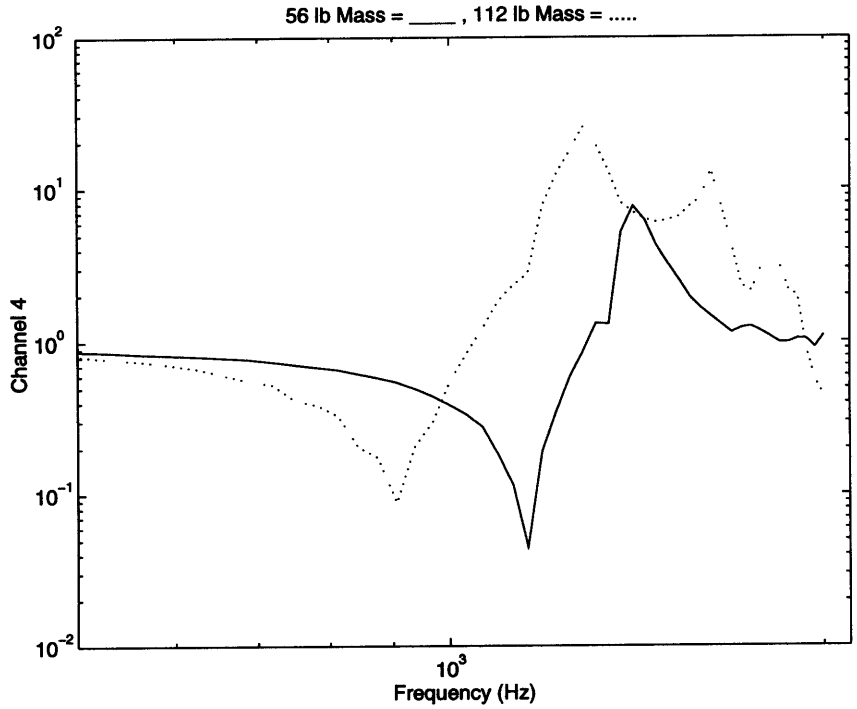

Figure 6-22: Analytically Predicted Effect at 4 of Adding a Mass Between 5 and 8

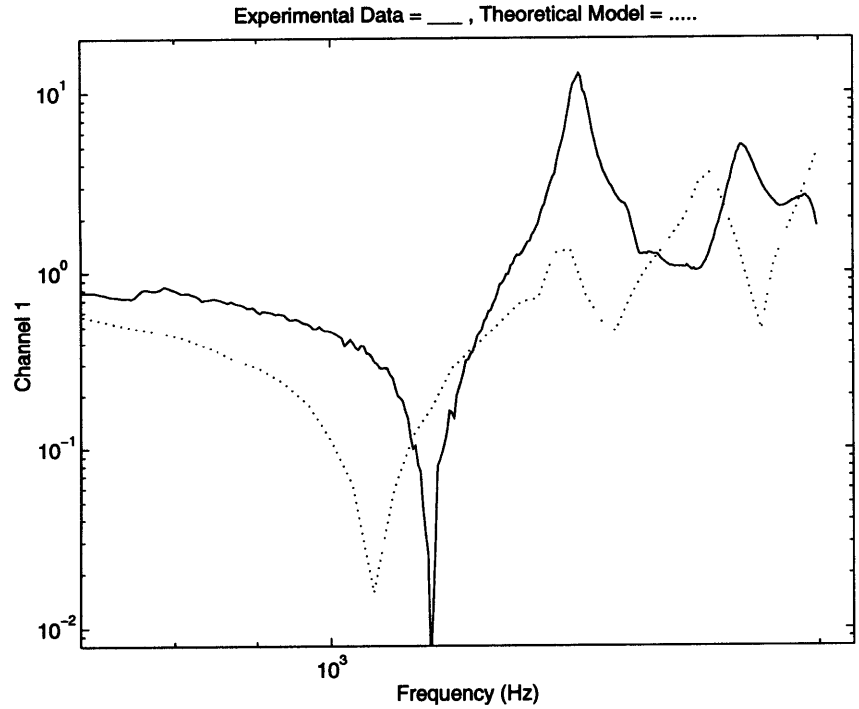

Figure 6-23: 56lb Mass Between 5 and 8: Comparison of Theoretically and Experimentally Attained Transfer Functions for Channel 1

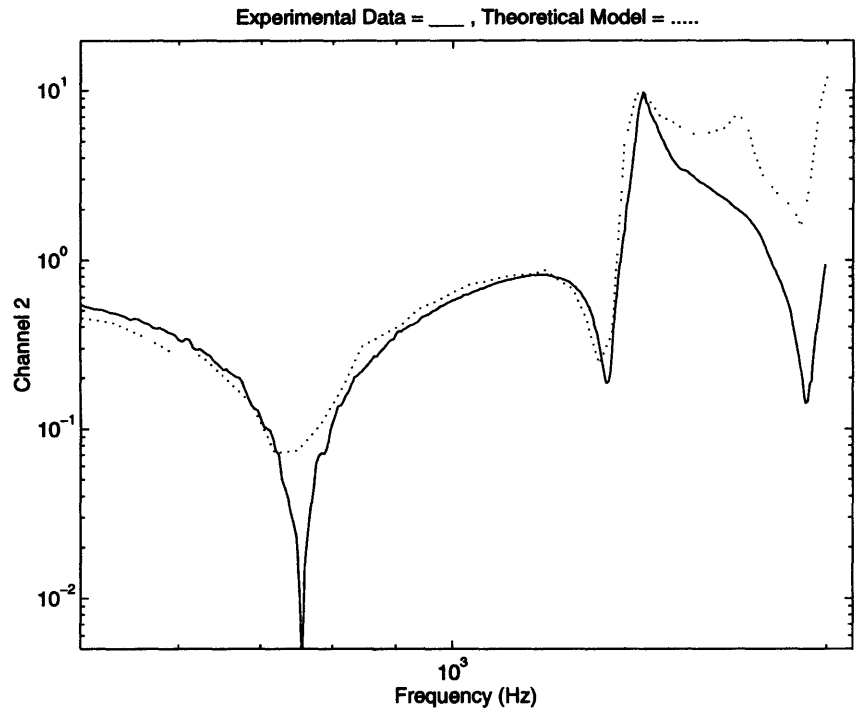

Figure 6-24: 56 lb Mass Between 5 and 8: Comparison of Theoretically and Experimentally Attained Transfer Functions for Channel 2

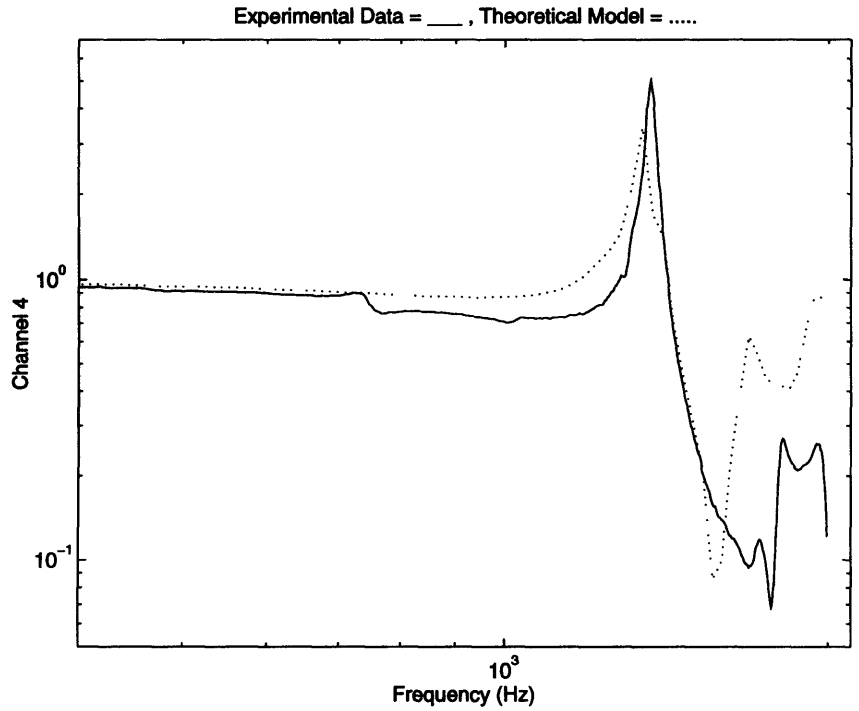

Figure 6-25: 56 lb Mass Between 2 and 5: Comparison of Theoretically and Experimentally Attained Transfer Functions for Channel 4

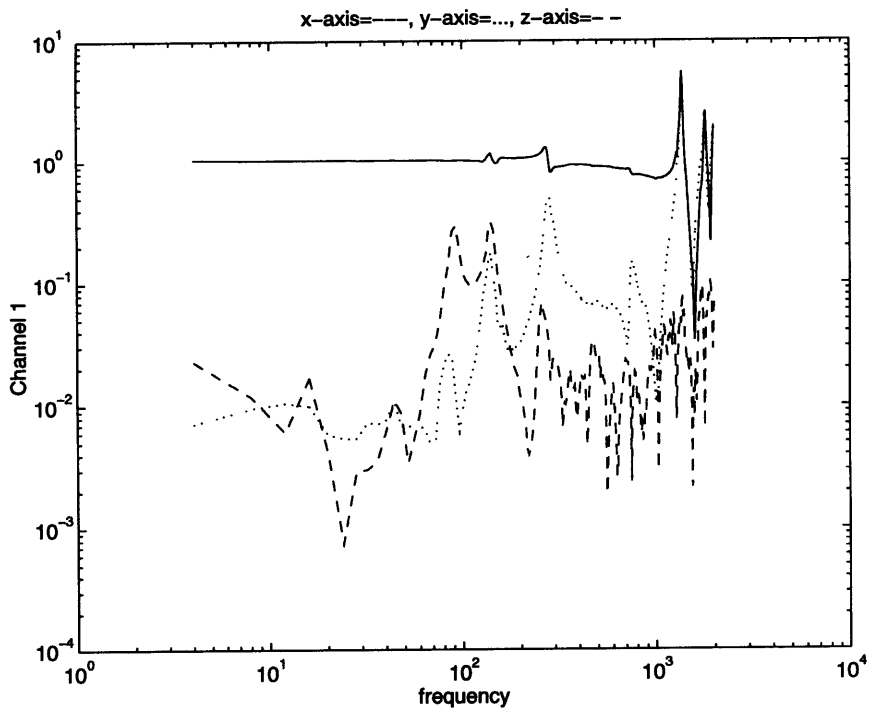

Figure 6-26: 56 lb Mass Between 2 and 5: Channel 1 Vibrations in the X, Y, and Z-Axes

6.5.4 Pitch and Yaw

Tests were run with attached masses to see the effects on y and z-axis behavior. Figures 6-26 and 6-27 show the transfer functions for channel 1 with a 56 lb mass attached between 2 and 5 and between 5 and 8, respectively. There is little difference between these results and those in the case of no attached mass; and, as before, y and z-axis contributions are larger than desired.

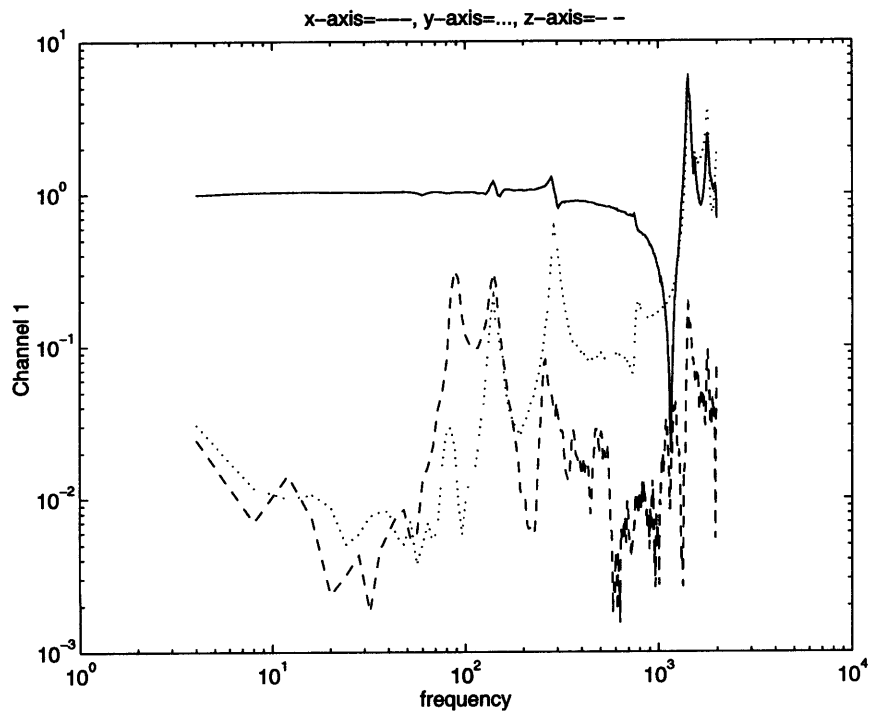

Figure 6-27: 56 lb Mass Between 5 and 8: Channel 1 Vibrations in the X, Y, and Z-Axes

6.6 Parametric Analysis of Shaker-Slip Table Interface

The stiffnesses of the fixture-driver bar interface were varied (a tighter and a looser fitting pin) to determine the effect of changing the stiffness of the joint. Both the weakened connection of the fixture-driver bar interface (80% spring values) and the strengthened one (120% spring values) resulted in little difference in the shape or node frequencies of the transfer functions for Channels 1-9, E, and F. In the rest of the shaker-slip table interface (A-H, excluding E and F), stiffening the attachment resulted in a higher notch frequency, while weakening the attachment resulted in a lower notch frequency. This is illustrated in Figure 6-28, and makes sense given the equation for the natural frequency of a single-degree-of-freedom system: $\omega_n = \sqrt{k/m}$. Also important to note is that the magnitude of the notch increases with reduced joint stiffness. If the stiffness of the connection was reduced or increased further, notch frequencies in the table would possibly be affected.

Slide-and-bang nonlinear motion of the fixture-driver bar interface was also modelled. The model took much longer than the linear models to converge to a solution. Difficulty arose in the Runge-Kutta algorithm, unless the step size was extremely small. The reason for this is understood if the time domain responses of the nonlinear model (Figure 6-29) are compared with those of the linear model with no masses attached (Figure 6-30). Amplitudes of motion are much larger and more erratic in the nonlinear model.

In addition, there were difficulties with the control update process. The program was not able to maintain a flat control spectrum at the control accelerometer. It would converge to the reference spectrum, jump out, converge, and then jump out again. Despite this erratic behavior, the transfer function data attained for the table indicated that the nonlinear spring had little effect on table behavior. This result is deceptive, however, since the drive update in the computer model is instantaneous. In the real system, where drive update takes 3.4 seconds, the controller would probably be unable to cope and the test would shut down. The situation modelled is a worst-

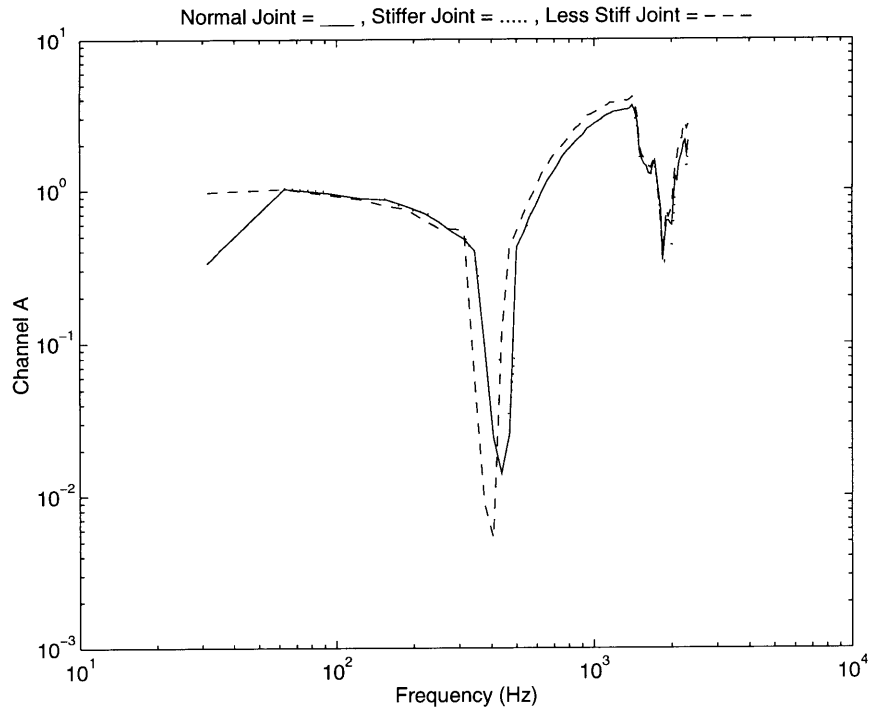

Figure 6-28: Channel A Vibrations Versus Joint Stiffness

case scenario, and would hopefully never be encountered; however, the implications of this study are quite interesting. It is indicated that a nonlinear joint can lead to erratic table behavior, and that while the control system may be able to handle this and produce reasonable transfer functions, the time domain response is undesirable. This can cause control difficulties which could result in the overtesting of attached test objects. Such behavior could be even worse in the real system, causing unpredictable and intermittent tests, and eventually leading to equipment shut down.

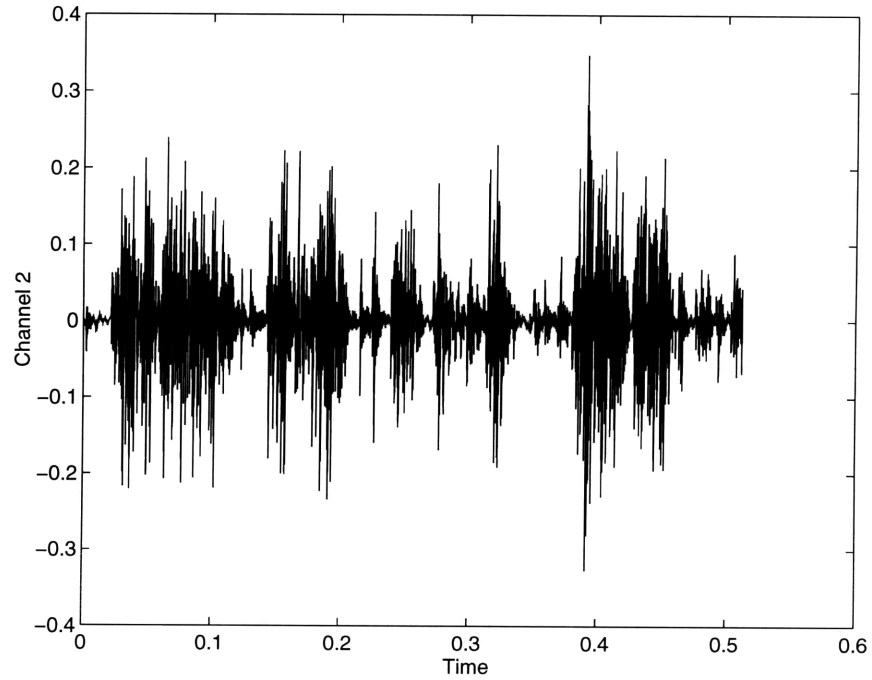

Figure 6-29: Nonlinear Time Domain Response at Channel 2

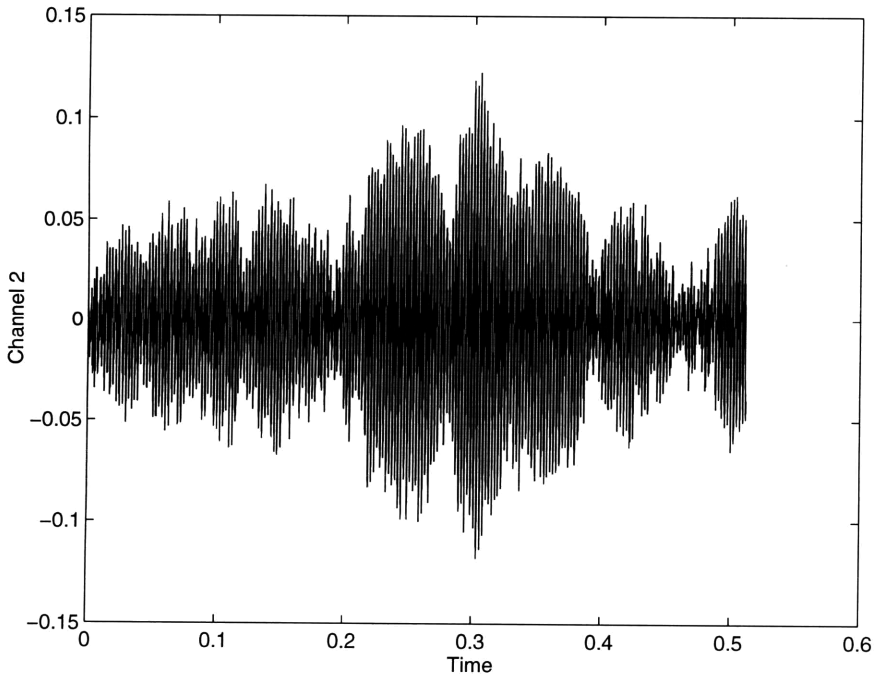

Figure 6-30: Linear Time Domain Response at Channel 2

Chapter 7

Conclusions and Recommendations

7.1 Conclusions

Experimental data was collected and two theoretical models produced to set forth a physical basis for selecting test specimen and control accelerometer locations for vibration tests conducted on a given test specimen, using a given shaker and slip table.

The results attained using the theoretical models correlated well with those attained experimentally. Notch frequency correlation was quite good, indicating that mass and stiffness properties for the system were chosen accurately. Notch magnitudes, on the other hand, differed between the experimental and analytical results. This discrepancy indicates that the method used for determining damping coefficients needs improvement. The closed form solution successfully determined system mode shapes, but did not accurately reflect boundary conditions or control algorithm. The explicit time simulation model accurately modelled the control system and solved the equations of motion, and thus was capable of predicting table behavior.

The experimental data, basic mass-spring models, and explicit time simulation Fortran code all indicate that the point on the table farthest away from the shaker input has the highest first anti-resonance frequency. Hence, a control accelerometer

and test object should be placed as far outboard of the shaker as possible to attain the largest control range. In addition, the experiments performed to determine the effects of varying control accelerometer location, confirmed that control becomes more difficult (and then impossible) as the control accelerometer is moved inboard (toward the shaker) along the table.

In order to accurately control and measure the input to a test specimen, the specimen and the control accelerometer for a given test must be located as close as possible to one another. This allows problems (such as testing an object at a frequency coinciding with one of the tables's resonances or anti-resonances) to be avoided; thus preventing a test object from receiving either more or less excitation than desired.

Attachment of a mass induces an anti-resonance at all table points, including the control location. Closed loop control compensates for this and results in overdriving the entire system, including the attached test object. In addition, the frequency of the first anti-resonance is reduced and mode shapes altered for all channels inboard of the attachment location. Attachment of a heavier mass results in larger changes than does a lighter one. Outboard attachment of the mass results in a higher frequency first anti-resonance and a smaller amplitude resonance in the transfer function of the mass, than inboard attachment. Therefore, attaching a mass between the outboard accelerometers is the best option.

Tests performed to measure out-of-axis accelerations (pitch and yaw) showed that y and z-axis motions are relatively insignificant compared to those in the x-direction up to about 80 Hz. Above 80 Hz, y and z-axis responses at times approach the x-axis responses. In addition, there are large y and z responses at the frequency of the x-axis rocking mode. This indicates that out-of-axis accelerations cause this x-axis behavior.

Changing the stiffness of the fixture-driver bar interface (pin joint) has little effect on the table behavior in the load and stiffness ranges tested ($\pm 20\%$). However, changes of more that 20% in the stiffness may more substantially affect slip table behavior. Starting with a higher stiffness connection (not experimental pin-joint) may have more effects as well: notch frequencies could be affected, and table behavior

might move out of the range of the controller.

Nonlinear slide-and-bang motion in the fixture-driver bar interface was modelled. While a worst-case scenario was tested, the model did indicate the limits of the shaker-slip table assembly. The computer model had great difficulty converging to a solution; erratic behavior was predicted. The actual system could be incapable of controlling table behavior.

Since the ideal of an infinitely stiff, heavily damped, massless connection between a shaker and a test item is non-physical, existing hardware is used to overcome the complications resulting from the use of a slip table. Understanding the behavior of the shaker-slip table assembly under different operating conditions and accordingly varying test object and control accelerometer placement as described here is a key step in this process.

7.2 Recommendations

A model has been presented to characterize the dynamic behavior of a slip table. The model can be used in its current form to perform other tests, or it can be modified and improved. Other tests might include varying control accelerometer location or testing an object with a clearly defined resonance. In addition more tests determining the effects of varying joint stiffnesses and nonlinear components could be run. Other nonlinear interfaces (gap elements, "sticktion" between the table, oil, bearings, and base) could be simulated and the input level for the nonlinear tests could be varied. Table thickness could also be varied.

To improve the model, a more accurate determination of the system properties of the shaker-slip table assembly could be undertaken. The assumption that all interfaces, except for the fixture-driver bar, can be approximated as solid pieces led to high interface stiffnesses, as well as to inaccurate mass distributions. A more exact measurement of the stiffness and mass properties of the interfaces could be performed. The analytical attachment of test objects would also be more accurately conducted if more experimental measurements were taken and further analysis performed. Ac-

curacy would also be improved by modelling the table as a continuous system rather than as a series of lumped masses. y and z axis motions could be included, since cross-axis accelerations causes variations in the in-axis response. The oil film upon which the table rests, and the bearings upon which it rides could be modelled. The damping of the oil and the friction of the bearings could be taken into consideration, with table warping included if necessary. Acceleration gradients between the glass composite layer and the magnesium slip plate could be considered. Extremal and average control, where more than one control accelerometer is used could be examined. Higher-order accuracy solutions, where masses beyond immediate neighbors are attached, could be tried. Curve fitting algorithms (such as circle fits) could be used to more accurately determine system properties. Collecting experimental data open, rather than closed, loop would also help, allowing the model to be based on system resonances rather than anti-resonances. Finally, a computer program to determine the ideal test object and control accelerometer location for a slip table test could be embedded in the control algorithm.

Appendix A

Fortran Code

```
c     xytest33.for with control loop
c       y-axis removed

c     4th order runge kutta ode solver with adaptive step size control

c     driver (sets initial conditions)
      implicit double precision (a-h, o-z), integer(i-n)
      parameter(nvar=38, updates=10.0, m=128, m4=4*m, k=15)
c     nvar=number of variables,m=length of overlap,k=number of averages
      common /path/ kmax,dtsav                                          10
c     common to driver, odeint
      common /counter/ kount
c     common to driver, odeint
c     kount=# of steps stored
      common /samprate/ sr
c     common to driver, odeint, input
c     sr = sample rate (actually half the sample rate, as defined here)
      common /xdotdot/ a(4096)
c     common to driver, odeint, input
      common /phase/ b(6528),dref(128)                                  20
c     common to driver, odeint
      common /file/ ifile
c     common to driver, odeint, spectrum
      common /inputlevel/ rlev
c     common to driver, spectrum
c     rlev=factor raw input is multiplied by
      dimension xstart(nvar),dxstart(nvar),w1(m4),w2(m)
      rlev=1e-2
      open(unit = 50, file = 'random.dat', status= 'old')
      do 10 i=1,4096                                                    30
       read(50,*) a(i)
       a(i)=a(i)*rlev
10    continue
```

```
      open(unit = 51, file = 'morerand.dat', status= 'old')
      do 11 i=1,6528
        read(51,*) b(i)
11    continue
      close(51)
      ifile=1
      rewind(50)
      call spectrum(dref,m,k,w1,w2)
c     create a reference spectrum using random.dat data
      close(50)
      sr=8000.
c     t0 = initial time, tf = final time
      t0=0.
      tf=(updates*4096.)/sr
c     Initial conditions follow
      do 20 i=1,nvar
        xstart(i)=0
        dxstart(i)=0
20    continue
      eps=1.0e-2
c     accuracy of integration
      h1=0.01
c     initial step size
      hmin=0.0
c     minimum step size
      kmax=10000000
c     max number of steps that can be stored
      dtsav=(tf-t0)/(sr*updates)
c     intermediate values recorded only at intervals greater than dtsav
      call odeint(xstart,dxstart,nvar,t0,tf,eps,h1,hmin,nok,nbad,m,k,
     *w1,w2,updates)
      write(6,*) 'Successful steps:  ',nok
      write(6,*) 'Bad steps:  ',nbad
      write(6,*) 'Stored intermediate values:  ',kount
      end

c     odeint (runge kutta driver with adaptive step size control)

      subroutine odeint(xstart,dxstart,nvar,t0,tf,eps,h1,hmin,
     *nok,nbad,m,k,w1,w2,updates)
c     nok and nbad = # okay and bad (but retried and fixed) steps taken
      implicit double precision (a-h, o-z), integer(i-n)
      double precision kk
      parameter (nmax=38,two=2.0,zero=0.0,tiny=1.e-15,kk=3.0)
c     kk is the control loop parameter pp=2**kk
      common /path/ kmax,dtsav
c     common to driver, odeint
      common /counter/ kount
c     common to driver, odeint
      common /samprate/ sr
c     common to driver, odeint, input
c     sr = sample rate
      common /xdotdot/ a(4096)
c     common to driver, odeint, input
```

```
      common /phase/ b(6528),dref(128)
c     common to driver, odeint
      common /file/ ifile                                                    90
c     common to driver, odeint, spectrum
      common /interp/ mkount,tp(64),xp(38,64),dxdtp(38,64)
c     common to odeint, interpolate
c     mkount=variable indicator for interpolator
      common /random/ r(64),jkount
c     common to odeint, input, interpolate
c     jkount=array counter (1-64)
      common /oldtime/ ttt
c     common to odeint,input
      dimension xstart(nvar),dxstart(nvar),xscal(nmax),x(nmax),              100
     *dxdt(nmax),tea(1),xea(38,1),dxdtea(38,1),rea(1),dold(128),
     *drive(128),cexp(128),cold(128),cdata(128),dinterim(512),
     *w1(4*m),w2(m)
      t=t0
      h=sign(h1,tf-t0)
c     transfer of sign, |h1| if (tf-t0)>=0, -|h1| if (tf-t0)<0
c     here in case tf<t0
      nok=0
      nbad=0
      kount=0                                                                110
      nframes=0
c     number of segments of length 64
      jupdate=0
c     number of drive updates
      ninit=1
c     used for array initialization
      ninterp=1
c     used to increment te
      ttt=0.
c     time of last update                                                    120
      ifile=ifile+1
      jkount=0
      p=dfloat(ninterp)-1.
      te=p/sr
c     te=equal time steps
c     initializes variables to previously specified ICs
      do 11 i=1,nvar
        x(i)=xstart(i)
        dxdt(i)=dxstart(i)
11    continue                                                               130
      tsav=t-dtsav*two
c     assures storage of first step
1     if (jkount.lt.64) then
        call derivs(t,x,dxdt)
        do 12 i=1,nvar
          xscal(i)=abs(x(i))+abs(h*dxdt(i))+tiny
c         xscal is the vector against which the error is scaled
c         absolute value + euler step + tiny (tiny in case others are 0)
12      continue
        if(kmax.gt.0)then                                                    140
          if(abs(t-tsav).gt.abs(dtsav)) then
```

```
c       store only for time step greater than dtsav
        if(kount.lt.kmax)then
          kount=kount+1
          jkount=jkount+1
          tp(jkount)=t
          do 13 i=1,nvar
            xp(i,jkount)=x(i)
            dxdtp(i,jkount)=dxdt(i)
13         continue                                                    150
          tsav=t
        else
          pause 'too many steps.'
          return
c          function returns control to main program
        endif
      endif
      if((t+h-tf)*(t+h-t0).gt.zero)  h=tf-t
c     if step can overshoot end, cut down step size                   160
      call rkqc(x,dxdt,nvar,t,h,eps,xscal,hdid,hnext)
      if(hdid.eq.h)then
        nok=nok+1
      else
        nbad=nbad+1
      endif
      if((t-tf)*(tf-t0).ge.zero)then
c     we are done
        if(kmax.ne.0)then
          kount=kount+1                                               170
          jkount=jkount+1
c         save final step
          tp(jkount)=t
          do 14 i=1,nvar
            xp(i,jkount)=x(i)
            dxdtp(i,jkount)=dxdt(i)
14         continue
        endif
        goto 2
      endif                                                           180
      if(abs(hnext).lt.hmin) pause 'step size smaller than minimum.'
      h=hnext
      goto 1
    endif
2   if (te.gt.tp(jkount)) then
      tp(1)=tp(64)
      r(1)=r(64)
      do 15 i=1,nvar
        xp(i,1)=xp(i,64)
        dxdtp(i,1)=dxdtp(i,64)                                        190
15     continue
      jkount=1
      goto 1
    else
      do 16 mkount=1,nvar
```

```
      call interpolate(te,xe,dxdte,re)
      tea(1)=te
      xea(mkount,1)=xe
      dxdtea(mkount,1)=dxdte
      rea(1)=re                                                    200
16    continue
c     write(31,100) tea(1), (xea(j,1),j=1,4)
c     write(32,100) (xea(j,1),j=5,9)
c     write(33,100) (xea(j,1),j=10,14)
c     write(34,100) (xea(j,1),j=15,19)
c     write(35,100) (xea(j,1),j=20,24)
c     write(36,100) (xea(j,1),j=25,29)
c     write(37,100) (xea(j,1),j=30,34)
      write(41,100) tea(1), (dxdtea(j,1),j=2,8,2)
      write(42,100) (dxdtea(j,1),j=10,18,2)                        210
      write(43,100) (dxdtea(j,1),j=20,28,2)
      write(44,300) (dxdtea(j,1),j=30,34,2)
      write(48,200) dxdtea(16,1)
      write(70,100) rea(1)
100   format(1x,5(e17.10,2x))
c     1x = carriage control, space in first column, necessary
c       for some printers
c     5 = # of fields; e = exponential, d = double precision;
c       17 = total field width, 17 columns;
c       10 # decimals right of decimal point; 2x = two             220
c       empty columns between each field
200   format(1x,1(e17.10))
300   format(1x,3(e17.10,2x))
      ninterp=ninterp+1
      p=dfloat(ninterp)-1.
      te=p/sr
      nframes=nframes+1
      pp=2.**kk
      if (nframes.eq.4096) then
        write(6,*) 'te = ',te                                      230
        ttt=t
c       drive update
        rewind(48)
        call spectrum(cdata,m,k,w1,w2)
        rewind(48)
        do 17 i=1,m
          write(52,200) cdata(i)
          write(53,200) dref(i)
17      continue
        if(ninit.eq.1) then                                        240
          do 18 j=1,m
            dold(j)=dref(j)
            cold(j)=cdata(j)
            ninit=ninit+1
18        continue
        endif
        do 19 j=1,m
          cexp(j)=(1-1/pp)*cold(j)+(1/pp)*cdata(j)
          drive(j)=dold(j)*(dref(j)/cexp(j))
```

```
          cold(j)=cexp(j)                                                    250
          dold(j)=(1-1/pp)*dold(j)+(1/pp)*drive(j)
          write(56,200) cexp(j)
          write(57,200) drive(j)
19        continue
        m44=4*m+4
        m43=4*m+3
        do 20 j=1,m
          drive(j) = (drive(j))**(0.5)
20        continue
        do 21 j=2,m                                                          260
          j2=2*j
          dinterim(j2-1)=drive(j)*cos(b(j+jupdate*128)*2*
     *3.141592653589793)
          dinterim(j2)=drive(j)*sin(b(j+jupdate*128)*2*
     *3.141592653589793)
          dinterim(m44-j2)=-(dinterim(j2))
          dinterim(m43-j2)=dinterim(j2-1)
21        continue
        do 22 j=1,2
          dinterim(j)=0                                                      270
          dinterim(j+256)=0
22        continue
        do 23 j=1,512
          write(54,200) dinterim(j)
23        continue
        call fft(dinterim,256,-1)
        do 24 j=1,512
          write(58,200) dinterim(j)
24        continue
        nkount = 1                                                           280
        do 25 j=1,511,2
c         imaginary part is negligible
          dinterim(nkount) = dinterim(j)
          nkount = nkount + 1
25        continue
        do 27 j=1,256
c       Divide by 16 instead of dividing by 256 since have
c         not multiplied by delta frequency above where took
c         square root.
          a(j)=dinterim(j)/16.                                               290
          do 26 i = 1,15
            a(j+256*i)=a(j)
26          continue
27        continue
        do 28 i =1,4096
          write(55,200) a(i)
28        continue
        call filter(a)
        do 29 i=1,4096
          write(59,200) a(i)                                                 300
29        continue
        nframes=0
        jupdate=jupdate+1
```

```
      endif
     endif
     if ((te-tf)*(tf-t0).ge.zero) then
      return
     else if (jupdate.eq.updates) then
      return
     else                                                          310
      goto 2
     endif
     end

c    rkqc (one "quality controlled" runge kutta step)

     subroutine rkqc(x,dxdt,n,t,htry,eps,xscal,hdid,hnext)
     implicit double precision (a-h, o-z), integer(i-n)
     parameter (nmax=38,fcor=.0666666667,
    *one=1.,safety=0.9,errcon=6.e-4)                               320
c    safety because error estimates not exact
c    fcor = 1/15
c    errcon = (4/safety)**(1/pgrow)
c    external derivs
     dimension x(n),dxdt(n),xscal(n),xtemp(nmax),xsav(nmax),
    *dxsav(nmax)
c    xscal(n) is the vector against which the error is scaled
     pgrow=-0.20
     pshrnk=-0.25
     tsav=t                                                        330
c    save initial values
     do 11 i=1,n
      xsav(i)=x(i)
      dxsav(i)=dxdt(i)
11   continue
c    htry = initial step size to be attempted
     h=htry
c    take two half steps
1    hh=0.5*h
     call rk4(xsav,dxsav,n,tsav,hh,xtemp)                          340
     t=tsav+hh
     call derivs(t,xtemp,dxdt)
     call rk4(xtemp,dxdt,n,t,hh,x)
     t=tsav+h
     if(t.eq.tsav) then
      pause 'step size not significant in rkqc.'
     endif
c    take the large step
     call rk4(xsav,dxsav,n,tsav,h,xtemp)
     errmax=0.                                                     350
c    evaluate accuracy
     do 12 i=1,n
      xtemp(i)=x(i)-xtemp(i)
c     x(i) = value from 2-step, xtemp(i) = value from big step
c     xtemp now contains the error estimate
      errmax=max(errmax,abs(xtemp(i)/xscal(i)))
c     xtemp(i) = difference, xscal(i) = absolute+euler step+tiny
```

```
12    continue
      errmax=errmax/eps
c     scale relative to required tolerance                                  360
      if(errmax.gt.one) then
c     truncation error too large, reduce step size
        h=safety*h*(errmax**pshrnk)
c         = .9h*errmaxˆ−.25
        goto 1
c       for another try
      else
c     step succeeded, compute size of next step
        hdid=h
c       hdid = the step size which was actually accomplished                370
        if(errmax.gt.errcon)then
c       errcon = 6e−4
          hnext=safety*h*(errmax**pgrow)
c             =.9h*errmaxˆ−.2
c         reduces or increases step size proportional to error
c         hnext = the estimated next step size
        else
          hnext=4.*h
c         if error was very small, increases step size
        endif                                                               380
      endif
      do 13 i=1,n
c     mop up fifth−order truncation error
        x(i)=x(i)+xtemp(i)*fcor
c       x(i) = value from two step method + correction term
13    continue
      return
      end

c     rk4 (one runge kutta step on a set of n differential equations)       390
      subroutine rk4(x,dxdt,n,t,h,xout)
      implicit double precision (a−h, o−z), integer(i−n)
      parameter (nmax=38)
      dimension x(n),dxdt(n),xout(n),xt(nmax),dxt(nmax),dxm(nmax)
      hh=h*0.5
      h6=h/6.
      th=t+hh
      do 11 i=1,n
c     first step
        xt(i)=x(i)+hh*dxdt(i)                                               400
11    continue
      call derivs(th,xt,dxt)
c     second step
      do 12 i=1,n
        xt(i)=x(i)+hh*dxt(i)
12    continue
      call derivs(th,xt,dxm)
c     third step
      do 13 i=1,n
        xt(i)=x(i)+h*dxm(i)                                                 410
        dxm(i)=dxt(i)+dxm(i)
```

```
13    continue
      call derivs(t+h,xt,dxt)
c     fourth step
      do 14 i=1,n
c     accumulate increments with proper weights
        xout(i)=x(i)+h6*(dxdt(i)+dxt(i)+2.*dxm(i))
c       xout(i)=x(i)+k1/6+k2/3+k3/3+k4/6
14    continue
      return                                                          420
      end

      subroutine derivs(t,x,dxdt)
      implicit double precision (a-z)
      dimension x(38),dxdt(38)
      call input(t,rin)
      m1=11.7
      m2=24
      m3=11.7
      m4=22.2                                                         430
      m5=44.4
      m6=22.2
      m7=11.1
      m8=22.2
      m9=11.1
      ma=7.2
      mb=7.2
      mg=10.6
      mh=10.6
      mc=3.4                                                          440
      md=3.4
      me=1.2
      mf=1.2
      mk=14.4
      ml=6.8
c     Shear Springs
      k21=-1.0550e9
      k32=-1.0550e9
      k54=-3.3948e8
      k65=-3.3948e8                                                   450
      k87=-1.6974e8
      k98=-1.6974e8
      kba=-2.2432e10
      kdc=-2.6638e9
      kfe=-6.2115e8
      khg=-2.4992e10
c     Longitudinal Springs
      k41=8.1234e8
      k52=1.6247e9
      k63=8.1234e8                                                    460
      k74=8.1234e8
      k85=1.6247e9
      k96=8.1234e8
      k1e=1.5878e9
      k2e=4.3688e9
```

```
      k2f=4.3688e9
      k3f=1.5878e9
      kec=9.4610e8
      kfd=9.4610e8
      kcg=2.6513e9                                                    470
      kdh=2.6513e9
      kga=2.2399e10
      khb=2.2399e10
c     Diagonal Springs
      k42=6.4261e8
      k51=6.4261e8
      k53=6.4261e8
      k62=6.4261e8
      k75=6.4261e8
      k84=6.4261e8                                                    480
      k86=6.4261e8
      k95=6.4261e8
      ked=1.4946e8
      kfc=1.4946e8
      kcl=7.4832e9
      kdl=7.4832e9
      kgl=5.5688e9
      khl=5.5688e9
      kgk=4.6446e10
      khk=4.6446e10                                                   490
      kak=4.3865e10
      kbk=4.3865e10
c     Shear
      c21=229.
      c32=229.
      c54=335.
      c65=335.
      c87=229.
      c98=229.
      cba=325.                                                        500
      cdc=317.
      cfe=764.
      chg=317.
c     Longitudinal
      c41=2409.
      c52=1673.
      c63=2409.
      c74=2409.
      c85=1673.
      c96=2409.                                                       510
      c1e=2442.
      c2e=4284.
      c2f=4284.
      c3f=2442.
      cec=5457.
      cfd=5457.
      ccg=7926.
      cdh=7926.
      cga=10840.
```

```
      chb=10840.                                                                520
c     Diagonal
      c42=1339.
      c51=1927.
      c53=1927.
      c62=1339.
      c75=1927.
      c84=1339.
      c86=1339.
      c95=1927.
      ccl=1110.                                                                 530
      cdl=1110.
      cgl=1110.
      chl=1110.
      cgk=325.
      chk=325.
      cak=325.
      cbk=325.
      ced=873.
      cfc=873.
      dxdt(1)=x(2)                                                              540
      dxdt(2)=(k41/m1)*(x(7)-x(1))+(c41/m1)*(x(8)-x(2))+(k21/m1)*
     *(x(3)-x(1))+(c21/m1)*(x(4)-x(2))+(k1e/m1)*(x(31)-x(1))+
     *(c1e/m1)*(x(32)-x(2))+(k51/m1)*(x(9)-x(1))+(c51/m1)*
     *(x(10)-x(2))
      dxdt(3)=x(4)
      dxdt(4)=(k21/m2)*(x(1)-x(3))+(c21/m2)*(x(2)-x(4))+(k32/m2)*
     *(x(5)-x(3))+(c32/m2)*(x(6)-x(4))+(k52/m2)*(x(9)-x(3))+
     *(c52/m2)*(x(10)-x(4))+(k2e/m2)*(x(31)-x(3))+(c2e/m2)*
     *(x(32)-x(4))+(k2f/m2)*(x(33)-x(3))+(c2f/m2)*(x(34)-x(4))+
     *(k62/m2)*(x(11)-x(3))+(c62/m2)*(x(12)-x(4))+(k42/m2)*                     550
     *(x(7)-x(3))+(c42/m2)*(x(8)-x(4))
      dxdt(5)=x(6)
      dxdt(6)=(k32/m3)*(x(3)-x(5))+(c32/m3)*(x(4)-x(6))+(k63/m3)*
     *(x(11)-x(5))+(c63/m3)*(x(12)-x(6))+(k3f/m3)*(x(33)-x(5))+
     *(c3f/m3)*(x(34)-x(6))+(k53/m3)*(x(9)-x(5))+(c53/m3)*
     *(x(10)-x(6))
      dxdt(7)=x(8)
      dxdt(8)=(k41/m4)*(x(1)-x(7))+(c41/m4)*(x(2)-x(8))+(k54/m4)*
     *(x(9)-x(7))+(c54/m4)*(x(10)-x(8))+(k74/m4)*(x(13)-x(7))+
     *(c74/m4)*(x(14)-x(8))+(k84/m4)*(x(15)-x(7))+(c84/m4)*                     560
     *(x(16)-x(8))+(k42/m4)*(x(3)-x(7))+(c42/m4)*(x(4)-x(8))
      dxdt(9)=x(10)
      dxdt(10)=(k52/m5)*(x(3)-x(9))+(c52/m5)*(x(4)-x(10))+
     *(k54/m5)*(x(7)-x(9))+(c54/m5)*(x(8)-x(10))+(k65/m5)*
     *(x(11)-x(9))+(c65/m5)*(x(12)-x(10))+(k85/m5)*(x(15)-x(9))+
     *(c85/m5)*(x(16)-x(10))+(k95/m5)*(x(17)-x(9))+(c95/m5)*
     *(x(18)-x(10))+(k75/m5)*(x(13)-x(9))+(c75/m5)*(x(14)-x(10))+
     *(k53/m5)*(x(5)-x(9))+(c53/m5)*(x(6)-x(10))+(k51/m5)*
     *(x(1)-x(9))+(c51/m5)*(x(2)-x(10))
      dxdt(11)=x(12)                                                            570
      dxdt(12)=(k63/m6)*(x(5)-x(11))+(c63/m6)*(x(6)-x(12))+
     *(k65/m6)*(x(9)-x(11))+(c65/m6)*(x(10)-x(12))+(k96/m6)*
     *(x(17)-x(11))+(c96/m6)*(x(18)-x(12))+(k86/m6)*(x(15)-x(11))+
```

```
*(c86/m6)*(x(16)-x(12))+(k62/m6)*(x(3)-x(11))+(c62/m6)*
*(x(4)-x(12))
 dxdt(13)=x(14)
 dxdt(14)=(k74/m7)*(x(7)-x(13))+(c74/m7)*(x(8)-x(14))+
*(k87/m7)*(x(15)-x(13))+(c87/m7)*(x(16)-x(14))+(k75/m7)*
*(x(9)-x(13))+(c75/m7)*(x(10)-x(14))
 dxdt(15)=x(16)                                                    580
 dxdt(16)=(k87/m8)*(x(13)-x(15))+(c87/m8)*(x(14)-x(16))+
*(k85/m8)*(x(9)-x(15))+(c85/m8)*(x(10)-x(16))+(k98/m8)*
*(x(17)-x(15))+(c98/m8)*(x(18)-x(16))+(k86/m8)*(x(11)-x(15))+
*(c86/m8)*(x(12)-x(16))+(k84/m8)*(x(7)-x(15))+
*(c84/m8)*(x(8)-x(16))
 dxdt(17)=x(18)
 dxdt(18)=(k98/m9)*(x(15)-x(17))+(c98/m9)*(x(16)-x(18))+
*(k96/m9)*(x(11)-x(17))+(c96/m9)*(x(12)-x(18))+(k95/m9)*
*(x(9)-x(17))+(c95/m9)*(x(10)-x(18))
 dxdt(19)=x(20)                                                    590
 dxdt(20)=rin
 dxdt(21)=x(22)
 dxdt(22)=rin
 dxdt(23)=x(24)
 dxdt(24)=(kga/mg)*(x(19)-x(23))+(cga/mg)*(x(20)-x(24))+
*(khg/mg)*(x(25)-x(23))+(chg/mg)*(x(26)-x(24))+(kcg/mg)*
*(x(27)-x(23))+(ccg/mg)*(x(28)-x(24))+(kgl/mg)*(x(37)-x(23))+
*(cgl/mg)*(x(38)-x(24))+(kgk/mg)*(x(35)-x(23))+(cgk/mg)*
*(x(36)-x(24))
 dxdt(25)=x(26)                                                    600
 dxdt(26)=(khb/mh)*(x(21)-x(25))+(chb/mh)*(x(22)-x(26))+
*(khg/mh)*(x(23)-x(25))+(chg/mh)*(x(24)-x(26))+(kdh/mh)*
*(x(29)-x(25))+(cdh/mh)*(x(30)-x(26))+(khl/mh)*(x(37)-x(25))+
*(chl/mh)*(x(38)-x(26))+(khk/mh)*(x(35)-x(25))+(chk/mh)*
*(x(36)-x(26))
 dxdt(27)=x(28)
 dxdt(28)=(kcg/mc)*(x(23)-x(27))+(ccg/mc)*(x(24)-x(28))+
*(kdc/mc)*(x(29)-x(27))+(cdc/mc)*(x(30)-x(28))+(kec/mc)*
*(x(31)-x(27))+(cec/mc)*(x(32)-x(28))+(kfc/mc)*(x(33)-x(27))+
*(cfc/mc)*(x(34)-x(28))+(kcl/mc)*(x(37)-x(27))+(ccl/mc)*          610
*(x(38)-x(28))
 dxdt(29)=x(30)
 dxdt(30)=(kdh/md)*(x(25)-x(29))+(cdh/md)*(x(26)-x(30))+
*(kdc/md)*(x(27)-x(29))+(cdc/md)*(x(28)-x(30))+(kfd/md)*
*(x(33)-x(29))+(cfd/md)*(x(34)-x(30))+(ked/md)*(x(31)-x(29))+
*(ced/md)*(x(32)-x(30))+(kdl/md)*(x(37)-x(29))+(cdl/md)*
*(x(38)-x(30))
 dxdt(31)=x(32)
 dxdt(32)=(kec/me)*(x(27)-x(31))+(cec/me)*(x(28)-x(32))+
*(kfe/me)*(x(33)-x(31))+(cfe/me)*(x(34)-x(32))+(k1e/me)*          620
*(x(1)-x(31))+(c1e/me)*(x(2)-x(32))+(k2e/me)*(x(3)-x(31))+
*(c2e/me)*(x(4)-x(32))+(ked/me)*(x(29)-x(31))+(ced/me)*
*(x(30)-x(32))
 dxdt(33)=x(34)
 dxdt(34)=(kfd/mf)*(x(29)-x(33))+(cfd/mf)*(x(30)-x(34))+
*(kfe/mf)*(x(31)-x(33))+(cfe/mf)*(x(32)-x(34))+(k2f/mf)*
*(x(3)-x(33))+(c2f/mf)*(x(4)-x(34))+(k3f/mf)*(x(5)-x(33))+
```

```
     *(c3f/mf)*(x(6)-x(34))+(kfc/mf)*(x(27)-x(33))+(cfc/mf)*
     *(x(28)-x(34))
      dxdt(35)=x(36)                                                    630
      dxdt(36)=(kak/mk)*(x(19)-x(35))+(cak/mk)*(x(20)-x(36))+
     *(kbk/mk)*(x(21)-x(35))+(cbk/mk)*(x(22)-x(36))+(kgk/mk)*
     *(x(23)-x(35))+(cgk/mk)*(x(24)-x(36))+(khk/mk)*(x(25)-x(35))*
     *(chk/mk)*(x(26)-x(36))
      dxdt(37)=x(38)
      dxdt(38)=(kgl/ml)*(x(23)-x(37))+(cgl/ml)*(x(24)-x(38))+
     *(khl/ml)*(x(25)-x(37))+(chl/ml)*(x(26)-x(38))+(kcl/ml)*
     *(x(27)-x(37))+(ccl/ml)*(x(28)-x(38))+(kdl/ml)*(x(29)-x(37))+
     *(cdl/ml)*(x(30)-x(38))
      return                                                            640
      end

      subroutine input(t,rin)
      implicit double precision (a-h, o-z), integer(i-n)
      integer tb, ta
      parameter(zero=0.0)
      common /samprate/ sr
c     common to driver, odeint, input
c     sr = sample rate
      common /xdotdot/ a(4096)                                          650
c     common to driver, odeint, input
      common /random/ r(64),jkount
c     common to odeint, input, interpolate
      common /oldtime/ ttt
c     common to odeint,input
      tind = (t-ttt)*sr
c     tind = time corresponding to random # index
      ta = int(tind) + 1
      tb = ta + 1
      tar = dfloat(ta)/sr                                               660
      tbr = dfloat(tb)/sr
      if (tind.eq.zero) then
        rin = a(ta)
        r(jkount)=rin
        return
      endif
      if (ta.ge.4096) then
        rin = a(4096)
        r(jkount)=rin
        return                                                          670
      endif
      rin = (a(ta) +((t-ttt)-tar)*(a(tb)-a(ta))/(tbr-tar))
      r(jkount)=rin
      return
      end

c     interpolate to equal time intervals

      subroutine interpolate(te,xe,dxdte,re)
      implicit double precision (a-h, o-z), integer(i-n)                680
      parameter(zero=0.0)
```

```
      common /interp/ mkount,tp(64),xp(38,64),dxdtp(38,64)
c     common to odeint, interpolate
      common /random/ r(64),jkount
c     common to odeint, input, interpolate
      jl = 1
      ju = 64
      if (te.eq.tp(ju)) then
        xe = xp(mkount,ju)
        dxdte = dxdtp(mkount,ju)                                    690
        re = r(ju)
        return
      endif
      if (te.eq.tp(jl)) then
        xe = xp(mkount,jl)
        dxdte = dxdtp(mkount,jl)
        re = r(jl)
        return
      endif
10    if (ju-jl.gt.1) then                                          700
        jm = (ju+jl)/2
        if ((tp(64).gt.tp(1)).eqv.(te.gt.tp(jm))) then
          jl = jm
        else
          if (te.eq.tp(jm)) then
            xe = xp(mkount,jm)
            dxdte = dxdtp(mkount,jm)
            re = r(jm)
            return
          endif                                                     710
          if (te.eq.zero) then
            xe = xp(mkount,1)
            dxdte = dxdtp(mkount,1)
            re = r(1)
            return
          endif
          ju = jm
        endif
      go to 10
      endif                                                         720
      j = jl
      k = j + 1
      xe = xp(mkount,j) + (te-tp(j))*(xp(mkount,k)-xp(mkount,j))/
     *(tp(k)-tp(j))
      dxdte = dxdtp(mkount,j) + (te-tp(j))*(dxdtp(mkount,k)-
     *dxdtp(mkount,j))/(tp(k)-tp(j))
      re = r(j)+(te-tp(j))*(r(k)-r(j))/(tp(k)-tp(j))
      return
      end
                                                                    730
      subroutine fft(data,nn,isign)
c     replaces data by its discrete Fourier transform, if isign is
c     input as 1; or replaces data by nn times its inverse discrete
c     Fourier transform, if isign is input as -1. data is the array
c     to be Fourier transformed.  data is a complex array of length
```

```
c     nn (in the form real,imag,real,imag) or, equivalently, a real
c     array of length 2*nn.  nn MUST be an integer power of 2.
      implicit double precision (a-h, o-z), integer(i-n)
      dimension data(2*nn)
      n=2*nn                                                          740
      j=1
      do 11 i=1,n,2
c     this is the bit-reversal section of the routine
        if(j.gt.i) then
c         exchange the two complex numbers
          tempr=data(j)
          tempi=data(j+1)
          data(j)=data(i)
          data(j+1)=data(i+1)
          data(i)=tempr                                               750
          data(i+1)=tempi
        endif
        m=n/2
1       if ((m.ge.2).and.(j.gt.m)) then
          j=j-m
          m=m/2
          goto 1
        endif
        j=j+m
11      continue                                                      760
      mmax=2
2     if (n.gt.mmax) then
c     calculate, in turn, transforms of length 2,4,8,...,nn
c     the outer loop is executed log2nn times.
        istep=2*mmax
        theta=6.28318530717959/(isign*mmax)
        wpr=-2.*sin(0.5*theta)**2
        wpi=sin(theta)
        wr=1.0
        wi=0.0                                                        770
        do 13 m=1,mmax,2
c       here are the two nested inner loops
          do 12 i=m,n,istep
            j=i+mmax
            tempr=sngl(wr)*data(j)-sngl(wi)*data(j+1)
            tempi=sngl(wr)*data(j+1)+sngl(wi)*data(j)
            data(j)=data(i)-tempr
            data(j+1)=data(i+1)-tempi
            data(i)=data(i)+tempr
            data(i+1)=data(i+1)+tempi                                 780
12        continue
          wtemp=wr
          wr=wr*wpr-wi*wpi+wr
          wi=wi*wpr+wtemp*wpi+wi
13      continue
        mmax=istep
      goto 2
c     not yet done
      endif
```

```
c     all done                                                              790
      return
      end

      subroutine spectrum(p,m,k,w1,w2)
c     p is the array containing the output spectrum (PSD)
c     m=number of points in 1/2 a segment (i.e. overlap length)
c     k is the number of segments of data;each is n=2m points long
c     w1 and w2 are workspaces to be used by this subroutine
c     reads data from input unit 9 and returns as p(j) the datas
c     power (mean square amplitude) at frequency (j-1)/(2*m) cycles         800
c     per gridpoint, for j=1,2,...,m based on (2*k+1)*m data
c     points.  The number of segments of the data is 2*k.
c     The routine calls fft k times, each call with
c     2 partitions each of 2*m real data points.
      implicit double precision (a-h, o-z), integer(i-n)
      dimension p(m), w1(4*m), w2(m)
      common /file/ ifile
c     common to driver, odeint, spectrum
      common /inputlevel/ rlev
c     common to driver, spectrum                                            810
c     rlev=factor raw input is multiplied by
      window(j)=0.5*(1.-cos(6.28318530717959*j/(m+1)))
c     Hanning window
c     useful factors:
      mm=m+m
      m4=mm+mm
      m44=m4+4
      m43=m4+3
      den=0.
      sumw=0.                                                               820
      do 11 j=1,mm
c     accumulate the squared sum of the weights.
        sumw=sumw+window(j)**2
11    continue
      do 12 j=1,m
c     initialize the spectrum to zero.
        p(j)=0.
12    continue
c     initialize the "save" half-buffer
      if(ifile.eq.1) then                                                   830
        read(50,*) (w2(j),j=1,m)
        do 13 j=1,m
          w2(j)=w2(j)*rlev
13      continue
      else
        read(48,*) (w2(j),j=1,m)
      endif
      do 20 kk=1,k
c     loop over data set segments in groups of two
        do 17 joff=-1,0,1                                                   840
c       get two complete segments into workspace
          do 14 j=1,m
            w1(joff+j+j)=w2(j)
```

```
14       continue
         if(ifile.eq.1) then
           read(50,*) (w2(j),j=1,m)
           do 15 j=1,m
             w2(j)=w2(j)*rlev
15         continue
         else                                                          850
           read(48,*) (w2(j),j=1,m)
         endif
         joffn=joff+mm
         do 16 j=1,m
           w1(joffn+j+j)=w2(j)
16       continue
17     continue
       do 18 j=1,mm
c      apply the window to the data
         j2=j+j                                                        860
         w=window(j)
         w1(j2)=w1(j2)*w
         w1(j2-1)=w1(j2-1)*w
18     continue
       call fft(w1,mm,1)
c      Fourier transform the windowed data
       p(1)=p(1)+w1(1)**2+w1(2)**2
c      sum results into previous segments
       do 19 j=2,m
         j2=j+j                                                        870
c        add beginning and end - one-sided spectral density
         p(j)=p(j)+w1(j2)**2+w1(j2-1)**2+w1(m44-j2)**2+w1(m43-j2)**2
19     continue
       den=den+sumw
20   continue
     den=4*den
c    correct normalization
     do 21 j=1,m
c    normalize the output
       p(j)=p(j)/den                                                 880
21   continue
     return
     end

     subroutine filter(y)
     implicit double precision (a-h, o-z), integer(i-n)
     dimension bb(9), aa(9), j(8), x(4096),y(4096)
c    Filter the data using a butterworth filter
c    bb and aa are the filter coefficients obtained from matlab
     bb(1) = 9.106016795404703e-02                                     890
     bb(2) = 4.440892098500626e-16
     bb(3) = -3.642406718161926e-01
     bb(4) = 1.065814103640150e-14
     bb(5) = 5.463610077242724e-01
     bb(6) = 5.995204332975845e-15
     bb(7) = -3.642406718161929e-01
     bb(8) = 1.387778780781446e-15
```

```
      bb(9) = 9.106016795404741e-02
      aa(1) = 1.000000000000000e+00
      aa(2) = -3.976098458961965e+00                                    900
      aa(3) = 6.438469646248612e+00
      aa(4) = -5.936856102361906e+00
      aa(5) = 3.966671732876289e+00
      aa(6) = -2.038495680342456e+00
      aa(7) = 6.063527349318363e-01
      aa(8) = -7.773803694252523e-02
      aa(9) = 1.769425610279400e-02
c     Initialize the x values
      do 10 i = 1,4096
        x(i) = y(i)                                                     910
10    continue
      do 11 i = 1,8
        j(i)=0
11    continue
      do 12 i = 1,8
        y(i) = bb(1)*x(i)+j(1)*bb(2)*x(i-1)+j(2)*bb(3)*x(i-2)+j(3)*
     *bb(4)*x(i-3)+j(4)*bb(5)*x(i-4)+j(5)*bb(6)*x(i-5)+j(6)*bb(7)*
     *x(i-6)+j(7)*bb(8)*x(i-7)+j(8)*bb(9)*x(i-8)-j(1)*aa(2)*y(i-1)-
     *j(2)*aa(3)*y(i-2)-j(3)*aa(4)*y(i-3)-j(4)*aa(5)*y(i-4)-j(5)*
     *aa(6)*y(i-5)-j(6)*aa(7)*y(i-6)-j(7)*aa(8)*y(i-7)-j(8)*aa(9)*      920
     *y(i-8)
        j(i)=1
12    continue
      do 13 i = 9,4096
        y(i) = bb(1)*x(i)+bb(2)*x(i-1)+bb(3)*x(i-2)+bb(4)*x(i-3)+bb(5)*
     *x(i-4)+bb(6)*x(i-5)+bb(7)*x(i-6)+bb(8)*x(i-7)+bb(9)*x(i-8)-aa(2)*
     *y(i-1)-aa(3)*y(i-2)-aa(4)*y(i-3)-aa(5)*y(i-4)-aa(6)*y(i-5)-
     *aa(7)*y(i-6)-aa(8)*y(i-7)-aa(9)*y(i-8)
13    continue
c     Disregard first few filtered points corrupted by startup          930
c     transients
      do 14 i = 1,10
        y(i)=y(i)*0.1
14    continue
      return
      end
```

Appendix B

Matlab Code for Random Input

```
% Generate random, filtered numbers for input into fortran program
clear
rand('normal');
input = rand(4096,1);
wn = [0.005 0.5];
[b,a] = butter(4,wn);
in = filtfilt(b,a,input);
save random.dat in /ascii
```

Appendix C

Experimental Data

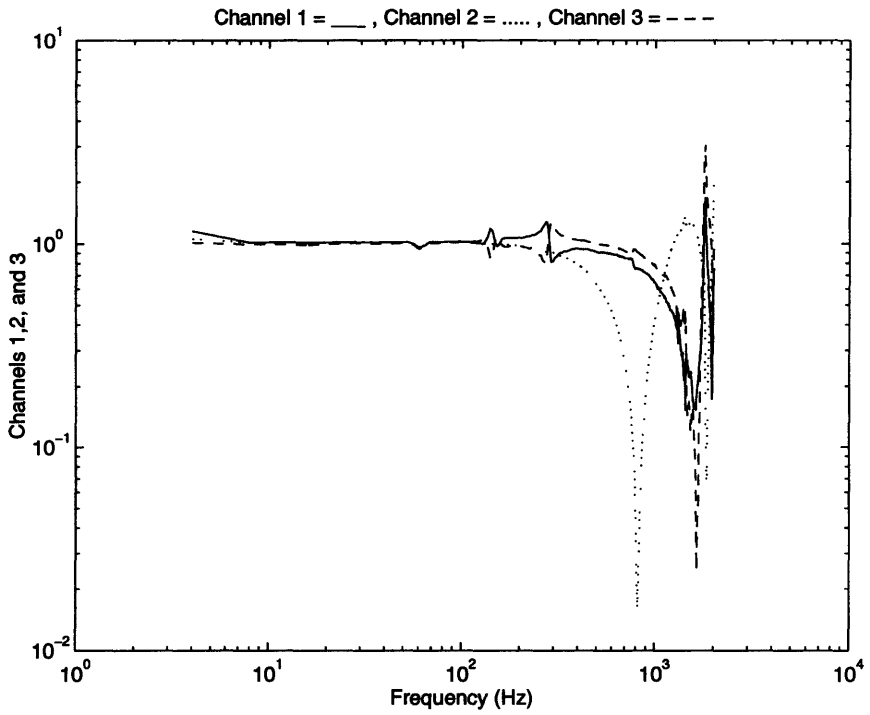

Figure C-1: X-Axis Tests, No Mass Attached–Channels 1, 2, and 3

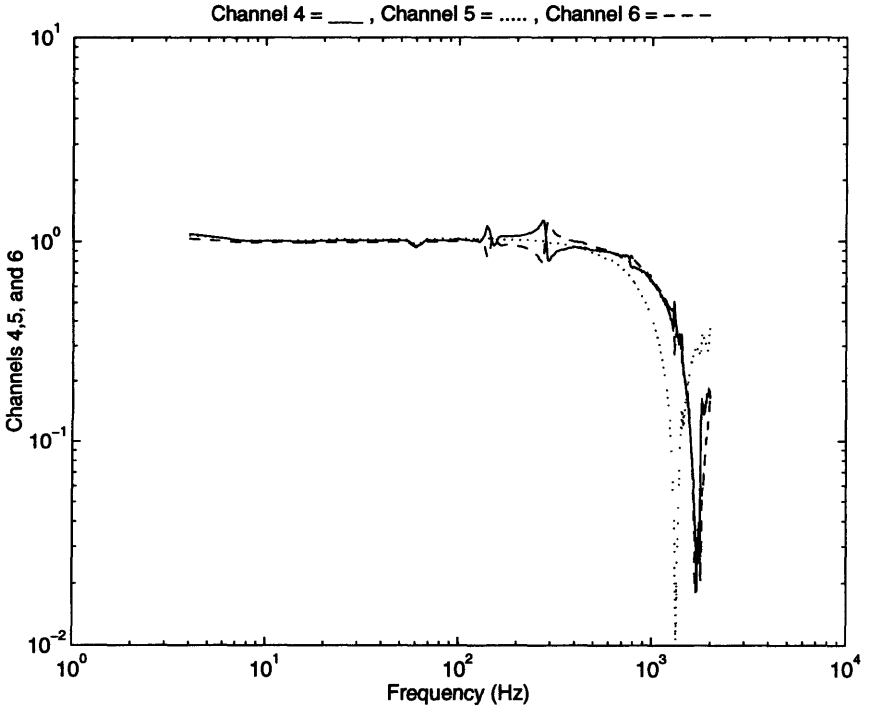

Figure C-2: X-Axis Tests, No Mass Attached–Channels 4, 5, and 6

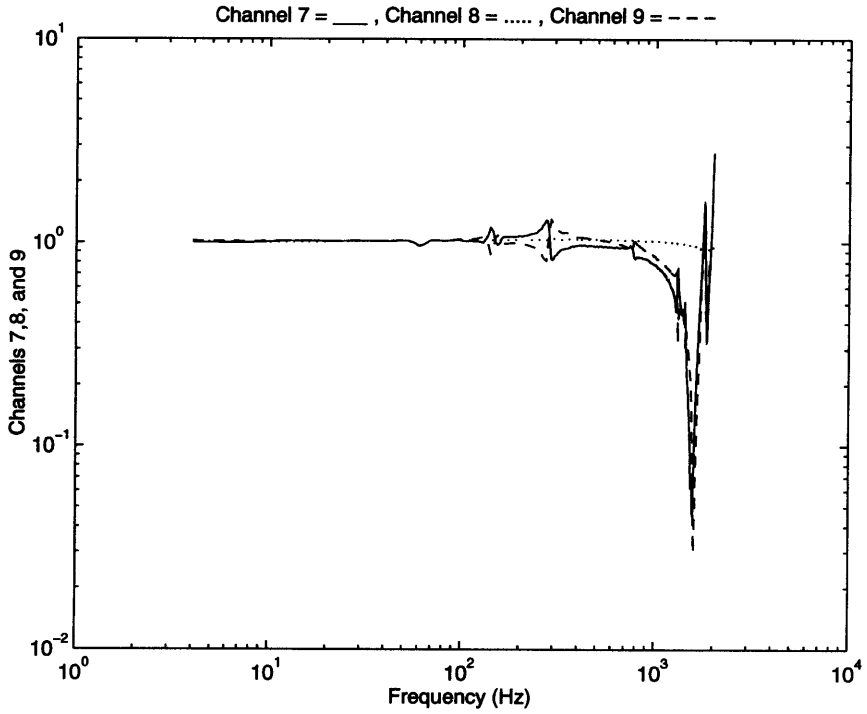

Figure C-3: X-Axis Tests, No Mass Attached–Channels 7, 8, and 9

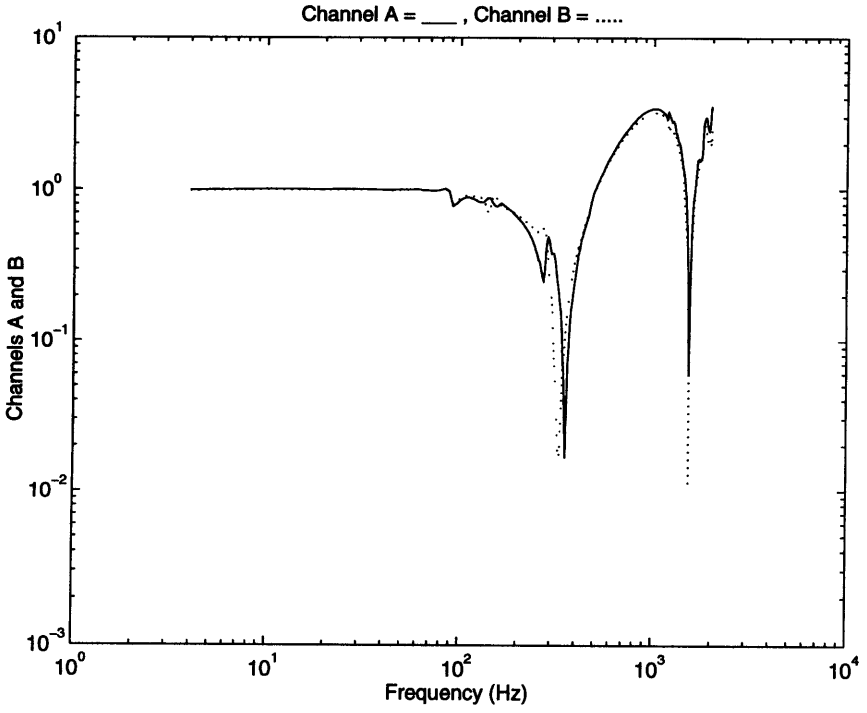

Figure C-4: X-Axis Tests, No Mass Attached–Channels A and B

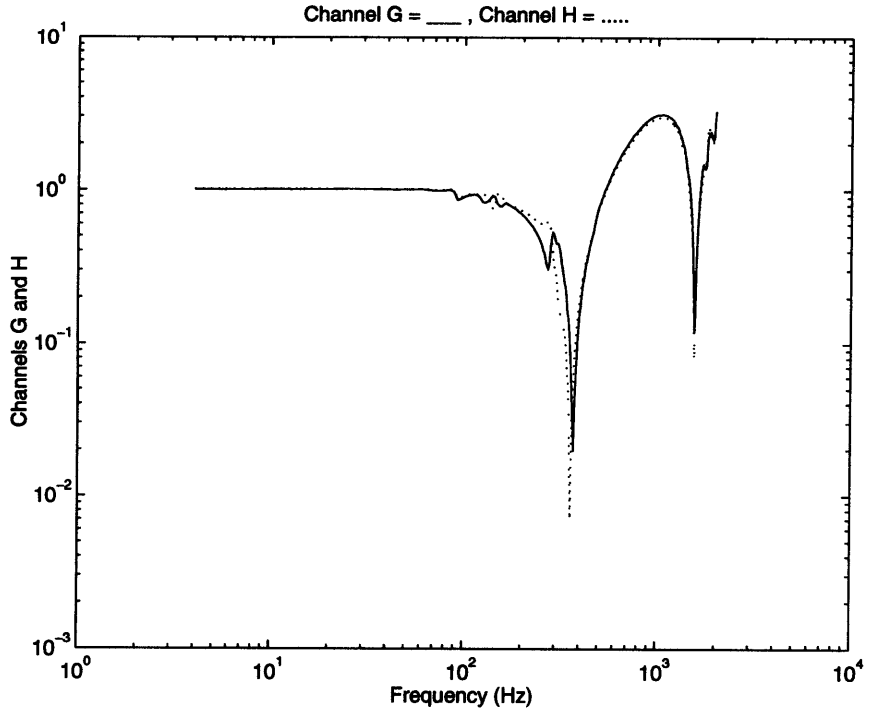

Figure C-5: X-Axis Tests, No Mass Attached–Channels G and H

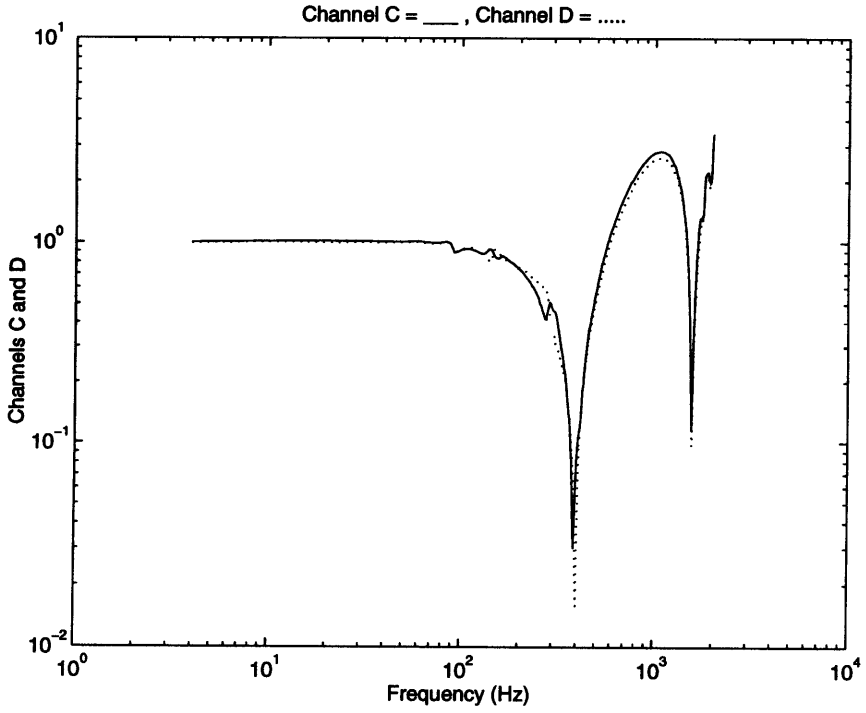

Figure C-6: X-Axis Tests, No Mass Attached–Channels C and D

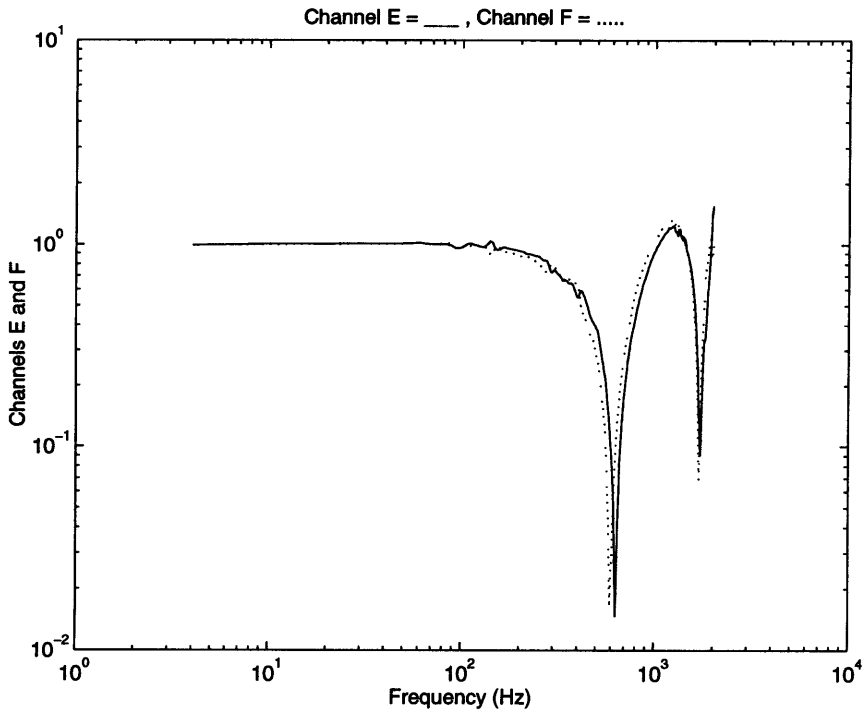

Figure C-7: X-Axis Tests, No Mass Attached–Channels E and F

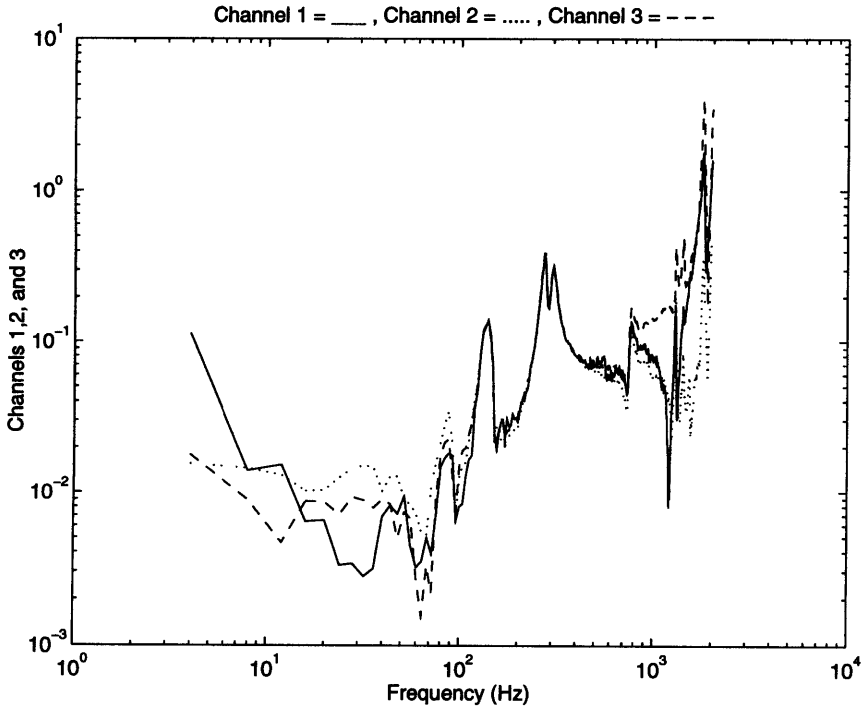

Figure C-8: Y-Axis Tests, No Mass Attached–Channels 1, 2, and 3

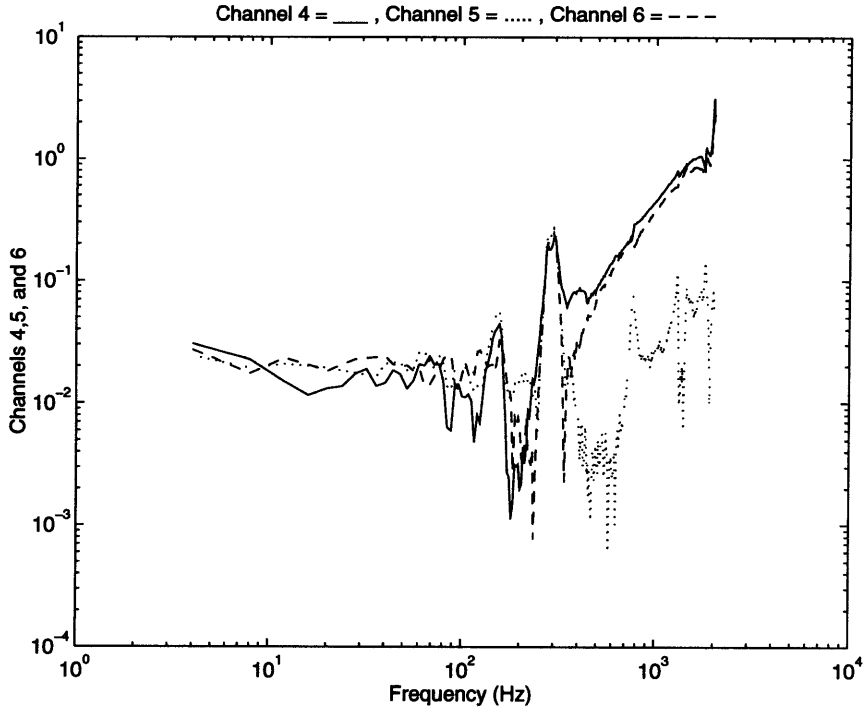

Figure C-9: Y-Axis Tests, No Mass Attached–Channels 4, 5, and 6

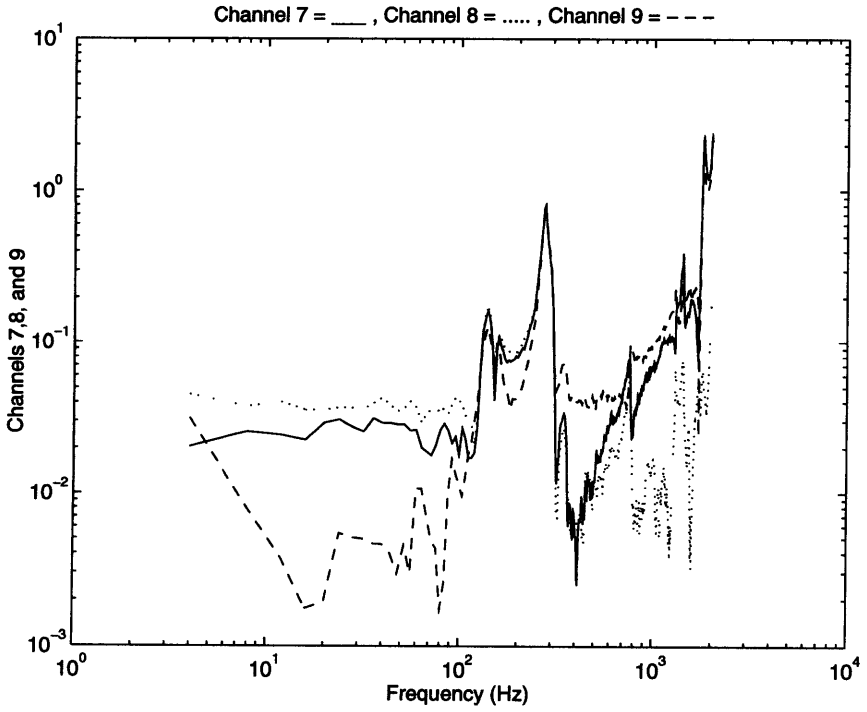

Figure C-10: Y-Axis Tests, No Mass Attached–Channels 7, 8, and 9

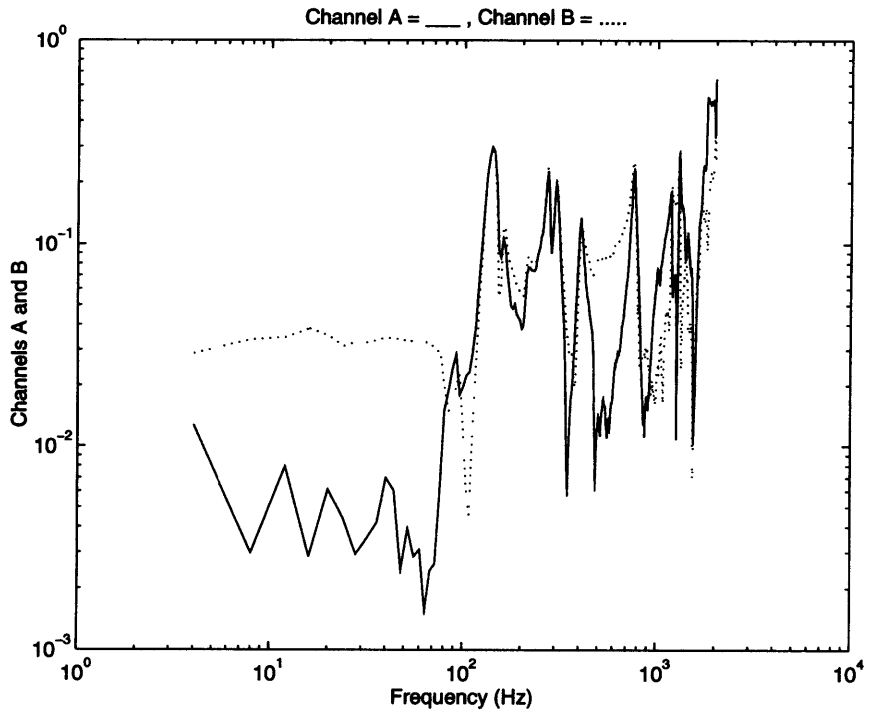

Figure C-11: Y-Axis Tests, No Mass Attached–Channels A and B

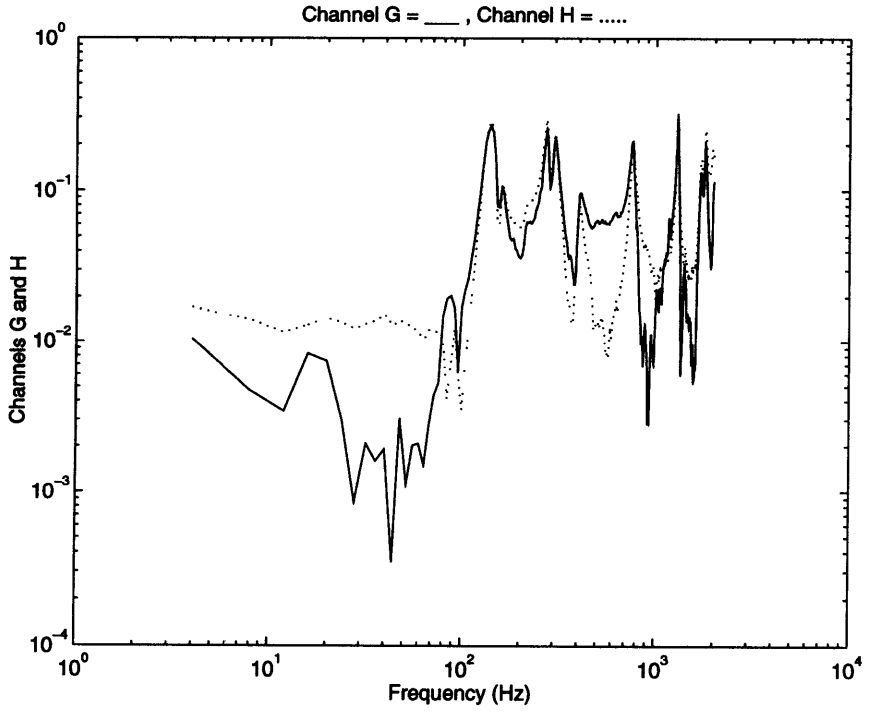

Figure C-12: Y-Axis Tests, No Mass Attached–Channels G and H

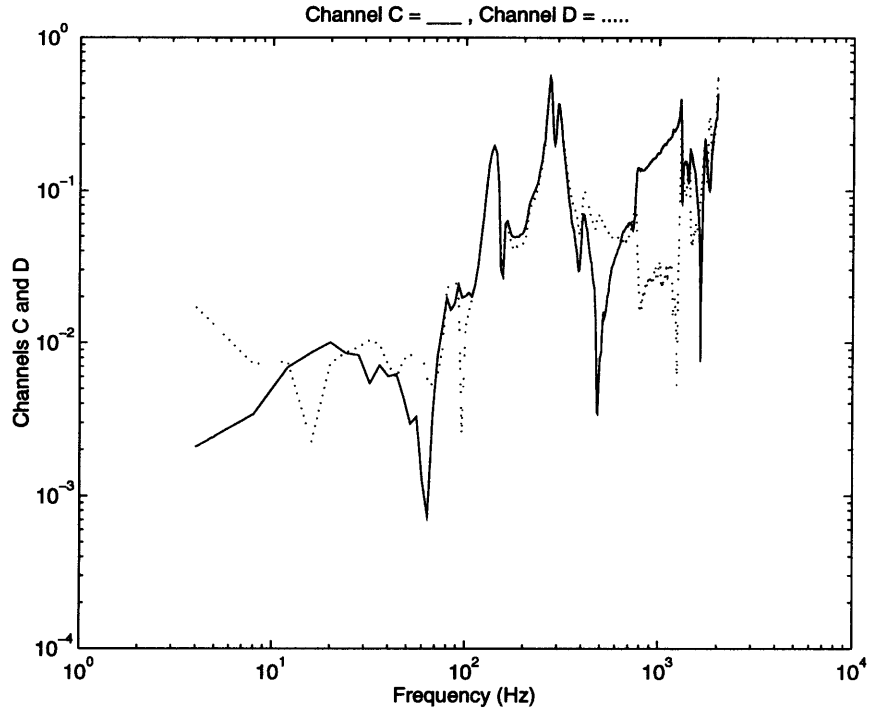

Figure C-13: Y-Axis Tests, No Mass Attached–Channels C and D

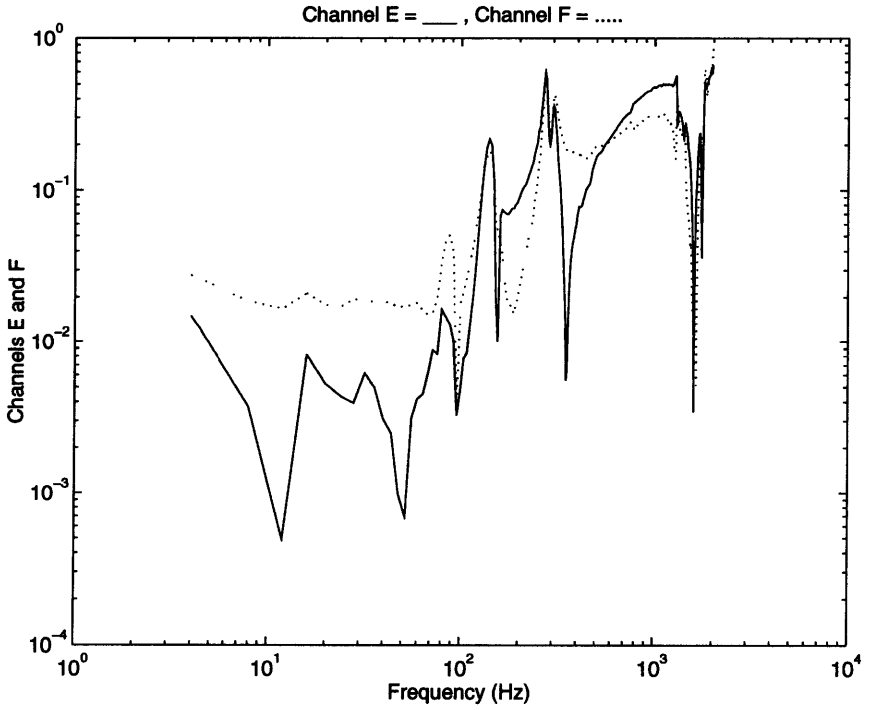

Figure C-14: Y-Axis Tests, No Mass Attached–Channels E and F

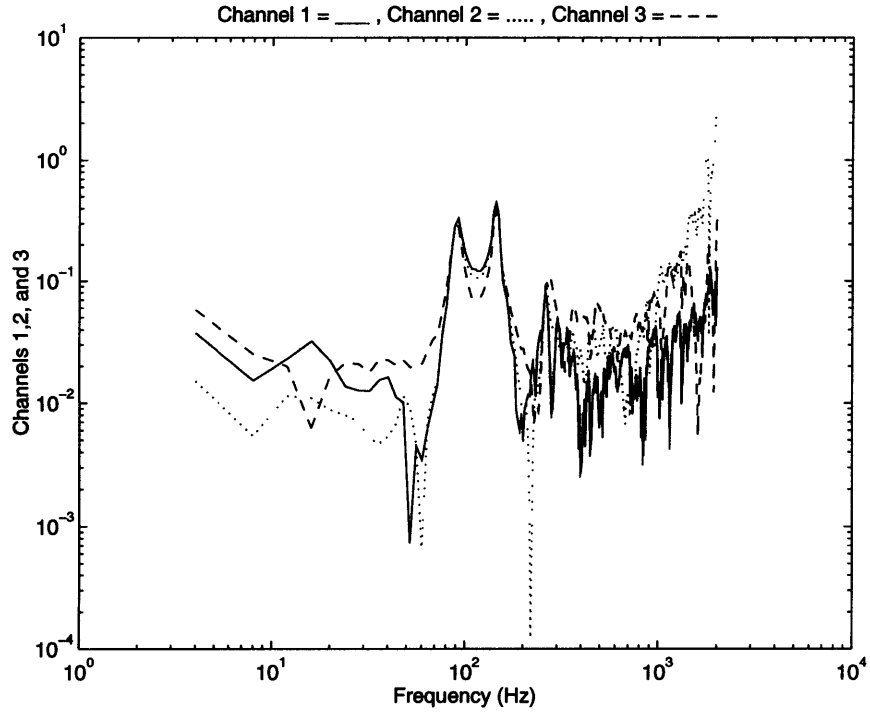

Figure C-15: Z-Axis Tests, No Mass Attached–Channels 1, 2, and 3

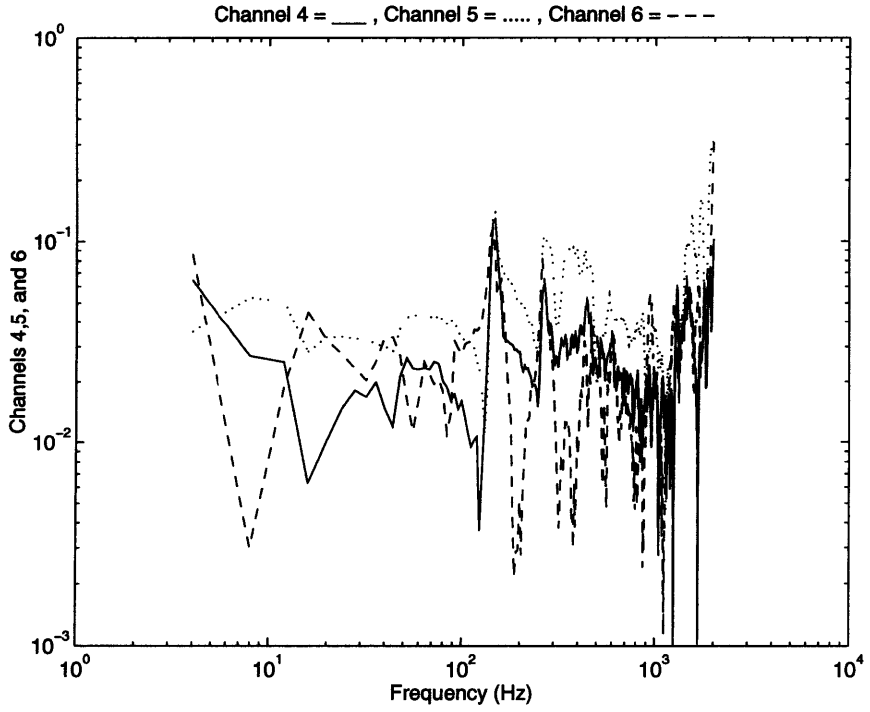

Figure C-16: Z-Axis Tests, No Mass Attached–Channels 4, 5, and 6

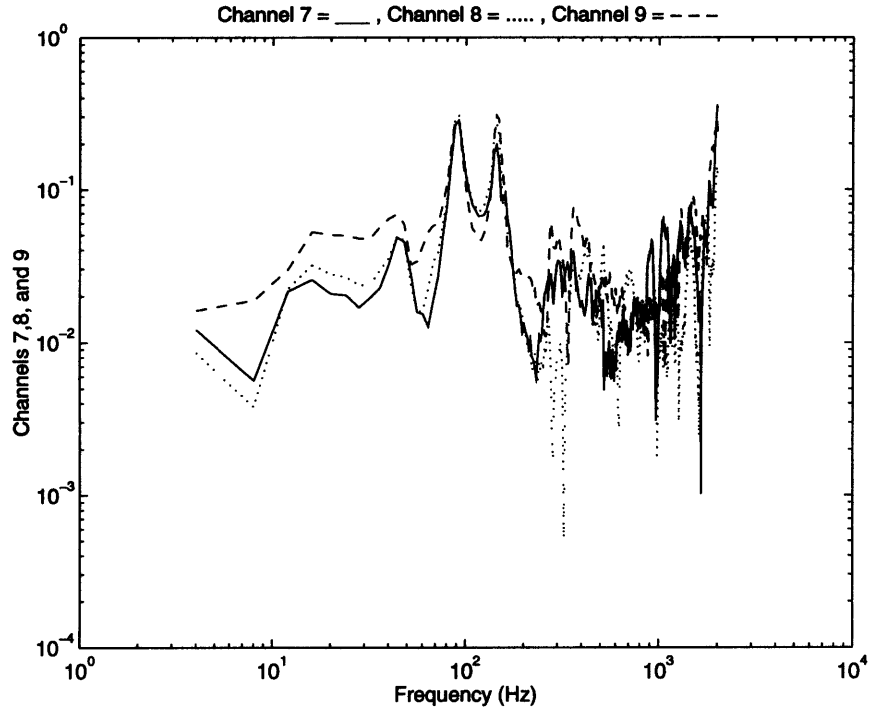

Figure C-17: Z-Axis Tests, No Mass Attached–Channels 7, 8, and 9

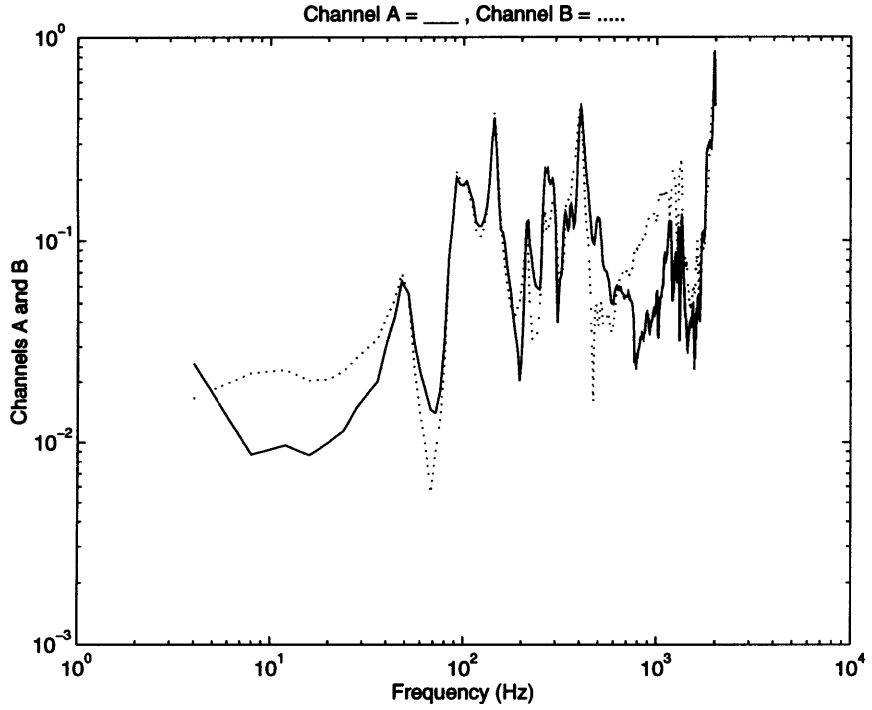

Figure C-18: Z-Axis Tests, No Mass Attached–Channels A and B

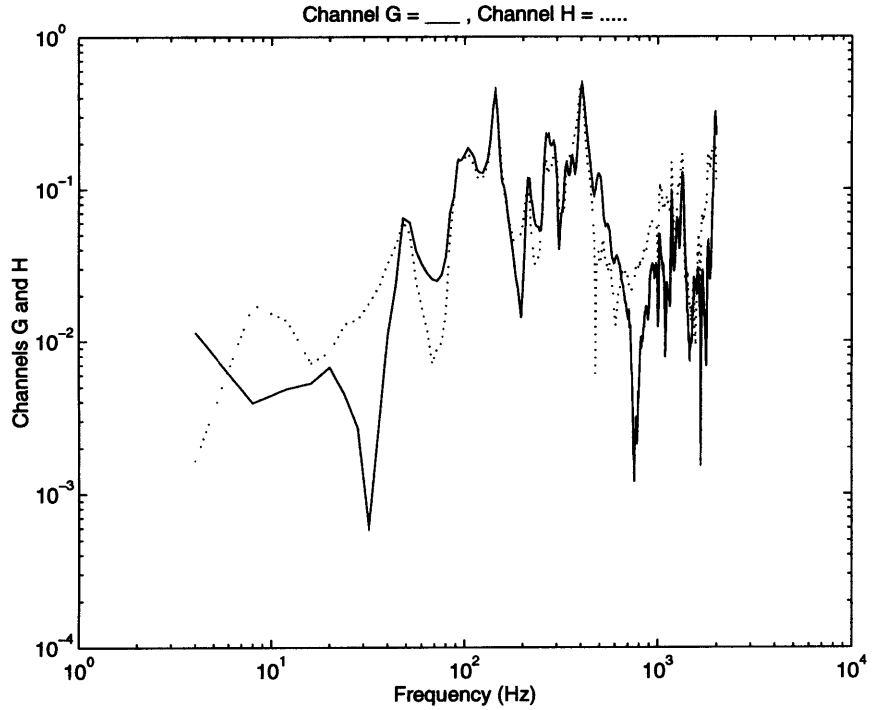

Figure C-19: Z-Axis Tests, No Mass Attached–Channels G and H

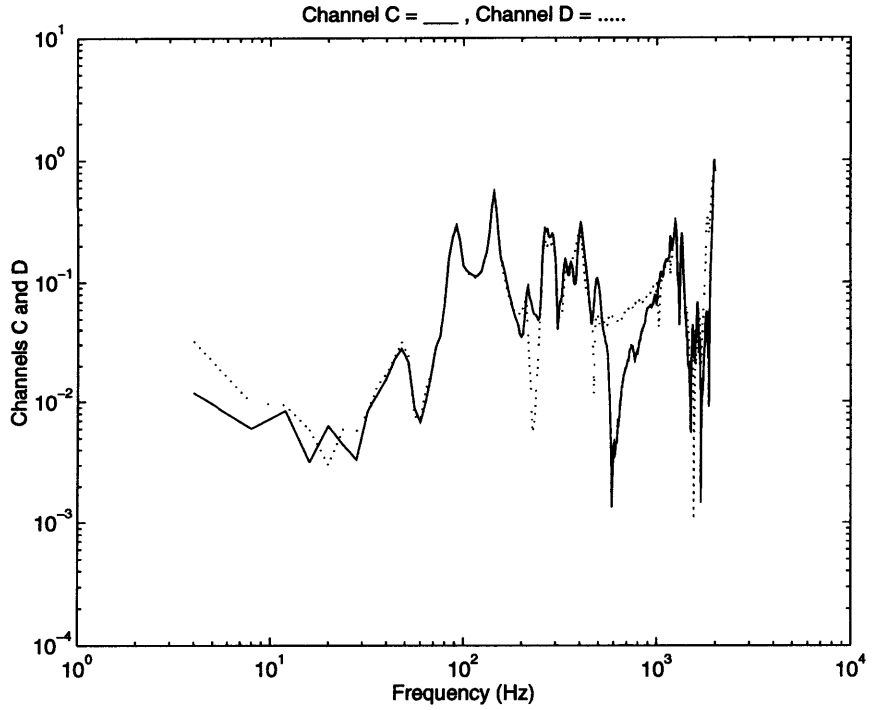

Figure C-20: Z-Axis Tests, No Mass Attached–Channels C and D

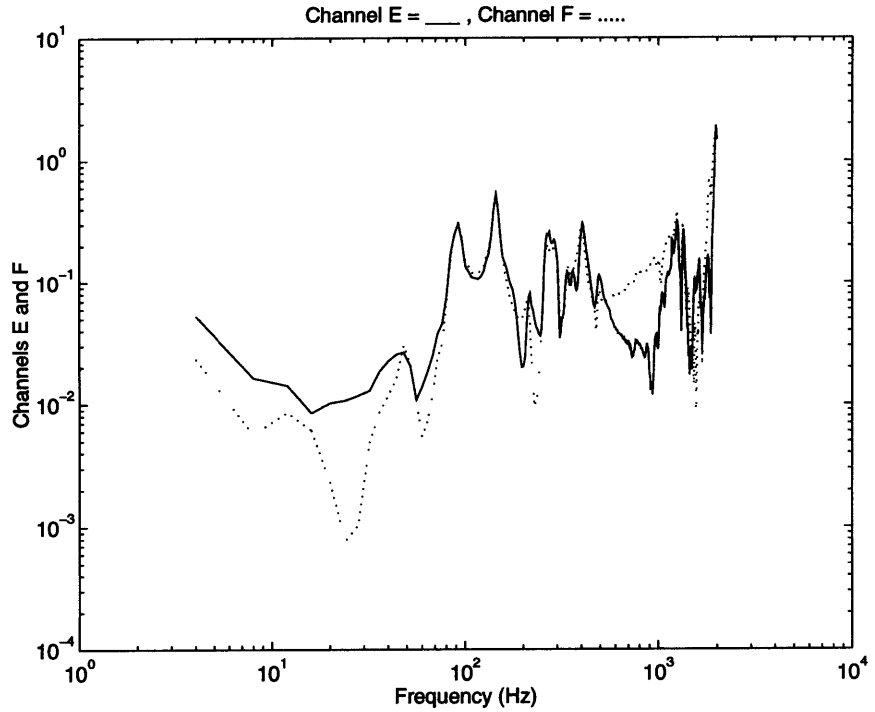

Figure C-21: Z-Axis Tests, No Mass Attached–Channels E and F

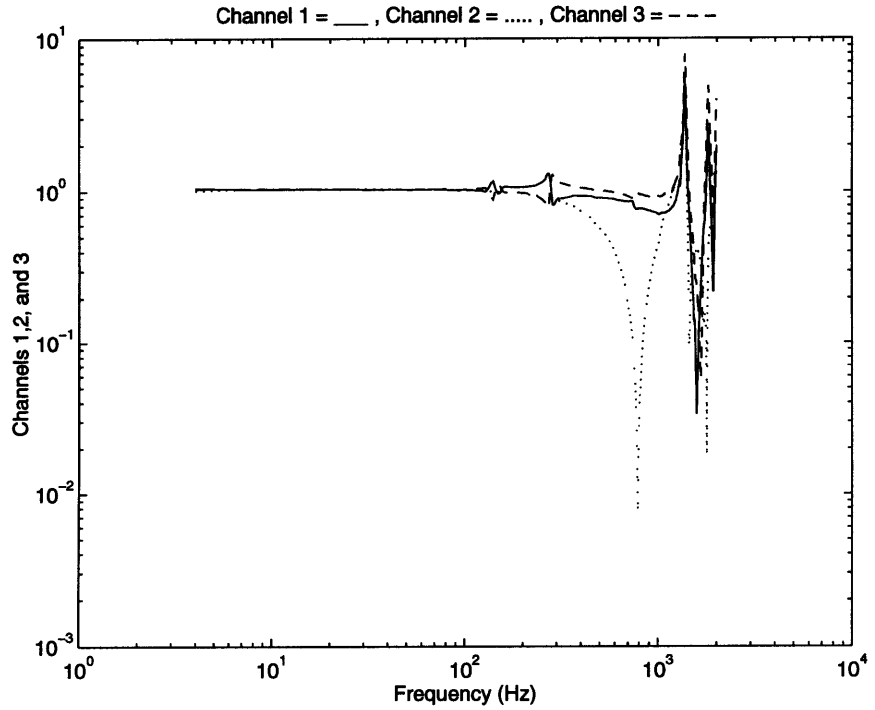

Figure C-22: X-Axis Tests, 56 lb Mass Between 2 and 5–Channels 1, 2, and 3

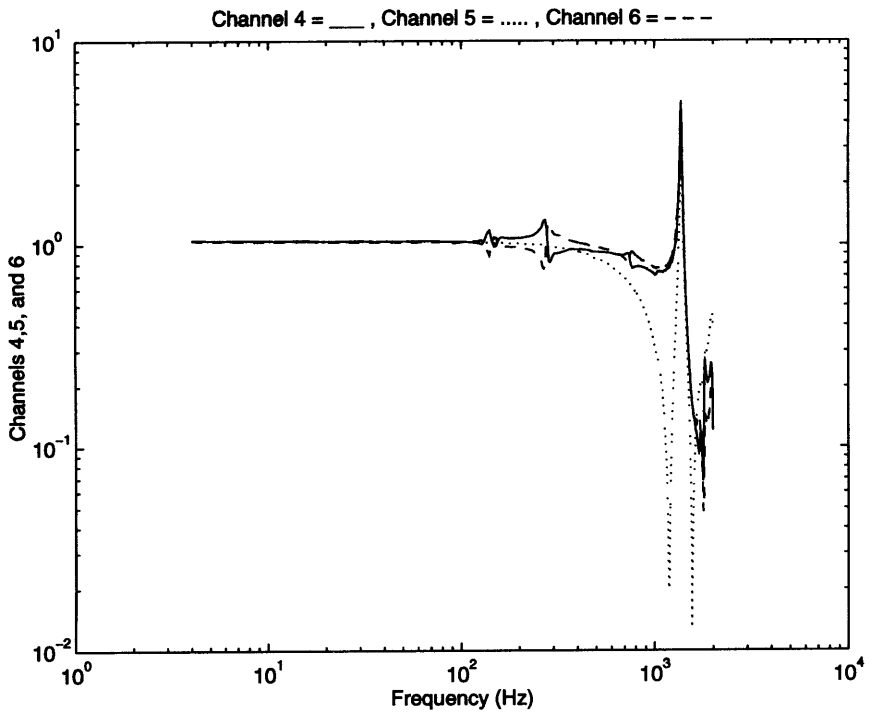

Figure C-23: X-Axis Tests, 56 lb Mass Between 2 and 5–Channels 4, 5 and 6

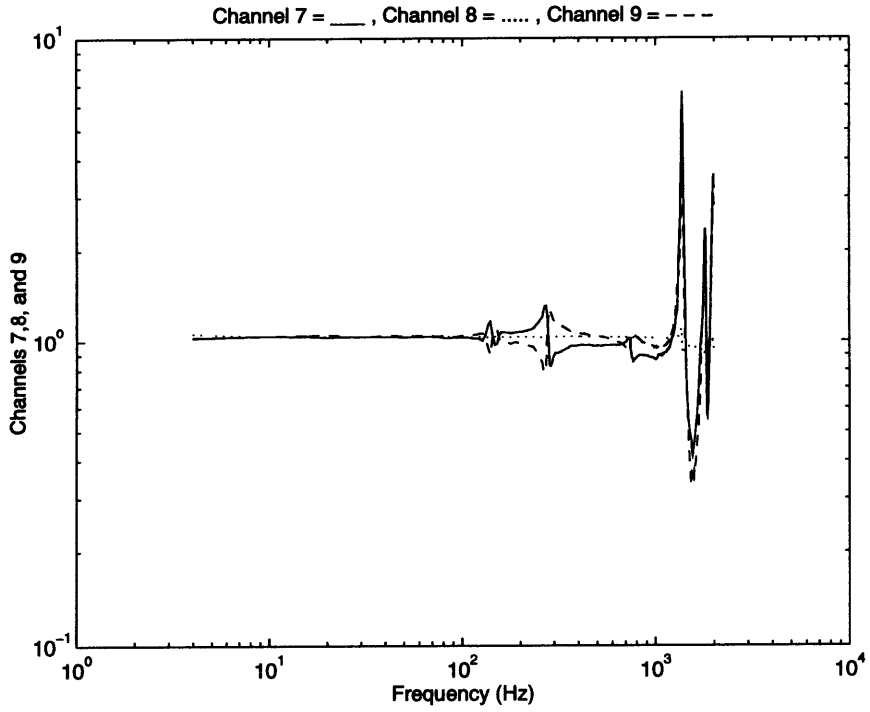

Figure C-24: X-Axis Tests, 56 lb Mass Between 2 and 5–Channels 7, 8, and 9

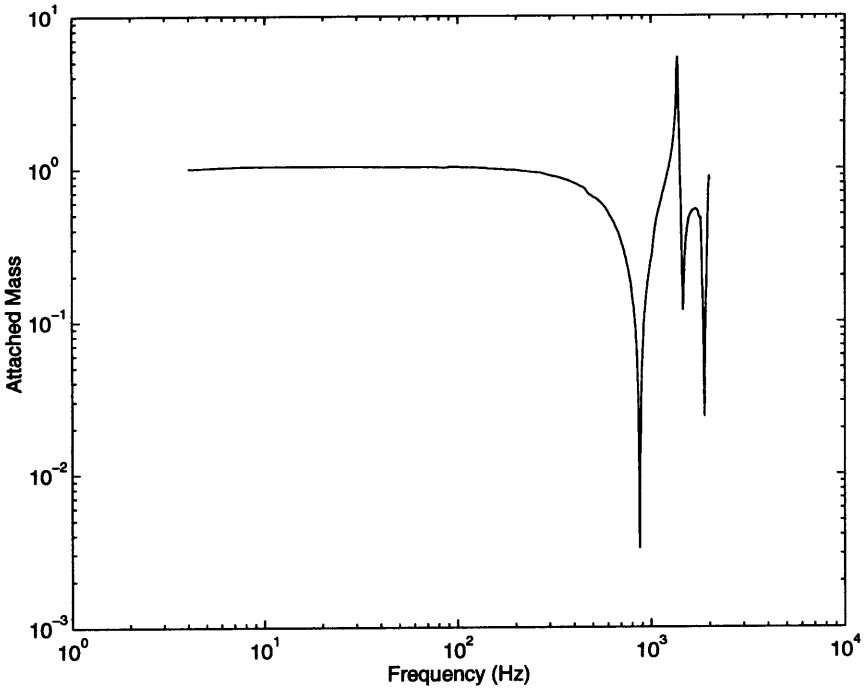

Figure C-25: X-Axis Tests, 56 lb Mass Between 2 and 5–Channel of Attached Mass

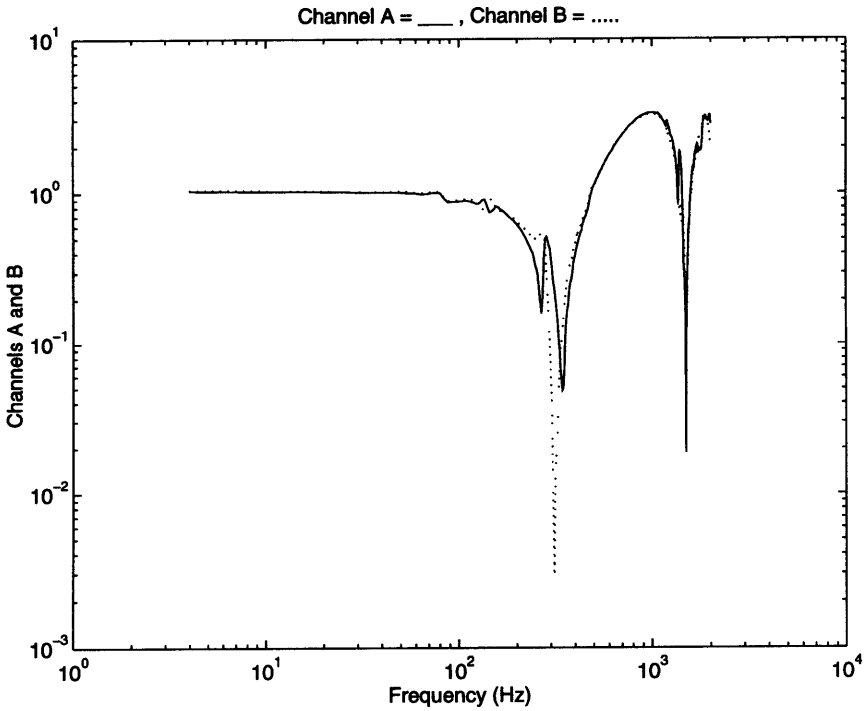

Figure C-26: X-Axis Tests, 56 lb Mass Between 2 and 5–Channels A and B

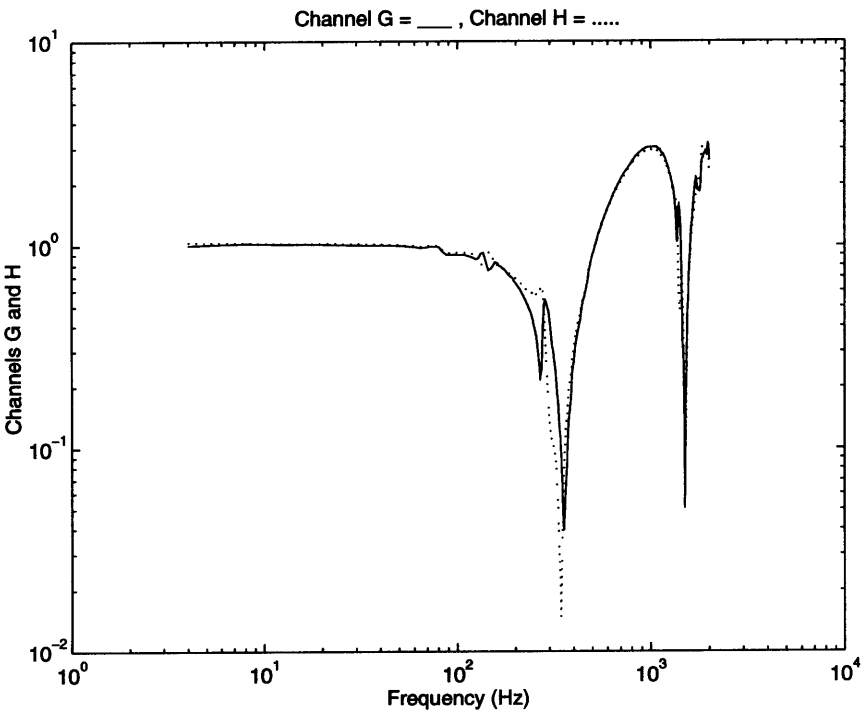

Figure C-27: X-Axis Tests, 56 lb Mass Between 2 and 5–Channels G and H

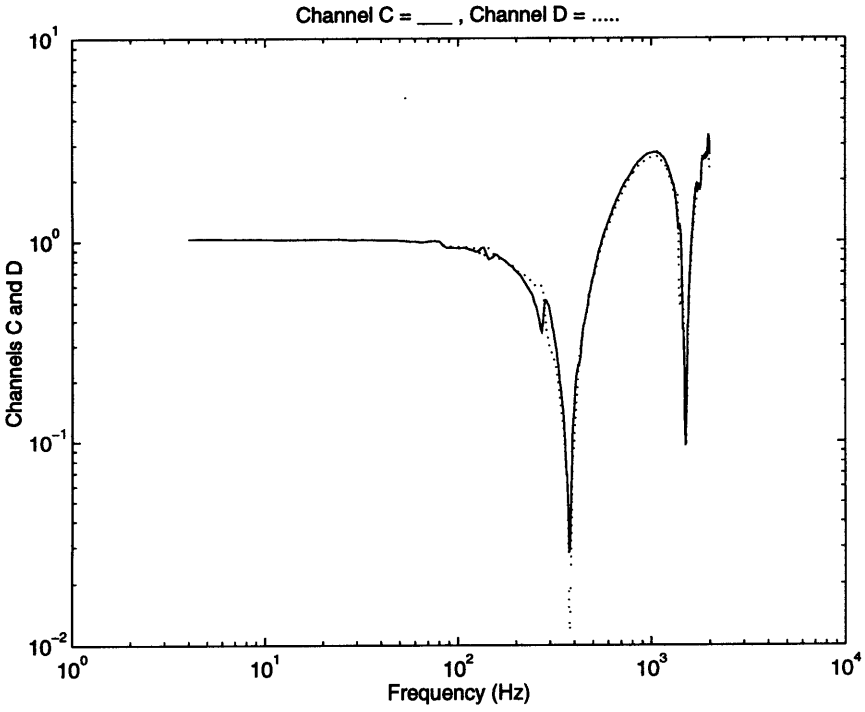

Figure C-28: X-Axis Tests, 56 lb Mass Between 2 and 5–Channels C and D

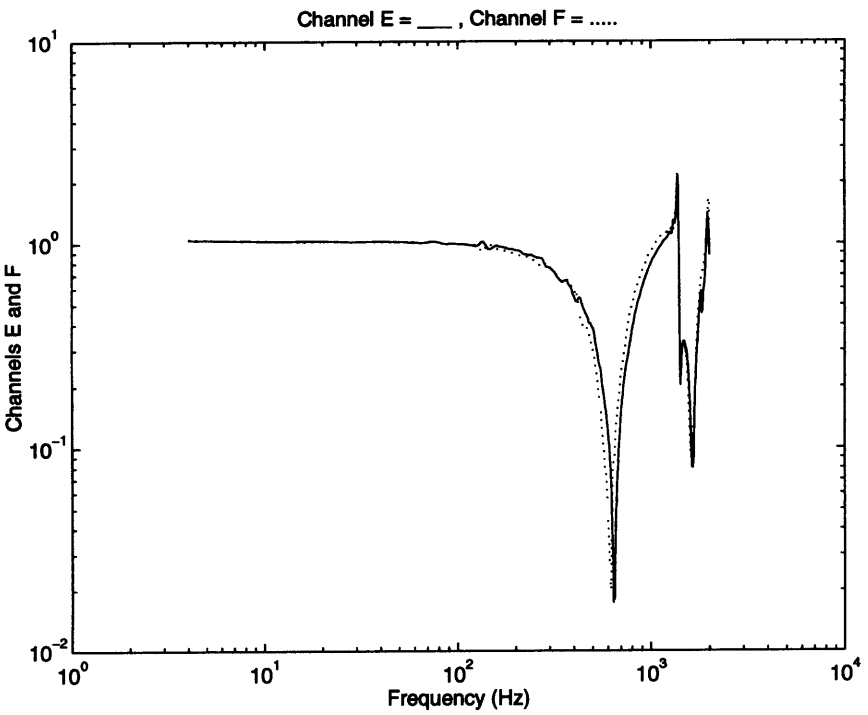

Figure C-29: X-Axis Tests, 56 lb Mass Between 2 and 5–Channels E and F

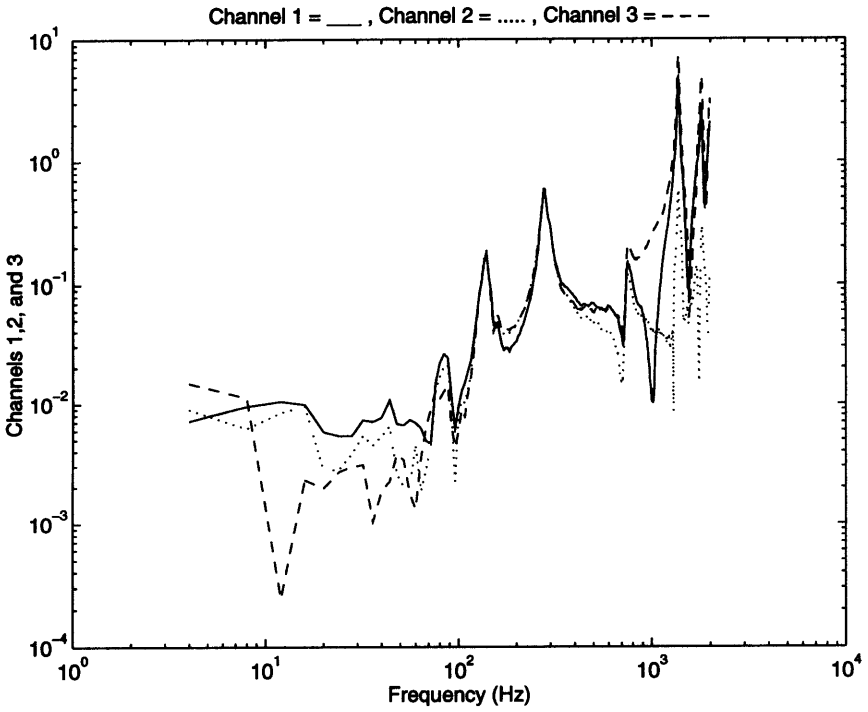

Figure C-30: Y-Axis Tests, 56 lb Mass Between 2 and 5–Channels 1, 2, and 3

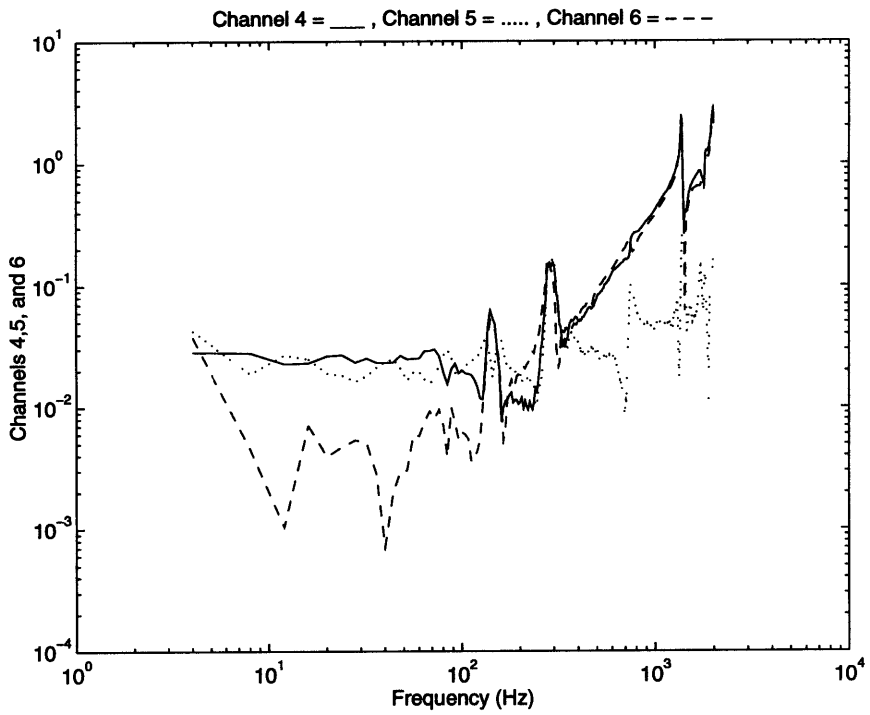

Figure C-31: Y-Axis Tests, 56 lb Mass Between 2 and 5–Channels 4, 5 and 6

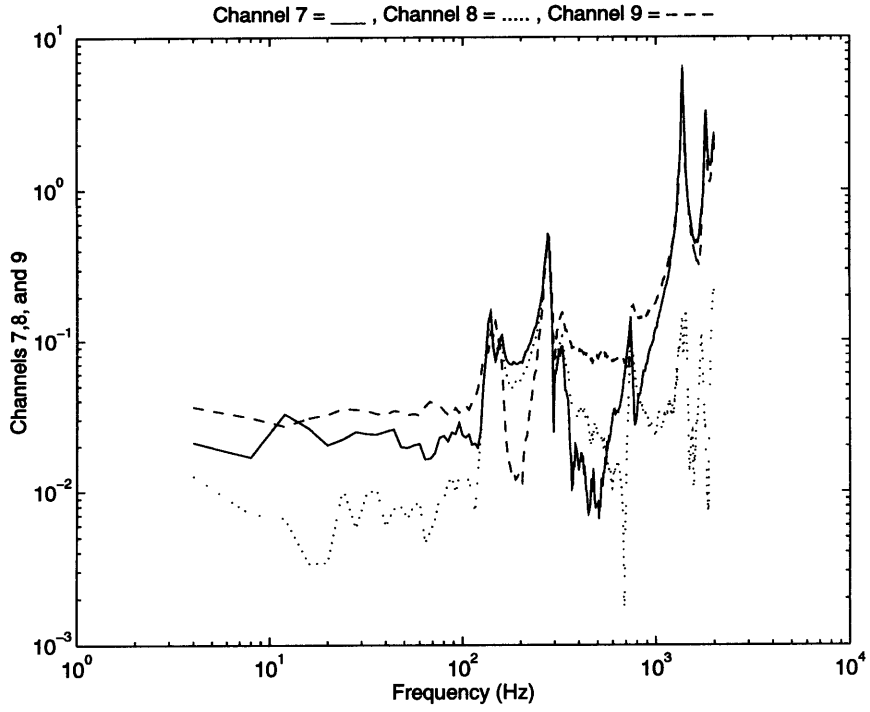

Figure C-32: Y-Axis Tests, 56 lb Mass Between 2 and 5–Channels 7, 8, and 9

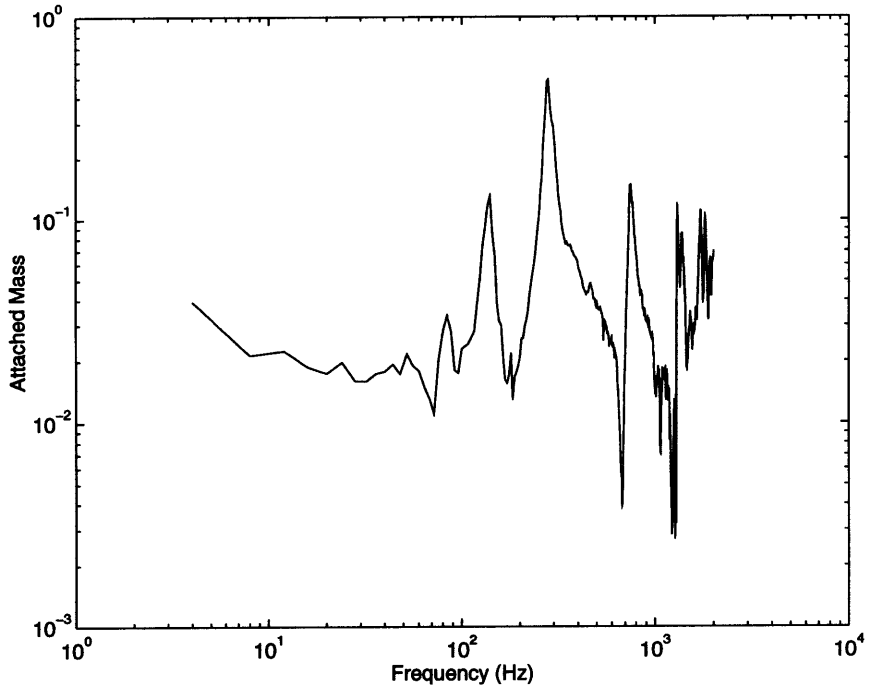

Figure C-33: Y-Axis Tests, 56 lb Mass Between 2 and 5–Channel of Attached Mass

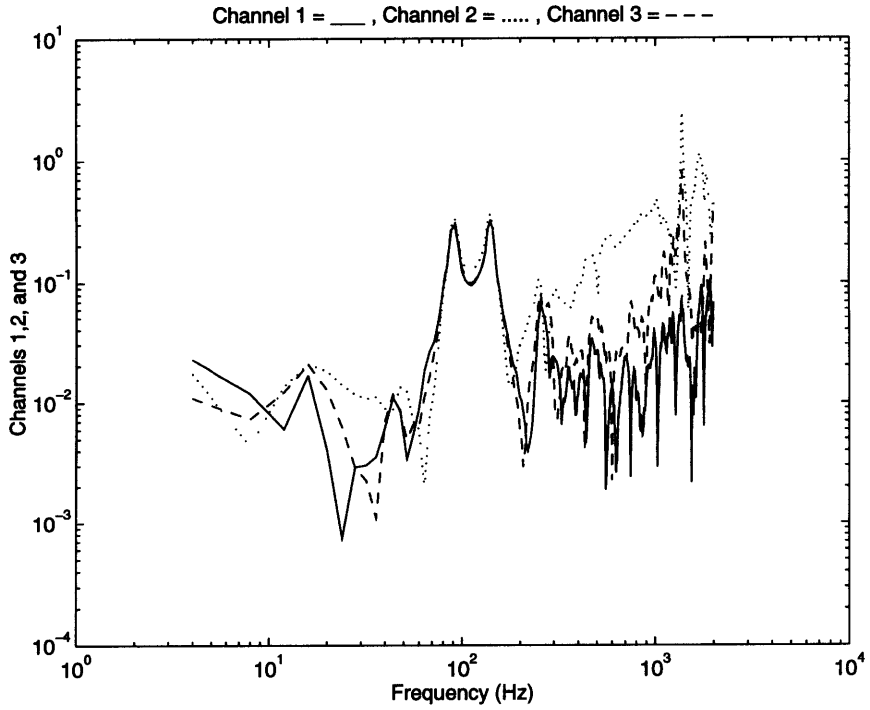

Figure C-34: Z-Axis Tests, 56 lb Mass Between 2 and 5–Channels 1, 2, and 3

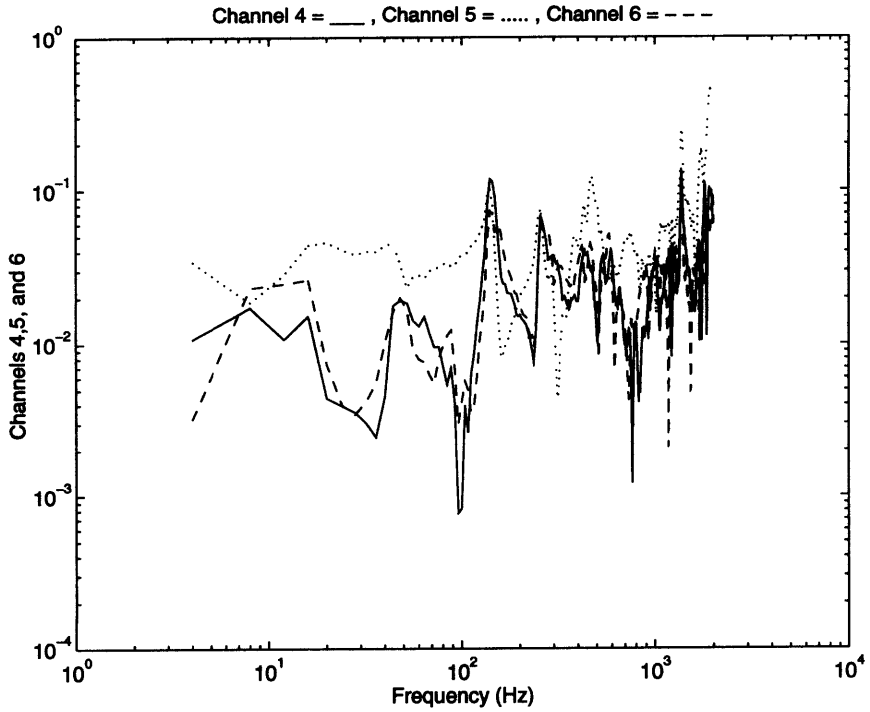

Figure C-35: Z-Axis Tests, 56 lb Mass Between 2 and 5–Channels 4, 5 and 6

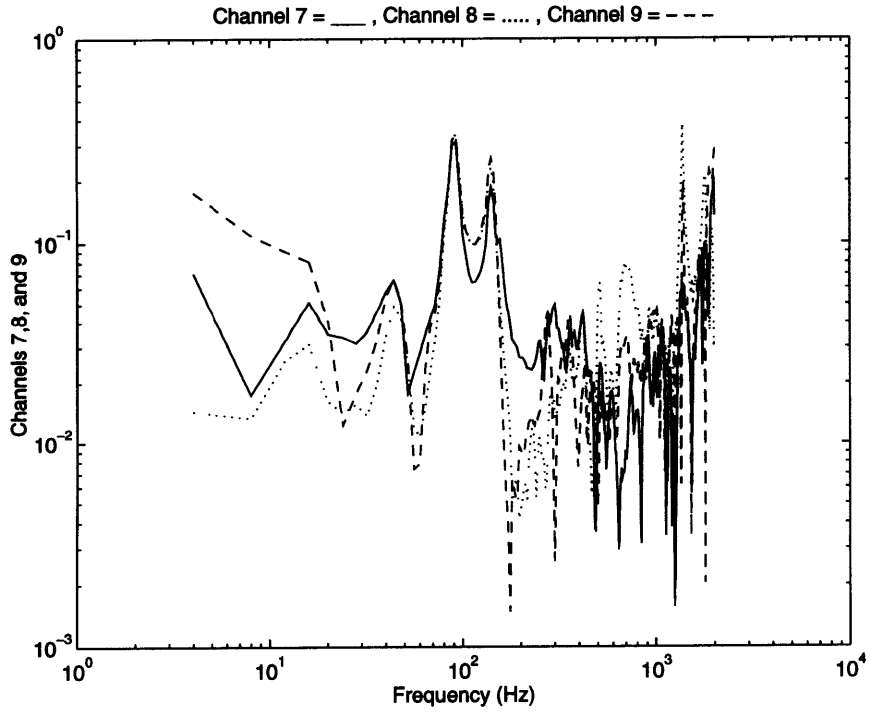

Figure C-36: Z-Axis Tests, 56 lb Mass Between 2 and 5–Channels 7, 8, and 9

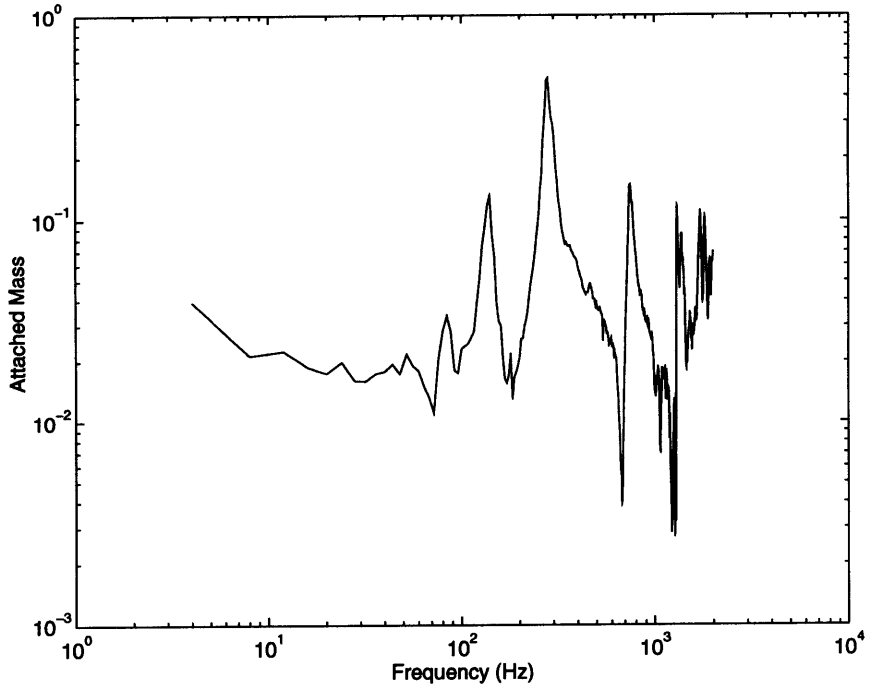

Figure C-37: Z-Axis Tests, 56 lb Mass Between 2 and 5–Channel of Attached Mass

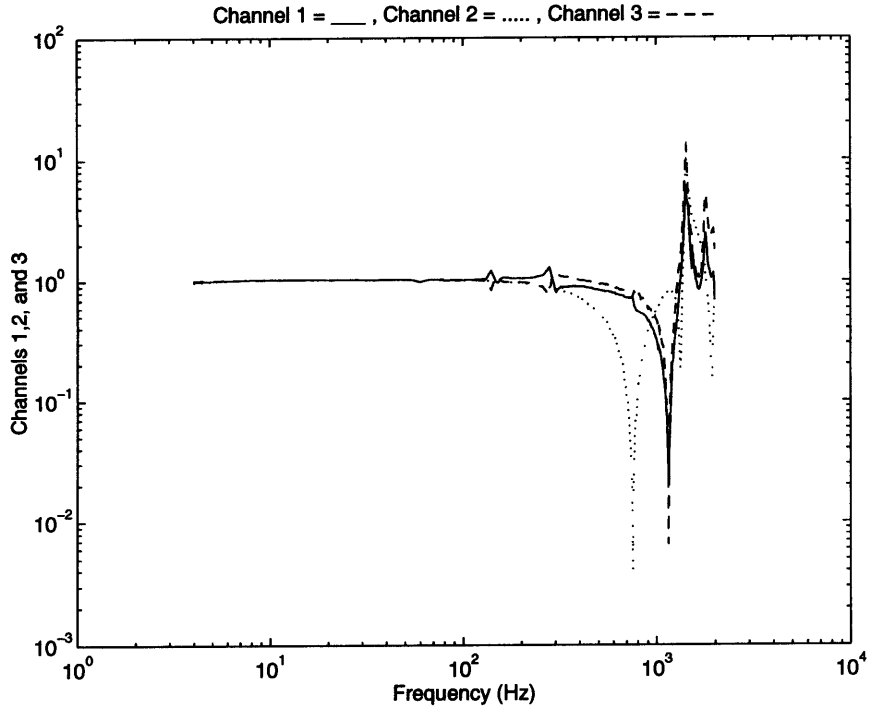

Figure C-38: X-Axis Tests, 56 lb Mass Between 5 and 8–Channels 1, 2, and 3

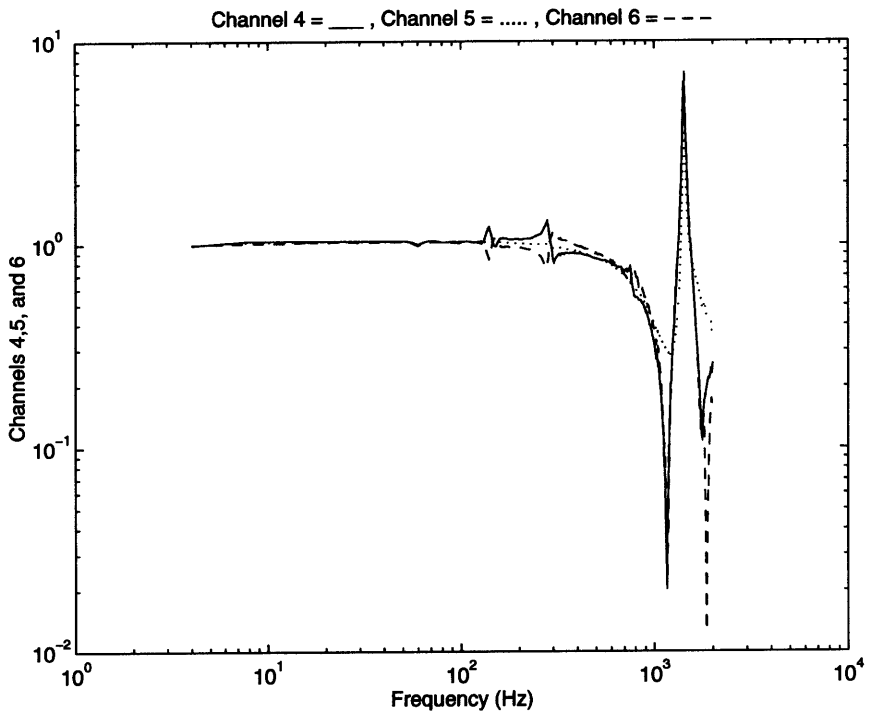

Figure C-39: X-Axis Tests, 56 lb Mass Between 5 and 8–Channels 4, 5 and 6

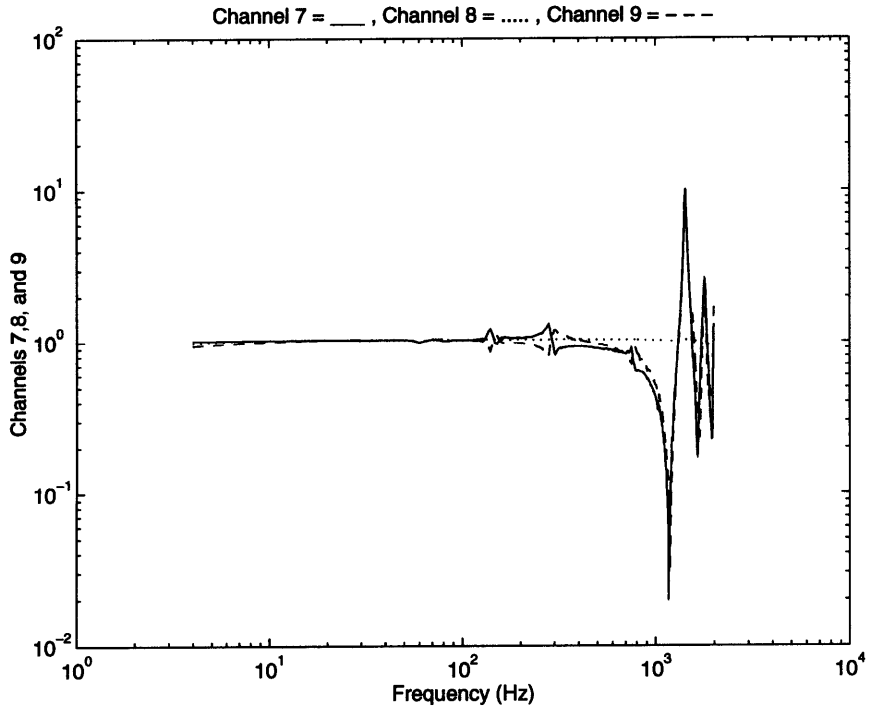

Figure C-40: X-Axis Tests, 56 lb Mass Between 5 and 8–Channels 7, 8, and 9

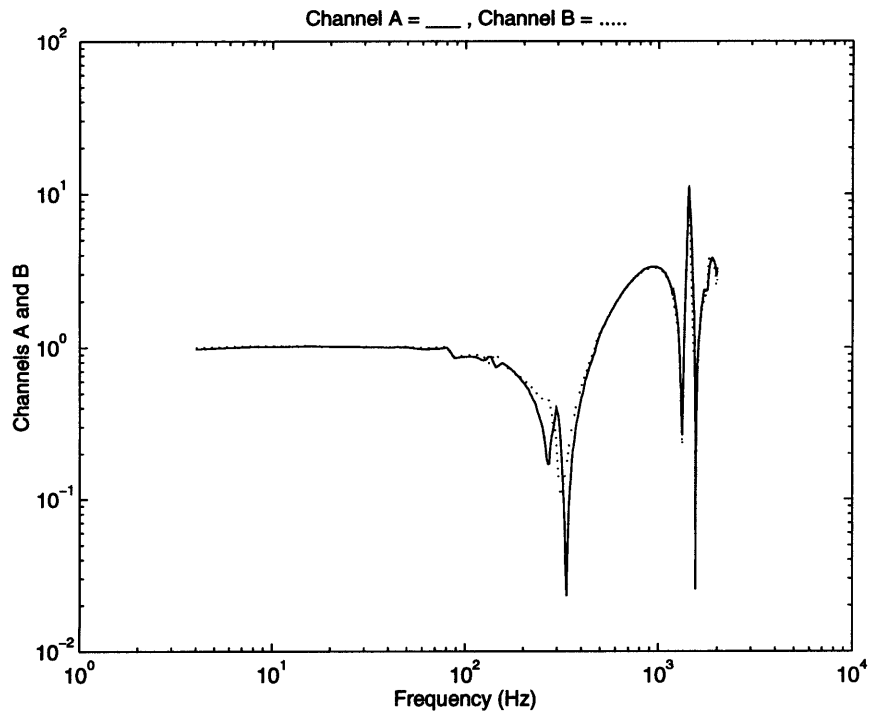

Figure C-41: X-Axis Tests, 56 lb Mass Between 5 and 8–Channels A and B

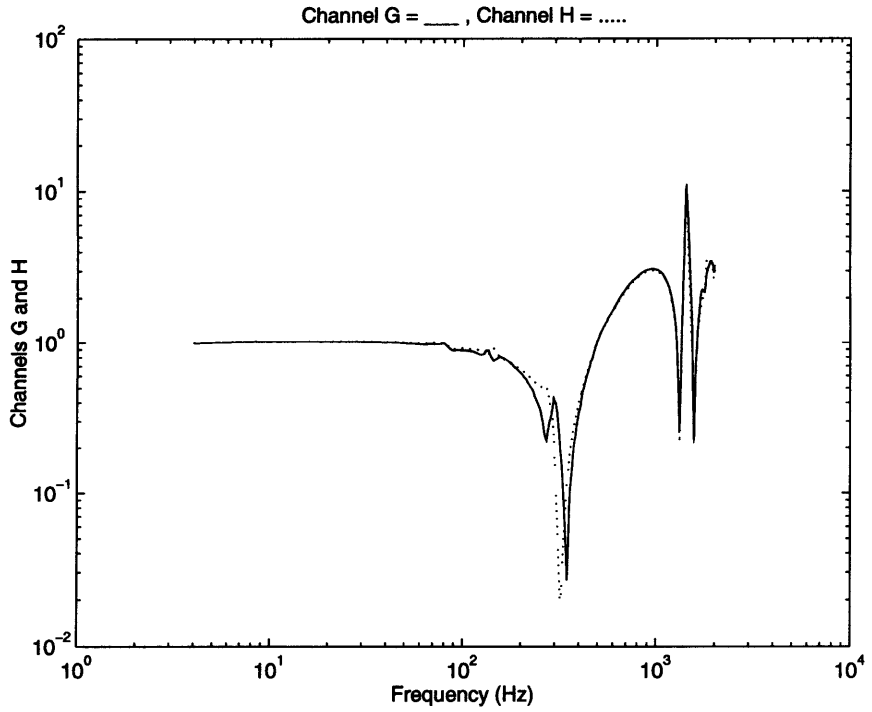

Figure C-42: X-Axis Tests, 56 lb Mass Between 5 and 8–Channels G and H

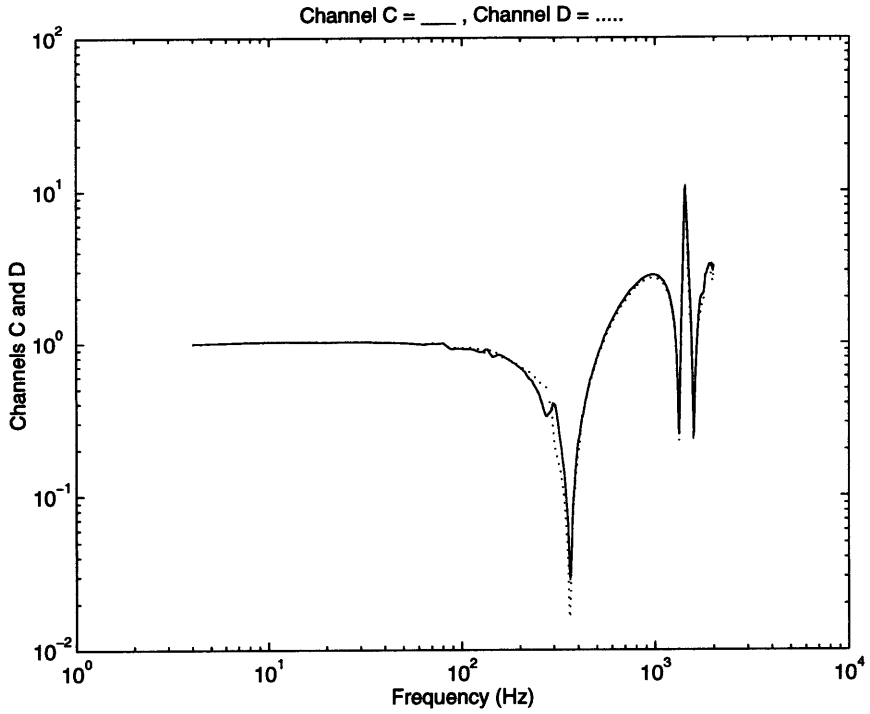

Figure C-43: X-Axis Tests, 56 lb Mass Between 5 and 8–Channels C and D

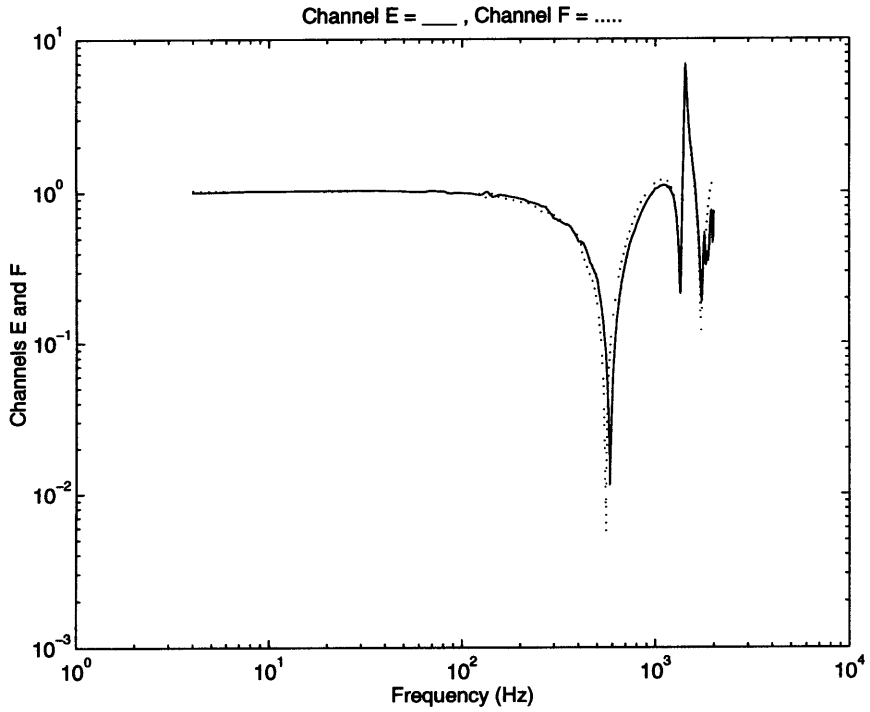

Figure C-44: X-Axis Tests, 56 lb Mass Between 5 and 8–Channels E and F

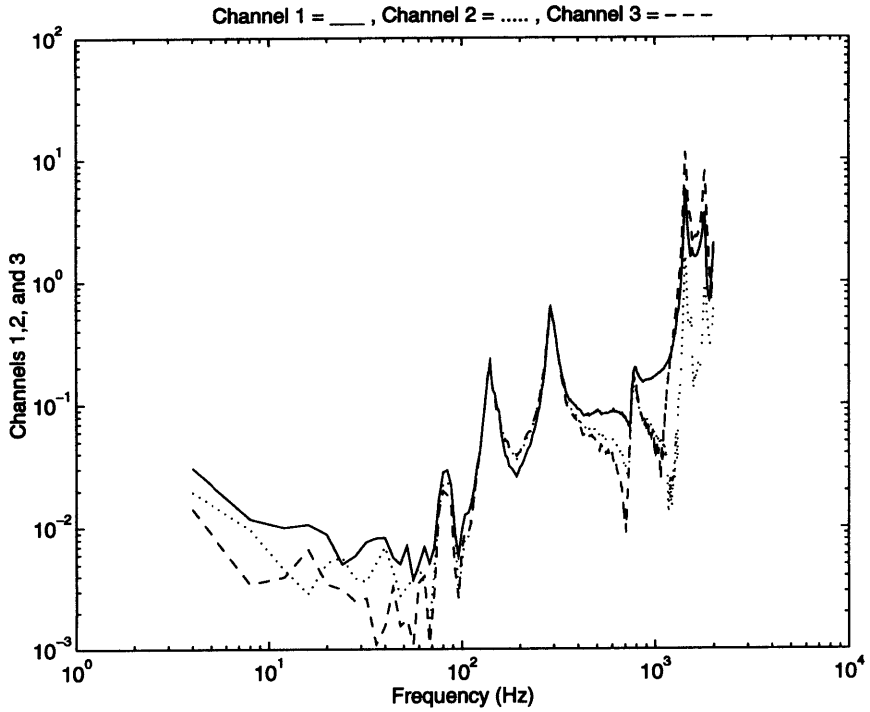

Figure C-45: Y-Axis Tests, 56 lb Mass Between 5 and 8–Channels 1,2, and 3

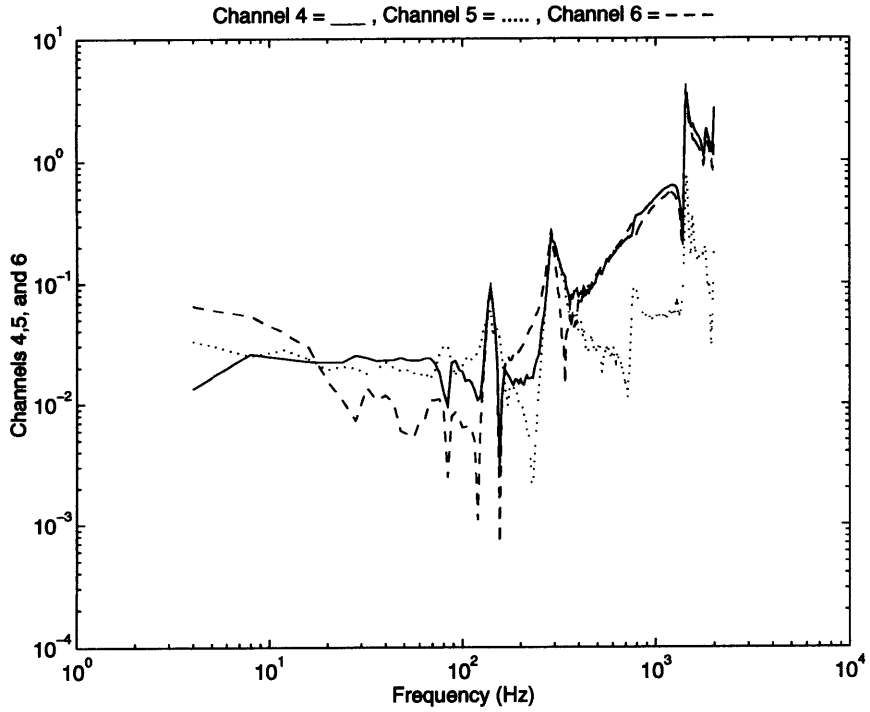

Figure C-46: Y-Axis Tests, 56 lb Mass Between 5 and 8–Channels 4,5, and 6

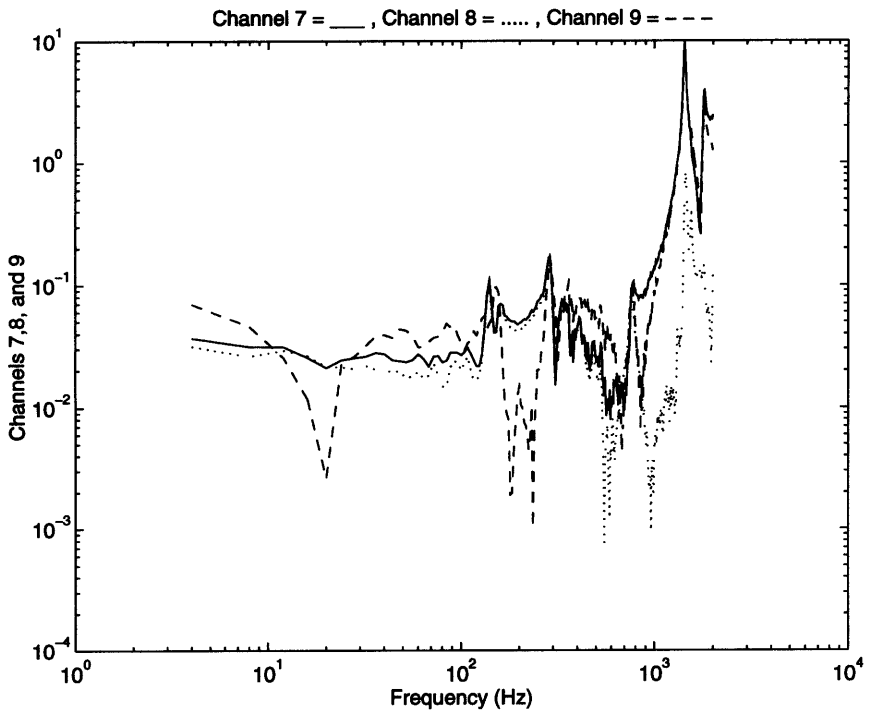

Figure C-47: Y-Axis Tests, 56 lb Mass Between 5 and 8–Channels 7,8, and 9

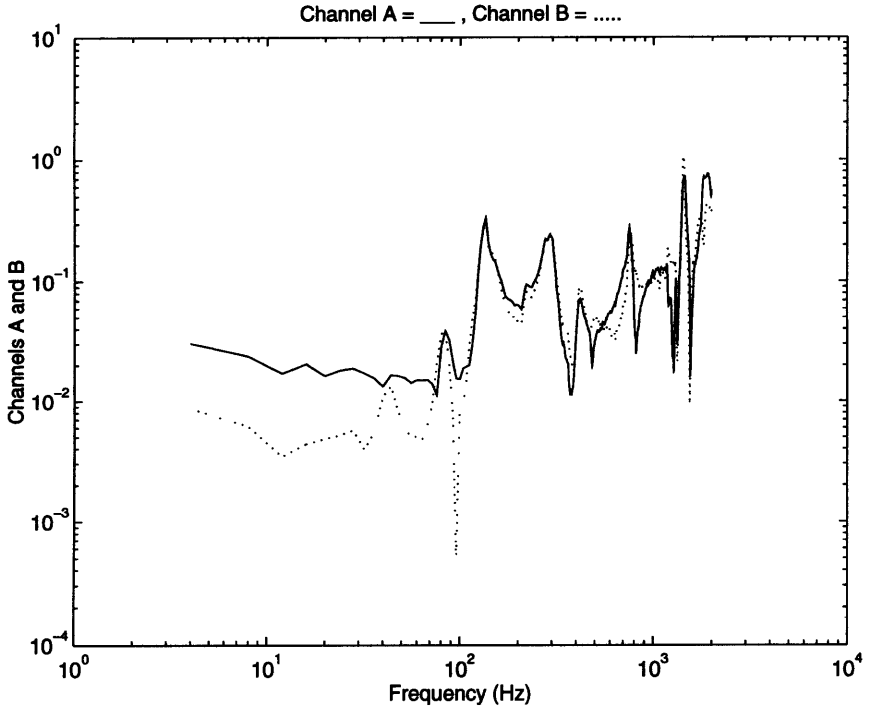

Figure C-48: Y-Axis Tests, 56 lb Mass Between 5 and 8–Channels A and B

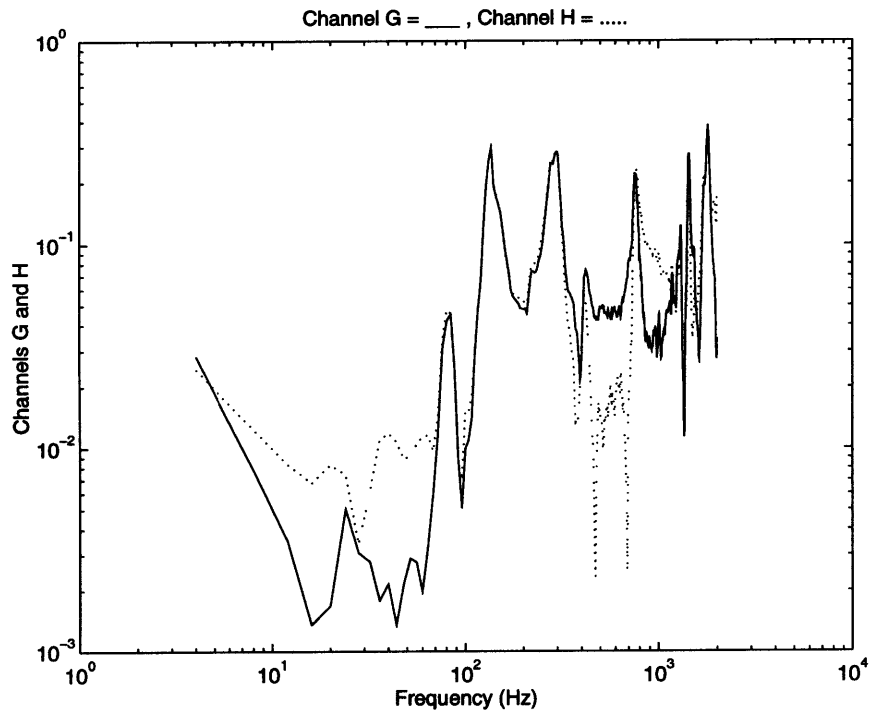

Figure C-49: Y-Axis Tests, 56 lb Mass Between 5 and 8–Channels G and H

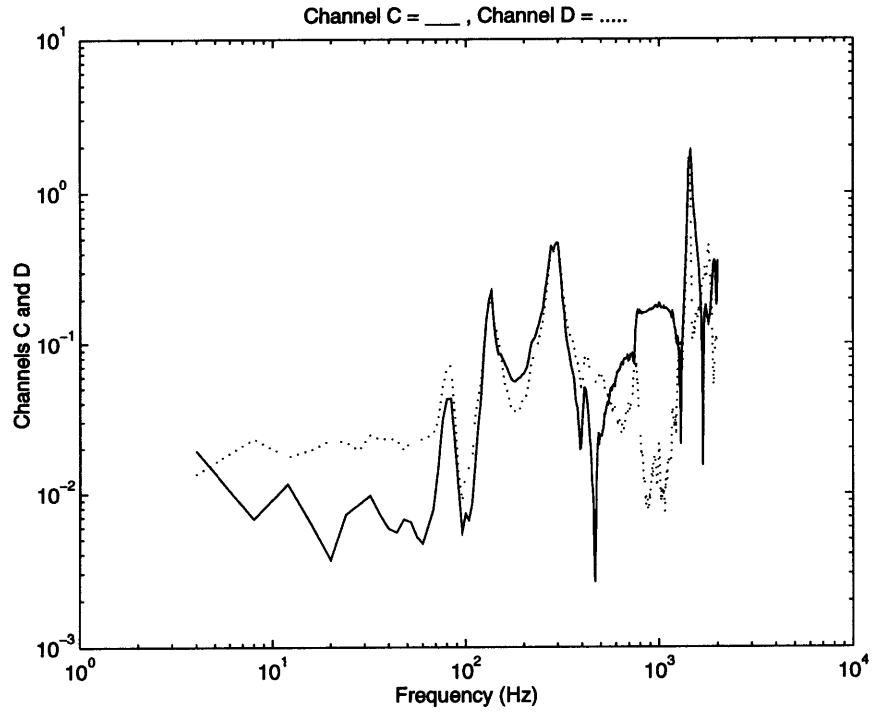

Figure C-50: Y-Axis Tests, 56 lb Mass Between 5 and 8–Channels C and D

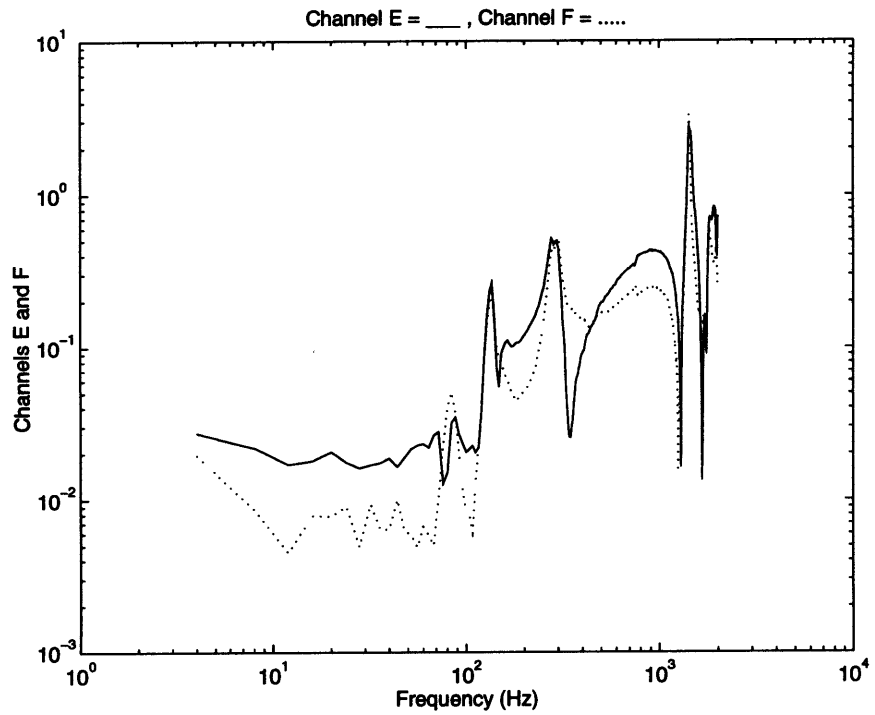

Figure C-51: Y-Axis Tests, 56 lb Mass Between 5 and 8–Channels E and F

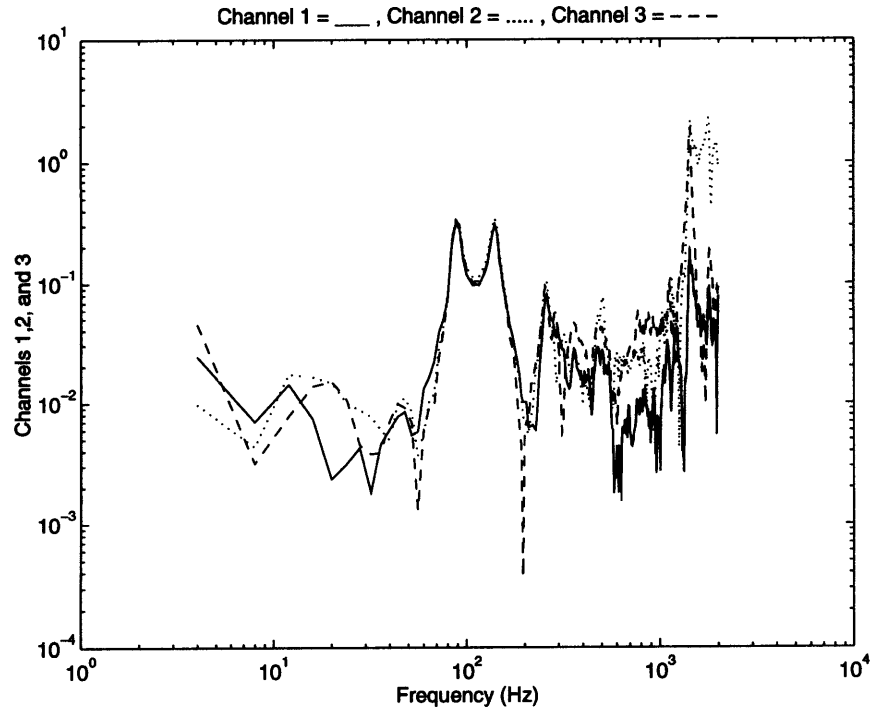

Figure C-52: Z-Axis Tests, 56 lb Mass Between 5 and 8–Channels 1,2, and 3

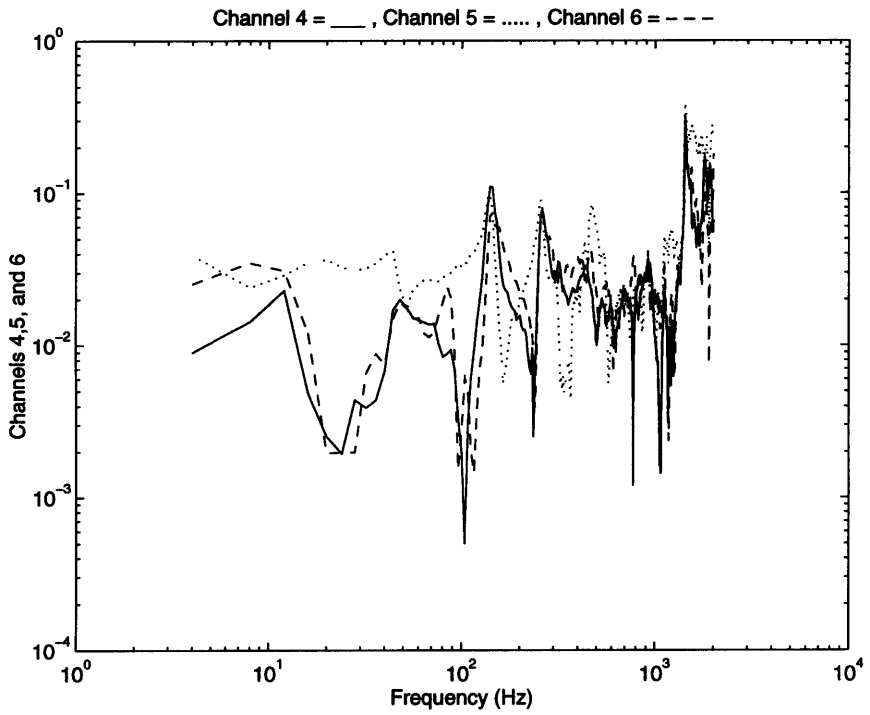

Figure C-53: Z-Axis Tests, 56 lb Mass Between 5 and 8–Channels 4,5, and 6

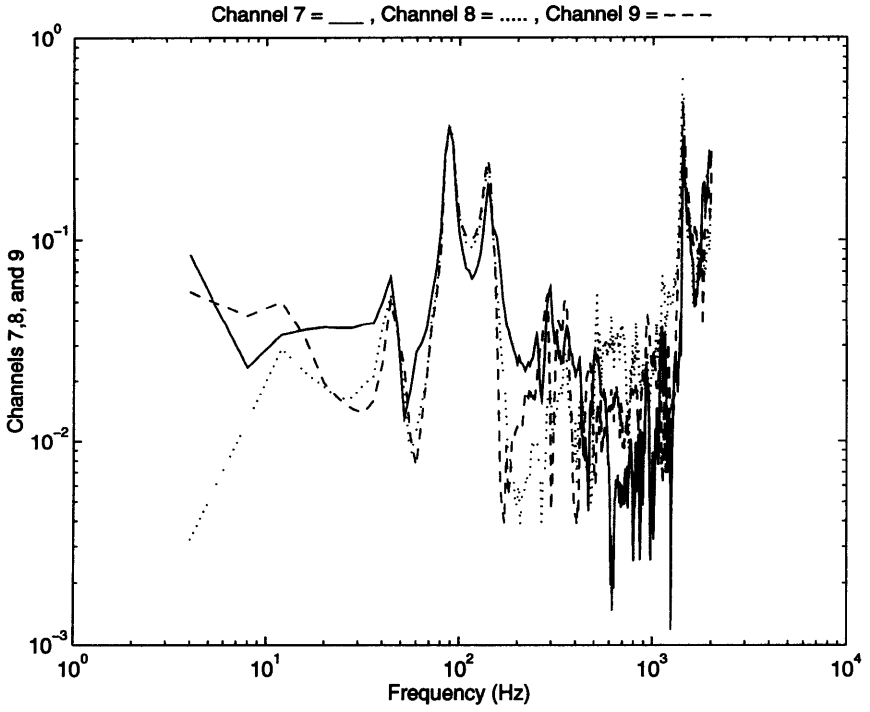

Figure C-54: Z-Axis Tests, 56 lb Mass Between 5 and 8–Channels 7,8, and 9

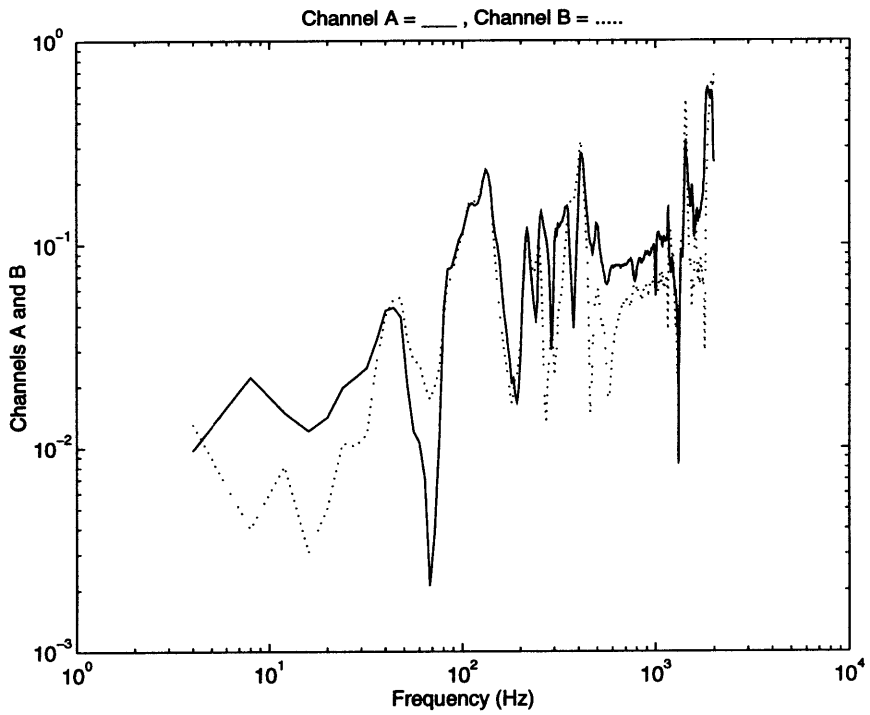

Figure C-55: Z-Axis Tests, 56 lb Mass Between 5 and 8–Channels A and B

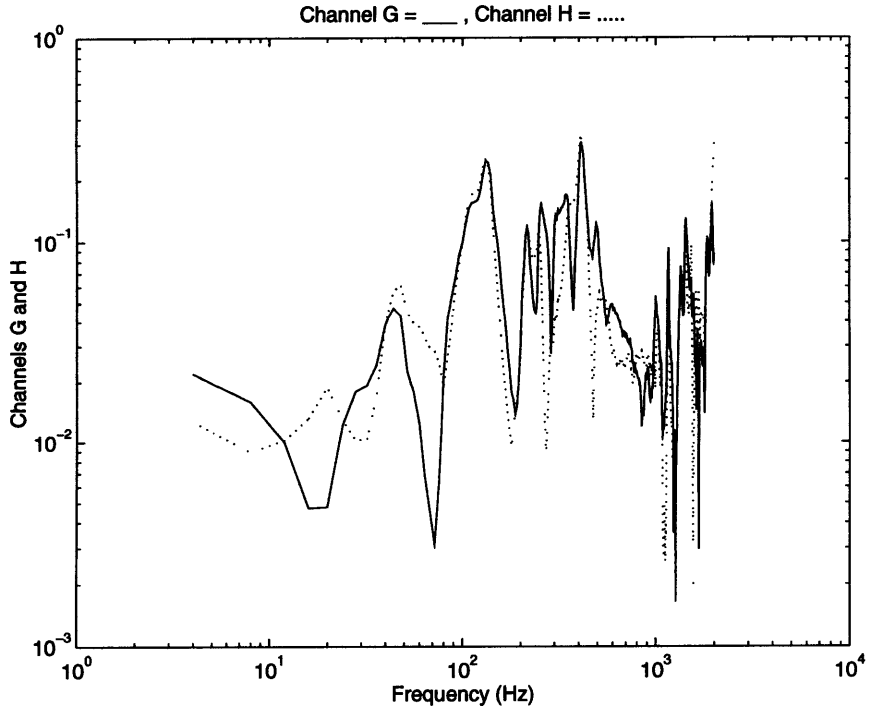

Figure C-56: Z-Axis Tests, 56 lb Mass Between 5 and 8–Channels G and H

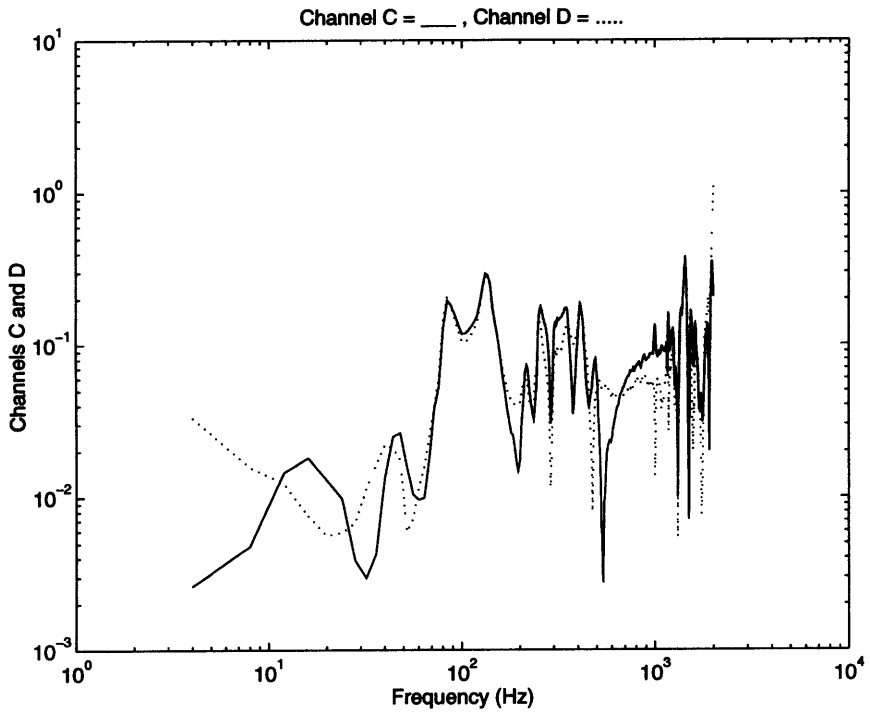

Figure C-57: Z-Axis Tests, 56 lb Mass Between 5 and 8–Channels C and D

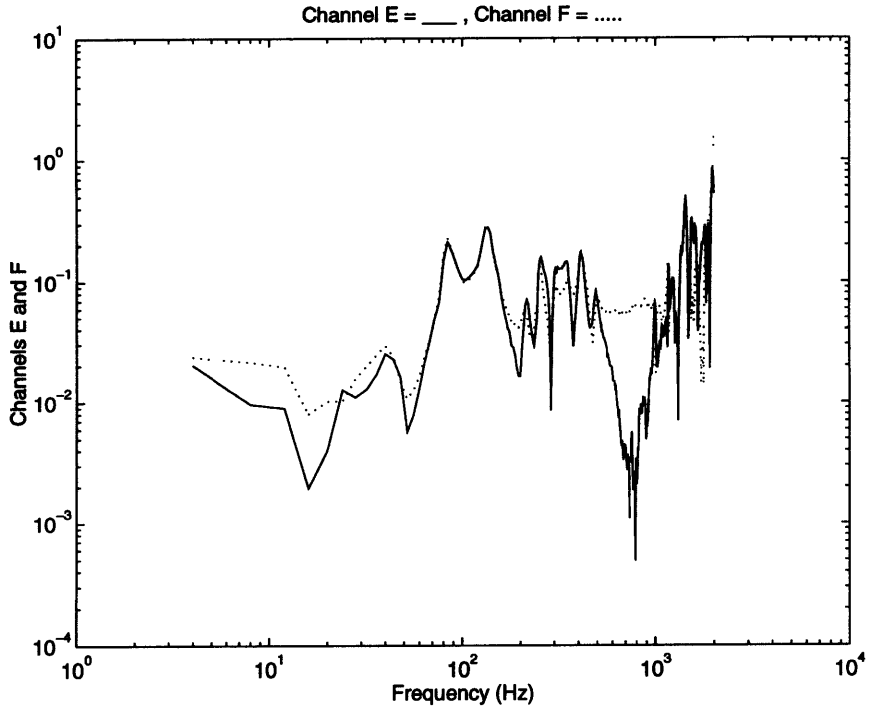

Figure C-58: Z-Axis Tests, 56 lb Mass Between 5 and 8–Channels E and F

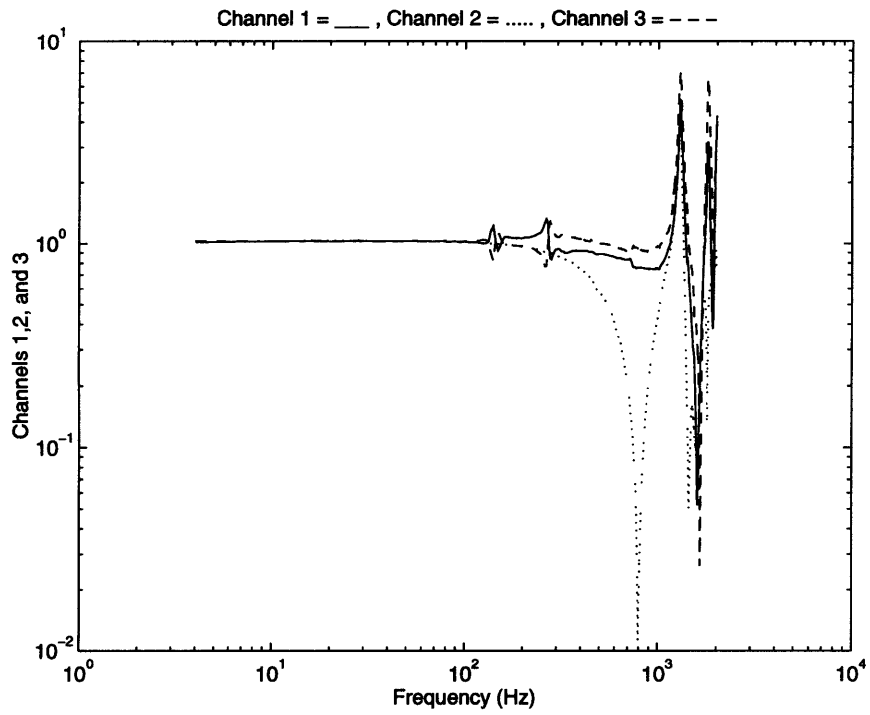

Figure C-59: X-Axis Tests, 112 lb Mass Between 2 and 5–Channels 1,2, and 3

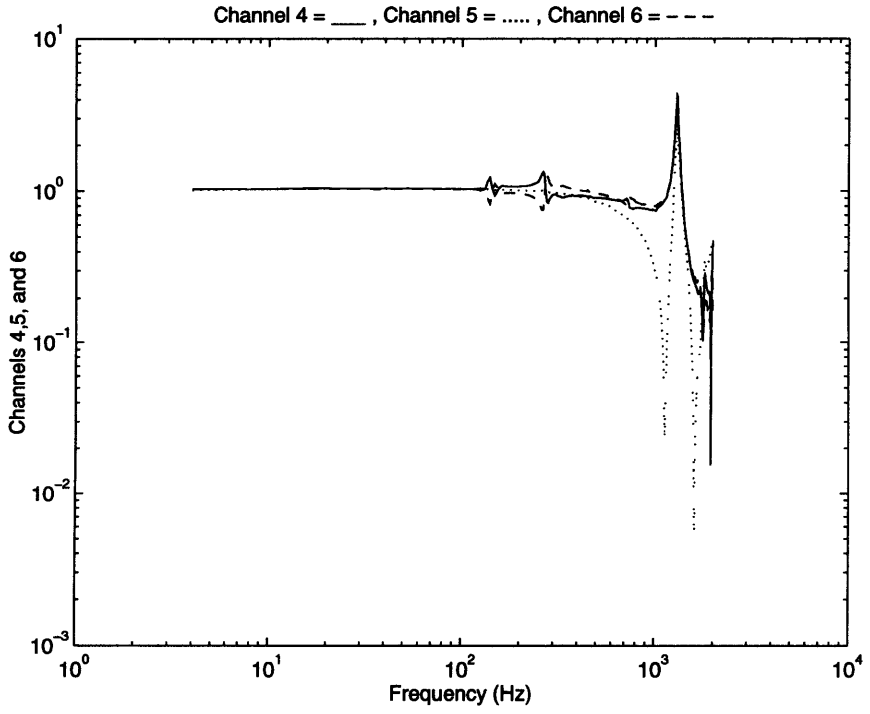

Figure C-60: X-Axis Tests, 112 lb Mass Between 2 and 5–Channels 4,5, and 6

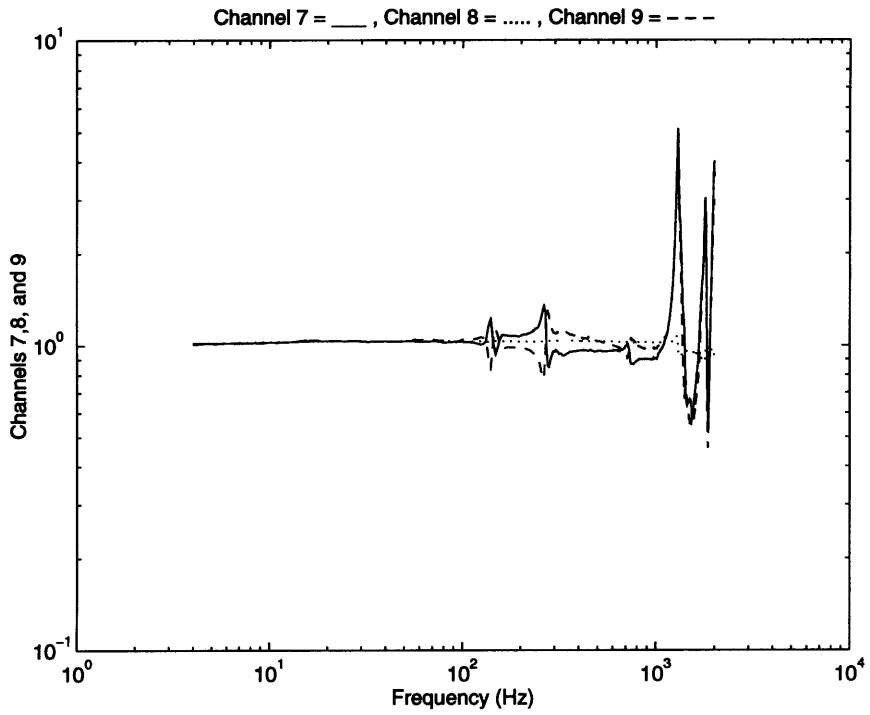

Figure C-61: X-Axis Tests, 112 lb Mass Between 2 and 5–Channels 7,8, and 9

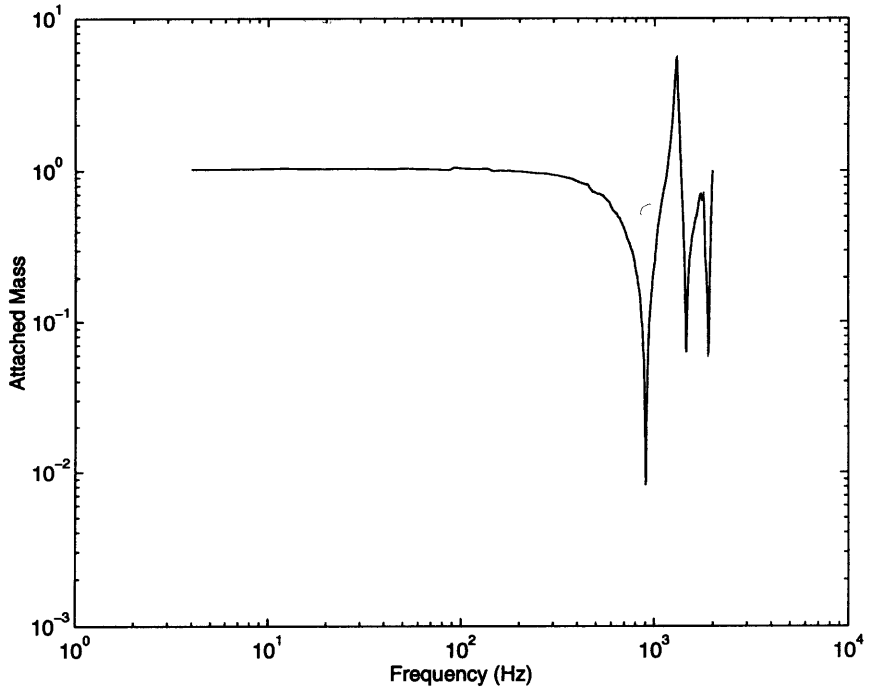

Figure C-62: X-Axis Tests, 112 lb Mass Between 2 and 5–Channel of Attached Mass

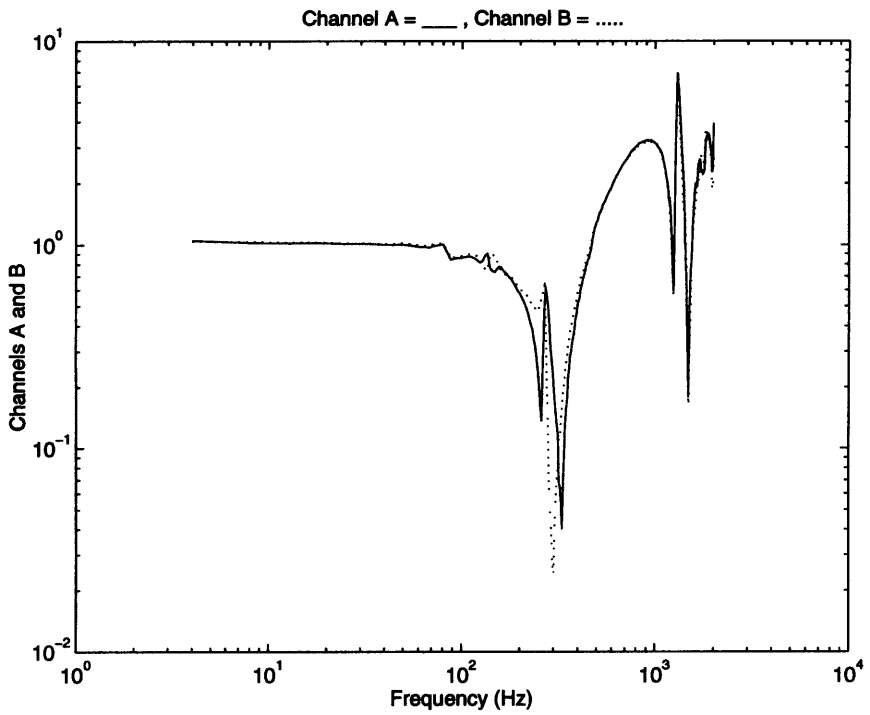

Figure C-63: X-Axis Tests, 112 lb Mass Between 2 and 5–Channels A and B

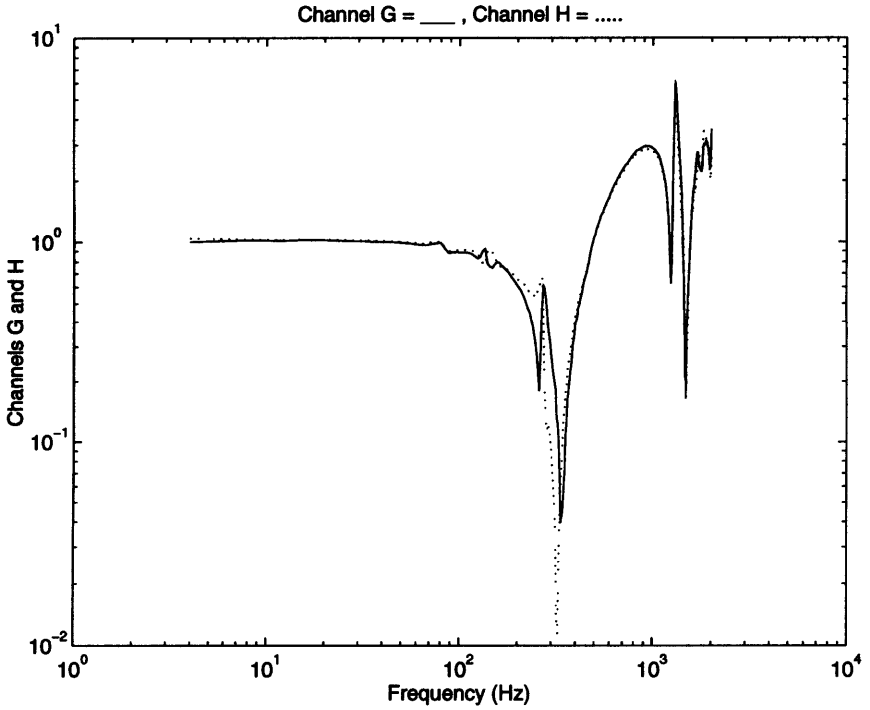

Figure C-64: Channels G and H

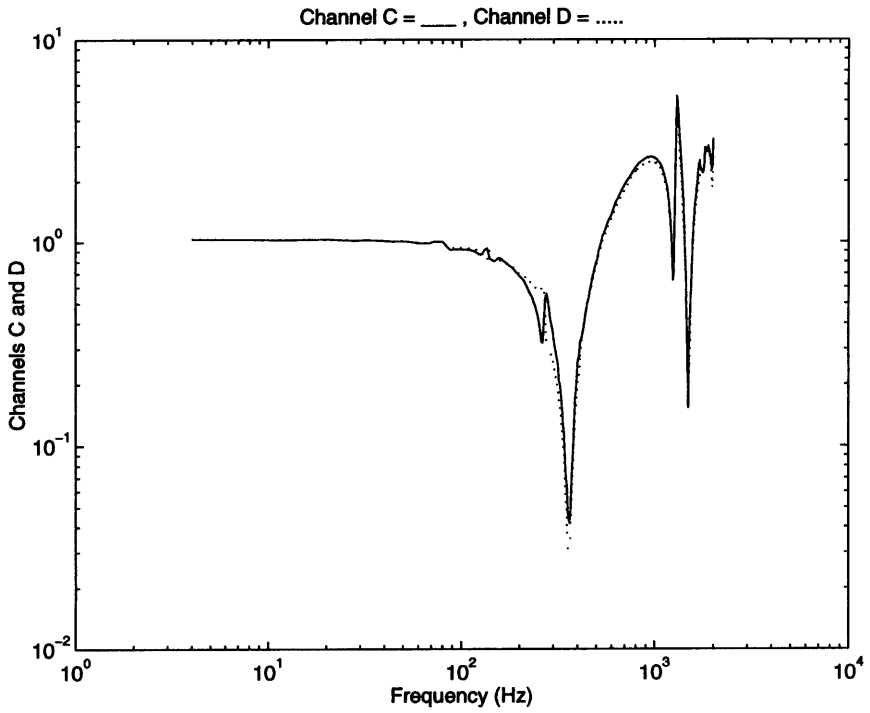

Figure C-65: X-Axis Tests, 112 lb Mass Between 2 and 5–Channels C and D

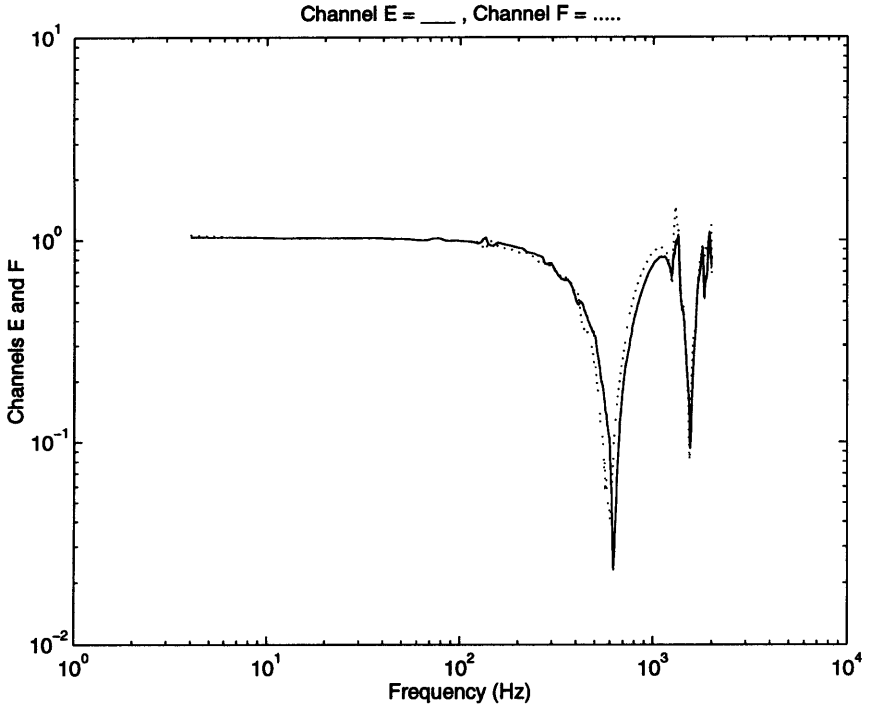

Figure C-66: X-Axis Tests, 112 lb Mass Between 2 and 5–Channels E and F

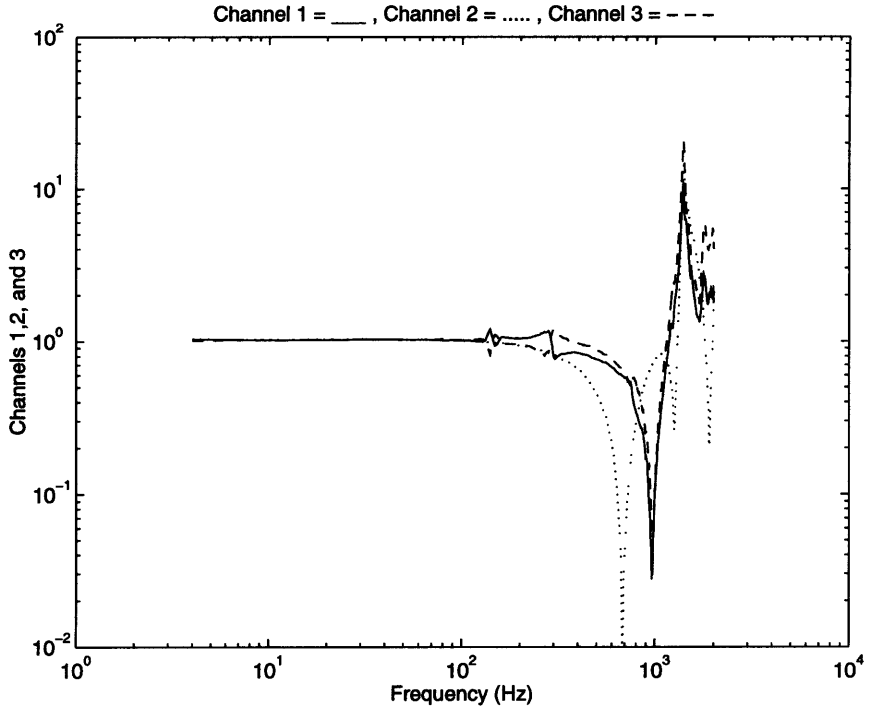

Figure C-67: X-Axis Tests, 112 lb Mass Between 5 and 8–Channels 1,2, and 3

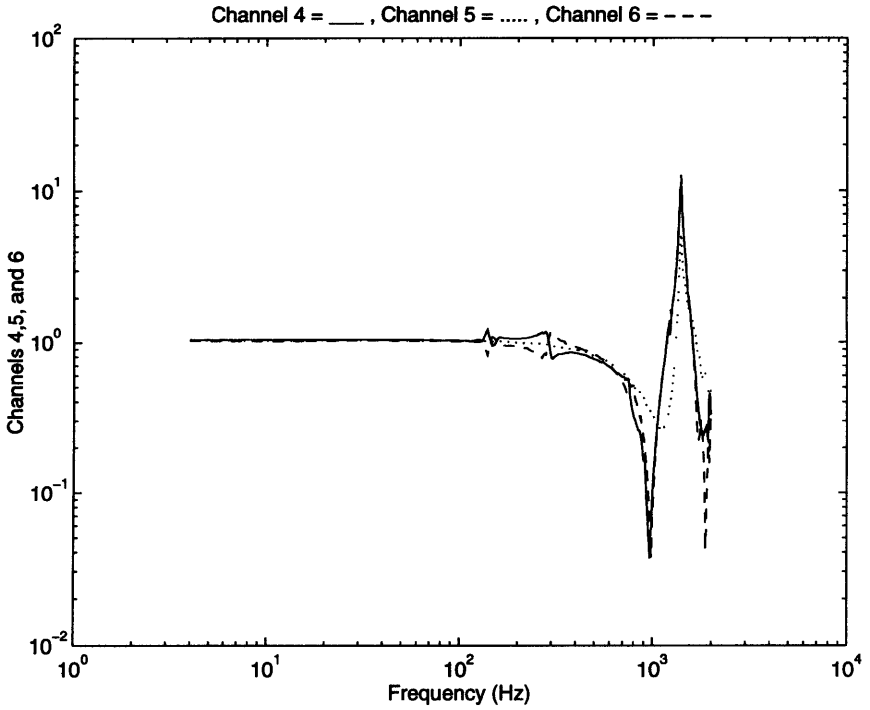

Figure C-68: X-Axis Tests, 112 lb Mass Between 5 and 8–Channels 4,5, and 6

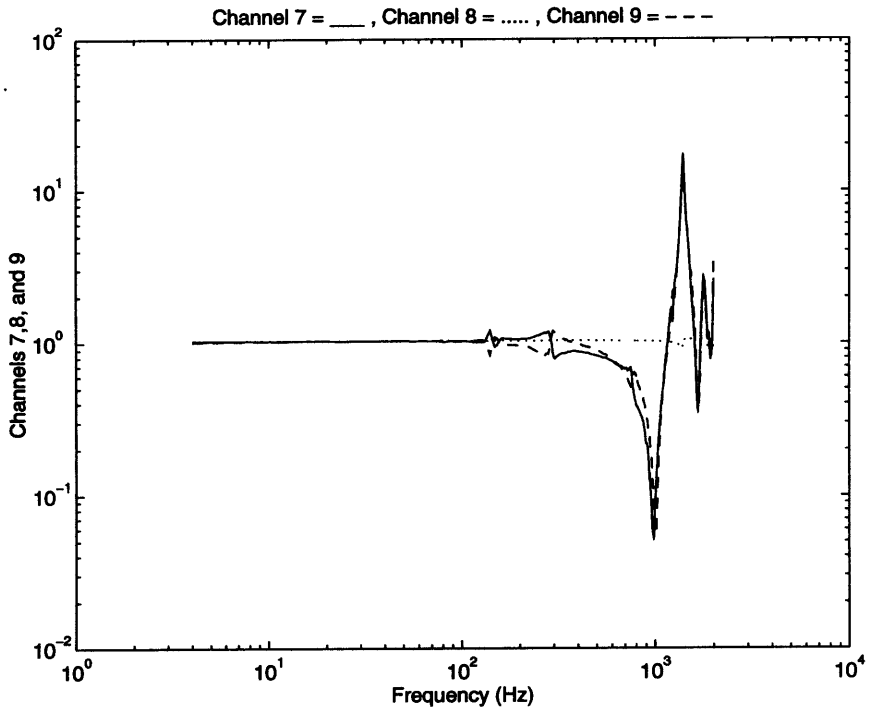

Figure C-69: X-Axis Tests, 112 lb Mass Between 5 and 8–Channels 7,8, and 9

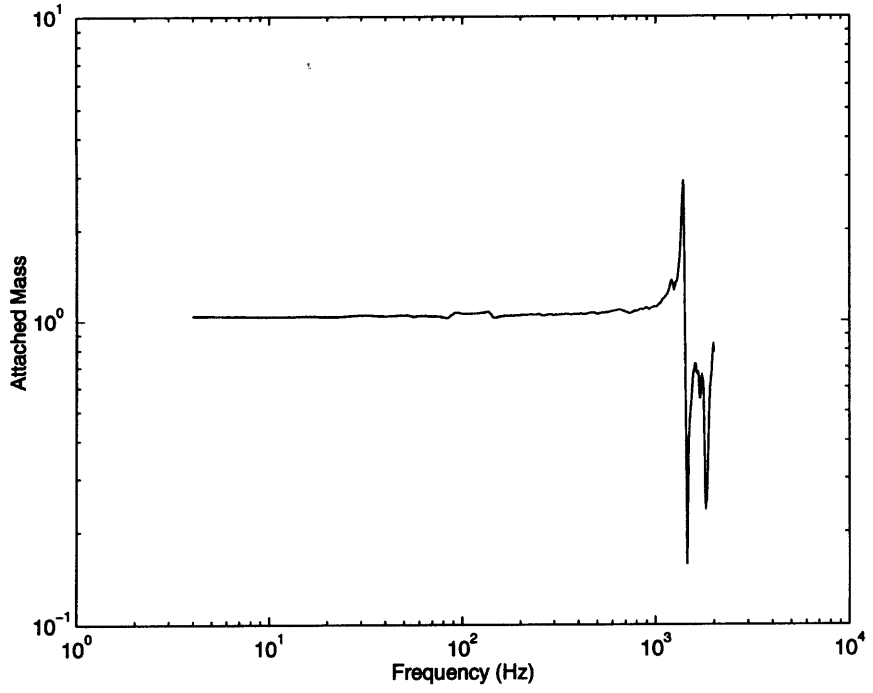

Figure C-70: X-Axis Tests, 112 lb Mass Between 5 and 8–Channel of Attached Mass

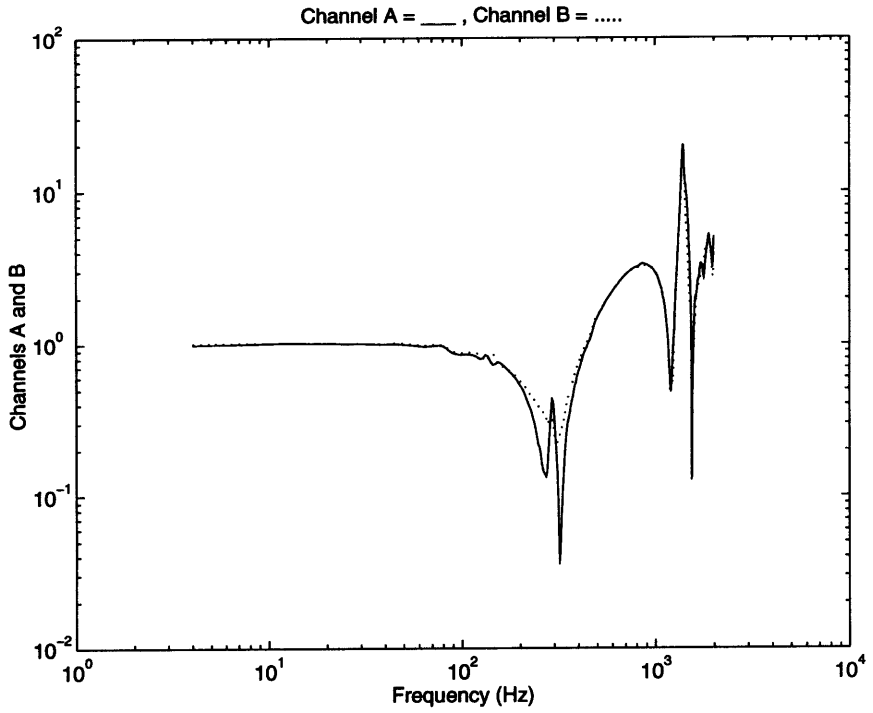

Figure C-71: X-Axis Tests, 112 lb Mass Between 5 and 8–Channels A and B

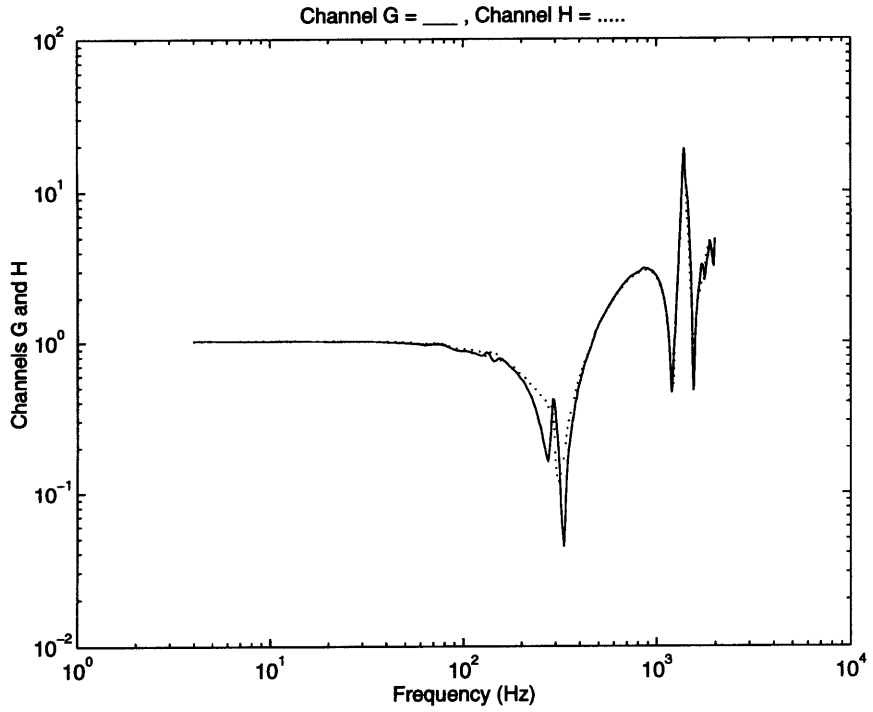

Figure C-72: X-Axis Tests, 112 lb Mass Between 5 and 8–Channels G and H

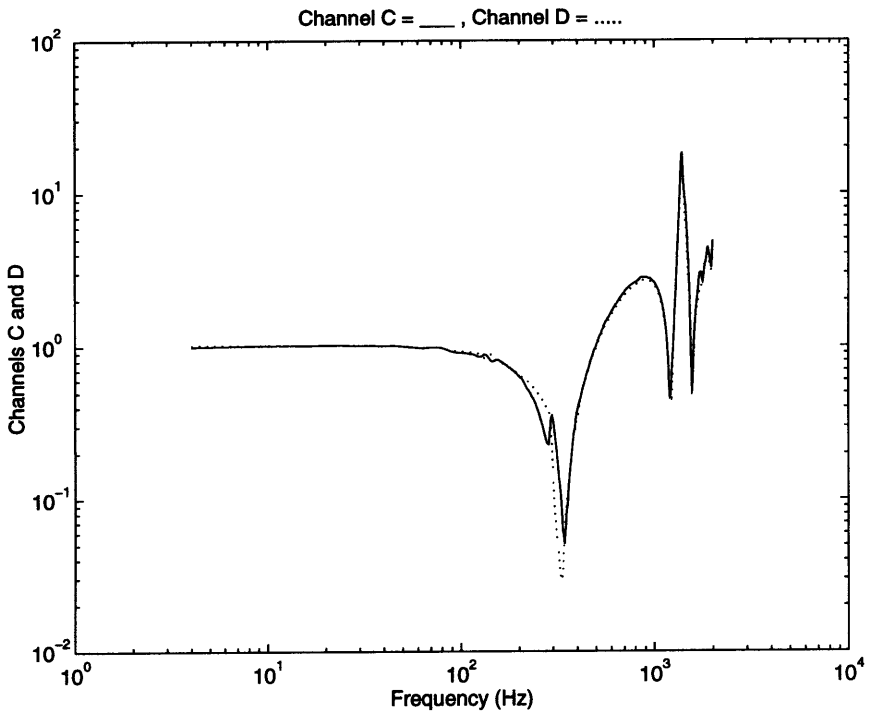

Figure C-73: X-Axis Tests, 112 lb Mass Between 5 and 8–Channels C and D

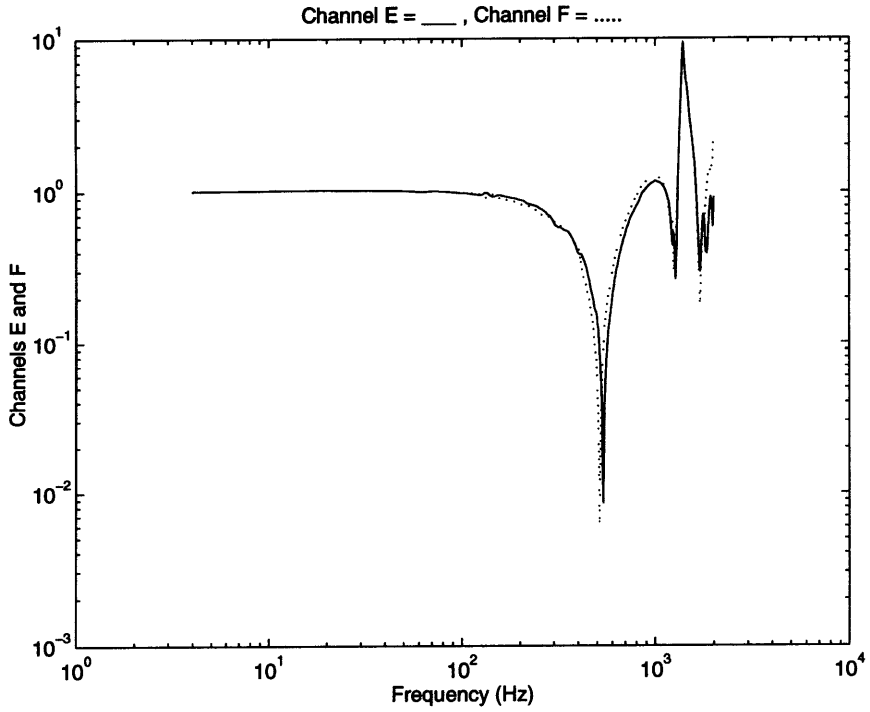

Figure C-74: X-Axis Tests, 112 lb Mass Between 5 and 8–Channels E and F

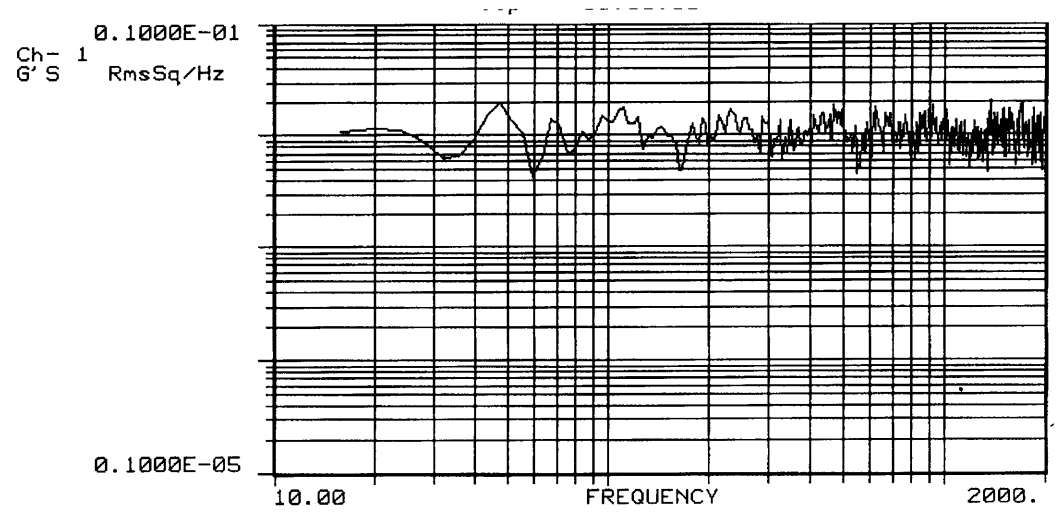

1KST
10:42:16
7/21/93 Ch- 1: CONTROL
T-1000 SLIP TABLE CK OUT
CONTROL AT OUTBOARD
ACCELEROMETERS ALONG CENTERLINE

Figure C-75: Control Spectrum for Outboard Control

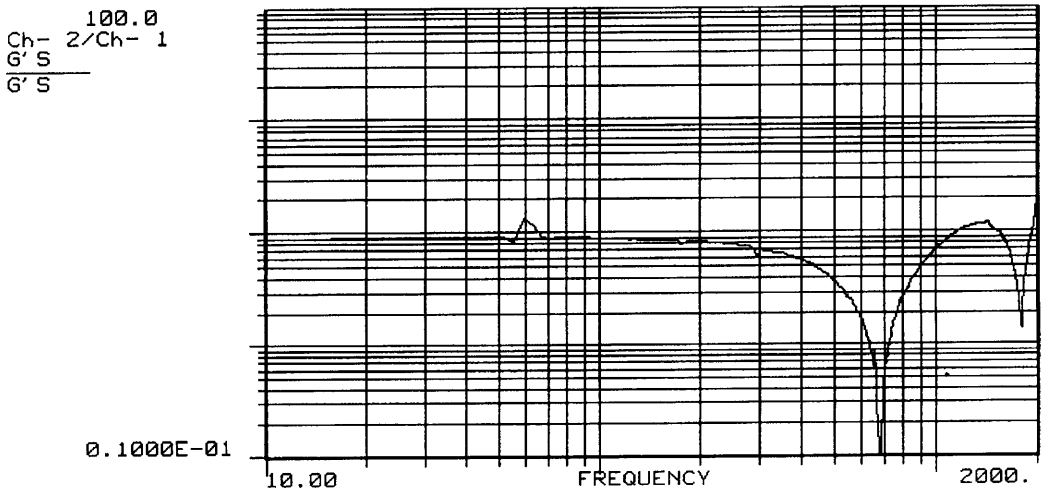

1KST
10:42:16 CH- 2: INBOARD
7/21/93 CH- 1: CONTROL
T-1000 SLIP TABLE CK OUT
CONTROL AT OUTBOARD
ACCELEROMETERS ALONG CENTERLINE

Figure C-76: Inboard Channel with Outboard Control

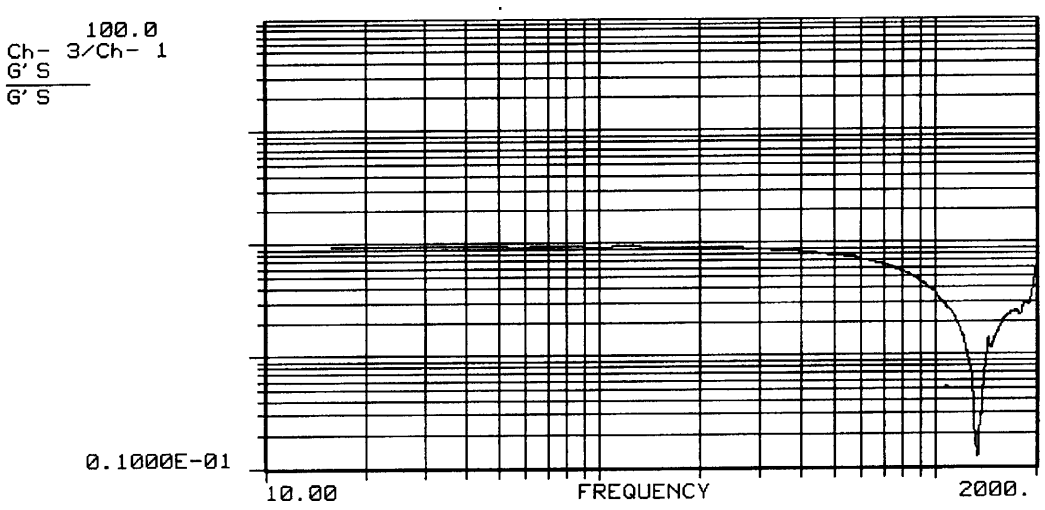

1KST
10:42:16 CH- 3: CENTER
7/21/93 CH- 1: CONTROL
T-1000 SLIP TABLE CK OUT
CONROL AT OUTBOARD
ACCELEROMETERS ALONG CENTERLINE

Figure C-77: Center Channel with Outboard Control

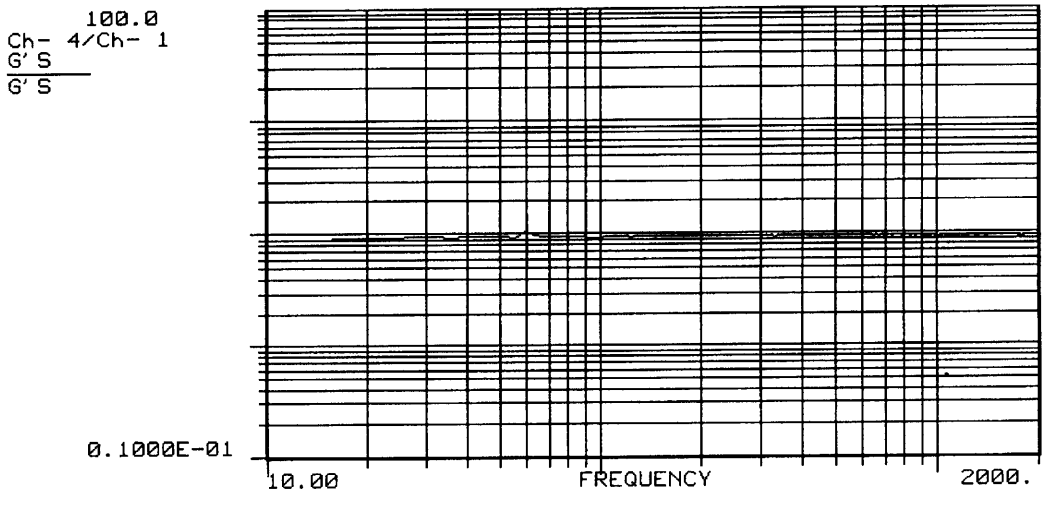

1KST
10:42:16 CH- 4: OUTBOARD
7/21/93 CH- 1: CONTROL
T-1000 SLIP TABLE CK OUT
CONROL AT OUTBOARD
ACCELEROMETERS ALONG CENTERLINE

Figure C-78: Outboard Channel with Outboard Control

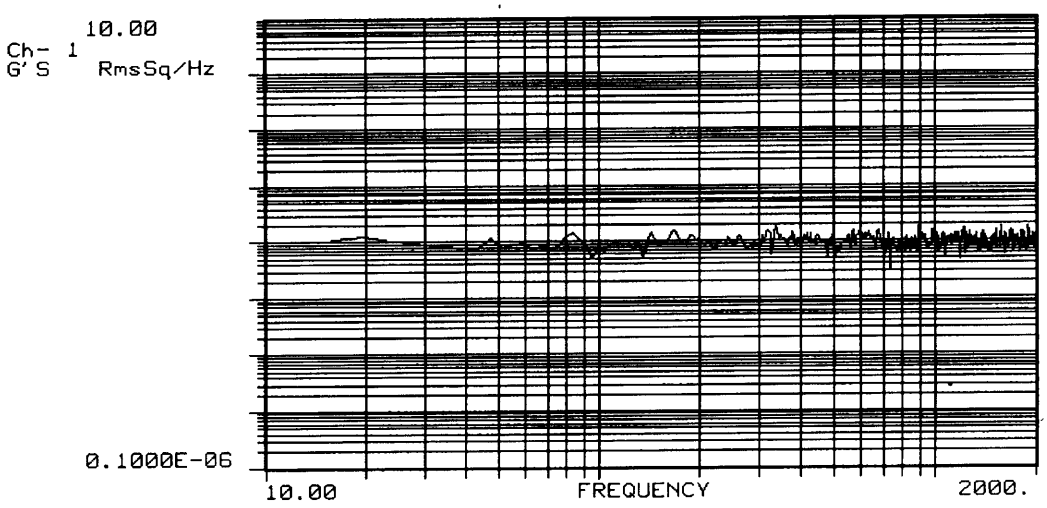

1KST
13:37:22
7/21/93 Ch- 1: CONTROL
T-1000 SLIP TABLE CK OUT
CENTER CONTROL
ACCELS ALONG CENTERLINE

Figure C-79: Control Spectrum for Center Control

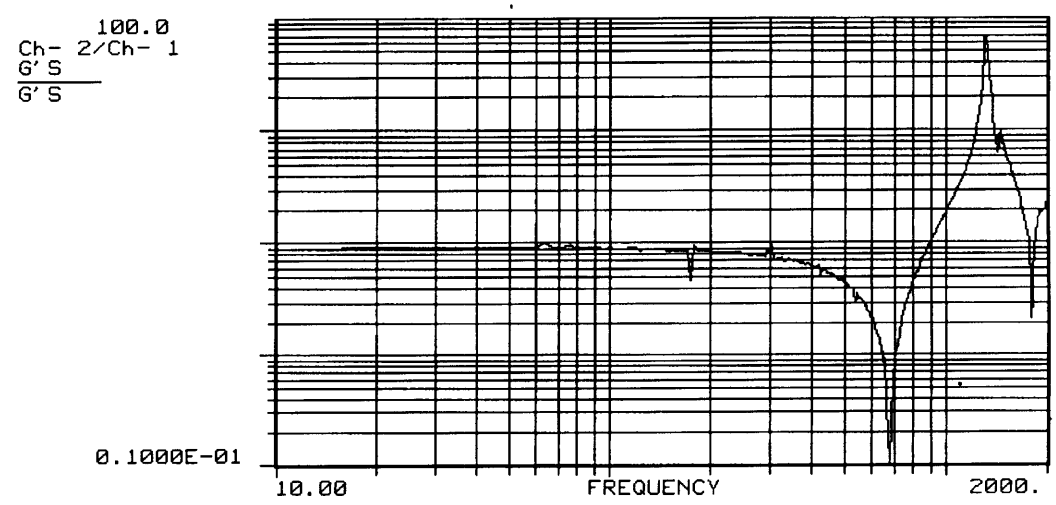

1KST
13:37:22 CH- 2: INBOARD
7/21/93 CH- 1: CONTROL
T-1000 SLIP TABLE CK OUT
CENTER CONTROL
ACCELS ALONG CENTERLINE

Figure C-80: Inboard Channel with Center Control

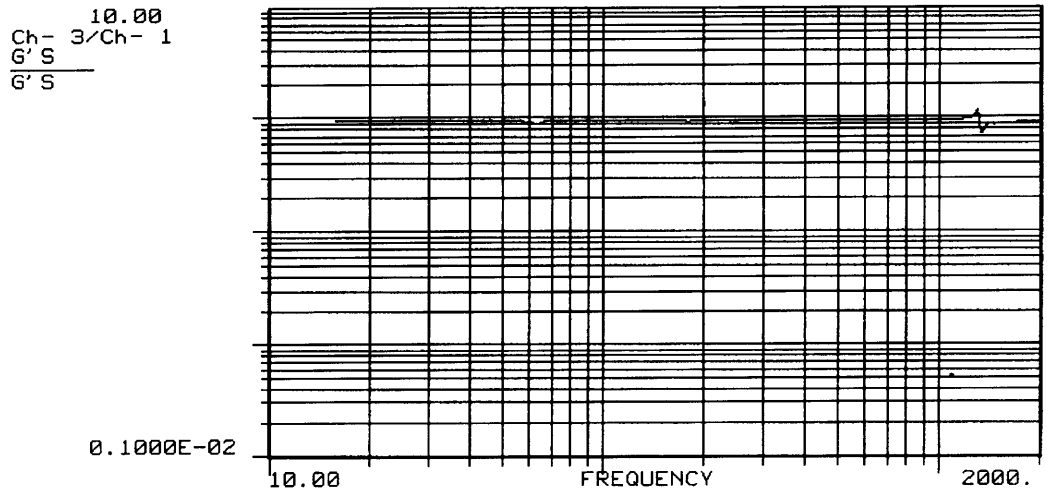

1KST
13:37:22 CH- 3: CENTER
7/21/93 CH- 1: CONTROL
T-1000 SLIP TABLE CK OUT
CENTER CONTROL
ACCELS ALONG CENTERLINE

Figure C-81: Center Channel with Center Control

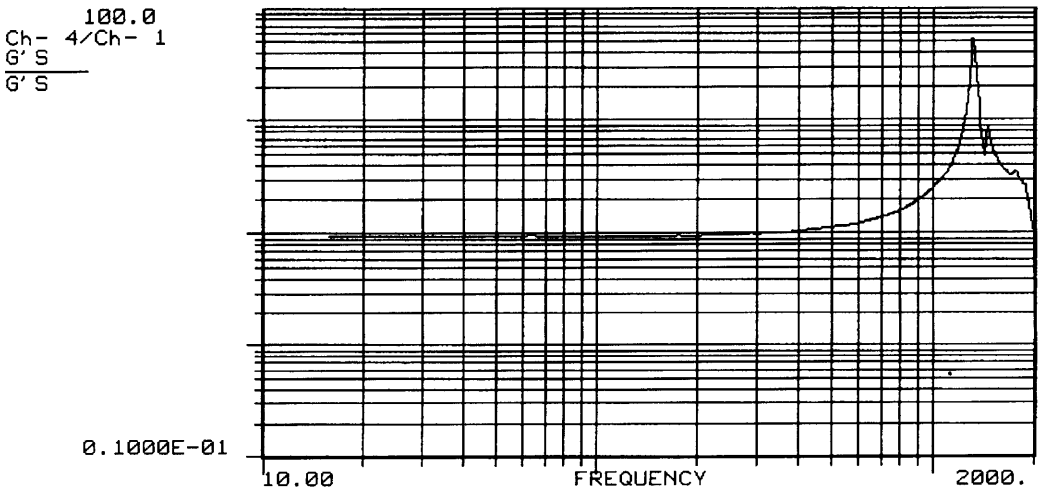

1KST
13:37:22 CH- 4: OUTBOARD
7/21/93 CH- 1: CONTROL
T-1000 SLIP TABLE CK OUT
CENTER CONTROL
ACCELS ALONG CENTERLINE

Figure C-82: Outboard Channel with Center Control

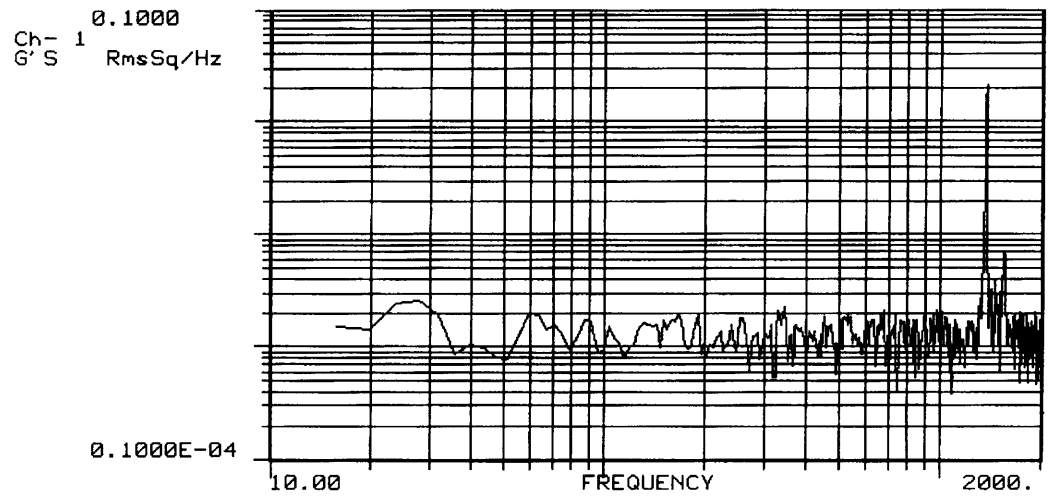

1KST
14:24:53
7/21/93 Ch- 1: CONTROL
T-1000 SLIP TABLE CK OUT
INBOARD CONTROL
ACCELS ALONG CENTERLINE

Figure C-83: Control Spectrum for Inboard Control

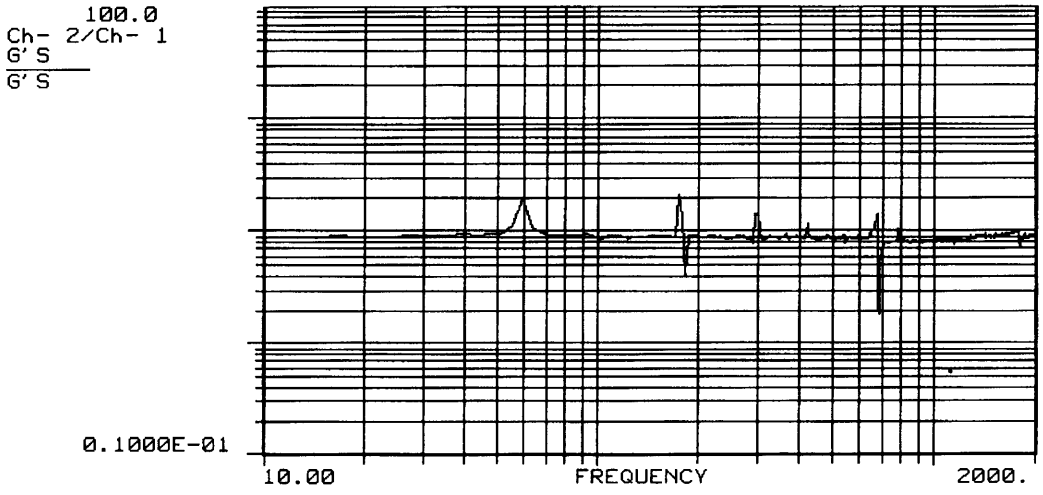

1KST
14:24:53 CH- 2: INBOARD
7/21/93 CH- 1: CONTROL
T-1000 SLIP TABLE CK OUT
INBOARD CONTROL
ACCELS ALONG CENTERLINE

Figure C-84: Inboard Channel with Inboard Control

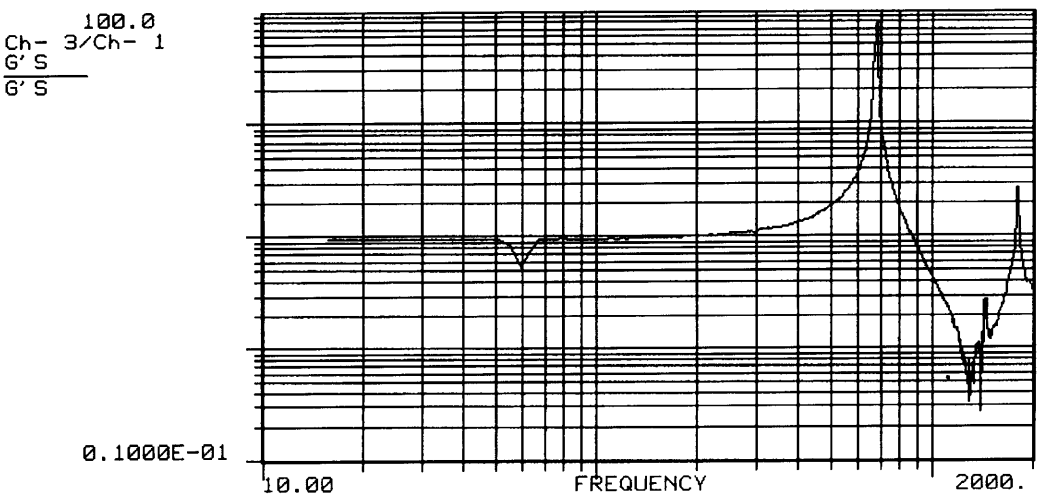

1KST
14:24:53 CH- 3: CENTER
7/21/93 CH- 1: CONTROL
T-1000 SLIP TABLE CK OUT
INBOARD CONTROL
ACCELS ALONG CENTERLINE

Figure C-85: Center Channel with Inboard Control

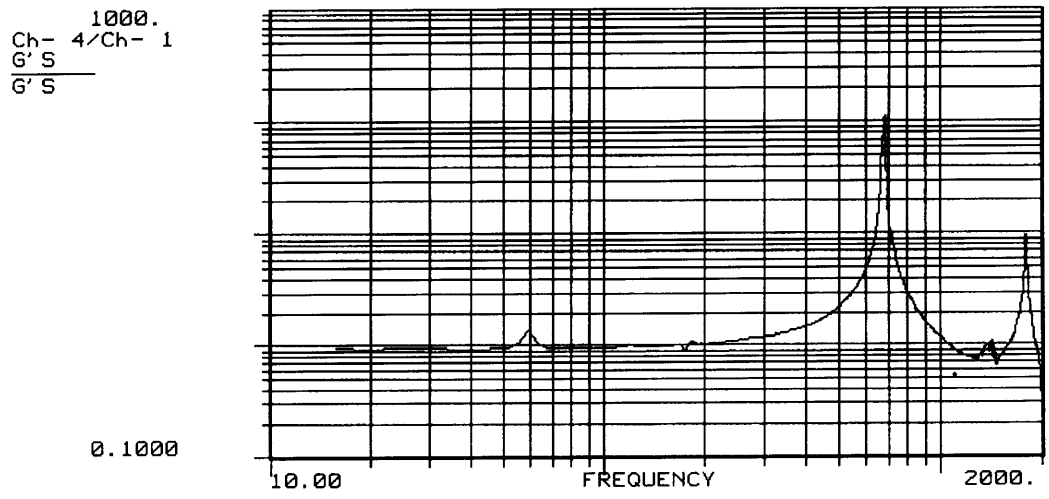

1KST
14:24:53 CH- 4: OUTBOARD
7/21/93 CH- 1: CONTROL
T-1000 SLIP TABLE CK OUT
INBOARD CONTROL
ACCELS ALONG CENTERLINE

Figure C-86: Outboard Channel with Inboard Control

Appendix D

Additional Analytical Results

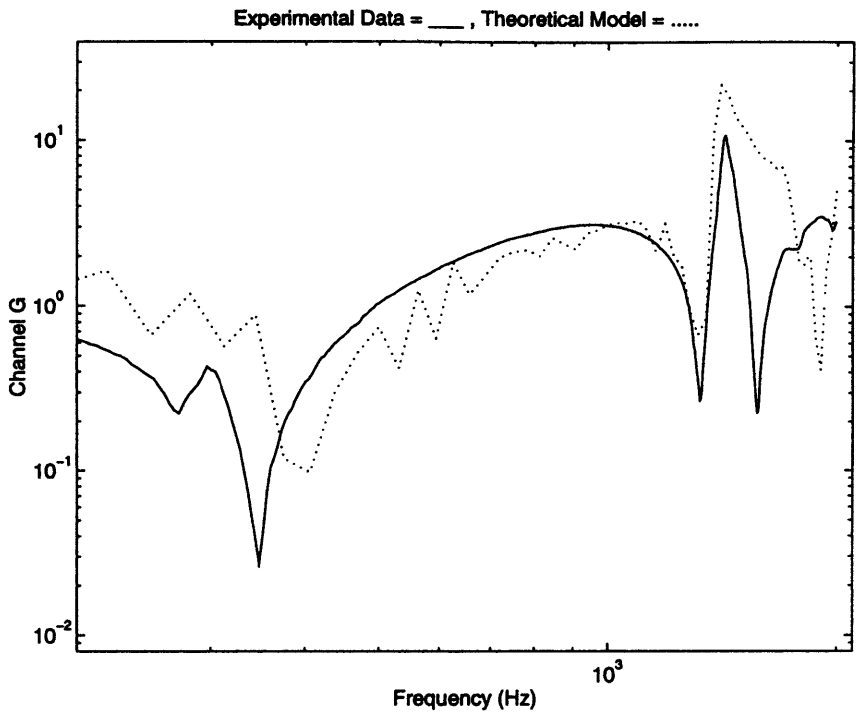

Figure D-1: 56 lb Mass Between 5 and 8: Comparison of Theoretically and Experimentally Attained Transfer Functions for Channel G

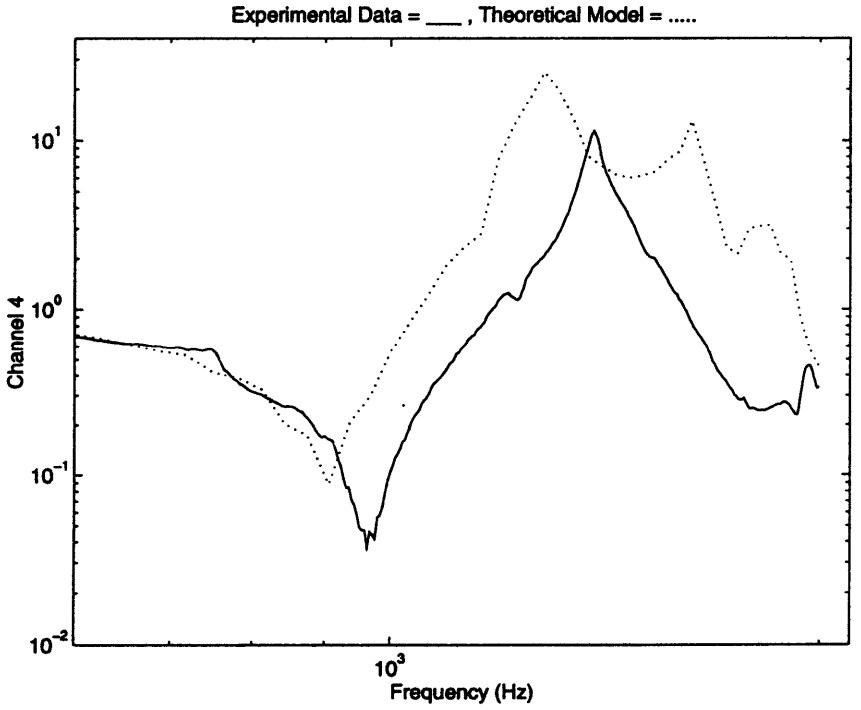

Figure D-2: 112 lb Mass Between 5 and 8: Comparison of Theoretically and Experimentally Attained Transfer Functions for Channel 4

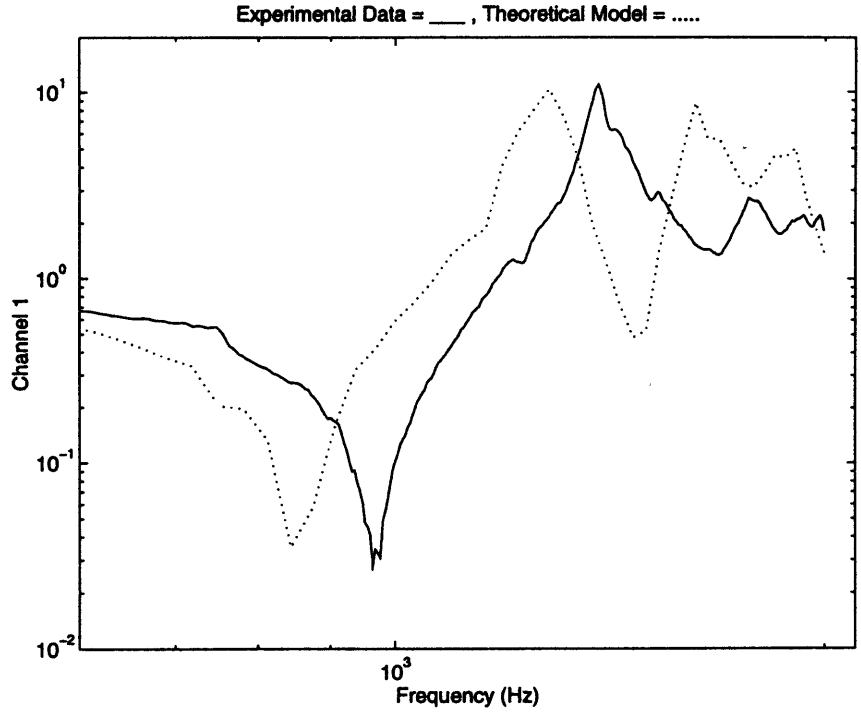

Figure D-3: 112 lb Mass Between 5 and 8: Comparison of Theoretically and Experimentally Attained Transfer Functions for Channel 1

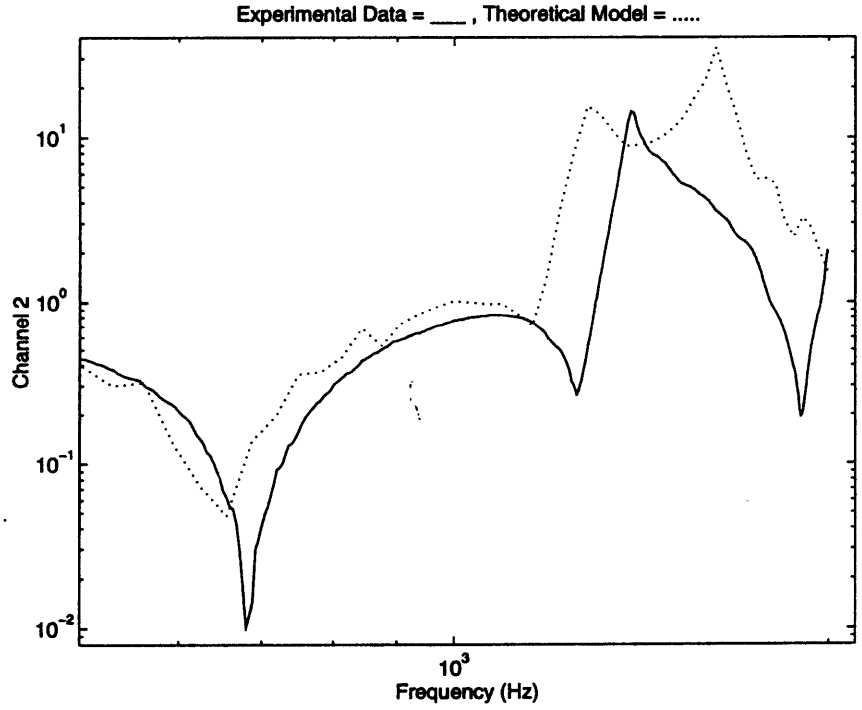

Figure D-4: 112 lb Mass Between 5 and 8: Comparison of Theoretically and Experimentally Attained Transfer Functions for Channel 2

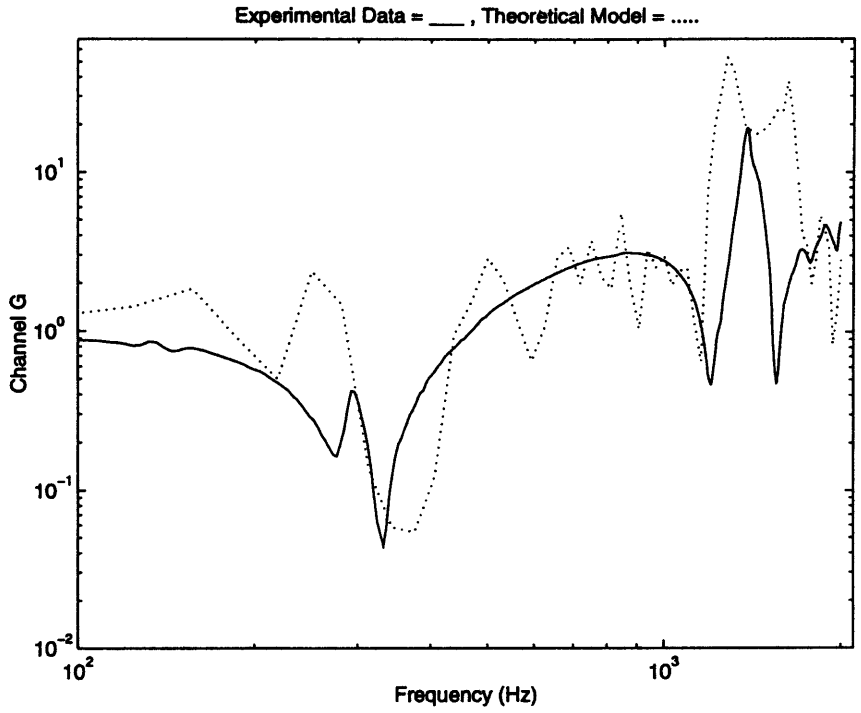

Figure D-5: 112 lb Mass Between 5 and 8: Comparison of Theoretically and Experimentally Attained Transfer Functions for Channel G

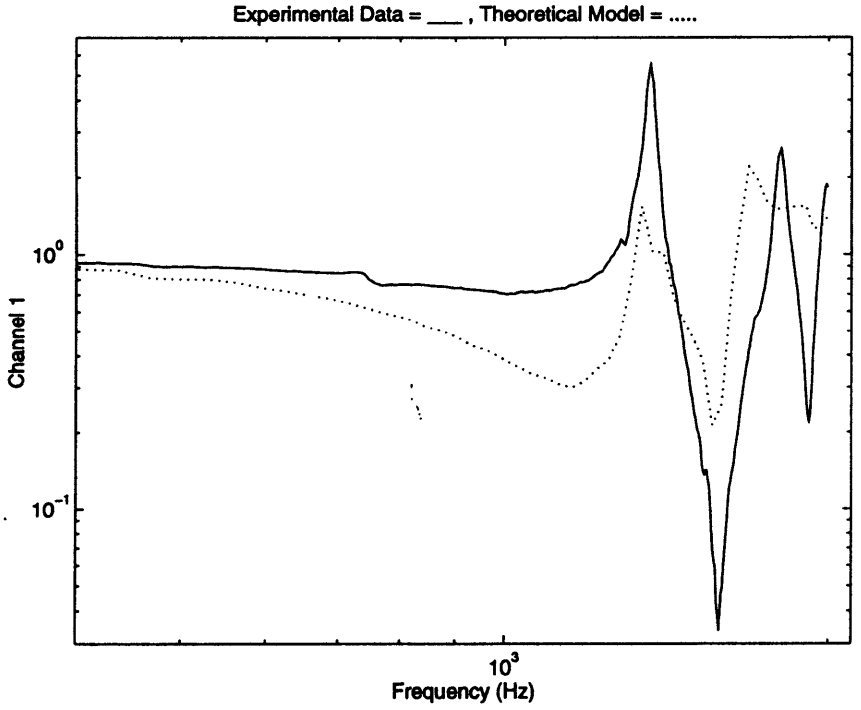

Figure D-6: 56 lb Mass Between 2 and 5: Comparison of Theoretically and Experimentally Attained Transfer Functions for Channel 1

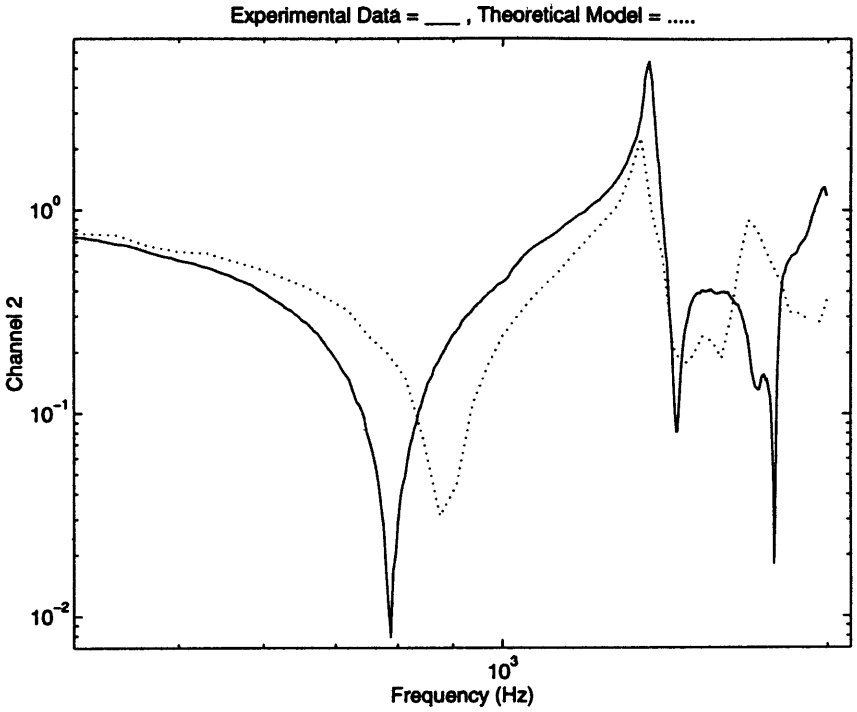

Figure D-7: 56 lb Mass Between 2 and 5: Comparison of Theoretically and Experimentally Attained Transfer Functions for Channel 2

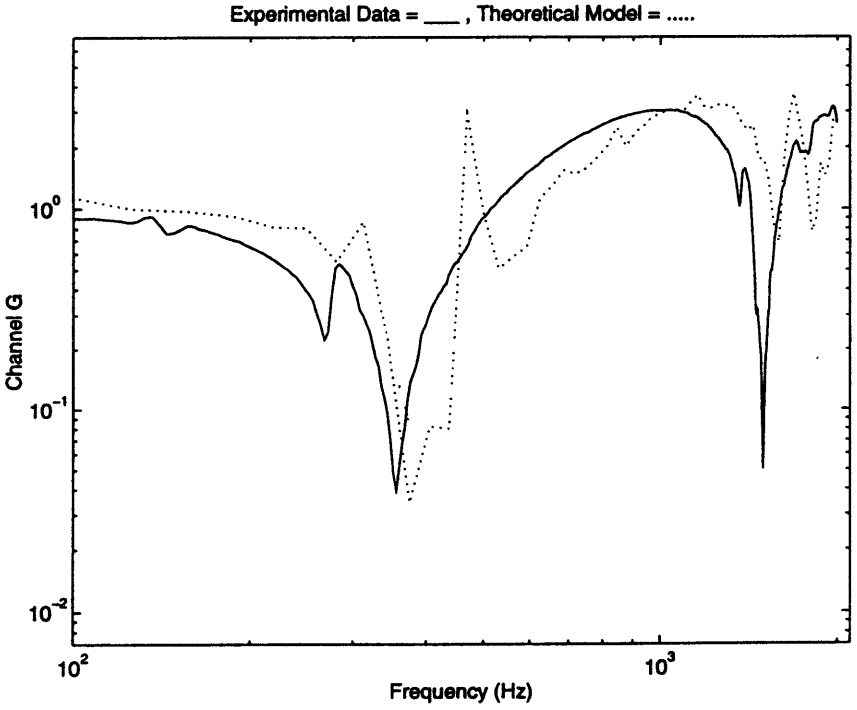

Figure D-8: 56 lb Mass Between 2 and 5: Comparison of Theoretically and Experimentally Attained Transfer Functions for Channel G

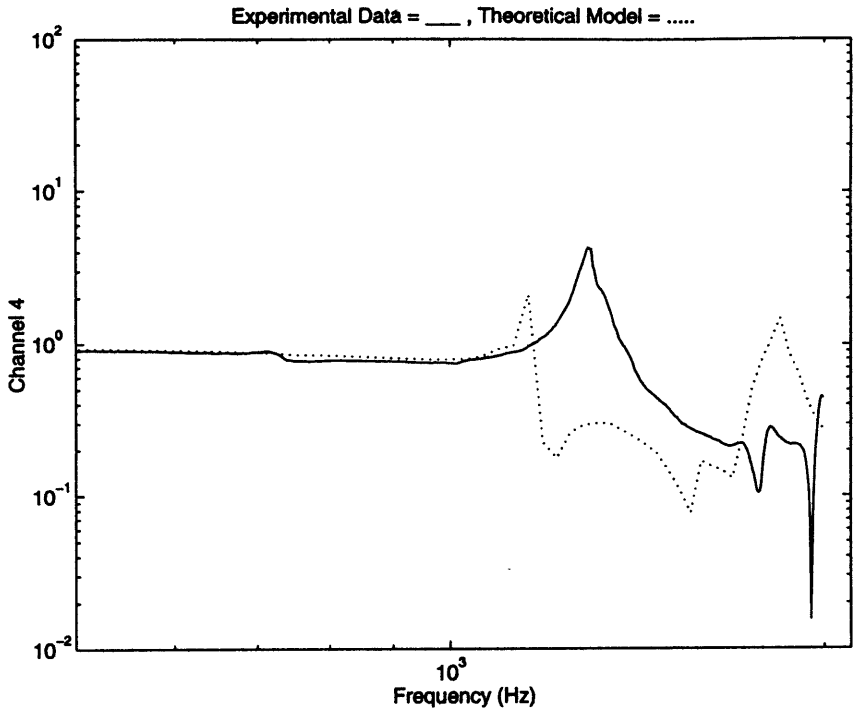

Figure D-9: 112 lb Mass Between 2 and 5: Comparison of Theoretically and Experimentally Attained Transfer Functions for Channel 4

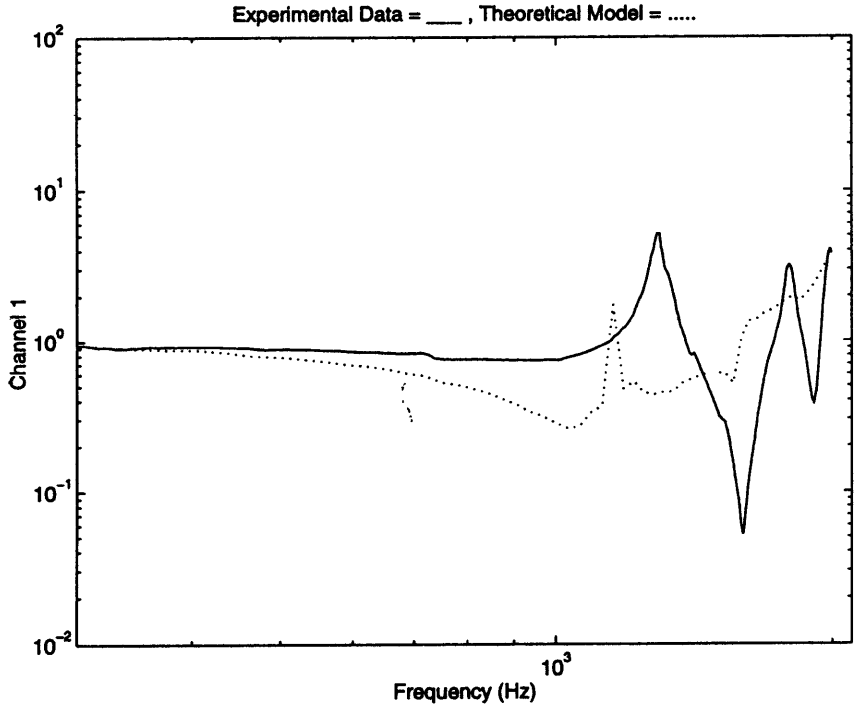

Figure D-10: 112 lb Mass Between 2 and 5: Comparison of Theoretically and Experimentally Attained Transfer Functions for Channel 1

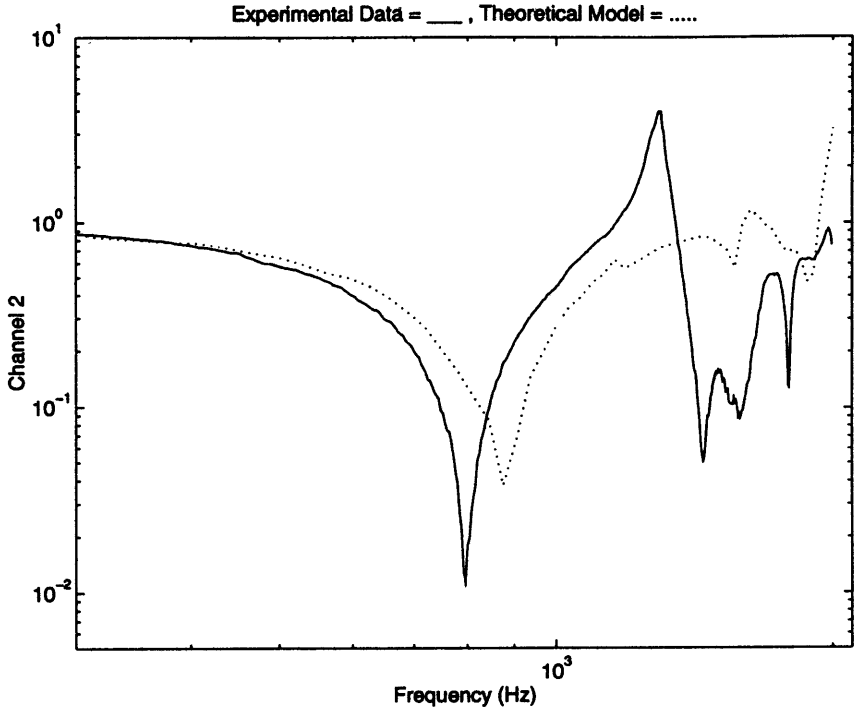

Figure D-11: 112 lb Mass Between 2 and 5: Comparison of Theoretically and Experimentally Attained Transfer Functions for Channel 2

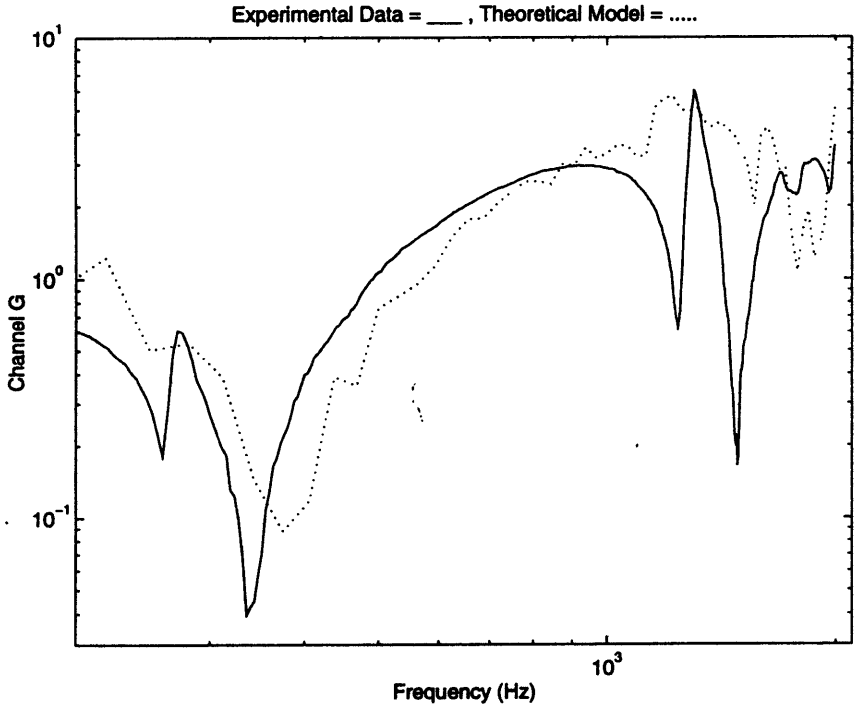

Figure D-12: 112 lb Mass Between 2 and 5: Comparison of Theoretically and Experimentally Attained Transfer Functions for Channel G

Bibliography

[1] Kimball Industries Incorporated, Monrovia, CA. *9100 Isolated Base with Bearing Line Table and SL Driver Bar*, January 1986.

[2] Malcolm Armstrong Cutchins. Preliminary investigation of the vibration characteristics of a slip table. Master's thesis, Virginia Polytechnic Institute, Engineering Mechanics, January 1964. Master's Thesis.

[3] Danny L. Gregory, Tommy G. Priddy, David O. Smallwood, and Tommy D. Woodall. Composite slip table of dissimilar materials for damping longitudinal modes. United States Patent 5,024,096, United States of America as Represented by the Department of Energy, Washingto, D.C., June 1991.

[4] Louie J. Lipp. Design consideration of expander heads for vibration testing–part i: Natural frequency equations for square, constant thickness expander heads. *Journal of the IES*, 1(1):45–55, March 1991.

[5] Louie J. Lipp. Design consideration of expander heads for vibration testing–part ii: Damping equations for square, constant thickness expander heads. *Journal of the IES*, 1(1):23–29, May 1991.

[6] Louie J. Lipp. Design consideration of expander heads for vibration testing–part iii: The inverted truncated pyramid expanding head. *Journal of the IES*, 1(1):39–46, July 1991.

[7] Robert S. Ballinger, Edward L. Peterson, and David L. Brown. Design optimization of a vibration exciter head expander. *Sound and Vibration*, 1(1):18–25, April 1991.

[8] Jr. C.H. Edwards and David E. Penney. *Elementary Differential Equations with Applications.* Prentice-Hall Inc., Englewood Cliffs, NJ, 1985.

[9] D.J. Ewins. *Modal Testing: Theory and Practice.* John Wiley and Sons, Inc., New York, NY, 1984.

[10] A.P. French. *Vibrations and Waves.* W.W. Norton and Company, New York, NY, 1971.

[11] Leonard Meirovitch. *Elements of Vibration Analysis.* McGraw-Hill Book Company, New York, NY, 1975.

[12] M.P. Norton. *Fundamentals of Noise and Vibration Analysis for Engineers.* Cambridge University Press, New York, NY, 1989.

[13] Singiresu S. Rao. *Mechanical Vibrations.* Addison-Wesley Series in Mechanical Engineering. Addison-Wesley Publishing Company, Reading, MA, second edition, June 1990.

[14] D.J. Benney, H.P. Greenspan, and J.E. Turner. *Calculus–An Introduction to Applied Mathematics.* McGraw-Hill Ryerson Limited, Canada, 1986.

[15] Brian P. Flannery, William H. Press, Saul A. Teukolsky, and William T. Vetterling. *Numerical Recipes–The Art of Scientific Computing (Fortran).* Cambridge University Press, New York, NY, 1986.

[16] Gilbert Strang. *Introduction to Applied Mathematics.* Wellesley-Cambridge Press, Wellesley, MA, 1986.

[17] J. S. Przemieniecki. *Theory of Matrix Structural Analysis*, pages 61–96. Dover Publications, Inc, Mineola, NY, 1985.

[18] D. E. Newland. *An Introduction to Random Vibrations, Spectral and Wavelet Analysis.* John Wiley and Sons, Inc., New York, NY, third edition, 1993.

[19] *GenRad Training Manual for the 2514*, 1987.

[20] Unholtz-Dickie Corporation. *Vibration Test Equipment*, 1980.

[21] K.W. Buesking and B.J. Sullivan. Dynamic analysis of carbon-carbon satellite truss. Final technical report, MSNW, Inc., San Marcos, CA, March 1993. Prepared Under: Naval Surface Warfare Center.

[22] Elizabeth Alpert, Rich Didday, and Rex Page. *FORTRAN 77 for Humans.* West Publishing Co., New York, NY, second edition, 1983.

[23] D.M. Etter. *Structured Fortran 77 for Engineers and Scientists.* The Benjamin/Cummings Publishing Co., Inc., Menlo Park, CA, 1983.

[24] Brian P. Flannery, William H. Press, Saul A. Teukolsky, and William T. Vetterling. *Numerical Recipes Example Book (Fortran).* Cambridge University Press, New York, NY, 1985.

[25] K. Gupta and J.S. Rao. *Introductory Course on Theory and Practice of Mechanical Vibrations.* John Wiley and Sons, New York, NY, 1984.

[26] Leslie Lamport. *Latex User's Guide and Reference Manual.* Addison-Wesley Publishing Company, Reading, MA, 1986.

[27] John Little and Loren Shure. *Signal Processing Toolbox for use with MATLAB.* The MathWorks, Inc., Natick, MA, August 1988.

[28] The MathWorks, Inc. *MATLAB User's Guide*, March 1991.

[29] John Ruminer, editor. *Environmental Testing*, Los Alamos, NM, April 1990. Los Alamos National Laboratory.

[30] Gilbert Strang. *Linear Algebra and its Applications.* Harcourt Brace Jovanovich, Publishers, San Diego, CA, third edition, 1988.

[31] Karl Unholtz. Vibration testing machines. In Cyril M. Harris, editor, *Shock and Vibration Handbook*. McGraw-Hill Book Company, New York, NY, 1988. Third Edition.